Terahertz scanning tunneling microscopy on metals, semiconductors, and carbon nanostructures

by

Jesús Alejandro Marín Calzada

A thesis submitted in partial fulfillment of the requirements for the degree of

Doctor of Philosophy

Department of Physics
University of Alberta

Abstract

Scanning probe microscopes routinely provide atomic resolution of numerous materials, but lack the tools to investigate their ultrafast dynamics. Laser pulses can be generated in the femtosecond or even attosecond regime, but their spatial application is restricted by the diffraction limit. Coupling ultrafast laser pulses to scanning tunneling microscopes (STM) has recently opened a window into an unexplored world where subnanometer spatial resolution and subpicosecond temporal resolution can be achieved simultaneously. As these techniques evolve in the scientific community, different characterization methods have been developed to gain a deeper understanding of the different aspects behind their operating principles. Great efforts are dedicated on this front, since any improvement in their performance will help to push the technological boundaries even further.

In this thesis, single-cycle terahertz pulses (1 THz bandwidth) were coupled to the tip of a scanning tunneling microscope (THz-STM), which enhances and localizes the fields of the incident pulse at the tip apex. The surface of Au(111) was first examined to establish a benchmark of the THz-STM system. A comparison of these measurements with previous results on Cu(111) shows agreement and similarities between these two metals. Nanostructures are ideal candidates for THz-STM because their dynamic response can be studied individually, thanks to the nanometer resolution of the system. Therefore, the properties of single-walled carbon nanotubes (6,5) were explored with THz-STM, but were found to be unstable in our experimental setting. Graphene islands, on the contrary, exhibited high stability and the first THz-STM images of graphene islands reported here show their capability to identify structural defects that have otherwise very similar profiles in a conventional topographic image. An attempt to perform a pump-probe experiment on these nanostructures revealed an undesired electron emission from the sample substrate. Consequently, the electron photoemission occurring at the STM junction under illumination by 70 fs ultrafast near-infrared laser pulses centered at 800 nm was investigated. Photoemission experiments with W and Au tips on an Au(111) substrate revealed that multiphoton photoemission (MPP) was the main emission mechanism in our experimental setting.

The use of a wide bandgap semiconductor as a substrate is proposed to eliminate its photoemission and facilitate optical pump-terahertz probe experiments on nanostructures. Three different semiconductive samples were studied: p-doped GaN, n-type Si-doped GaAs(110), and p-type Zn-doped GaAs(110). The results demonstrated that MPP was suppressed on a wide bandgap semiconductor, such as GaN, confirming it is a good candidate as a substrate for ultrafast pump-probe experiments. An initial attempt to perform an optical pump-THz probe experiment on a single-walled carbon nanotube on GaN is presented. However, the pump-probe signal closely resembled the THz near field waveform at the tip apex observed with photoemission sampling. The thermal expansion of the semiconductors was additionally investigated in the STM since thermal effects from a pump beam can also interfere with the experiments. The measurements showed that the tip expansion is usually small compared to that of the sample, and that the least thermal expansion occurred on the GaN sample which reinforces the proposal to use it as a substrate.

Finally, the design and construction of a home-built ambient STM is included. Basic THz-STM measurements on a single-walled carbon nanotube and the acquisition of a THz-induced photoemission waveform proved that the system is capable of performing THz-STM and ultrafast optical pump-THz probe experiments.

Preface

The research presented in this thesis was carried out from September 2016 to February 2023 at the University of Alberta under the supervision of Professor Frank A. Hegmann. The results presented in Chapters 5 to 9 were obtained with assistance and feedback from Peter Nguyen, Howe Simpson, David Purschke, Nils Refvik, and Christina Strilets, and Chapters 5 and 6 were done in collaboration with Yang Luo. The GaN sample used in Chapter 8 was provided by Andreas Zeidler. The ambient STM presented in Chapter 10 was designed and built by me, with advice from Mark Salomons, and constructed with the help and support of Beipei Shi, Vedran Jelic, Yang Luo, and Howe Simpson. Subsequently, it was debugged and operated by Christina Strilets. All the figures in this thesis were created by myself except for Fig. 1.1, which contains a 3D model of a tungsten tip apex created by the research group of Robert Wolkow and a Si(111)-7x7 image taken by Vedran Jelic, Figs. 2.3, 2.5 to 2.9, 2.11 and 2.13, which were adapted from other references, and Fig. 10.7, which was acquired by Christina Strilets. The work presented here has contributed to one collaborative refereed publication, one oral presentation, and two conference poster presentations, which are described below. Two collaborative refereed publications that are not directly related to this work but were published during the time of this thesis are also included at the end of this preface.

Collaborative refereed publication:

- Y. Luo, V. Jelic, G. Chen, P. H. Nguyen, Y.-J. R. Liu, J. A. M. Calzada, D. J. Mildenberger, and F. A. Hegmann, "Nanoscale terahertz STM imaging of a metal surface", *Physical Review B*, vol. 102, no. 20, Nov. 2020. Available: https://doi.org/10.1103/physrevb.102.205417

Oral presentation:

- J. A. M. Calzada, *Terahertz scanning tunneling microscopy (THz-STM)*, Canadian Photonics Online Meetup (CANPOM), Dec. 2020. Available: https://canpom.photonicsonlinemeetup.org

Conference poster presentations:

- J. A. M. Calzada, V. Jelic, Y. Luo, P. H. Nguyen, and F. A. Hegmann, *Home-built ambient THz-STM system*, The 8th International Conference on Optical Terahertz Science and Technology (OTST), Mar. 2019. Available: http://www.otst.org/

- Y. Luo, J. A. M. Calzada, G. Chen, P. H. Nguyen, V. Jelic, Y.-J. R. Liu, D. J. Mildenberger, H. R. J. Simpson, and F. A. Hegmann, *Characterization of THz-induced bias voltage modulation in an STM*, 45th International Conference on Infrared, Millimeter, and Terahertz Waves (IRMMW–THz), Nov. 2020. Available: https://doi.org/10.1109/IRMMW-THz46771.2020

Collaborative refereed publications not directly related:

- M. Malac, D. Homeniuk, M. Kamal, J. Kim, M. Salomons, M. Hayashida, J. A. M. Calzada, D. Vick, D. Price, and R. Egerton, "NanoMi: An open source electron microscope component integration", *Microscopy and Microanalysis*, vol. 28, no. S1, pp. 3164–3165, Aug. 2022. Available: https://doi.org/10.1017/s1431927622011746

- M. Malac, J. A. M. Calzada, M. Salomons, D. Homeniuk, P. Price, M. Cloutier, M. Hayashida, D. Vick, S. Chen, S. Yakubu, Z. D. Wen, M. Leeson, M. Kamal, J. Pitters, J. Kim, X. Wang, O. Adkin-Kaya, and R. Egerton, "NanoMi: An open source electron microscope hardware and software platform", *Micron*, vol. 163, p. 103 362, Dec. 2022. Available: https://doi.org/10.1016/j.micron.2022.103362

"But I am not afraid to consider the final question as to wether, ultimately - in the great future - we can arrange the atoms the way we want; the very atoms, all the way down!"

- Richard P. Feynmann

"I don't study to know more, but to ignore less."

- Sor Juana Inés de la Cruz

Acknowledgments

I am deeply grateful to my supervisor Frank Hegmann for being patient, for being constantly involved in the experiments, for teaching me to think deeper by questioning everything, for the discussions and support throughout the project, and for the memorable experiences outside of the lab. I am grateful for the advice and guidance of my committee members, Mark Freeman and John Davis, since the beginning of the project. Special gratitude is extended to Vedran Jelic for teaching me how to use the THz-STM system, for the good laughs and for showing me how exciting science can be. I am grateful to the people who worked with me on the THz-STM project: Peter Nguyen, Daniel Mildenberger, Tianwu Wang, Yang Luo, Howe Simpson, Hüseyin Azazoglu, Ray Liu, Nils Refvik, and Christina Strilets, as well as to my colleagues in the lab: Mary Narreto, Charles Jensen, Cameron Hough, David Purschke, Naaman Amer, Chenxi Huang, Aran McDowell, Julieta Hernández, Sam Ruttiman, Makoto Schreiber, Max Stratmann and Niloufar Sadeghi.

I would like to thank Greg Popowich and James Chaulk for their technical support in the lab, and especially thank Beipei Shi for his great efforts helping me build the mechanical parts for the ambient STM. I want to thank Mark Salomons for his guidance and advice during the design and construction of the ambient STM, Daniel Berard for providing the software and basic electronic components of the ambient STM, and Andreas Zeidler for providing the p-type Zn-doped GaN sample used in the photoemission experiments. And I thank Sarah Derr, Kailey Robertson, Raj Joshi, and Rae Beaumont for the administrative assistance.

I am grateful for the financial support provided by Consejo Nacional de Ciencia y

Tecnología (CONACyT- México) during the first four years of this Ph.D. This work was also supported by the Natural Sciences and Engineering Research Council of Canada (NSERC), the Canada Foundation for Innovation (CFI), and the Alberta Innovates Technology Futures (AITF) Strategic Chairs Program, as well as internal funding from the University of Alberta. And I would like to thank Marek Malac for the opportunity to be part of the NANOMI project at the National Research Council Canada (NRC), this project has taught me a lot and it also provided the necessary funding to complete my degree.

Finally, I would like to thank my parents, Alejandra Calzada and Jesús Marín, for their unconditional love, guidance, and support. I am thankful to my wife, Liliana Wilson, for her patience and support throughout this journey. And with great joy, I dedicate this work to our daughter Gaia Marín Wilson, who has brought a new light into our family, and to our bright little spark, who is waiting to be born.

Contents

List of Tables

List of Figures

Abbreviations & Acronyms

ABH Apparent Barrier Height.

AC Analog Current.

ADC Analog-to-Digital Converter.

AFM Atomic Force Microscopy.

AITF Alberta Innovates Technology Futures.

AlN Aluminium Nitride.

CAD Computer-Aided Design.

CANPOM Canadian Photonics Online Meetup.

CFI Canada Foundation for Innovation.

CoMoCAT Cobalt-Molybdenum Catalyst.

CONACyT Consejo Nacional de Ciencia y Tecnología.

CPA Chirped-Pulse Amplification.

CVD Chemical Vapor Deposition.

CW Continuous-Wave.

DAC Digital-to-Analog Converter.

DC Direct Current.

DCB Dichlorobenzene.

DCE Dicholorethane.

DMF Dimethyl-formamide.

DOS Density of States.

EFM Electric Force Microscopy.

EO Electro-Optic.

EOS Electro-Optic Sampling.

FCC Face-Centered Cubic.

FD Fowler-DuBridge.

FE Field Emission.

FEA Finite Element Analysis.

FWHM Full-Width-Half-Maximum.

GaAs Gallium Arsenide.

GaBiAs Gallium Bismide Arsenide.

GaN Gallium Nitride.

GS Guided Structure.

HCP Hexagonal Close Packing.

HOPG Highly Oriented Pyrolytic Graphite.

HV High Voltage.

ID Internal Diameter.

InGaAs Indium Gallium Arsenide.

IRMMW Infrared, Millimeter, and Terahertz Waves.

LDOS Local Density of States.

LTEM Laser Terahertz Emission Microscopy.

MCB Monochlorobenzene.

MFM Magnetic Force Microscopy.

MPP Multiphoton Photoemission.

MWCNTs Multi-Walled Carbon Nanotubes.

NaOH Sodium Hydroxide.

NMP N-methylpyrrolidone.

NRC National Research Council Canada.

NSERC Natural Sciences and Engineering Research Council of Canada.

OTST Optical Terahertz Science and Technology.

PC Photoconductive.

PCB Printed Circuit Board.

PE Photoemission.

PtIr Platinum Iridium.

PZT Lead Zirconate Titanate.

QE Quantum Efficiency.

RLC Circuit containing a Resistor, an Inductor and a Capacitor.

RMS Root Mean Square.

SNOM Scanning Near-Field Optical Microscopy.

SPM Scanning Probe Microscopy.

STM Scanning Tunneling Microscopy.

STS Scanning Tunneling Spectroscopy.

SWCNT Single-Walled Carbon Nanotubes.

TCB Trichlorobenzene.

TE Thermionic Emission.

TEM Transmission Electron Microscopy.

THz Terahertz.

TPX Polymethylpentene.

TSM Three-Step Model.

UHV Ultra-High-Vacuum.

WKB Wentzel-Kramers-Brillouin.

WO Tungsten Oxide.

ZnTe Zinc Telluride.

Chapter 1

Introduction

To develop new and better electronic devices, technological boundaries must be pushed to the limit in order to explore new phenomena at smaller length scales and faster probing times. To study the world on a small scale, scanning probe microscopy (SPM) has proven to be a powerful technique that allows us to examine the topography and the local properties of a sample surface [1]. The SPM family includes high spatial resolution techniques such as scanning tunneling microscopy (STM) [2–4], atomic force microscopy (AFM) [5], electric force microscopy (EFM) [6], magnetic force microscopy (MFM) [7, 8], and scanning near-field optical microscopy (SNOM) [9, 10]. On the other hand, for the temporal aspect, great efforts have been made to explore ultrafast phenomena in the picosecond regime due to the carrier and molecular dynamics that occur at this time scale. However, experiments in this regime proved to be challenging because of the temporal response limitations of purely electronic devices. Fortunately, the creation of ultrafast lasers that generate femtosecond pulses opened the possibility for new techniques to be developed [11], such as the generation and detection of electromagnetic radiation in the terahertz regime with picosecond time duration [12–14], which allowed for the use of single-cycle THz pulses to probe ultrafast dynamics.

THz spectroscopy is spatially restricted by the diffraction limit ($\lambda/2 = 0.15\,\mathrm{mm}$ at 1 THz). One solution to overcome this limitation is to combine scanning probe microscopes and THz radiation to simultaneously obtain high spatial and temporal resolution. Sub-micrometer spatial resolution has been achieved with techniques such as aperture-coupled detectors [15–17], laser terahertz emission microscopy (LTEM) [18], tapered photoconductive probes [19] and electro-optic sampling in the terahertz near field [20–22]. However, techniques that have achieved $< 100\,\mathrm{nm}$ spatial resolution are based on coupling the radiation to sharp metal tips, mainly due to their ability to enhance and confine THz radiation at the apex [23]. Two examples are scattering-type (apertureless) scanning near-field optical microscopy (s-SNOM) [24–31] and lightwave-driven terahertz scanning tunneling microscopy (THz-STM) [32–48], which is illustrated in Fig. 1.1.

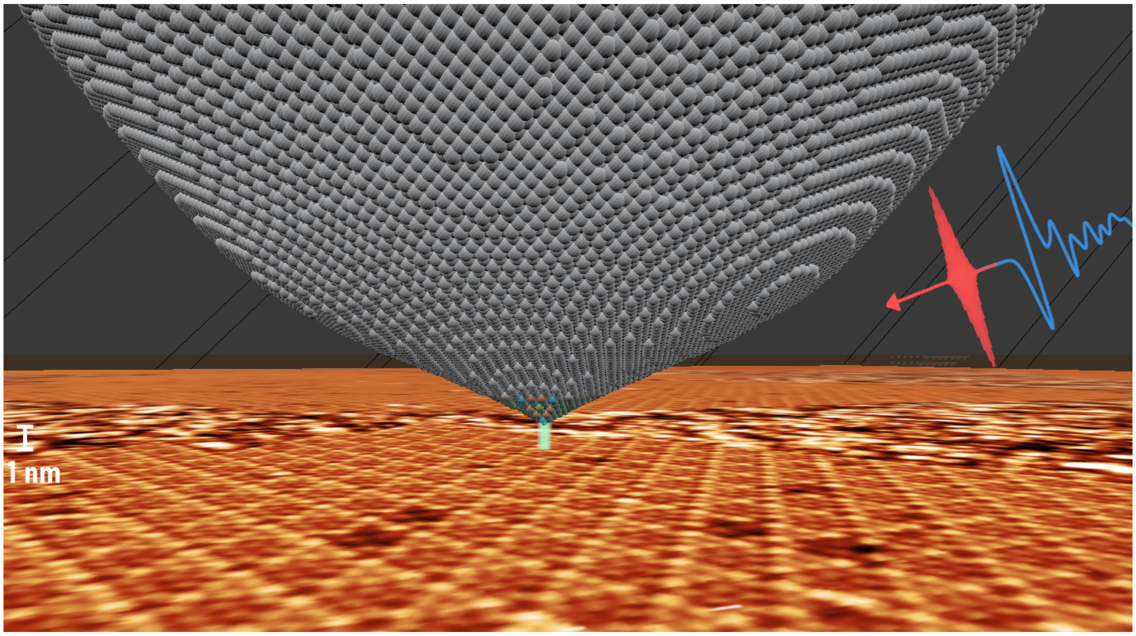

Figure 1.1: Scaled model of an STM tip apex scanning the surface of a Si(111)-7x7 sample. The actual topographic corrugation of the sample surface is included, but it is so small that it looks flat. The distance from the lowest atom of the tip to the sample surface was set to be 1 nm. A schematic of an ultrafast near-infrared pulse (red) and a single-cycle THz pulse (blue) are shown to illustrate their integration with the STM. *[Credits: the 3D model of the atomic structure of the W tip apex was created by Robert Wolkow's group, and the Si(111)-7x7 image was taken by Vedran Jelic.]*

The spatial resolution of s-SNOM is determined by the tip apex size, typically a few or tens of nanometers, while for THz-STM, it is determined by the quantum tunnel junction, which is typically smaller than a nanometer [23]. The exponential dependence of the STM tunnel current as a function of tip-sample distance is the key to obtaining spatially localized measurements with sub-nanometer resolution [1, 4, 49]. The uniqueness of THz-STM is the fact that the confined and enhanced THz pulses at the tip apex produce a transient modulation of the bias voltage between the tip and the sample, which in turn modulates the tunneling current. The THz-STM has been successfully established as a new technique to investigate the ultrafast at the nanoscale. For instance, studies on single molecules [35, 40, 50], nanostructures [32, 44] and materials surface dynamics [34, 37, 39, 41, 44] have recently been published. However, different aspects of this technique are still being explored. One aspect is the relation between the free-space THz pulse and the near field waveform at the tip apex once it has been coupled [50]. For this, terahertz photoemission sampling has been used to measure the near field waveform at the apex of a tip [39, 42, 51]. Although more characterization is needed, the THz-STM technique has proven to be a powerful tool to investigate the ultrafast at the nanoscale.

Because of the promising future of the THz-STM technique, this work focuses on the system characterization and understanding of THz-STM as a research tool, on the exploration of nanostructures using THz-STM, and on the proposal of a sample substrate suitable for pump-probe experiments. The outline of this thesis is as follows: Chapter 2 will discuss the theoretical background of STM, ultrafast lasers, terahertz pulses, their integration into a THz-STM, and various mechanisms of electron emission. Chapter 3 will present all the components that form the THz-STM system, the experimental methods for data collection, and the preparation procedures of STM tips. The sample preparation procedures are presented in Chapter 4, together with conventional STM and scanning tunneling spectroscopy (STS) measurements. The samples include Au(111), single-walled carbon nanotubes, gallium arsenide and gallium nitride. Chapter 5 contains the results of THz-STM measurements performed on the surface of Au(111), which acted as a benchmark and helped calibrate the THz-induced current channel of the THz-STM system. These results are also compared to previous results obtained on Cu(111). Chapter 6 shows the results of THz-STM measurements performed on single-walled carbon nanotubes and on graphene islands, and their capability to identify structural defects. Then, in Chapter 7, the photoemission of electrons from metallic tips (Au and W) induced by ultrafast laser pulses was investigated over an Au(111) substrate, and a discussion on the photoemission generation mechanism is presented. In Chapter 8, photoemission measurements with a W tip were obtained from different semiconductive samples to find a suitable substrate candidate for optical pump-THz probe experiments. Additionally, Chapter 9 discusses thermal expansion effects of laser pulse illumination on those semiconductors in the STM. Finally, Chapter 10 includes a brief description of the design and construction of a home-built ambient STM system, which was aimed at being a rapid turn-around THz-STM system to study the coupling of THz pulses onto a variety of different tips and under different conditions.

Chapter 2

Theoretical background

Understanding the physical principles behind an experiment is crucial to properly interpret the resulting data. The fundamentals of a THz-STM experiment will be covered in this chapter, including the operation principles of STM, the elemental techniques to produce ultrafast laser pulses, and the subsequent methods used for the generation and detection of THz pulses. The coupling of THz pulses onto STM tips and the electron emission mechanisms relevant to the photoemission experiments will also be discussed.

2.1 Scanning Tunneling Microscopy

In classical mechanics, when particles encounter a potential barrier with energy higher than their own, they cannot cross the barrier and are reflected back. However, in quantum mechanics, these particles can penetrate the potential barrier and “tunnel” through it, as shown in Fig. 2.1a. Based on this principle, the scanning tunneling microscope (STM), initially developed by G. Binnig, H. Rohrer, C. Gerber and E. Weibel [2], has led to many discoveries in nanoscience since its invention in the early 1980s [52]. The STM consists of a sharp metallic tip that is brought in close proximity to the surface of a conductive sample (Fig. 2.1b). The distance between the metallic tip and the sample is so small (a few Ångströms) that the potential barrier width of the vacuum (or air) is reduced considerably and the wavefunction of the electrons from the tip and sample begins to overlap. The energy diagram shown in Fig. 2.1c is commonly used to represent the potential barrier at the STM junction, where it is assumed that the tip and sample are ideal conductors with work functions Φ_t and Φ_s, respectively, and that the system is in electrical equilibrium. (The work function Φ is the minimum energy needed to extract an electron from the surface.) In conventional STMs, the tip is electrically grounded and a bias voltage can be applied to the sample. A positive (negative) bias voltage will lower (raise) the Fermi energy level of the sample with respect to the tip, and a tunneling current will start to flow (Fig. 2.1d).

The distance between tip and sample, also called tip height, z, can be adjusted in real-time to maintain a constant tunneling current. To achieve this, the tip is attached to a piezoelectric transducer that expands and contracts when a potential difference is applied across its body, providing control over the tip height with picometer resolution. Once the tunneling current is measured, the tip height is adjusted to match the current setpoint by means of a feedback loop circuit. The tip can also be moved laterally to raster scan the sample surface while recording the tunneling current and the tip height at each point in space to create an image of the sample surface [4]. This scanning technique is known as constant current mode. If the feedback loop is turned off, and the tip only moves laterally to raster scan the surface, then the STM operates in constant height mode; however, this mode implies a higher risk of the tip crashing into the sample if the surface is not flat or if there is any drift at the junction.

The simplest representation of the STM junction (Fig. 2.1a) can be solved as a 1D square potential barrier, where the transmission probability [4] is given by

$$T = \exp\left(-2z\sqrt{\frac{2m}{\hbar^2}(\Phi - \epsilon)}\right) , \tag{2.1}$$

where z is the distance between the tip and the sample, m is the electron mass, $\hbar$ is the reduced Planck constant, ϵ is the electron energy relative to the Fermi level, and Φ is the barrier height which is determined by the work function of the sample and tip relative to the Fermi level. Notice that x is the coordinate axis, to avoid confusion with z the tip-sample distance. Due to the exponential dependence of the tunneling current on the tip height, a retraction of 1 Å will reduce the tunneling current by a factor of 10. This means that most of the current will flow through the last atom of the tip, which is the reason why the STM can probe the sample surface locally with high spatial resolution [3, 4]. Furthermore, the atomic resolution obtained on metal surfaces can only be explained if the tunneling current is produced by d_{z^2} or p_z dangling-bond states near the Fermi level on the apex atom of the tip [53]. This means that tips made of d-band metals (such as W, Pt, Ir) with d_{z^2} states on the apex atom can provide the highest spatial resolution.

It is important to highlight that an STM image does not represent the actual topography of the surface. The tunneling current depends not only on the tip-sample separation but also on the local density of states (LDOS), which varies at different

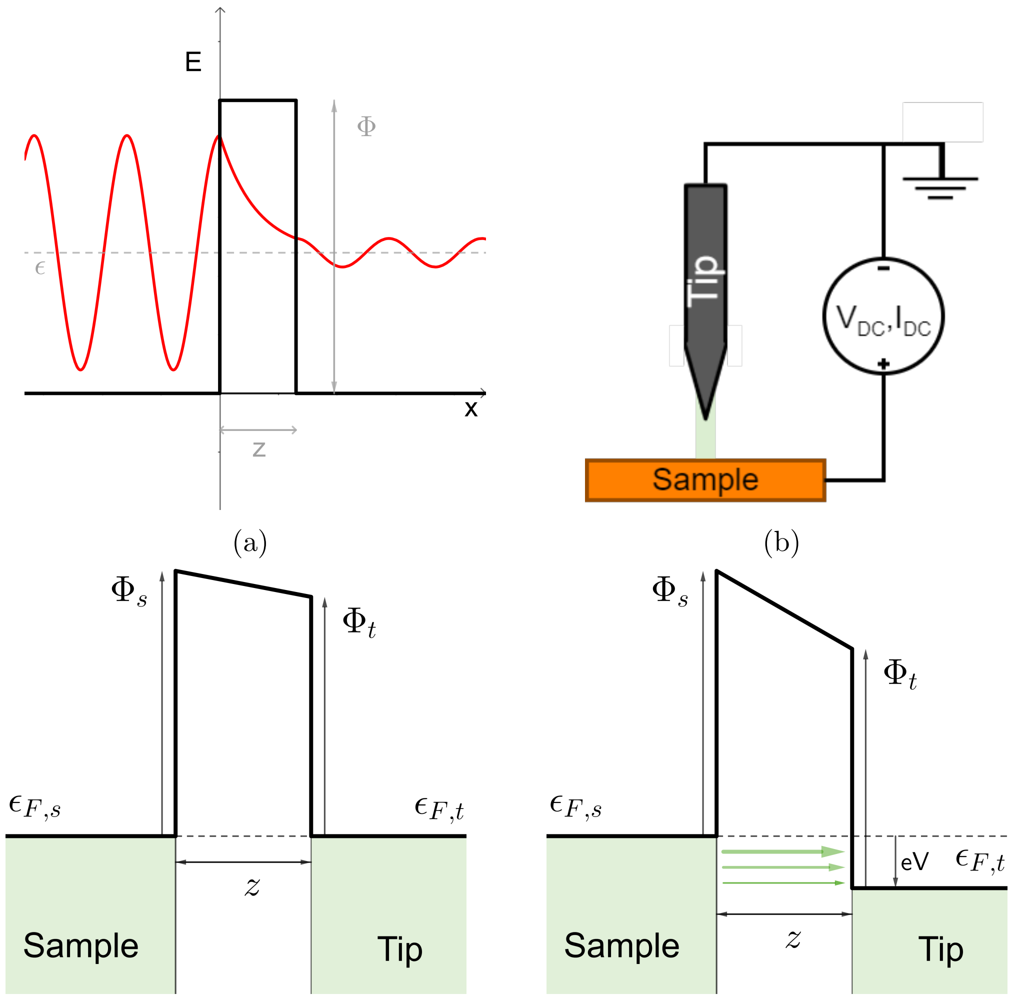

(a) (b)

(c) (d)

Figure 2.1: Quantum tunneling, the fundamental principle behind the operation of an STM. a) Illustration of the electron wavefunction penetrating through a potential barrier. The horizontal axis is x, to avoid confusion with z the tip-sample distance. b) Simplified schematic of an STM showing the tunneling junction formed by the tip, the sample surface, and the vacuum gap in between. c) Energy diagram that illustrates the potential barrier at the STM junction. It shows the Fermi level of the tip ($\epsilon_{\mathrm{F},t}$) and sample ($\epsilon_{\mathrm{F},s}$), the work function of the tip (Φ_{t}) and sample (Φ_{s}), and the tip height (z), when the system is in electrical equilibrium. d) The application of a bias voltage to the sample shifts its Fermi energy with respect to the tip by an amount (eV) proportional to the applied voltage, which produces a tilt on the potential barrier and facilitates the tunneling of electrons through the gap.

points on the surface. This aspect will be discussed in the following section. Only if the LDOS was constant along the surface, such as in a clean metal, then the STM image can reflect the true topography [54].

2.1.1 Theoretical models

Theoretical models of different complexity have been proposed to describe with increasing accuracy the quantum tunneling at an STM junction. Some of the most commonly used models will be presented here.

Only a few potential barrier problems have an analytical solution for the Schrödinger equation, but there are different techniques that can be used to approach this kind of system. One example is the Wentzel-Kramers-Brillouin (WKB) approximation, where the potential is a function of position and is assumed to change slowly compared to the wavelength of the wavefunction. The general WKB solution for the wavefunction, when the electron energy ϵ is smaller than the potential barrier $\Phi(x)$, is given by

$$\psi(x) \cong \frac{C}{\sqrt{|p(x)|}} \exp\left(\pm\frac{1}{\hbar}\int |p(x)|dx\right), \tag{2.2}$$

where C is a constant, $p(z) \equiv \sqrt{2m[\epsilon - \Phi(x)]}$ is the classical momentum, and m is the electron mass. An energy diagram to illustrate this approximation is presented in Fig. 2.2.

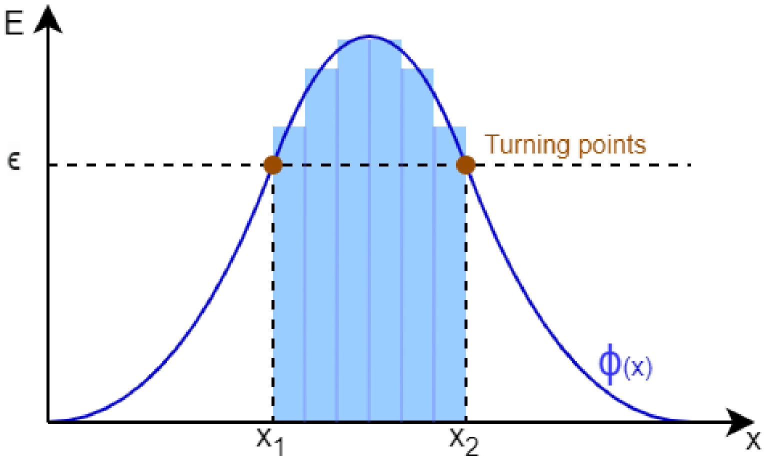

Figure 2.2: Energy diagram to illustrate the WKB approximation for a general potential barrier, which is a function of position $\Phi(x)$. The turning points (x_1,x_2) define the positions where the electron energy ϵ meets the barrier potential.

Defining the turning points as x_1 and x_2, the total transmission probability through the potential barrier, using the WKB approximation, would be given by the integration within that region as follows

$$T \cong \exp\left(-2\int_{x_1}^{x_2} \frac{\sqrt{2m[\Phi(x)-\epsilon]}}{\hbar} dx\right) . \tag{2.3}$$

This approach provides an analytic expression for the tunneling transmission probability in general cases. It should be noted that this approximation does not hold at the *turning points*, where the *Connection Formulas* have to be used [55].

2.1.1.1 Simmons model

In 1963, Simmons presented a generalized formula to describe the tunneling current between two electrodes separated by a thin insulating film [56]. Although it is a simplified model of the STM junction, it has been applied successfully as a first approach to model the tunneling currents of the STM. This is a 1D model that does not consider the temperature or the density of states of the tip and sample. However, it takes into account the applied bias voltage across the STM junction and the potential barrier height as a function of position, which allows for the inclusion of an image potential in the gap. The formula for the tunneling current I is given by [57]

$$I = \frac{meA}{2\pi^2\hbar^3}\left[eV\int_0^{\epsilon_\mathrm{F}-eV} T(\epsilon)d\epsilon + \int_{\epsilon_\mathrm{F}-eV}^{\epsilon_\mathrm{F}} (\epsilon_\mathrm{F}-\epsilon)T(\epsilon)d\epsilon\right] , \tag{2.4}$$

where A is the spatial area of the tunneling current, V is the applied bias voltage, ϵ_F is the Fermi energy and $T(\epsilon)$ is the transmission probability

$$T(\epsilon) = \exp\left(-\frac{2\sqrt{2m}}{\hbar}\int_{x_1}^{x_2} \sqrt{\epsilon_\mathrm{F}-\epsilon+\Phi(x)}dx\right) . \tag{2.5}$$

This model can be used to solve the problem in one dimension and assumes that the material is a free electron metal. However, it is difficult to extend this solution to a complex geometry and a real metal [58]. Therefore, this model has limited applications and should be used with caution.

2.1.1.2 Bardeen model

John Bardeen proposed a three-dimensional model in which he defined the wavefunction of two electrodes as independent, and analyzed the system evolution in time. Bardeen's tunneling theory was published in 1961 [59], but was applied to the STM in 1983 by Tersoff and Hamann [60]. By using a 1D-approximation and considering zero-temperature, the general formula can be simplified to yield the following tunneling current equation

$$I = \frac{4\pi e}{\hbar} \int_0^{eV} \rho_{\mathrm{t}}(\epsilon - eV)\rho_{\mathrm{s}}(\epsilon) T(\Phi_{\mathrm{t}}, \Phi_{\mathrm{s}}, \epsilon, V, z) d\epsilon \, , \tag{2.6}$$

where ρ_{t} (ρ_{s}) is the tip (sample) density of states and the transmission probability T is given by

$$T(\Phi_{\mathrm{t}}, \Phi_{\mathrm{s}}, \epsilon, V, z) = \xi \cdot \bar{\Phi}(\Phi_{\mathrm{t}}, \Phi_{\mathrm{s}}, \epsilon, V, z) \cdot \exp\left(-2z\sqrt{\frac{2m}{\hbar^2} \cdot \bar{\Phi}(\Phi_{\mathrm{t}}, \Phi_{\mathrm{s}}, \epsilon, V, z)}\right) . \tag{2.7}$$

In this equation, $\xi = 2\left[\hbar A \psi_i(0)\psi_f(z)\right]^2/m$, where A is the tunneling area, and ψ_i and ψ_f are the wavefunctions of the tip and sample, respectively. The average barrier height $\bar{\Phi}$ is given by

$$\bar{\Phi}(\Phi_{\mathrm{t}}, \Phi_{\mathrm{s}}, \epsilon, V, z) = \frac{1}{z}\int_{x_1}^{x_2} \left(\Phi_{\mathrm{t}} \pm e|V| \mp |\epsilon| + \frac{x}{z}(\Phi_{\mathrm{s}} - \Phi_{\mathrm{t}} \mp e|V|)\right) dx \, , \tag{2.8}$$

where Φ_{t} and Φ_{s} are the work functions of the tip and sample. For $x_1 = 0$ and $x_2 = z$, it reduces to

$$\bar{\Phi}(\Phi_{\mathrm{t}}, \Phi_{\mathrm{s}}, \epsilon, V) = \left(\frac{\Phi_{\mathrm{t}} + \Phi_{\mathrm{s}} \pm e|V|}{2}\right) \mp |\epsilon| \, . \tag{2.9}$$

Bardeen's theory is considered to be reliable when the tip and sample are not too close ($>\sim 5\,\text{Å}$) and in the low bias voltage regime ($<\sim 2\,\mathrm{V}$) [61, 62].

2.1.2 Scanning Tunneling Spectroscopy

The tunnel current from an STM not only provides information about the sample topography but it contains information about the density of states and the work functions. For example, the electron states can be probed at different energies along the surface by selecting different bias voltages. Furthermore, by changing the polarity of the bias voltage, one can study the occupied or unoccupied states of the sample.

Scanning tunneling spectroscopy (STS) is useful for studying the surface properties of a material, such as its $I - V$ characteristic response, the LDOS, the surface conductance, and the apparent barrier height (ABH), which contains information about its work function Φ_{s} [63].

STS is usually performed at a single point on the sample surface, which takes advantage of the spatial localization of the tunneling current to study the properties of single atoms or molecules. However, sequential spectroscopic measurements can also be taken at multiple points while the tip is scanning the surface. This can provide energy-dependent images of the sample, although the acquisition time is long and thermal drift in the system can limit the spatial accuracy of these measurements.

In the present work, only single-point spectroscopic measurements were performed. The most common STS measurements are described below.

- $I-V$ **curve**

  The current-voltage characteristic is obtained by turning the feedback loop off to maintain a constant tip height, and sweeping the bias voltage while the tunneling current is recorded. The sample conductance is therefore obtained with this measurement. The tunneling current dependence on bias voltage is shown in Eq. 2.6. The curvature of the $I-V$ characteristic contains information about the density of states of the tip and sample. The $I-V$ curve is also useful for identifying the voltage regimes where the response of the sample will be linear or nonlinear to a change in bias voltage.

- dI/dV **curve**

  The differential conductance or dI/dV can be directly calculated by numerically differentiating the $I-V$ curve. A more accurate measurement can be obtained with lock-in detection if a small sine-wave bias modulation is superimposed on the STM bias voltage. With this method, the $I-V$ and dI/dV curves can be measured simultaneously. Tersoff and Hamann showed that the derivative of the tunneling current is proportional to the LDOS of the sample [64]. From Eq. 2.6, it follows that

  $$\frac{dI}{dV} \propto \frac{d}{dV}\left(\int_0^{eV} \rho_{\mathrm{t}}(\epsilon - eV)\rho_{\mathrm{s}}(\epsilon)T(\Phi_{\mathrm{t}}, \Phi_{\mathrm{s}}, \epsilon, V, z)d\epsilon\right) \tag{2.10}$$

  However, if the matrix elements of T and the density of states of the tip ρ_{t} are assumed to be constant in the voltage range studied, then dI/dV becomes proportional to the density of states of the sample.

  $$\frac{dI}{dV} \propto \rho_{\mathrm{t}}(0)\rho_{\mathrm{s}}(eV)T(\Phi_{\mathrm{t}}, \Phi_{\mathrm{s}}, eV, V, z)\,. \tag{2.11}$$

  This approximation works if the bias voltage is small. However, T actually produces an exponential increase in current as the voltage increases (Eq. 2.7). This can be compensated for by dividing dI/dV by I, which presents the same exponential behavior. Furthermore, to prevent a divergence at zero voltage, everything can be multiplied by V, which results in a dimensionless quantity [58]. Therefore, the normalized differential conductance will be given by $(dI/dV)/(I/V)$. Due to these assumptions and corrections, one does not expect to measure the exact density of states with this technique, but it can still be used to obtain a rough estimation.

- **$I - z$ curve**
  The current-distance characteristic is measured when the feedback loop is off and the tip-sample distance is varied while the tunneling current is recorded with a constant bias voltage. The tunnel current will decay exponentially with increasing distance. Furthermore, following Eq. 2.1 for the 1D potential barrier, if the bias voltage is small compared to the work function ($\epsilon \ll \Phi$), then the following expression can be obtained

  $$\Phi_{\mathrm{ABH}} = \frac{\hbar}{8m}\left(\frac{d\ln I}{dz}\right)^2 , \tag{2.12}$$

  where Φ_{ABH} is the apparent barrier height (ABH). The ABH measures the overlap between the wave functions of the tip and sample, and is not the same as the work function, but is related. $I - z$ curves can be displayed on a semi-log plot where a linear trend of Φ_{ABH} can be identified more easily.

- **$z - V$ curve**
  For this measurement, the feedback loop is kept on to have a constant current and the bias voltage is swept while the tip height is recorded. Having the feedback loop on reduces the risk of tip crashes, but the interpretation of the $z - V$ results requires a deeper analysis, since it does not provide direct information about any of the sample properties, which is the reason why it is not widely used for spectroscopic measurements. However, it can be useful, for example, to identify the transition between the tunneling regime and the field emission regime as the bias voltage surpasses the material work function.

2.2 Ultrafast lasers and terahertz pulses

2.2.1 Femtosecond laser pulses

Ever since the invention of the first maser [65] and the subsequent development of the first laser [66], this technology has evolved fruitfully in multiple directions and has proven useful in many fields. One of the main improvements in the area of pulsed laser technology was the generation of ultrafast laser pulses that are tens of femtoseconds long [67]. This advancement was revolutionary mainly because these laser pulses have two important unique features. First, their short duration, on the order of tens of femtoseconds, enables the study of ultrafast dynamics in materials and chemical systems. Second, they can be used to generate extremely high-intensity peak values, which enabled the study of highly nonlinear processes in solid-state, molecular and atomic physics. Ultrafast lasers have been widely adopted for use in fundamental research and in practical applications.

One of the main milestones in this path was the development of the chirped-pulse amplification (CPA) technique, which enabled the generation of high-intensity femtosecond pulses without damaging the amplification medium [68, 69]. Strickland and Mourou were awarded a share of the 2018 Nobel Prize in Physics due to the importance of this development. In the CPA technique, the laser pulse is expanded in time using optical pulse compression techniques [70, 71], meaning that it is dispersed or chirped in a reversible way. This avoids damage due to high peak powers in the gain medium, and the amplification of the laser pulses can be increased. A simplified schematic of the CPA technique is illustrated in Fig. 2.3. The oscillator is a modelocked laser that generates low energy ultrashort laser pulses at a high repetition rate that are used as the seed for the amplification process. It was in 1990 when Sibbet [72] developed a self-modelocked laser, whose operation was based on the Kerr nonlinearity of the laser crystal. In a modelocked laser, different wavelengths or longitudinal modes satisfy the condition that an integer number of half-wavelengths can fit in the cavity. Those modes interfere constructively and destructively with each other randomly, but they can be forced to be locked in phase with each other and add together to generate a high-intensity pulse. The larger the number of modes, the higher the intensity, which can reach values higher than 10^{11} W/cm^2 and can induce nonlinear effects in the gain medium. The index of refraction of the laser crystal can be altered at high light intensities, and due to the spatial Gaussian profile of the pulse, a Kerr lens can be formed, which narrows the beam inside the crystal and induces self-modelocking.

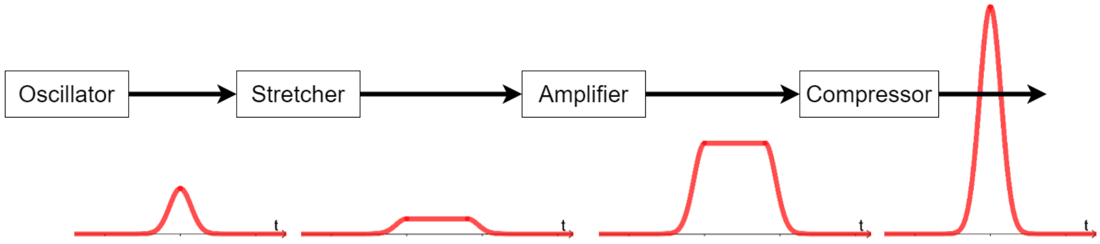

Figure 2.3: Steps to generate ultrafast laser pulses using the chirped pulse amplification technique. A laser pulse from an oscillator, tens of femtoseconds long, is stretched in time to be then amplified in a gain medium without damaging it, and finally, it is recompressed to produce high-energy ultrafast laser pulses. Adapted from *Principles of Terahertz Science and Technology*, by Yun-Shik Lee, 2009, Springer US. [73].

A simplified schematic of a modelocked laser is shown in Fig. 2.4. A pair of prisms is commonly used to compensate for group velocity dispersion. An adjustable slit helps to select the central wavelength of the laser. A titanium-doped aluminum oxide (Ti:sapphire) crystal is typically used as the gain medium. The absorption spectrum of Ti:sapphire peaks near 500 nm, therefore, it is usually pumped with CW argon-ion lasers or diode-pumped solid-state lasers near that wavelength. The photoexcited electrons then relax into more stable states, and the crystal lases due to stimulated emission near 800 nm.

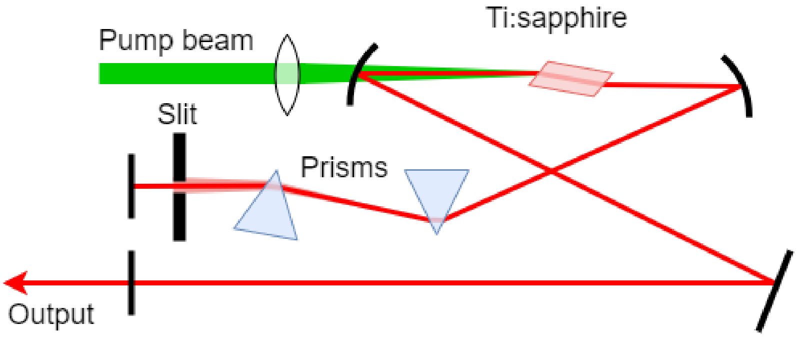

Figure 2.4: Schematic of a self-modelocked laser. The gain medium is a Ti:sapphire crystal which is pumped by a green CW laser through a dichroic mirror. Ultrashort laser pulses are generated by Kerr lens modelocking. A pair of prisms are used to compensate for group velocity dispersion and the position of the slit selects the central wavelength of the laser. Adapted from *Principles of Terahertz Science and Technology*, by Yun-Shik Lee, 2009, Springer US. [73].

A modelocked oscillator based on Ti:sapphire usually delivers $10 - 100\,\mathrm{fs}$ short pulses with energy $\sim 10\,\mathrm{nJ}$ and a repetition rate of $\sim 80\,\mathrm{MHz}$. These femtosecond pulses are then chirped with a diffraction-grating arrangement, which stretches the pulses from 100 fs to 100 ps. After the pulse has been stretched, the peak power is usually reduced by 3 orders of magnitude. For the amplification stage, two different techniques can be used to amplify the laser pulses, regenerative and multipass amplification. In regenerative amplification, the stretched pulses from the oscillator enter a resonant laser cavity where they pass through a gain medium multiple times (typically tens of times), as shown in Fig. 2.5a. Pockels cells are used to electronically manipulate the laser beam polarization and control the injection/ejection of the laser pulses. Ideally, ejection occurs just before the amplification reaches the saturation point [73]. In a multipass amplification scheme, there is no cavity, and only an array of mirrors is required to make the laser pulses pass through the gain medium multiple times at different angles. Each pass amplifies the laser pulse before it leaves the optical setup, as shown in Fig. 2.5b. The crystal of choice for amplification purposes is typically Ti:sapphire, because it presents unique properties that make it ideal for a gain medium, such as high damage threshold, high thermal conductivity, high saturation threshold and a broad gain bandwidth that goes from 650 to 1100 nm [74]. During the amplification stage, the pulse peak power is typically increased by $10^6 - 10^9$ times.

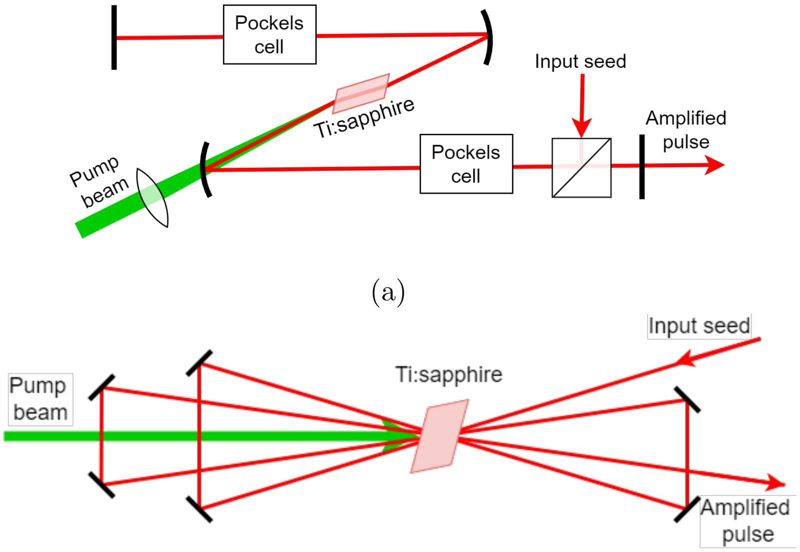

(a)

(b)

Figure 2.5: Laser pulse amplification techniques. a) Regenerative amplification. The laser pulse passes multiple times through the gain medium, and Pockels cells are used to electronically control the injection/ejection of the laser pulses. b) Multipass amplification. An array of mirrors is used to make the laser pulse pass through the gain medium multiple times at different angles. Adapted from *Principles of Terahertz Science and Technology*, by Yun-Shik Lee, 2009, Springer US. [73].

Finally, a second diffraction-grating arrangement is used to compress the pulse into femtosecond pulses again. With this CPA technique, energy amplification factors on the order of 10^6 can be easily achieved nowadays, which translates into peak powers of 10^{12} W [74]. When the beam is focused, peak intensities greater than 10^{20} W/cm^2 can be achieved. Such high light intensities have electric fields larger than what is binding the valence electrons to the core of an atom.

2.2.2 THz pulses

We just mentioned how the introduction of ultrafast pulsed lasers opened up a whole new window of opportunities to explore new phenomena. One clear example is the terahertz (THz) region of the electromagnetic spectrum. It is usually considered to cover the region from 100 GHz to 10 THz, and it remained relatively inaccessible for a long time, due to a lack of broadly tunable sources; it was even referred to as the "THz gap". Electronic transistor-based devices at the lower frequencies and optical methods at the higher frequencies did not have the capability to reach this region. The development of ultrafast lasers producing femtosecond pulses [11] provided the necessary tools for the generation and detection of THz pulses, which enabled the study of this part of the spectrum. The THz band is very attractive because of the fundamental phenomena that occur in this frequency range. THz frequencies are typical for Rydberg transitions in atoms [75, 76], intraband transitions in semiconductor nanostructures [77, 78], impurity state transitions in semiconductors [79], lattice vibrations and excitons in solids [80–82], vibrational and rotational motions in molecules [83], and transient photoconductivity in materials [12, 84]. Furthermore, because of their low photon energy, THz pulses do not cause harmful ionization of biological tissues and they can penetrate through plastics, fabrics, paper, wood, and other non-conducting materials, although they are attenuated by water and cannot penetrate metals. Because of these properties, they have been successfully applied for security screening purposes, such as the detection of explosives, weapons, and drugs [85, 86].

This work will focus on THz radiation produced by pulsed lasers, since continuous-wave (CW) THz radiation is not within the scope of this thesis. There are multiple techniques to generate and detect THz pulses, but this section will describe the generation (photoconductive emission) and detection (electro-optic sampling) techniques that were used for the experiments presented here. Their counterpart, photoconductive detection and optical rectification, will also be covered for completeness. Finally, thermal detectors commonly used to measure the average power of THz radiation will also be covered briefly.

2.2.2.1 Generation

The THz generation techniques discussed here are based on two different mechanisms: Photoconductive emitters that are based on transient photocurrents in a semiconductor, and optical rectification based on nonlinear optical processes in a nonlinear crystal.

Photoconductive emitter Photoconductive emitters based on semiconductor technology, triggered by ultrafast laser pulses, were first reported in the 1980s [87, 88]. Photoconductive antennas are commonly built on high-resistivity semiconductor substrates, generally III-V compounds such as GaAs, GaBiAs or InGaAs. Metallic contacts are deposited on the surface of the semiconductor with a gap spacing of

$1 - 50\,\mu$m. When a bias voltage is applied between the two contacts, the current produced is negligible due to the high resistance of the substrate. But when an ultrashort laser pulse illuminates the area between the contacts, photocarriers are generated in the substrate, increasing its conductivity. The photon energy must be larger than the semiconductor bandgap to excite these carriers. The generated electron-hole pairs will then be accelerated towards the contacts, producing a transient current that generates radiation [89, 90]. A schematic of the photoconductive emitter is shown in Fig. 2.6.

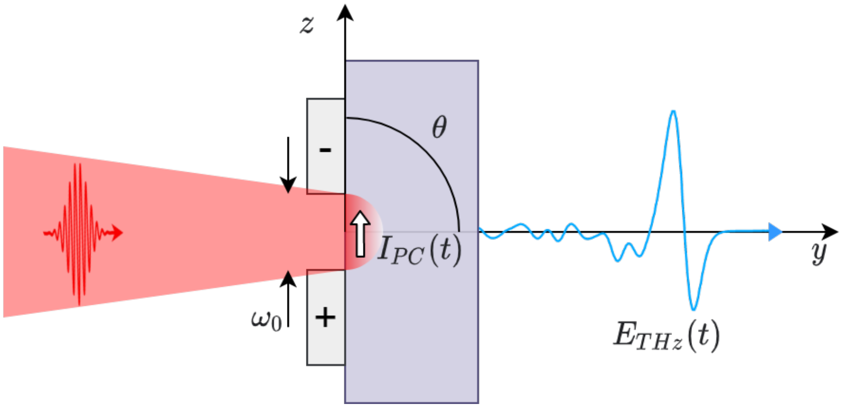

(a)

Figure 2.6: Schematic of a photoconductive antenna. A bias voltage applied between the metallic contacts (gray) deposited on a high-resistivity semiconductor substrate (purple) produces a negligible current. But an ultrafast laser illuminating the substrate induces electron-holes that are accelerated towards the contacts, producing a transient current $I_{\mathrm{PC}}(t)$ that generates THz radiation. Adapted from *Principles of Terahertz Science and Technology*, by Yun-Shik Lee, 2009, Springer US. [73].

For a photoconductive antenna to detect or emit THz radiation, the transient currents in the substrate should occur in the subpicosecond regime. This means that the excitation pulse must be short (typically $\sim 100\,$fs). Once the photocarriers are created, the charge density decreases due to carrier recombination or carriers being trapped in defect sites, which occurs in the span of their lifetime [73]. It is this acceleration and decay of free carriers that produce the THz radiation.

Since the electrode spacing (tens of μm) is usually smaller than the emitted radiation wavelength ($300\,\mu$m at $1\,$THz), a Hertzian dipole antenna can be used to model a photoconductive emitter, where the emitted electric field E_{THz} in the far-field can be described as

$$E_{\mathrm{THz}}(t) = \frac{\mu_0 \omega_0}{4\pi} \frac{\sin\theta}{r} \frac{d}{dt_{\mathrm{r}}} \left[I_{\mathrm{PC}}(t_{\mathrm{r}}) \right] \hat{\theta}\,, \tag{2.13}$$

where μ_0 is the permeability of free space, ω_0 is the illuminated spot size diameter, r and θ are the distance and angle from the source, t_r is the retarded time, and I_PC is the photocurrent in the photoconductive gap of the antenna. The electric field of the emitted THz pulse will then be proportional to the derivative of the generated photocurrent [91].

In the regime where the bias voltage and the optical pump power are low, the output power increases linearly when any of these two parameters increases. However, both the bias voltage and the pump power have limits. The applied bias voltage is limited by the breakdown voltage of the substrate; and when the optical pump power is high, the bias voltage gets screened by the photocarriers, which saturates the output power.

Optical rectification Optical rectification occurs when an electromagnetic field with a high amplitude interacts with a noncentrosymmetric crystal. Zinc Telluride (ZnTe) is a noncentrosymmetric crystal typically used for this purpose. The electronegativity of Te is higher than that of Zn, which produces an asymmetric charge distribution towards Te. This creates an asymmetric potential energy along these bonds in the crystal. The equation that describes this potential energy can be Taylor expanded around the equilibrium position, where the potential asymmetry is represented by a cubic term, as shown in Fig. 2.7a. When a sufficiently large electric field is applied to the material, the charge displacement deviates from the linear response, and a nonlinear component is produced with a frequency of 2ω (Fig. 2.7b). This nonlinear component contains the second harmonic and the optical rectification (DC offset). The polarization induced by the optical rectification will closely follow the magnitude of the light intensity. Therefore, if a femtosecond laser pulse illuminates the material, the induced rectified polarization will follow the laser pulse envelope (Fig. 2.7c), and it is this subpicosecond change in polarization that generates the THz radiation.

As the optical laser pulse travels through the nonlinear crystal, THz radiation will be generated at each point in space. If the optical pulse and the THz radiation travel with the same velocity, the THz radiation will be continuously amplified with each step. However, if their velocity does not match, the THz radiation produced at different points in space will destructively interfere, and after traveling through a certain thickness of the crystal, the THz radiation will be washed out. The ultrafast laser pulses used for the experiments were centered at 800 nm with a refractive index of $n_\mathrm{o} = 2.853$ in ZnTe and the spectrum of the THz pulses was centered at 0.5 THz with a refractive index of $n_\mathrm{THz} = 3.155$ in ZnTe, which means that destructive interference

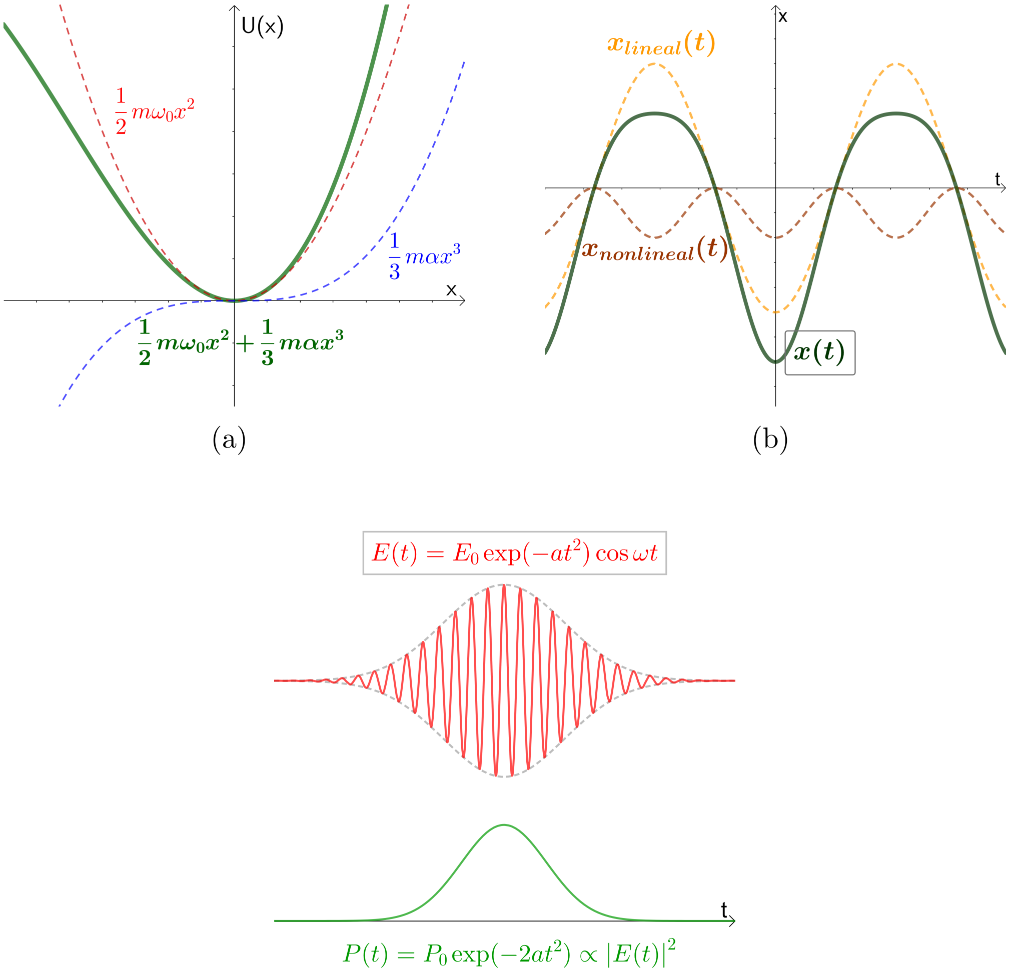

(a)

(b)

(c)

Figure 2.7: Optical rectification illustrations. a) Asymmetric potential energy of a noncentrosymmetric crystal (solid green line) that contains a quadratic (dashed red line) and a cubic term (dashed blue line). b) The charge displacement $x(t)$ (solid green line) induced in a noncentrosymmetric crystal deviates from the linear response (dashed yellow line) by a second harmonic and a DC offset (dashed brown line). c) The polarization induced in the crystal (green) will closely follow the exciting laser pulse envelope (dashed black line). Adapted from *Principles of Terahertz Science and Technology*, by Yun-Shik Lee, 2009, Springer US. [73].

will occur and should be taken into account when selecting the ZnTe crystal thickness.

2.2.2.2 Detection

The detection of THz radiation presented fewer challenges than its generation, because previously known techniques could be used. The different types of THz detection techniques can generally be classified into coherent or incoherent methods. A coherent technique measures the amplitude and the phase of the THz electric field. Detection techniques such as electro-optic sampling [92] and photoconductive antenna detection [90] fall into this category. These techniques are closely related to the generation techniques discussed in the previous section, because they share the same basic mechanisms. Incoherent techniques, on the other hand, measure only the intensity of the THz radiation. Thermal detectors fall into this category, such as bolometers, pyroelectric and Golay cell detectors [13]. One of the main disadvantages of thermal detectors is their slow response [73].

Electro-optic sampling Electro-optic sampling (EOS) detection is based on the Pockels effect in a nonlinear crystal, which shares the same fundamental mechanism as optical rectification. In this case, birefringence is induced in the medium when an electric field is applied to the crystal. To probe the THz field, the THz pulse propagates collinearly with a short optical pulse through the nonlinear crystal. The optical pulse needs to be shorter than the THz pulse duration so that the THz field is almost constant in the probing time window. Additionally, the velocity matching condition, required for optical rectification, is also required for EOS detection. The two pulses need to travel with the same velocity through the crystal for the optical pulse to probe a THz field that is almost constant.

The typical EOS setup is shown in Fig. 2.8. In the absence of a THz field, a linearly polarized optical pulse will travel through the electro-optic (EO) crystal without any modification. The quarter-wave-plate ($\lambda/4$) turns its linear polarization into circular, and the Wollaston prism splits the beam into its orthogonal components. The intensity of the linearly polarized horizontal and vertical components is measured with a pair of photodiodes, which in the absence of a THz field, should have the same intensity. Conversely, if the electric field of the THz pulse is present in the EO crystal, it will induce birefringence, which will turn the linear polarization of the optical pulse into a slightly elliptical polarization as it propagates through it. This will translate into a different intensity for the two orthogonal components at the balanced photodiodes. The intensity difference ($I_y - I_x$) is proportional to the THz field amplitude [73], and the expression for the THz electric field as a function of

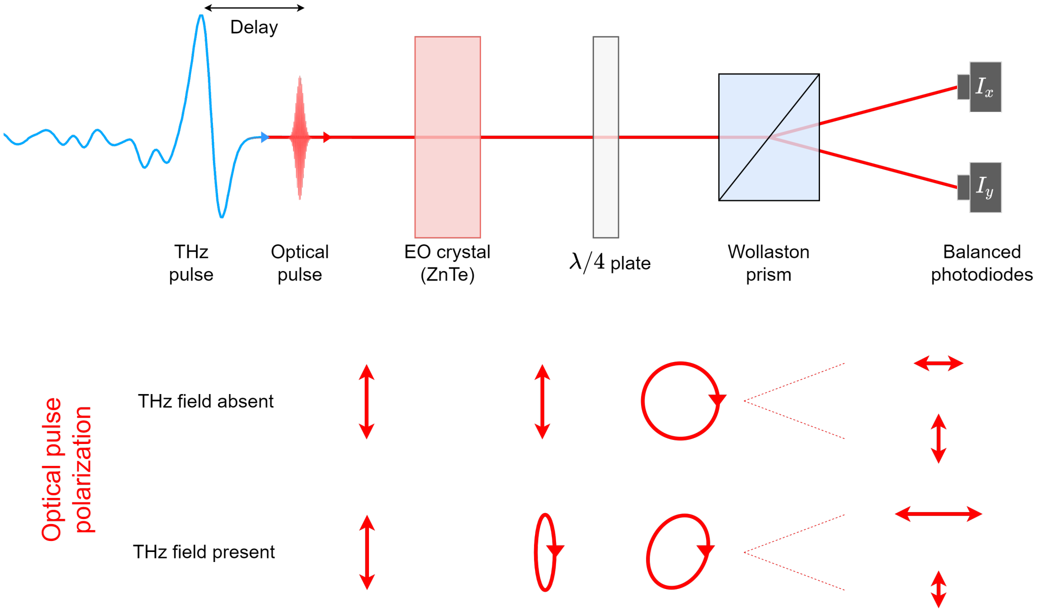

Figure 2.8: Electro-optic sampling diagram. A THz pulse and an ultrafast optical pulse travel collinearly through an electro-optic crystal. The THz-induced birefringence in the crystal modifies the polarization of the optical pulse, which after traveling through a $\lambda/4$ waveplate goes from circular when the THz field is absent, to elliptical when the THz field is present. The optical pulse is then split into two perpendicular polarization components by a Wollaston prism, and their intensity difference is measured by a pair of balanced photodiodes. By changing the time delay between the two pulses, the complete THz pulse waveform can be measured. Adapted from *Principles of Terahertz Science and Technology*, by Yun-Shik Lee, 2009, Springer US. [73].

intensity difference is

$$E_{\mathrm{THz}}(\tau) = \frac{\lambda}{2\pi n_{\mathrm{o}}^3 r_{41} L} \sin^{-1}\left(\frac{I_y - I_x}{I_y + I_x}\right) , \tag{2.14}$$

where λ is the optical pulse wavelength, n_{o} is the refractive index of the crystal for λ ($n_{\mathrm{o}} = 2.853$ for ZnTe at 800 nm), r_{41} is the electro-optic coefficient of the crystal ($r_{41} = 4\,\mathrm{pm/V}$ for ZnTe), L is the crystal thickness and I_x, I_y are the intensities of the two orthogonal components of the optical pulse measured by the balanced photodiodes. Additionally, the THz field attenuation caused by reflection losses at the ZnTe crystal surface needs to be considered. The Fresnel equations for the transmission of s and p-polarized light, respectively, at the interface are given by

$$t_s = \frac{2n_1 \cos\theta_i}{n_1 \cos\theta_i + n_2 \cos\theta_t} , \; t_p = \frac{2n_1 \cos\theta_i}{n_2 \cos\theta_i + n_1 \cos\theta_t} , \tag{2.15}$$

where n_1 and n_2 are the refractive index of the first and second medium, θ_i and θ_t are the incident and transmitted angles. In an interface made of air ($n_1 = 1$) and a ZnTe crystal ($n_2(0.5\,\mathrm{THz}) = 3.155$), at normal incidence, the transmission coefficient is $t_{s,p} = 0.48$ [93].

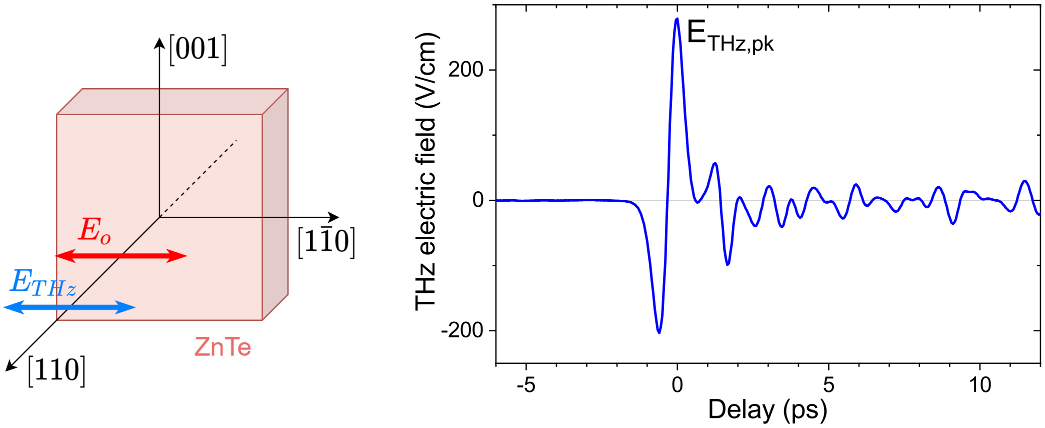

(a) (b)

Figure 2.9: a) EO crystal diagram. The EOS detection sensitivity is optimized in a ZnTe crystal when the linear polarization of the THz pulse ($E_T Hz$) and the optical pulse (E_{o}) are parallel to the $[1\bar{1}0]$ axis of the EO crystal. Adapted from *Principles of Terahertz Science and Technology*, by Yun-Shik Lee, 2009, Springer US. [73]. b) An example of a single-cycle THz pulse waveform measured in the lab with EOS in a ZnTe crystal.

To maximize the birefringence in the EO crystal, both the optical pulse and the THz pulse linear polarization should be parallel to the $[1\bar{1}0]$ axis, as shown in Fig. 2.9a. Increasing the crystal thickness will also increase the detection sensitivity; however, the bandwidth will decrease because of dispersion in the medium and the velocity mismatch between the two pulses. Finally, by changing the delay between the two pulses while the intensity difference is being recorded, the full THz field waveform can be measured in the time domain (Fig. 2.9b).

Photoconductive detector Detection in an unbiased photoconductive antenna occurs when an ultrafast optical pulse and a THz pulse are collinearly incident on the gap between the antenna electrodes. The optical pulse will photoexcite carriers in the semiconductor substrate, and the electric field from the THz pulse will accelerate these photocarriers towards the electrodes. The optical pulse should be short, so that the THz field is mostly constant during the probing time. The carrier lifetime should also be short to limit their presence to the time duration of the optical pulse. The THz-induced transient current can then be measured across the antenna electrodes. The current density produced in the PC antenna can be described by [73]

$$J(t) = \int_{-\infty}^{t} \sigma_{\mathrm{s}}(t-t')E_{\mathrm{THz}}(t')dt' \,, \tag{2.16}$$

where $\sigma_{\mathrm{s}}(t)$ is the transient surface conductivity, which depends on the optical intensity, carrier drift velocity, and carrier population. The THz-induced current will be proportional to the THz electric field amplitude. Therefore, if the THz-induced current is measured while the time delay between the THz pulse and the optical pulse is changed, the THz pulse waveform can be measured in the time domain.

Thermal detectors Thermal detectors can be used to measure radiation for a wide range of frequencies of the electromagnetic spectrum, making them suitable to measure THz radiation. The main disadvantage is their slow response time. Thermal detectors usually consist of a radiation absorber connected to a heat sink, where the energy absorbed is converted to heat [73]. The change in temperature is then measured by different mechanisms; the most common ones are as follows.

A bolometer measures the temperature change using a material whose electric resistance varies with temperature. Highly doped semiconductors, such as Si or Ge cooled to low temperatures are commonly used for this purpose. One disadvantage of such bolometers is the fact that they need to operate at cryogenic temperatures, which limits their application.

In a pyroelectric detector, a spontaneous electric polarization is induced in a material by a change in its temperature, which changes the dielectric constant of the material. The thermally-induced polarization produces an electric charge across two electrodes, which can be measured.

A Golay cell detector contains a sealed chamber with a small amount of gas that is heated when the radiation is incident on an absorbing surface. One of the sides of the chamber has a flexible membrane that is reflective. The membrane is monitored by optical reflectivity to measure the deformation induced by a pressure change inside the chamber. Alternatively, the membrane deformation can also be monitored by its capacitance as a parallel planar capacitor.

2.3 Terahertz scanning tunneling microscopy

One of the main limitations of the STM (Fig. 2.10a) is its poor time resolution. It can take seconds or minutes to record one single image. The STM feedback loop usually operates with a frequency of a few kilohertz, which means that all the dynamics occurring faster than a millisecond get averaged out. By combining the STM with high bandwidth ultrashort laser pulses, time-resolved experiments such as optical pump-optical probe can be performed, which provide a better temporal resolution [94–102]. However, thermal-induced effects from the optical laser pulses are one of the main challenges in such experiments, and the bandwidth of the STM electronic equipment, such as the current amplifier, still limits the system response to a few hundreds of kHz.

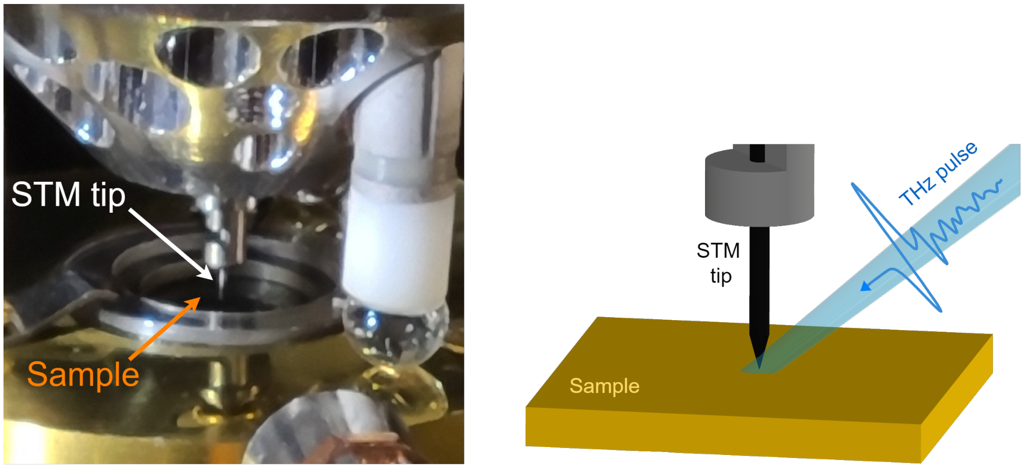

(a) (b)

Figure 2.10: a) Photograph of an STM that highlights the location of the tip and sample. b) Schematic of a free-space propagating THz pulse being coupled to the tip of an STM.

An alternative solution has been developed in recent years. Free-space propagating single-cycle THz pulses can be coupled to the tip of the STM to produce a transient bias modulation at the STM junction (Fig. 2.10b), which in turn generates a rectified tunneling current that can be measured by the conventional STM equipment. The use of THz pulses avoids capacitive coupling effects, and the low energy of the THz frequencies (4 meV for 1 THz) minimizes the thermal effects, which makes this approach unique. It provides a non-contact method to probe ultrafast phenomena with sub-picosecond temporal resolution at the nanoscale. This technique where THz pulses are coupled to the STM tip, is commonly known as THz-STM. After THz-STM was first demonstrated in 2013 [32], it has been used to study the properties of silicon and copper surfaces [37, 41], the pentacene and magnesium phthalocyanine molecules [35, 40] and the THz near fields [39, 42], to mention some examples.

2.3.1 Field enhancement at the tip apex

The fact that the sharp edges of an object produce an enhancement of an electric field is well known, where the enhancement amount depends on the radius of the sharp point. Nanometric tips have a very sharp apex (tip radius in the nanometers range), and when they are illuminated with a laser pulse, the optical fields will experience a strong local field enhancement at the apex. The enhancement factor will depend on the tip material and the radiation wavelength. For example, free-standing tips with a radius of 10 nm illuminated with 630 nm light exhibit a field enhancement of ∼ 50 for Au, ∼ 15 for W, ∼ 9 for Si, and ∼ 3 for glass [103]. The tip geometry and the illumination conditions also influence the field enhancement at the apex [104, 105]. This phenomenon by itself has many applications; however, when the tip is brought into close proximity to a sample, the field enhancement at the apex increases rapidly when the tip-sample distance is comparable to or less than the tip radius distance. Furthermore, the fields at the apex are laterally confined the closer the tip is to the sample, and the confinement can be comparable to the tip radius [103]. The enhancement and confinement of the fields will be present at the apex even when the wavelength of the incident radiation is larger than the nanometric dimensions of the tip. In this work, we take advantage of this phenomenon by coupling single-cycle THz pulses (0.3 mm wavelength at 1 THz) onto STM tips, which is a topic that will be discussed in the next section.

2.3.2 Coupling of THz pulses to the STM

When a THz pulse couples to a metal tip, the metal tip behaves like a long-wire antenna [106]. An antenna can be thought of as a device that couples the near field and the far field [107]. The most common type of antenna is known as the dipole antenna, which is formed by two conductive wires that extend in opposite directions. If the antenna has only one arm, it is known as a monopole. However, when a monopole antenna is positioned perpendicular to a ground plane, its reflection produces a virtual monopole below the ground plane, as shown in Fig. 2.11a. This monopole above a ground plane can be described in the same way as a dipole antenna [108].

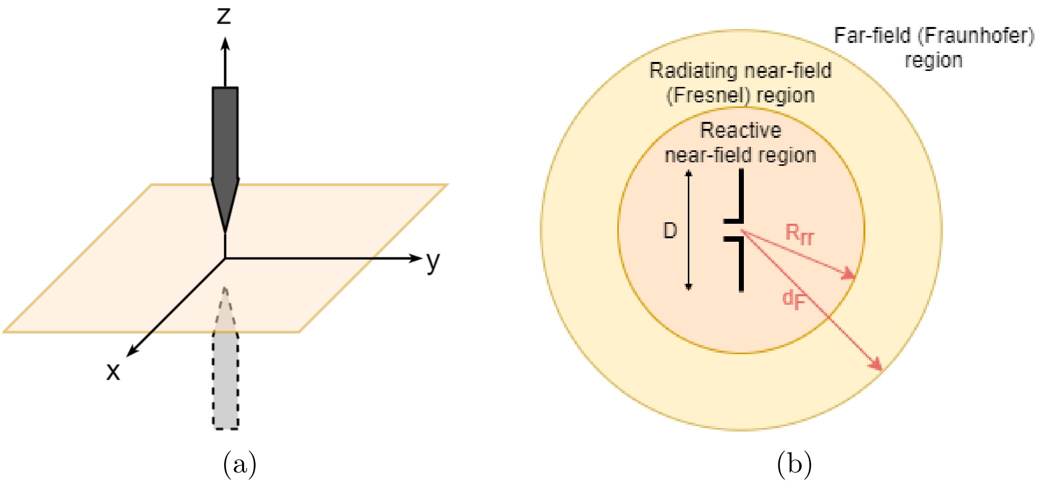

(a) (b)

Figure 2.11: a) Illustration of the STM junction represented by a monopole antenna (tip) above a ground plane (sample) with a virtual monopole underneath (dashed line). b) Field regions of the space around a long wire antenna. The near-field is divided into reactive and radiating subregions. The far-field is also known as the Fraunhofer region. D is the antenna arms length, $R_{\mathrm{rr}} = 0.62\sqrt{D^3/\lambda}$, $d_{\mathrm{F}} = 2D^2/\lambda$ and λ is the radiation wavelength. Adapted from Ref. [108].

Depending on the total length of the arms (D), antennas can be classified into two categories. It is considered a "short antenna" if D is shorter than half the wavelength of the emitted radiation (λ) and can be described as a Hertzian or infinitesimal dipole. If the antenna length is larger than half the wavelength, then it is classified as a "long wire antenna" [108]. The space around a long wire antenna is commonly divided into two regions, the far-field and near-field regions, as shown in Fig. 2.11b. Although the boundaries are not strictly defined, the Fraunhofer distance (d_{F}) is commonly used to identify the limit between the far and near field regions, which is given by

$$d_{\mathrm{F}} = \frac{2D^2}{\lambda}\,. \tag{2.17}$$

The far-field, or Fraunhofer zone, is defined as the region in space where the angular distribution of the fields does not depend on the distance from the antenna. The near-field zone is further divided into a "radiating near-field" region, where the radiating fields are predominant but the angular distribution depends on the distance from the antenna; and a "reactive near-field" region, where the electric field is significant but it does not propagate radially and is mainly reactive [108]. The boundary between these two near-field regions is defined as $R_{\rm rr} = 0.62\sqrt{D^3/\lambda}$. These region definitions are given for regular antennas; however, on a nanometric tip, the fields are enhanced and confined, as described in Section 2.3.1. And, since the fields at the apex can be laterally confined to a region of the size of the tip radius when it is brought into close proximity to a sample, it is commonly accepted that the near field region at the apex of an STM nanometric tip is delimited by the tip radius [24, 109]. It is worth mentioning that for THz pulses, large field enhancement factors ranging from 10^2 to 10^4 have been reported in previous studies [32, 33, 37, 51], as compared with those for 630 nm mentioned before.

In general, the near fields can be divided into two categories, those that are permanent such as "electrostatic surface fields" and those that are induced by an external excitation, such as "optical near fields" [110]. The optical near fields on a sharp tip have been described with a simple model consisting of a small polarizable sphere, representing the apex of the tip, and a single dipole moment located at the center of the sphere [111, 112]. This approach can produce good results for certain cases, but it has been shown that a more refined model is needed to take into account the contributions to the near fields from the tip shaft [29, 113, 114]. If the tip is treated as a dipole antenna, the current induced by an external excitation field can be described with an electronic circuit model [42, 115], which consists of a radiation resistor $R_{\rm r}$, an inductance L and a capacitor C in series. The driving voltage of the circuit is the external excitation, which induces a current in the antenna (Fig. 2.12).

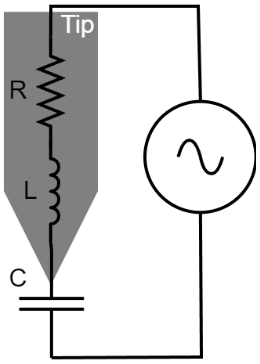

Figure 2.12: Long wire antenna model represented as an RLC circuit.

Using the RLC approach [116] provides a method to characterize a tip-sample system excited by external incident fields using a long wire antenna model and an electronic RLC circuit model. This approach shows good agreement in some cases;

however, recent experiments have shown that this simplified method might not be sufficient to accurately describe the relationship between the incident field and the near field in a THz-STM system, since other factors, such as the tip shape or a field phase shift, can have an effect on the resulting near fields. Several groups are currently doing research on this front in search of a more accurate model [33, 39, 41, 42, 46, 50].

2.3.3 THz-induced current

The electric field of a THz pulse coupled to the STM tip will produce a bias voltage modulation $V_{\mathrm{THz}}(t)$ between the tip and the sample, that will follow the THz near field waveform at the apex. This voltage transient will induce a tunneling current across the STM junction. A static bias V_{DC} induces a constant current I_{DC} at the junction in accordance to the current–voltage characteristic ($I-V$ curve) of the sample. If we assume that the dynamic response of the sample also follows the static $I-V$ curve, then the transient $V_{\mathrm{THz}}(t)$ will induce a transient current $I_{\mathrm{THz}}(t)$, as shown in Fig. 2.13a. A scaling factor to convert the electric field amplitude of the THz pulse E_{THz} to a bias voltage V_{THz} has been previously estimated to be $S\,[\mathrm{cm}] = V_{\mathrm{THz}}\,[\mathrm{V}]/E_{\mathrm{THz}}\,[\mathrm{V/cm}] \sim 1/45\,\mathrm{cm}$ [37, 41]. However, the THz near-field waveform at the junction might not be the same as the far-field waveform of the THz pulse, which is an aspect still under investigation.

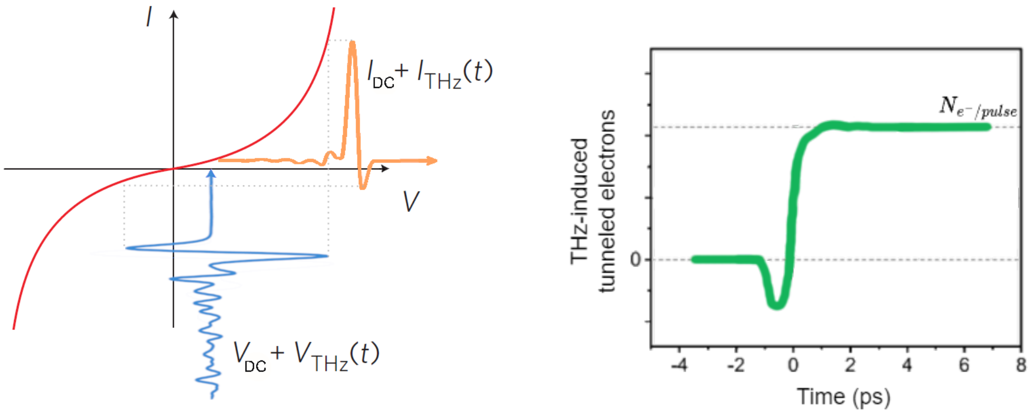

(a) (b)

Figure 2.13: Plots to illustrate the THz-induced current. a) The total bias voltage at the STM junction (blue) is the sum of a static V_{DC} and a transient $V_{\mathrm{THz}}(t)$ voltage. The total induced tunneling current (orange) is assumed to follow the static $I-V$ curve of the sample (red). It contains a static I_{DC} and a transient $I_{\mathrm{THz}}(t)$ current. b) The nonlinearity of the $I-V$ curve produces an asymmetric number of tunneled electrons per pulse $N_{\mathrm{e^-/pulse}}$ that can be measured. (Adapted from Refs. [32, 117].)

The transient THz-induced current occurs on a sub-ps or ps timescale, and electronic devices do not have the temporal resolution to measure it directly. However, as shown in Fig. 2.13b, the total number of tunneled electrons per pulse $N_{\mathrm{e^-/pulse}}$ will be different than zero. Even though $E_{\mathrm{THz}}(t)$ must satisfy $\int_{-\infty}^{\infty} E_{\mathrm{THz}}(t)dt = 0$, a rectified tunneling current is being produced thanks to the nonlinearity of the $I-V$ curve. The THz-induced charge would be given by $Q_{\mathrm{THz}} = \int_{-\infty}^{\infty} I_{\mathrm{THz}}(t)dt$. To extract the rectified THz-induced current I_{THz} from the total tunneling current, the THz pulse generation can be chopped or modulated in order to use lock-in detection. The THz modulation frequency needs to be greater than the STM feedback loop bandwidth, otherwise, the STM tip height would be adjusted to compensate for the tunneling current difference in the presence and absence of the THz pulses, which could potentially crash the tip into the sample. On the other hand, the THz modulation frequency needs to be within the system bandwidth (usually limited by the preamp bandwidth) for the modulated current changes to be detected. Using lock-in detection, the THz-induced current is continuously recorded while the STM is in operation. Therefore, when the STM performs a scan, a 2D image can be formed with the I_{THz} signal at each point in space, which is known as a *THz image*.

The THz-induced current is sometimes presented in units of electrons/pulse instead of amperes, because it offers a more intuitive representation of the induced transient dynamics. The number of electrons produced per THz pulse can be calculated as

$$N_{\mathrm{e^-/pulse}} = I_{\mathrm{THz}}/(e \times f_{\mathrm{rep}})\,, \tag{2.18}$$

where e is the electron charge and f_{rep} is the laser repetition rate.

2.4 Electron emission

2.4.1 Emission mechanisms

The emission of electrons from solid material surfaces has been extensively studied in the past, and the underlying mechanisms are well understood. However, the development of ultrafast lasers with high peak intensities offers a new tool to study the nonlinear effects of electron emission. The experiments performed here mainly presented multiphoton photoemission, but it is important to be aware of and understand all the mechanisms that can potentially contribute to electron emission from a solid material. These mechanisms will be briefly reviewed in the following sections.

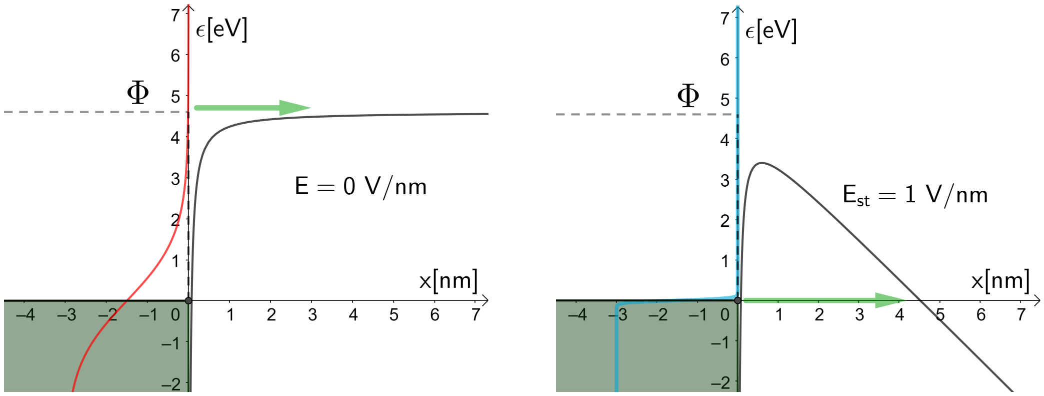

(a) Thermionic emission (b) Field emission

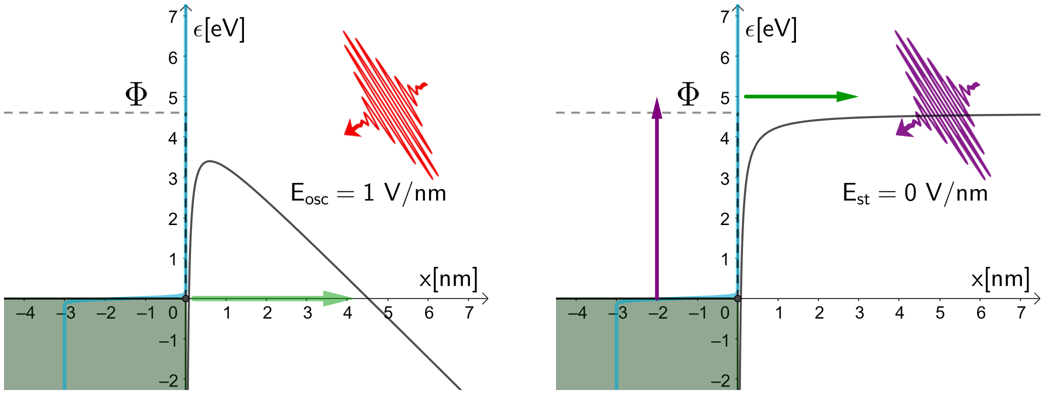

(c) Optical field emission (d) Photoelectric emission

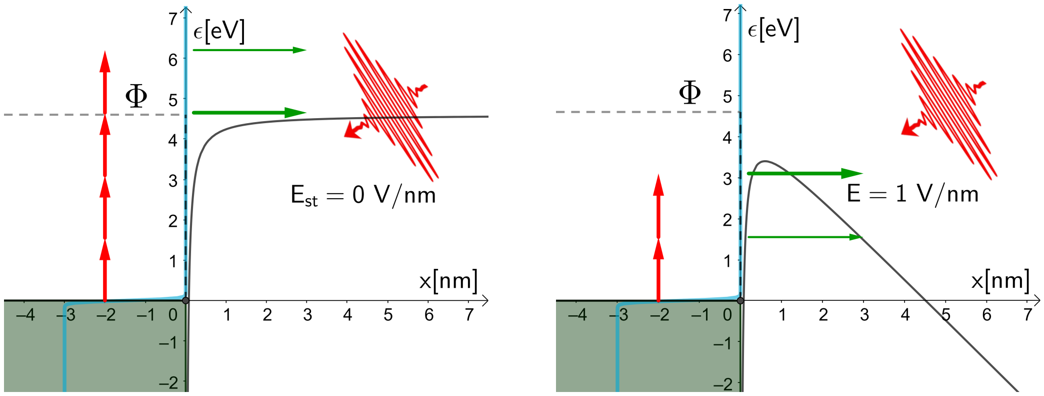

(e) Multiphoton photoemission (above-threshold photoemission) (f) Tunnel-assisted below-threshold photoemission

Figure 2.14: Energy diagrams of the physical mechanisms that can trigger the emission of electrons from a metal surface. The zero energy corresponds to the Fermi level, the black solid line is the potential barrier, the dashed line is the vacuum level, and the blue line represents the Fermi-Dirac distribution at room temperature (red line for the thermionic emission case, $T = 10,000\,\mathrm{K}$). The green arrows indicate electron emission and the vertical arrows represent the energy of one photon (red: $1.55\,\mathrm{eV}$, violet: $5\,\mathrm{eV}$). The electric field can be induced by the static bias voltage E_{st}, the oscillating laser field E_{osc}, or the addition of both E.

2.4.1.1 Thermionic emission

Thermionic emission occurs when the thermal energy transferred to an electron in a medium is larger than the work function of the material, which provides the electron with enough energy to overcome the potential barrier and be ejected into vacuum. Thermionic emission is described by Richardson's Law [118], which states that

$$J = AT^2 \exp\left(-\Phi/kT\right), \tag{2.19}$$

where J is the emission current density, T is the temperature, Φ is the work function of the material, k is Boltzmann constant and the Richardson coefficient A is given by

$$A = \lambda_{\mathrm{R}} A_0\,, \tag{2.20}$$

where λ_{R} is a material-specific coefficient and A_0 is a constant given by

$$A_0 = \frac{4\pi m_e k^2 e}{h^3} = 1.20173 \times 10^6\,\mathrm{Am^{-2}K^{-2}}\,, \tag{2.21}$$

where h is Planck's constant, and e and m_e are the electron charge and mass, respectively.

Electrons are fermions, which can only occupy one state per particle, therefore, the energy distribution can be described by Fermi-Dirac statistics. As the temperature of the medium increases, the Fermi-Dirac distribution spreads and it develops a tail at high energies that can reach the work function energy. This is illustrated in Fig. 2.14a, where the Fermi distribution is presented in red and the work function energy level is shown with a black dashed line. The kinetic energy of an emitted electron is given by the difference between the electron energy and the work function. The electrons kinetic energy spread will follow the tail of the Fermi-Dirac distribution. In general, the material temperature needs to reach a few thousand Kelvin for the electrons to have enough energy to overcome the potential barrier.

2.4.1.2 Field emission

Field emission occurs when a static or quasi-static electric field lowers the potential barrier in a material, increasing the probability of electrons tunneling into vacuum due to the reduced barrier width. The formula to describe this quantum tunneling through a triangular barrier was first proposed by Fowler-Nordheim [119]. When the electron emission occurs at the apex of a nanometric sharp tip, additional modifications to the model have been proposed to account for geometrical effects when the tip radius is less than tens of nanometers [120, 121]. The general formula for the field emission current density [122] has the form

$$J = AE^2 \exp\left(-B\Phi^{3/2}/E\right), \tag{2.22}$$

where

$$A = e^3 / \left[16\pi^2\hbar\Phi \; t^2\left(\frac{(e^3E)^{1/2}}{\Phi}\right)\right], \tag{2.23}$$

$$B = \frac{4}{3e}\left(\frac{2m_e}{\hbar^2}\right)^{1/2} v\left(\frac{(e^3E)^{1/2}}{\Phi}\right), \tag{2.24}$$

E is the applied electric field, Φ is the work function, e is the electron charge, m_e is the electron mass, $t\left(\frac{(e^3E)^{1/2}}{\Phi}\right)$ and $v\left(\frac{(e^3E)^{1/2}}{\Phi}\right)$ are functions that arise from image charge effects, but they are usually neglected since they are close to unity for typical conditions. A linear behavior is expected when $\ln\left(J/E^2\right)$ is plotted versus $1/E$. In general, an electric field on the order of a few V/nm is required to bend the potential barrier enough for the electrons to tunnel, as shown in Fig. 2.14b. Most of the electrons emitted with field emission have energies close to the Fermi energy level.

2.4.1.3 Optical field emission

The high peak intensity achieved with ultrafast laser pulses provides large electric fields that can temporarily lower the potential barrier of a material to allow electrons to tunnel through the reduced barrier. This process is known as optical field emission or photofield emission, and is shown in Fig. 2.14c. The principle is the same as in regular field emission, but in this case, the electric fields are provided by the incident electromagnetic radiation and are applied to the material for a short time. Eq. 2.22 can still be used to describe the current density produced by optical field emission. The relation between the laser intensity I and the oscillating electric field of the laser pulse E_{osc} is given by $E_{\text{osc}} = \sqrt{2I/\varepsilon_0 c}$, where ε_0 is the vacuum permittivity and c is the speed of light.

2.4.1.4 Photoelectric emission

The photoelectric effect describes when an electron absorbs the energy of a photon ($\hbar\omega$) and is promoted to a higher energy level. If the absorbed photon energy is higher than the work function of the material (Φ), then the electron will be emitted into vacuum. This mechanism is known as photoelectric emission or photoemission, and it is illustrated in Fig. 2.14d. The photoemission from metal surfaces has been explained by classical models such as the three-step model (TSM) [123–126] and the

Fowler-DuBridge (FD) model [127–129]. The formula for the photoemission current density [130, 131] has the form

$$J = e(QE)\frac{I}{\hbar\omega}\,, \tag{2.25}$$

where the Quantum Efficiency (QE) is the number of emitted electrons per incident photon, ω is the photon frequency, and I is the laser intensity, which is a function of the laser electric field E_{osc} as follows $I = \varepsilon_0 c E_{\text{osc}}^2/2$. If the photon energy is higher than the work function, then the emitted current density will increase linearly with laser intensity. The kinetic energy of the emitted electrons will be independent of the laser intensity, and it will be determined by the energy difference between the photon energy and the work function.

2.4.1.5 Multiphoton photoemission

Multiphoton absorption is a nonlinear process that occurs under high-intensity radiation, and it can provide electrons with enough energy to overcome the potential barrier even if the incident photon energy is lower than the work function [132]. In the regular photoelectric effect, photons can only be absorbed when their energy is equal to the energy difference between two quantum states in the material. However, multiple photons can be absorbed when electrons are temporarily excited into virtual states (Fig. 2.14e).

The lifetime of the virtual states is determined by the uncertainty principle $\Delta\epsilon\Delta t \geq \hbar/2$, where $\Delta\epsilon$ is the photon energy, except when there is a real state nearby, then $\Delta\epsilon$ is the difference between the virtual state and the nearest real state [133, 134]. In general, $\Delta\epsilon$ is so large that Δt approaches zero, and it is assumed that the absorption of multiple photons occurs simultaneously [135]. For example, when 800 nm photons illuminate a metal, the lifetime of the first virtual state would be around $\Delta t \approx 0.2$ fs.

The ionization rate for a single photon is defined as $W = \sigma_1 I$, where I is the laser intensity and σ_1 is the 1-photon absorption cross-section with units of cm^{-2}. Then, for two photons, the ionization rate is $W_2 = \sigma_2 I^2$, where $\sigma_2 = \sigma_1\tau$ and τ is the lifetime of the first virtual state [133]. Therefore, this relation can be extended to describe the electron emission current density produced by the absorption of multiple photons as

$$J = \sigma_n I^n\,, \tag{2.26}$$

where n is the number of photons being absorbed and σ_n is the n-photon ionization or absorption cross-section [136, 137]. When J is plotted versus I in a log-log plot, it follows a linear trend where the slope of the line indicates the n number of photons being absorbed. Even though the electrons absorb only integer numbers of photons, the experimentally measured values for n do not have to be integers, since the total photoemission current contains the contribution from electrons that absorbed a different number of photons. Furthermore, the electron emission can also be thermally assisted. The kinetic energy of the emitted electrons will be given by the difference between the photon energy times the number of absorbed photons and the work function.

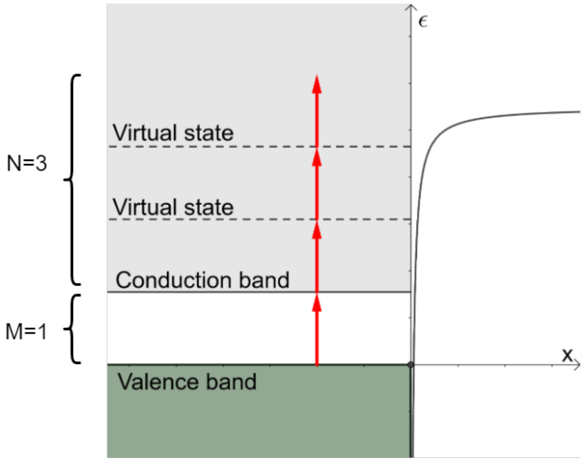

Figure 2.15: Energy diagram of the multiphoton photoemission in a semiconductor. In this specific example, electrons first transition into real states in the conduction band and then into virtual states before they are emitted from the surface.

In the case of semiconductors, there are certain situations where electrons can first transition into real states and then into virtual states, as shown in Fig. 2.15. In that case, the absorption probability has to be calculated independently for both cases [138].

2.4.2 Keldysh parameter

The electron emission mechanisms described in the previous section are not exclusive of each other and can occur simultaneously. The optical field emission and the multiphoton photoemission are of special interest for the experiments presented here, because of the high fields achieved by the ultrafast pulses. There will be situations when the absorbed energy of one or multiple photons is still lower than the material work function, and photoemission will not occur. However, the laser electric field will still tilt the potential barrier in vacuum, which means that these hot electrons experience a reduced barrier width and will have a higher probability of tunneling through the barrier (Fig. 2.14f). This process is known as tunnel-assisted below-threshold photoemission [139]. The emitted electrons will keep the energy they had when tunneling through the reduced barrier. The Keldysh model [132], which describes photoionization, has been used to identify the dominant emission mechanism in those situations. It shows that the transition between the multiphoton and tunneling emission regimes can be characterized by a parameter that depends on the laser and material properties, known as the Keldysh parameter [132], which is given by

$$\gamma = \sqrt{\frac{\Phi}{2K}} = \frac{\omega}{eE_{\mathrm{osc}}}\sqrt{2m_e\Phi}\,, \tag{2.27}$$

where Φ is the work function of the material, $K = \frac{e^2E_{\mathrm{osc}}^2}{4m_e\omega^2}$ is the ponderomotive force, ω is the laser frequency, m_e is the electron mass and E_{osc} is the laser peak electric field. According to this model, when the Keldysh parameter is lower than unity ($\gamma < 1$), it is an indication of optical field emission. On the contrary, $\gamma > 1$ indicates that multiphoton photoemission is occurring. This approach has been successfully used to study the transition regime between optical field emission and multiphoton emission induced by ultrafast laser pulses in metallic tips [140–142].

2.4.3 Schottky effect

When an electric field is applied to the surface of a material, the potential barrier in vacuum will be lowered, and the effective work function will be reduced; this is known as the Schottky effect. The work function Φ, as a function of time and distance from the sample surface, is given by

$$\Phi(x,t) = \epsilon_{\mathrm{F}} + \Phi_{\mathrm{eff}}(t) - \frac{e}{16\pi\varepsilon_0 x} - E_{\mathrm{st}}x - E_{\mathrm{osc}}x\cos\omega t\,, \tag{2.28}$$

where $\Phi(x,t)$ is the sum of the Fermi energy ϵ_{F}, the effective work function Φ_{eff}, the image charge potential, the applied static electric field E_{st}, and the oscillating electric field of a laser pulse E_{osc}. The effective work function, in turn, is given by [130]

$$\Phi_{\mathrm{eff}}(t) = \Phi_0 - \sqrt{\frac{e(E_{\mathrm{st}} + E_{\mathrm{osc}}\cos\omega t)}{4\pi\varepsilon_0}}\,, \tag{2.29}$$

where Φ_0 is the material work function, e is the electron charge, ω is the laser frequency, and ε_0 is the vacuum permittivity. The lowering of the potential barrier under static and oscillating fields is illustrated in Figs. 2.14b, 2.14c and 2.14f with black solid lines.

Chapter 3

Experimental background

The THz-STM technique is accomplished by a complex system that involves an ultra-high-vacuum chamber, lasers, specialized electronic and optical devices, signal amplification stages, synchronization schemes and an STM that operates with home-made nanometric tips. The experimental details required to operate the THz-STM system will be presented in this chapter, along with the procedures for the data acquisition during the experiments.

3.1 THz-STM Instrumentation

The laser system consists of a modelocked oscillator (Coherent Micra) that delivers femtosecond pulses centered at 800 nm, with a repetition rate of 80 MHz and $\sim 4.5\,\text{nJ}$ of energy per pulse. These pulses are then stretched and used as a seed for a Ti:sapphire regenerative amplifier (Coherent RegA), which, after the compressor, delivers 70 fs pulses centered at 800 nm, with a repetition rate of $f_{\text{rep}} = 250\,\text{kHz}$ and $\sim 3\,\mu\text{J}$ of energy per pulse. The amplifier crystal was pumped with a CW diode-pumped laser (Coherent Verdi-18) centered at 532 nm that provides 14 W of power (18 W max). This CW pump laser was at one point replaced by a similar laser (Sprout-G) with the same characteristics. The ultrafast laser pulses are then split into three main beams (Fig. 3.1), and each one of them goes into a manual coarse delay stage. Two of them then go into a motorized delay stage (Thorlabs NRT150), with a 15 cm range and $7.5\,\mu\text{m}$ step size, to control the temporal delay between the different beam lines with a 50 fs step size resolution.

The first beam containing 80% of the power is focused onto a large-area GaAs-based photoconductive antenna [143, 144] (Tera-SED), which generates single-cycle THz pulses with peak electric fields of $E_{\text{THz,pk}} = 520\,\text{V/cm}$ and a measured average power of $P_{\text{THz,avg}} = 27\,\mu\text{W}$. To extend the lifetime of the PC antenna, instead

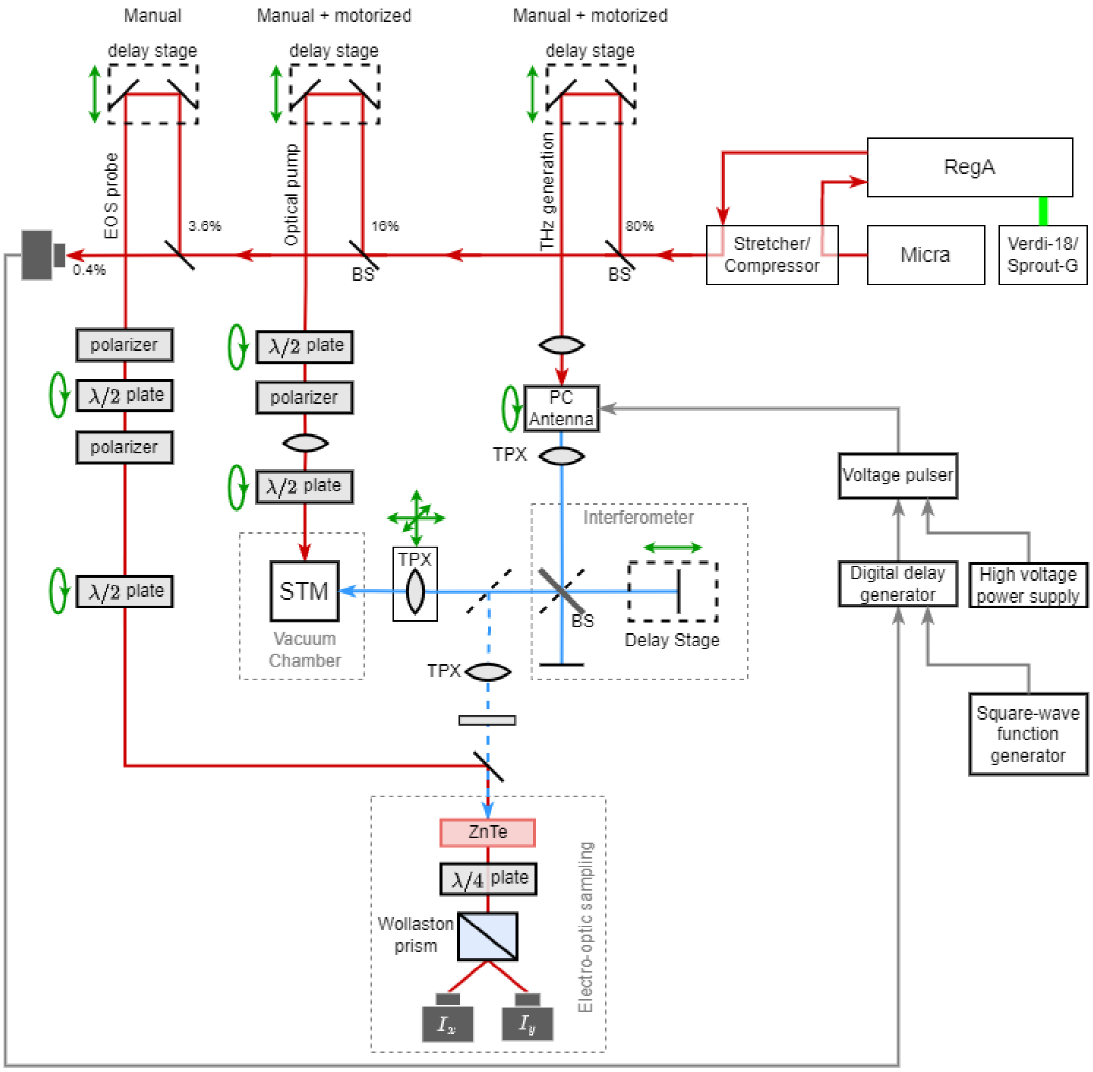

Figure 3.1: Simplified layout of the optical setup of the THz-STM system. The light green line is the pump laser beam of the RegA, the red line is the 800 nm optical pulse train, the blue line is the THz pulse train, and the blue dashed line is the alternative path of the THz pulse train for EOS. The gray lines represent the electrical connections for the equipment used to trigger and modulate the THz generation at the PC antenna. The green arrows illustrate the degrees of freedom of the components.

of a DC voltage, it is biased with a voltage pulse of 30 V and 55 ns long from a high-voltage-pulser (Directed Energy HV1000) that was powered by a high-voltage supply (Lambda Electronics Model 71). The voltage pulser was triggered by a delay generator (Stanford Research Systems DG645) that was, in turn, triggered by the signal from a Si Biased detector (Thorlabs DET10A) that monitors the optical laser pulses. The delay generator ensures the synchronous application of the voltage pulse with the arrival of the optical laser pulse at the PC antenna. The generation of the THz pulses is electronically modulated by enabling the delay generator with a 5077 Hz square wave from a function generator (BK Precision BK4052), which allows for the lock-in detection of the THz-induced signal at the STM or the EOS setup. The PC antenna is mounted on a motorized rotation stage (Thorlabs PRM1Z8) to control the polarization angle of the emitted THz fields. After the antenna, the divergent THz beam is collimated by a polymethylpentene lens (Menlo Systems TPX lens) with a 35 mm focal length. The THz beam can be split, with a 2” diameter high resistivity silicon wafer, into the two arms of an interferometer, where one of the mirrors is mounted on a delay stage (Thorlabs MTS50-Z8) to perform autocorrelation measurements. The silicon wafer can also be replaced with a gold mirror to skip the autocorrelator and send the THz beam directly into the EOS setup or into the STM vacuum chamber. A triple-axis inverted viewport (MDC Vacuum Products PSM-1502) manipulates the position of a 54 mm focal length TPX lens that is used to focus the THz beam onto the STM junction at an angle of 40° above the horizontal plane.

The second beam, containing 16% of the power, is meant to be used as a pump beam for the STM junction. The pump beam power can be controlled remotely by changing the rotation angle of a half-wave-plate mounted on a rotation stage (Thorlabs PRM1Z8) placed before a Glan-Taylor polarizer. The average power measured just outside the vacuum chamber ranges from 0 to 26.3 mW. The pump beam polarization angle can also be controlled by a second half-wave-plate mounted on a rotation stage. The pump beam is then focused at the STM junction with a 500 mm focal length lens at an angle of 40° above the horizontal plane. Such a large focal length was required due to the large distance from the vacuum port window to the STM junction. This limited the tightness of the laser spot size at its focus. From Gaussian optics, it follows that the beam waist diameter at the focus is given by

$$2\omega_0 = \frac{4\lambda F}{\pi D}\,, \tag{3.1}$$

where ω_0 is the beam radius, λ is the wavelength, D is the diameter illuminated on the lens, and F is the focal length. With $\lambda = 800\,\mathrm{nm}$, $F = 500\,\mathrm{mm}$ and $D = 10\,\mathrm{mm}$, a spot diameter of $50\,\mu$m is expected. However, when it was experimentally measured outside the chamber with the slit method, a beam diameter of $216\,\mu$m was obtained. The discrepancy is most likely due to aberrations from the lens and a non Gaussian input beam.

The third laser beam is used as a probe for electro-optic sampling detection of the THz pulses. The beam power is manually controlled by a half-wave-plate on a rotation mount that is placed in between two crossed polarizers. The manual rotation of a second half-wave-plate controls the polarization angle of the sampling beam. The electro-optic sampling setup consists of a 5 mm × 5 mm ZnTe crystal that is 1 mm thick, a quarter-wave-plate, a Wollaston prism and a pair of photodiodes (Thorlabs PDB210A), as shown in Fig. 3.1. A flip-up mirror can be used to reroute the THz beam into the EOS setup. A 54 mm focal length TPX lens focuses the THz beam onto the ZnTe crystal and a 4 mm thick disc of fused-silica is placed on its path to simulate the viewport of the ultra-high-vacuum (UHV) chamber.

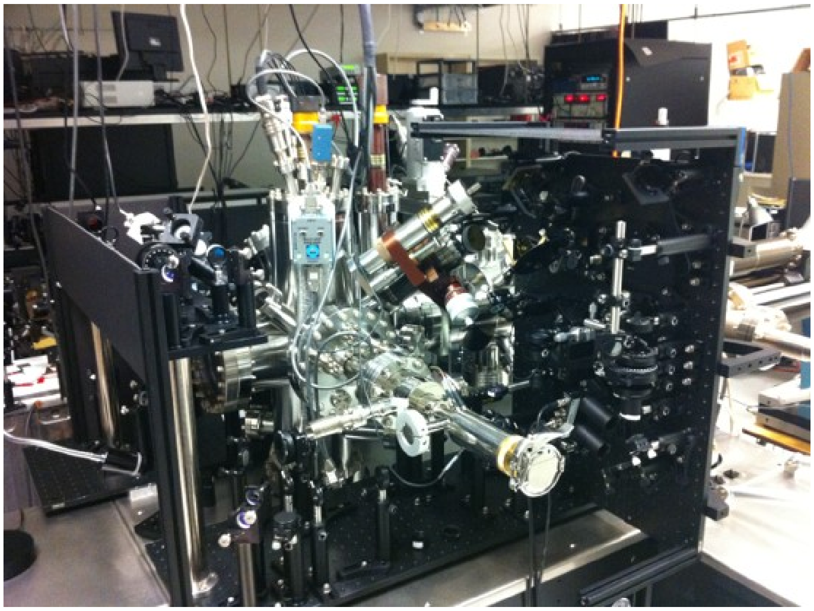

Figure 3.2: Photograph of the STM chamber surrounded by the optical components used to guide the laser pulses inside the vacuum chamber.

A photograph of the microscope is shown in Fig. 3.2 , which is a commercial UHV STM system (RHK-UHV-SPM 3000) where the tip is connected to virtual ground and the sample is biased. The samples can be cooled using an open-flow cryostat (CryoIndustries RC-110), which can lower the sample temperature down to 100 K (30 K) using liquid nitrogen (liquid helium). As shown in Fig. 3.3, the tunnel current signal from the STM is initially handled by a first-stage commercial current preamplifier, which can be either an RHK IVP-100, IVP-200, or IVP-300, with a gain of 10^7, 10^8 or 10^9 V/A, and a bandwidth of 250, 50 or 5 kHz, respectively. The most sensitive preamp (IVP-300), which has an RMS noise of 0.3 pA at 1.5 kHz, was used for all the experiments. The tunneling current signal then goes through a second-stage amplifier (RHK IVP-PGA) with a configurable gain of 1,10 or 100 and a low-pass-filter that can be set to 0.5 kHz, 1.5 kHz, 5 kHz, 15 kHz, 50 kHz, 150 kHz or no-filter. A gain of 1 (experimentally measured to be 1.04) and a bandwidth of 5 kHz were used for all the experiments. The amplified tunneling current signal then goes into the STM controller (RHK SPM 1000), which handles the operation of the STM in general and communicates with the STM software (XPMPro 2.0) to save the collected data. The STM controller provides a current monitor channel output that can be used to externally record and further process the amplified tunneling current signal. A data acquisition analog-to-digital converter (National Instruments USB6212DAQ) is used to save this signal directly into the computer. In parallel, that signal is sent to a low-noise amplifier (Stanford Research Systems SR560) with a gain of 10 and a low-pass-filter of 100 Hz, which can be used for sensitive average current measurements. A lock-in amplifier (SR 830 DSP) referenced to the THz pulse modulation frequency (5077 Hz) is also connected in parallel to extract the THz-induced current from the total tunneling current signal, as shown in Fig. 3.3.

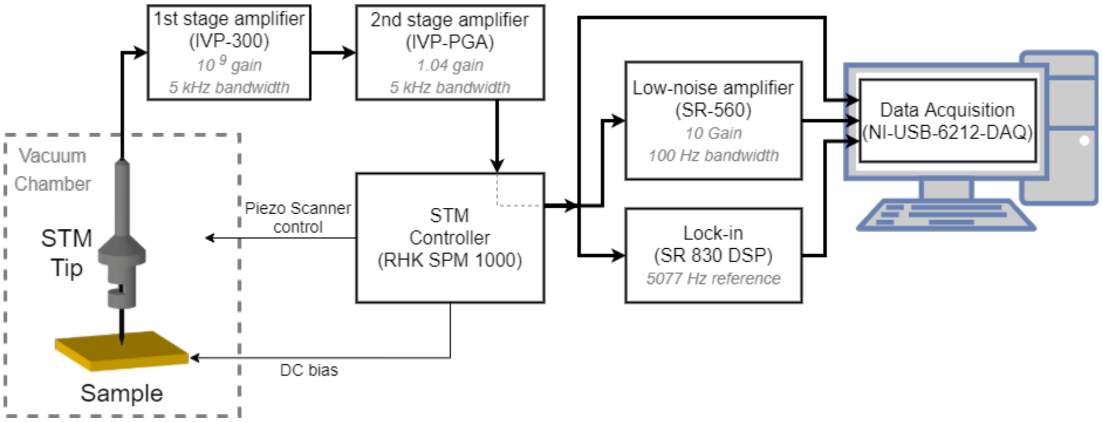

Figure 3.3: Schematic of the electronic equipment used to monitor, filter, amplify, and record the tunneling current signal from the STM. The signal first goes through a 2-stage amplification process before it reaches the STM controller, where it is recorded and processed. The signal is then split into three branches that will be saved into the computer: the signal from the first branch is recorded as is, the second one is cleaned by a low-pass filter for sensitive measurements, and the third one is used to extract the THz-induced current signal by lock-in detection.

When the STM operates in constant current mode with a DC bias and the THz is on, the polarity of the THz-induced current cannot be determined directly by looking at the total tunneling current, since its contribution to the total current is usually small and close to the noise level (a few pA). However, it can be determined on a metallic sample with the following procedure: The STM controller inverts the output signal of the tunneling current when the bias voltage is set to negative. Therefore, the first step is to set the STM bias to a positive value to ensure that the tunneling current matches the positive STM controller output. This can be monitored from the STM software oscilloscope. The output signal from the SR-560 amplifier should also be positive; if not, it needs to be inverted on its front panel. The feedback loop can then be turned off, and the bias voltage should be set to zero. The THz electric field can be increased until a THz-induced current is detected by both the SR-560 amplifier and the lock-in amplifier. The polarity of the THz-induced current should be the same on both amplifiers; if not, the lock-in phase needs to be adjusted to make them match. This will ensure that the lock-in displays the correct polarity of the THz-induced current, and it can be confirmed by rotating the polarization of the THz pulses by 180°, which should generate a negative THz-induced current.

In a THz-STM experiment, the number of tunneling electrons per THz pulse is the most useful quantity to monitor, and the formula to convert the lock-in output signal into the number of electrons per pulse $N_{\mathrm{e/pulse}}$ is given by

$$N_{\mathrm{e/pulse}} = \frac{1}{e\, f_{\mathrm{rep}}} Z_{\mathrm{exp}}\, K_1\, K_2\, K_{\mathrm{Lck}}\, V_{\mathrm{Lck,sens}} \frac{V_{\mathrm{Lck,out}}}{10\,\mathrm{V}}\,, \tag{3.2}$$

where Z_{exp} is a correction factor obtained experimentally (see Section 5.1), e is the electron charge, f_{rep} is the repetition rate of the laser, K_1 and K_2 are the 1st and 2nd stage amplifiers inverse gain for a given THz modulation frequency (see Ref. [117]), K_{Lck} is a lock-in calibration factor for a squarewave with 50% duty cycle, $V_{\mathrm{Lck,sens}}$ is the lock-in sensitivity and $V_{\mathrm{Lck,out}}$ is the lock-in output signal. For the experiments presented here, the THz modulation frequency was 5077 Hz and the following parameters were used: $Z_{\mathrm{exp}} = 0.832$, $f_{\mathrm{rep}} = 250\,\mathrm{kHz}$, $K_1 = 1.7\,\mathrm{nA/V}$, $K_2 = 0.96$, $K_{\mathrm{Lck}} = 2.13$ and $V_{\mathrm{Lck,sens}} = 50\,\mathrm{mV}$. This results in a total conversion factor of $N_{\mathrm{e/pulse}} = (361 \frac{\mathrm{e}}{\mathrm{V\,pulse}}) V_{\mathrm{Lck,out}}$.

Alternatively, $N_{\mathrm{e/pulse}}$ can also be obtained from the SR-560 amplifier output $V_{\mathrm{SR560,out}}$, where the conversion formula is

$$N_{\mathrm{e/pulse}} = \frac{1}{e\, f_{\mathrm{rep}}} D\, Z_{\mathrm{exp}}\, K_1\, K_2\, K_3\, V_{\mathrm{SR560,out}}\,, \tag{3.3}$$

where D is the THz modulation duty cycle and K_3 is the SR-560 amplifier inverse gain.

The UHV STM system described here has the capability to perform THz-STM experiments on a variety of samples. There are three different types of STM sample holders: one for semiconductors, one for metals, and one for sample cleaving, as shown in Fig. 3.4. All samples undergo a bakeout of at least 6 hrs at 120 °C when placed in the vacuum chamber. In the case of semiconductors, a sapphire washer beneath the sample provides electrical insulation from the rest of the sample holder. A pair of tantalum stripes are placed underneath the sample to provide an electrical connection with an ohmic contact. These electrical contacts are used to bias the sample during the STM operation. Alternatively, a voltage can be applied between these two contacts to drive a current through the sample and raise its temperature for degassing or flashing purposes. A thermocouple can be placed under the first sapphire washer to monitor the sample temperature. In this configuration, the body of the sample holder can be either connected to bias or ground; however, a connection to bias usually presents less electrical noise in the system.

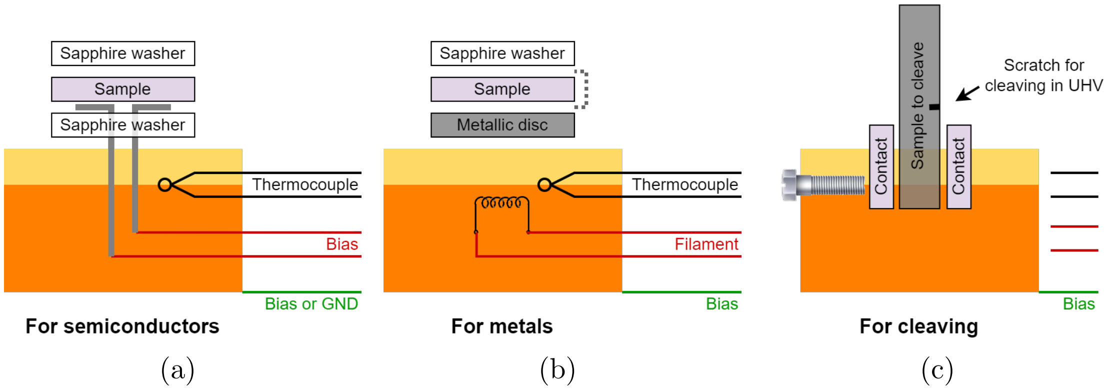

(a) (b) (c)

Figure 3.4: Cross-section diagrams of the STM sample holders that illustrate their electrical connections for a) semiconductors, b) metals and c) cleaving samples, respectively, from left to right.

In the case of metals, the sample is placed on top of a metallic disc. During STM scans, the metallic crystal is electrically connected to bias through mechanical contact with the metallic disc, which in turn is in contact with the sample holder. When the metal is deposited on an insulating substrate, a tantalum stripe is placed on top and around the sample (dotted gray line) to ensure its electrical connectivity with the metallic disk. A tungsten filament placed underneath can be resistively heated for annealing purposes. The filament is biased with a negative potential with respect to the sample and a typical current of up to 2.4 A heats the filament, which thermally emits electrons towards the metallic plate underneath the sample. The sample is heated through its mechanical contact with the metallic disc, which provides an even heat distribution across the sample. The sample can be thermally isolated, to minimize heat loss from thermal contact with the sample holder, by adding a sapphire washer underneath the metallic disc, but making sure that a tantalum stripe is in place around the washer to maintain the electrical connectivity between the disc and the sample holder. In this configuration, a thermocouple can also be used to monitor the sample temperature.

In the sample holder for cleaving, everything is electrically connected to the same potential. The sample is then placed vertically between two molybdenum contacts, and it is held in place by tightening a set-screw on the side of the sample holder. To set a preferential direction for cleaving, a scriber tool with a diamond tip is commonly used to scratch a line along the surface of the sample before it is mounted. A thermocouple cannot be used in this configuration. Finally, the electrical connections of the sample holder when it is installed on the STM stage are illustrated in Fig. 3.5 for reference.

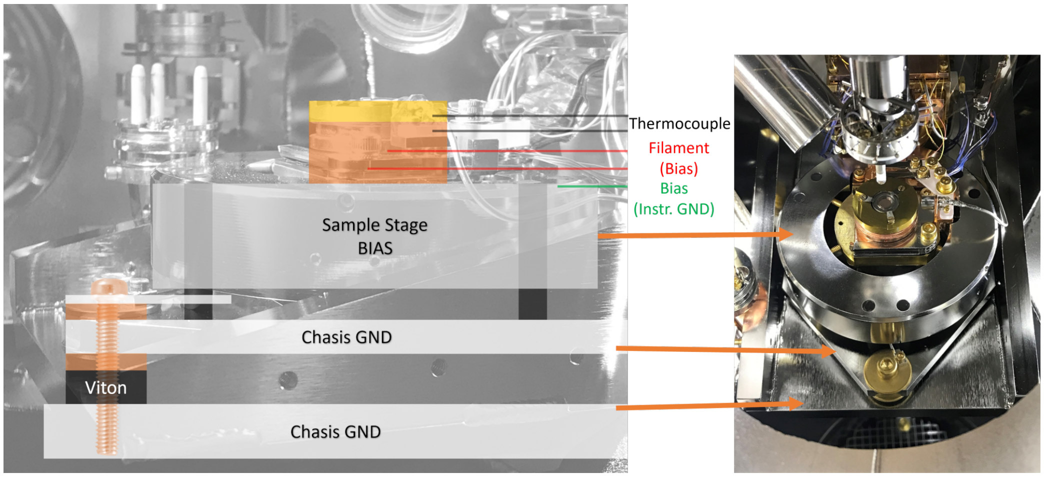

Figure 3.5: A photograph/schematic illustrating the physical electrical connections of the different platforms of the STM. Depending on the sample holder type, the sample stage can be connected to bias or ground (green line).

3.2 Tip preparation

The STM tips of the experiments presented here were made of either tungsten (W) or gold (Au), and they were all shaped by chemical etching. The W and Au wires with a purity of 99.95% and 99.998%, respectively, and a diameter of 0.25 mm were purchased from Alfa Aesar. A custom-made pneumatic baseplate is used to provide stable support for the etching setup and to reduce mechanical vibrations during the etching process to produce smoother tips.

For the case of Au, the wire was first sonicated in methanol to remove any contaminants from the surface, then it was partially submerged in a solution made of Ethanol

(UN1170 with 95% purity) and Hydrochloric Acid with a ratio of 1:1. A schematic of the submerged electrochemical etching method [145] is shown in Fig. 3.6a. A ring-shaped tungsten wire is used as the negative electrode around the Au wire. This electrode is submerged and then slightly lifted above the surface of the solution to form a meniscus. A programmable DC power supply (BK Precision 9120A) applies a voltage of 2.3 V between the Au wire and the electrode, and it also measures the current flowing through the circuit. A Labview program monitors the current and turns off the voltage as soon as it falls below 0.25 mA, which indicates that the etching process has finished and the tip is ready. Following this procedure produces tips with a conic shape as shown in Fig. 3.7d.

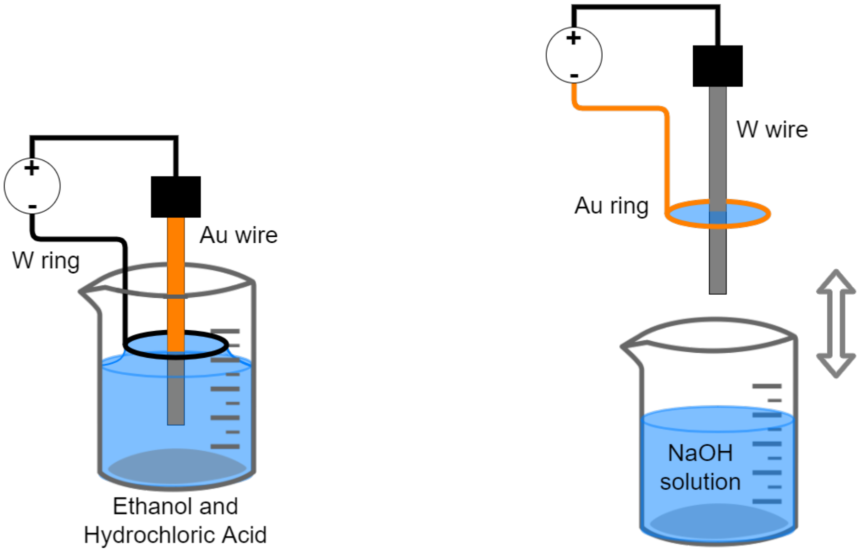

(a) Schematic of the submerged electrochemical etching method used for gold tips. The Au wire is 0.25 mm thick. The solution has Ethanol and Hydrochloric Acid with a ratio of 1:1. A voltage of 2.3 V is applied.

(b) Schematic of the single lamella electrochemical etching method used for tungsten tips. The W wire is 0.25 mm thick. The solution has 8 g of NaOH dissolved in 100 ml of deionized water. A voltage of 4 V is applied.

Figure 3.6: Schematic diagrams of the electrochemical etching methods used to fabricate the STM tips.

The W tips were made using the single lamella electrochemical etching method shown in Fig. 3.6b. The W wire is first sanded to remove the oxide from the surface, and it is then cleaned by sonication in methanol for a few minutes. The W wire is then vertically centered inside a ring-shaped Au wire that is used as the negative electrode in the circuit. A solution with 8 g of NaOH dissolved in 100 ml of deionized water is made in a small beaker. Both wires are momentarily submerged in the solution to form a lamella across the Au ring. The programmable DC power supply applies a voltage of 4 V between the W wire and the electrode, which is stopped by the Labview program when the current falls below 0.5 mA. This process will produce two tips, one that hangs from the holding fixture and one that drops after the wire is etched. A cup placed underneath the wire catches the part that falls, because it usually has a sharper tip profile. The tips are then cleaned with deionized water and kept in methanol, to avoid oxidation, until they are placed into the vacuum chamber. This method provides W tips with a conic shape, as shown in Figs. 3.7a and 3.7b. Variations in the etching method produce different tip profiles. For example, when the W wire is submerged in the solution, a tip with a cusp is formed (Fig. 3.7c). The cusp-shaped W tips are the most commonly used in STM and probably the most used for THz-STM experiments too. However, in the experiments presented here, the conic-shaped W tips coupled better with THz pulses and were more stable under high electric fields.

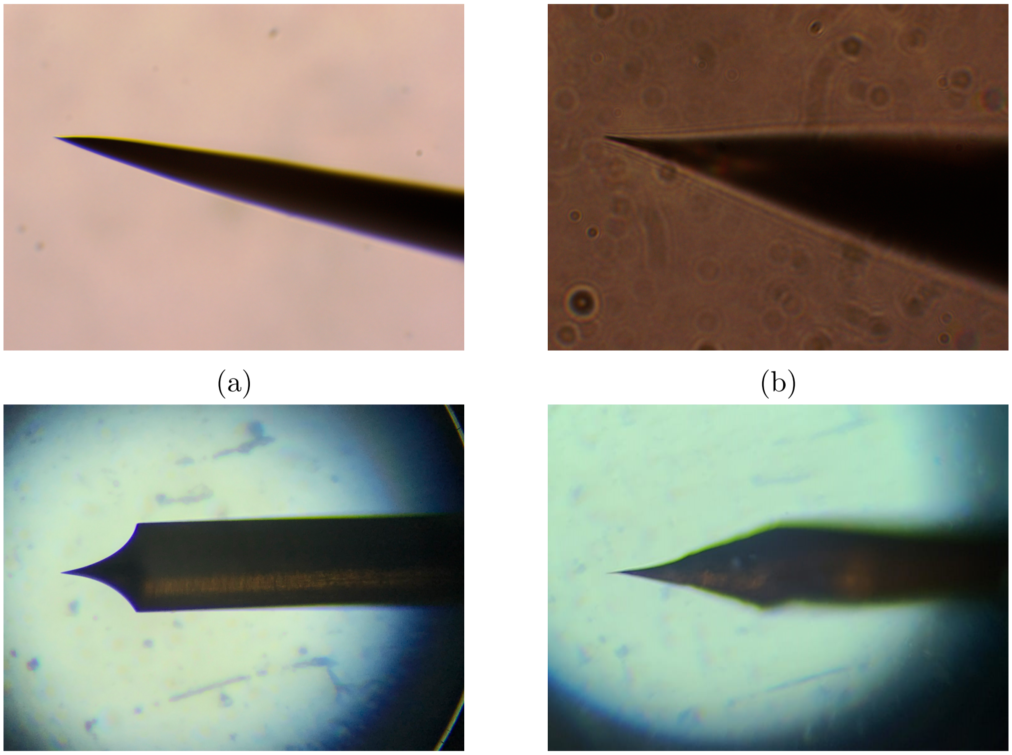
(a) (b) (c) (d)

Figure 3.7: Photographs of STM tips from an optical microscope. The single lamella electrochemical etching method (Fig. 3.6b) produced conic-shaped tungsten tips as shown by the top images where the magnification is a) 10x and b) 80x. c) When the tungsten wire is submerged in the NaOH solution, a tip with a cusp is formed instead. d) The submerged electrochemical etching method for Au wires (Fig. 3.6a) produced conic-shaped tips.

During the chemical etching process [146], a residual layer made primarily of tungsten trioxide WO_3, a few nm thick, is natively formed on the surface of the W tips [147, 148], although other contaminants such as carbon, NaOH and $WO_3 - Na$ microcrystals have also been found [149]. When the W tip is heated to 800 °C, the WO_3 reduces to WO_2, which is volatile [150]. Therefore, once inside the vacuum chamber, this oxide layer can be removed by heating up the tip with electron bombardment. This is done with the setup shown in Fig. 3.8a, where a current source is used to heat a thoriated-tungsten filament that thermally emits electrons into vacuum. A positive potential is applied to the tip to accelerate the emitted electrons towards it. When the electrons reach the tip, they are decelerated to the tip's Fermi velocity and the energy difference is transferred into heat. Because of the field enhancement at the tip apex, electrons will mainly heat the apex of the tip locally, removing surface contaminants in the area. Typical emission currents of $0.1 - 1\,\mathrm{mA}$ were produced with filament currents of $1 - 2\,\mathrm{A}$ and voltages of $100 - 1\,\mathrm{kV}$ between the tip and the filament.

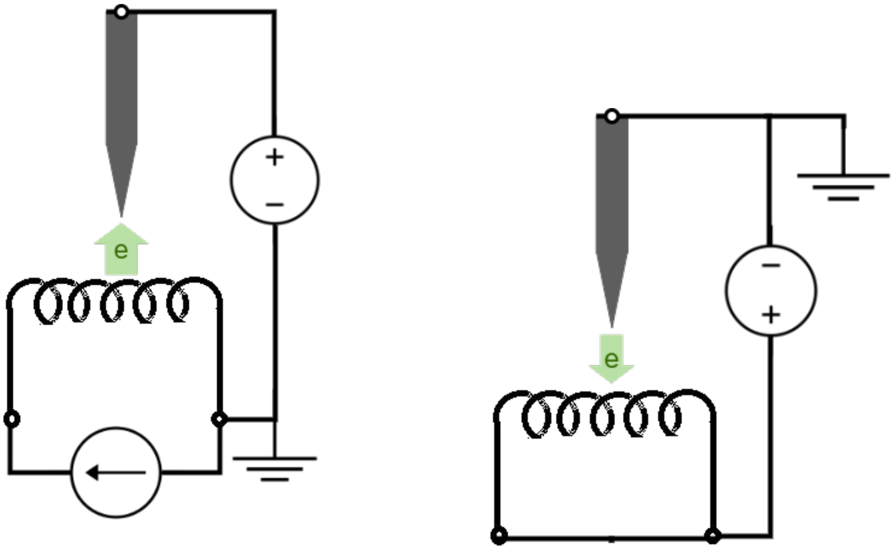

(a) (b)

Figure 3.8: Tip conditioning procedures. a) Schematic of the electron bombardment setup, where typical currents of $1 - 2\,\mathrm{A}$ resistively heat up a thoriated-tungsten filament that thermally emits electrons that are accelerated towards the tip by a potential difference of $100 - 1\,\mathrm{kV}$. Electrons absorbed by the tip will anneal it and remove contaminants from the surface. b) Schematic of the field emission setup, where a high positive potential is applied to a filament with respect to the tip to induce a field emission current that is used to characterize the tip sharpness.

Once the oxides and contaminants are removed from the tip surface, the same tip stage with a different configuration can be used to characterize the tip sharpness. A simplified schematic of this setup is shown in Fig. 3.8b, where a high field is applied between the tip and the filament to induce electron field emission mainly from the tip apex. The general formula of the current density for field emission is given by Eq. 2.22. If the tip is represented by a sphere of radius r at the end of a cone-shaped shank, then the electric field at the tip surface would be [151]

$$E = V/kr\,, \tag{3.4}$$

where V is the applied voltage and k is a geometrical factor, typically $k \approx 5$. Substituting Eq. 3.4 into Eq. 2.22 results in

$$I \propto \left(\frac{V}{r}\right)^2 \exp\left(b\,\Phi^{3/2}\frac{r}{V}\right), \tag{3.5}$$

where b is a constant. This equation shows the field emission current dependence on the tip radius. A sharper tip will require a smaller voltage to produce the same field emission current.

Field emission measurements are made on the tips after each cycle of electron bombardment to monitor their sharpness. A field emission current of $\sim$ 100 nA was typically used to monitor the tip sharpness. The applied voltage to induce field emission could range from a few hundred volts to 5 kV, which is the limit in our setup, but the voltage value was expected to decrease after each e-bombardment cycle. The voltage value depends on the distance between the tip and the filament, which varies from tip to tip, hence, this value is relative for each tip. Additionally, continuous field emission over long periods of time helps to reconfigure the tip apex, making it more stable to high currents.

3.3 THz-STM Spectroscopy

The coupling of the THz pulses to the STM not only provides a noncontact method to temporarily probe the junction, but also provides the capability to perform spectroscopy studies of the sample, since the THz field will induce a different response from the sample depending on its amplitude. Some of the most common spectroscopic techniques are described below.

3.3.1 $I_{\mathrm{THz}} - E_{\mathrm{THz,pk}}$ curve

A single-point measurement where the THz-induced current I_{THz} is recorded as a function of THz pulse peak electric field ($E_{\mathrm{THz,pk}}$), which is known as an $I_{\mathrm{THz}} - E_{\mathrm{THz,pk}}$ curve. This is one of the standard measurements that can be performed in a THz-STM system. The tip is positioned over a point of interest on the sample surface, while the THz pulses are off. The tip height is set by the DC bias, V_{DC}, and the current setpoint I_{DC}. The STM feedback loop is then turned off, V_{DC} can optionally be set to zero to obtain the sample response around its unbiased state, and I_{THz} is recorded as $E_{\mathrm{THz,pk}}$ is varied. This measurement is commonly used to find the onset of the THz-induced current. It is particularly useful when multiple features or multiple materials are present in the same sample because their onset will usually be different. Therefore, the THz peak field amplitude can be set to selectively highlight certain sample features on a THz-STM image and not others.

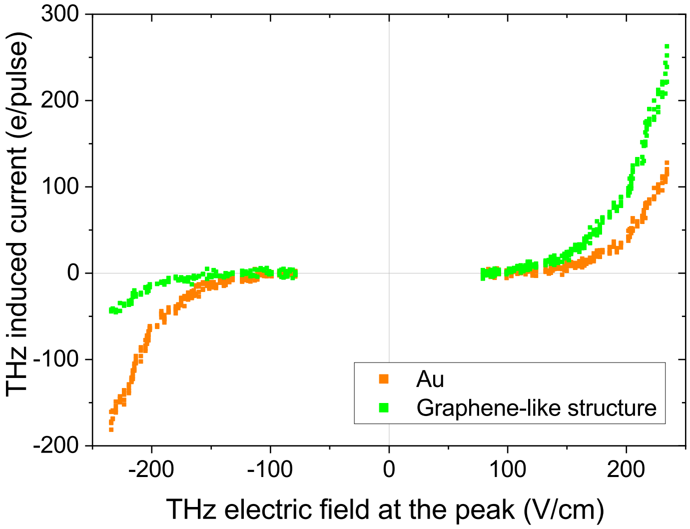

Figure 3.9: I_{THz} as a function of $E_{\mathrm{THz,pk}}$ on the gold surface and a graphene-like structure. The data was acquired with the feedback loop off, and the initial tip height was set by a +100 mV bias and a current setpoint of 50 pA.

An example of an $I_{\mathrm{THz}} - E_{\mathrm{THz,pk}}$ plot is shown in Fig. 3.9, where measurements were taken over a gold substrate (orange) and over a graphene-like structure (green) (See Sec. 4.2.4) on the same sample. The onset of these signals can be found from the logarithmic plot when the signal rises above the noise floor (2 e/pulse). Gold presents an onset around 115 V/cm for positive and negative $E_{\mathrm{THz,pk}}$. The graphene-like structure, on the other hand, presents an early onset around $E_{\mathrm{THz,pk}} = +100\,\mathrm{V/cm}$ and a late onset around $E_{\mathrm{THz,pk}} = -150\,\mathrm{V/cm}$. Therefore, in this case, a THz-STM image acquired, for example, with $E_{\mathrm{THz,pk}} = -200\,\mathrm{V/cm}$ will highlight the Au substrate, while $E_{\mathrm{THz,pk}} = +200\,\mathrm{V/cm}$ would highlight the graphene-like structure. Fig. 3.10 shows the $I - V$ curves of the same points for comparison, to demonstrate that these two plots can be fundamentally different, since one is obtained with a static voltage and the other one with a transient electric field.

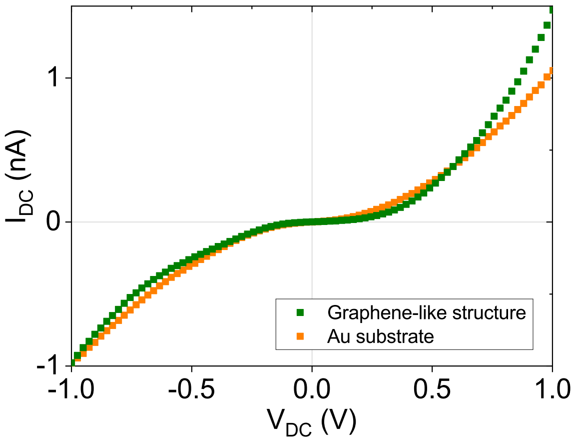

Figure 3.10: $I - V$ curves that were obtained on the gold substrate (orange) and a graphene-like structure (green), with a current setpoint of 1 nA and −1 V bias.

3.3.2 $I_{\mathrm{THz}} - V$ curve

The THz-induced current I_{THz} is recorded as a function of V_{DC} on a single point at the sample. The tip height is set by V_{DC} and I_{DC} with the THz pulses off. The feedback loop is then disabled, and the THz pulses are turned on. V_{DC} is swept while I_{THz} is recorded by means of a lock-in amplifier with the THz pulse generation being electronically modulated. When a THz field is present, the total current response ($I_{\mathrm{total,avg}} = I_{\mathrm{DC}} + I_{\mathrm{THz}}$) deviates from that of the static case, as can be seen in Fig. 3.11a, where three $I-V$ curves, acquired on the surface of Au(111) with $E_{\mathrm{THz,pk}} = +295\,\mathrm{V/cm}$, $E_{\mathrm{THz,pk}} = 0\,\mathrm{V/cm}$ and $E_{\mathrm{THz,pk}} = -284\,\mathrm{V/cm}$ are shown in blue, black, and red, respectively. The initial tip height was set by $V_{\mathrm{DC}} = -0.5\,\mathrm{V}$ and $I_{\mathrm{DC}} = 50\,\mathrm{pA}$.

The $I_{\mathrm{THz}}-V$ curves shown in Fig. 3.11b were acquired simultaneously with Fig. 3.11a. When $V_{\mathrm{DC}} = 0\,\mathrm{V}$, a positive (negative) $E_{\mathrm{THz,pk}}$ will induce a total positive (negative) I_{THz} due to the nonlinearity of the $I-V$ curve, as can be noted in both plots. The THz fields sweep a limited voltage window of the $I-V$ curve (Fig. 2.13). V_{DC} will offset that window towards the sides, therefore, a positive V_{DC} will increase the I_{THz} contribution of a positive $E_{\mathrm{THz,pk}}$, but will decrease for a negative $E_{\mathrm{THz,pk}}$. The opposite effect is observed for a negative V_{DC}. Information about the nonlinear response of the sample could be inferred from this measurement. If $V_{\mathrm{DC}} = 0\,\mathrm{V}$ then $I_{\mathrm{DC}} = 0\,\mathrm{A}$; therefore, $I_{\mathrm{total,avg}} = I_{\mathrm{THz}}$. In that case, for $E_{\mathrm{THz,pk}} = +295\,\mathrm{V/cm}$ ($E_{\mathrm{THz,pk}} = -284\,\mathrm{V/cm}$) the lock-in measured a value of $N_{\mathrm{e/pulse}} = 260\,\mathrm{e/pulse}$ ($N_{\mathrm{e/pulse}} = -105\,\mathrm{e/pulse}$) which corresponds to $I_{\mathrm{THz}} = 5.2\,\mathrm{pA}$ ($I_{\mathrm{THz}} = 2.1\,\mathrm{pA}$). These values can be used as a reference for the maximum current setpoint that can be safely used to operate in THz-driven mode with that specific $E_{\mathrm{THz,pk}}$ amplitude.

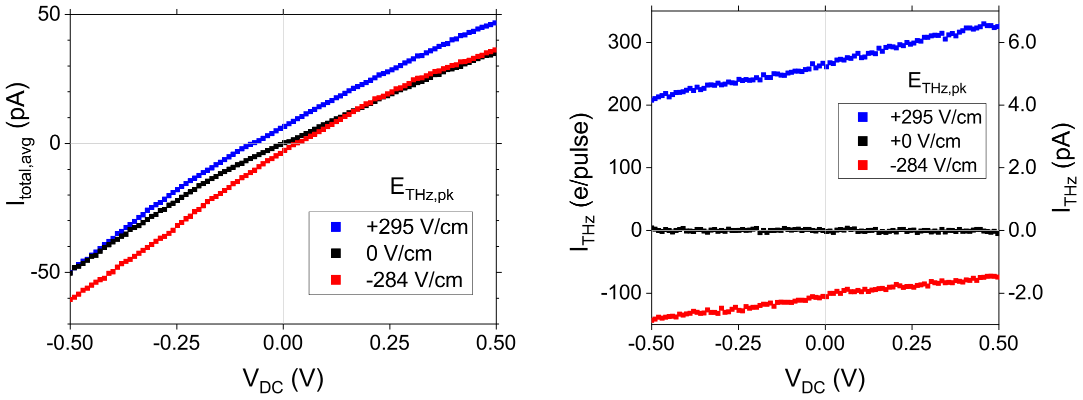

(a) (b)

Figure 3.11: $I - V$ and $I_{\mathrm{THz}} - V$ curves that were acquired simultaneously on the Au(111) surface with an initial tip height set by $V_{\mathrm{DC}} = -0.5\,\mathrm{V}$ and $I_{\mathrm{DC}} = 50\,\mathrm{pA}$. Three THz field amplitude cases are shown: $E_{\mathrm{THz,pk}} = +295\,\mathrm{V/cm}$, $0\,\mathrm{V/cm}$ and $-284\,\mathrm{V/cm}$ in blue, black, and red, respectively. a) $I - V$ curves showing the total current ($I_{\mathrm{total,avg}} = I_{\mathrm{DC}} + I_{\mathrm{THz}}$), including the DC and THz-induced contributions. b) $I_{\mathrm{THz}} - V$ curves showing I_{THz}, which is acquired by lock-in detection.

3.3.3 $I_{\mathrm{THz}} - z$ curve

The THz-induced current as a function of relative tip height (z) can also provide information about the sample, as it induces variations in the apparent barrier height at the junction. For this measurement, the initial tip height is set by I_{DC} and V_{DC} with $E_{\mathrm{THz,pk}} = 0\,\mathrm{V/cm}$. The feedback loop is then turned off, the THz pulses are turned on and I_{THz} is recorded as the tip is retracted away from the sample surface. The total current ($I_{\mathrm{total,avg}} = I_{\mathrm{DC}} + I_{\mathrm{THz}}$) can also be recorded simultaneously. Fig. 3.12a shows a semilog plot with $I_{\mathrm{total,avg}}$ data obtained on the surface of Au(111) with an initial tip height set by $I_{\mathrm{DC}} = 50\,\mathrm{pA}$ and $V_{\mathrm{DC}} = 50\,\mathrm{mV}$. There are three different cases $E_{\mathrm{THz,pk}} = +295\,\mathrm{V/cm}$, $E_{\mathrm{THz,pk}} = 0\,\mathrm{V/cm}$ and $E_{\mathrm{THz,pk}} = -180\,\mathrm{V/cm}$, which are shown in blue, black, and red, respectively. The experimental data, shown with squares, was then fitted with a decaying exponential following Eq. 2.12, which is also shown with solid lines.

The apparent barrier height extracted from the exponential fits for each case is shown in Fig. 3.12b. When $E_{\mathrm{THz,pk}}$ has the same polarity as V_{DC} (positive in this case), a larger tunneling current is observed, which translates into a reduced ABH as shown by the blue data point. When $E_{\mathrm{THz,pk}}$ has the opposite polarity to V_{DC}, the tunneling current decreases since the ABH increases. This effect is illustrated in Fig. 3.13, which shows the energy diagram of the tunnel junction. The static case is presented by a solid black line, where the applied V_{DC} induces an energy difference

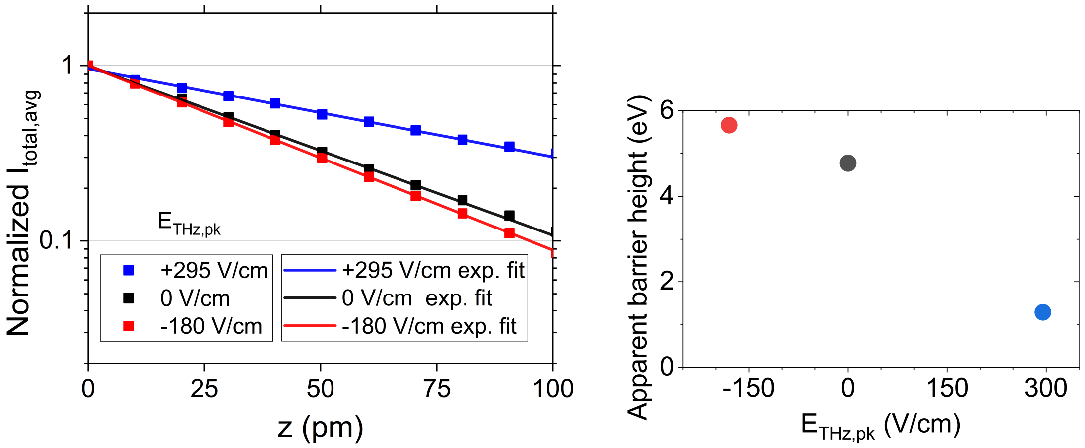

(a) (b)

Figure 3.12: a) Semilog plot of the $I - z$ curves measured on the Au(111) surface with an initial tip height set by $I_{\mathrm{DC}} = 50\,\mathrm{pA}$ and $V_{\mathrm{DC}} = 50\,\mathrm{mV}$. The data in blue, black, and red show the cases where $E_{\mathrm{THz,pk}} = +295\,\mathrm{V/cm}$, $E_{\mathrm{THz,pk}} = 0\,\mathrm{V/cm}$ and $E_{\mathrm{THz,pk}} = -180\,\mathrm{V/cm}$, respectively.

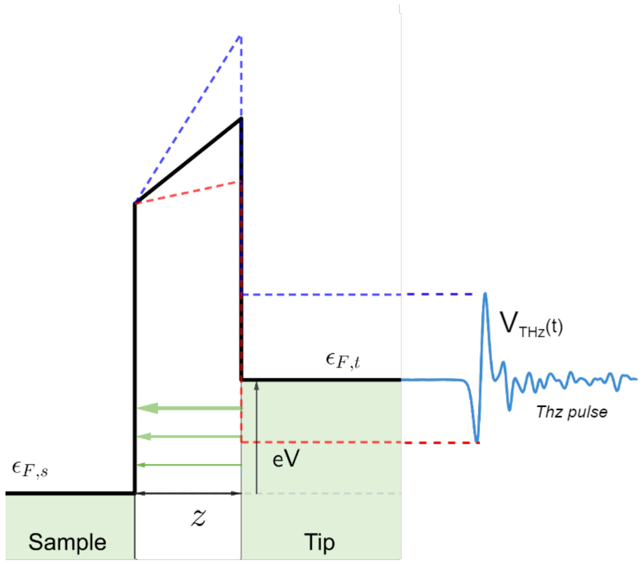

Figure 3.13: Energy diagram of the STM junction, where the Fermi energy of the tip $\epsilon_{\mathrm{F}t}$ is raised compared to the Fermi energy of the sample $\epsilon_{\mathrm{F}s}$ by a bias voltage V_{DC}, inducing a tunneling current. The potential barrier for the static case is shown with a solid black line. When a THz pulse couples to the junction, the transient THz voltage $V_{\mathrm{THz}}(t)$ induced by the THz field, modulates the energy difference between the Fermi levels. A positive THz field (blue dashed line) increases the energy difference, lowering the apparent barrier height. The opposite occurs for a negative THz field (red dashed line).

between the Fermi level of the tip ($\epsilon_{\mathrm{F},t}$) and the sample ($\epsilon_{\mathrm{F},s}$), which in turn generates a static tunnel current (green horizontal arrows). As shown by the dashed lines, when a THz pulse couples to the STM, the transient THz voltage $V_{\mathrm{THz}}(t)$ modulates the energy difference between the Fermi levels, which in turn modifies the apparent barrier height. In this case, when $V_{\mathrm{THz}}(t)$ is positive (blue dashed line), the energy difference increases and the ABH is reduced. When $V_{\mathrm{THz}}(t)$ is negative (red dashed line), the energy difference decreases and if the THz fields are large enough, $\epsilon_{\mathrm{F}t}$ could even be lower than $\epsilon_{\mathrm{F}s}$, which would induce a tunneling current in the opposite direction.

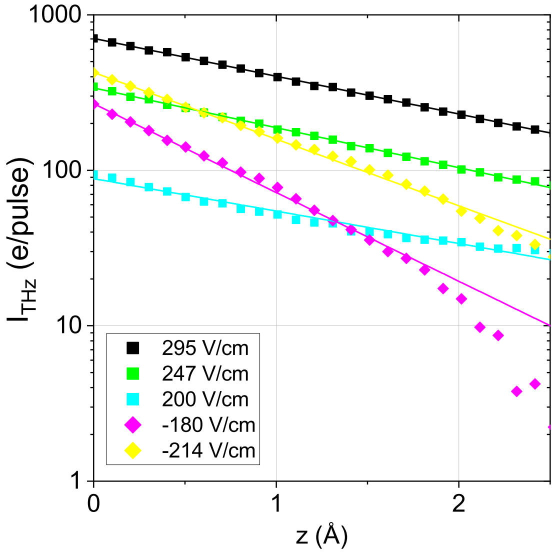

Figure 3.14: $I_{\mathrm{THz}} - z$ measurement on Au(111), acquired by lock-in detection for positive and negative $E_{\mathrm{THz,pk}}$ values. The initial tip height was set by $V_{\mathrm{DC}} = +5\,\mathrm{mV}$ and $I_{\mathrm{DC}} = 50\,\mathrm{pA}$. The experimental data is shown with colored squares, and it was fitted by single exponential functions, which are shown with colored solid lines.

The actual $I_{\mathrm{THz}} - z$ curves for several $E_{\mathrm{THz,pk}}$ values are shown in Fig. 3.14, where the experimental data (squares) was fitted with a decaying exponential (solid lines). It can be noticed that the slope of the $I_{\mathrm{THz}} - z$ curves, which corresponds to the THz-ABH, is similar for the cases when $E_{\mathrm{THz,pk}} > 0$, but it does change for the cases where $E_{\mathrm{THz,pk}} < 0$. Therefore, this measurement can provide information about the transient response of the sample to THz pulses.

3.3.4 Optical-pump THz-STM-probe

A great advantage of the THz-STM technique is its potential to probe ultrafast dynamics at the nanoscale. One of the techniques used for this purpose is known as optical-pump THz-probe, where an ultrafast optical pulse first photoexcites carriers in the sample, which are then probed by a THz pulse, as illustrated in Fig. 3.15. The temporal delay $\Delta\tau$ between the two pulses is controlled by a delay stage; hence, by recording I_{THz} as a function of time delay, the carrier dynamics can be studied. It should be noted that this measurement is not the result of a single event, but the average of multiple excitation events. Carrier dynamics, such as the generation and recombination times, can be extracted from this measurement, as long as they are in $< 1\,\mathrm{ns}$ timescales. The optical-pump THz-probe technique can be executed as a single-point measurement or as an imaging technique. Since the tip is in the tunneling regime and the THz fields are localized at the tip apex, the high spatial resolution of the STM can be maintained during this measurement. A THz-STM image acquired with a specific pulse delay would represent a snapshot of the carrier dynamics at that time. If the pulse delay is varied between the acquisition of images, then, the sequence of images will produce a movie of the carrier dynamics evolution in time.

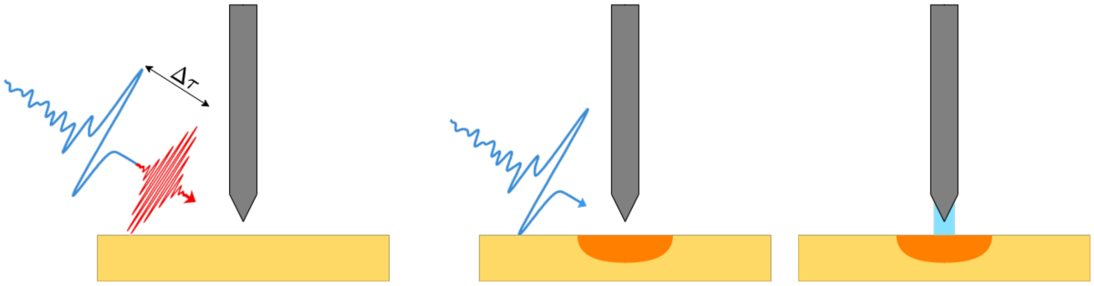

(a) (b) (c)

Figure 3.15: Schematic to illustrate the optical-pump THz-probe technique at the STM junction. a) An ultrafast optical pulse and a THz pulse are coupled onto the STM junction. The temporal delay between the two pulses $\Delta\tau$ is controlled by a linear delay stage. b) The optical pulse, which arrives first in this example, pumps and photoexcites carriers in the sample. c) The THz pulse can then probe the sample state by inducing a transient tunneling current. By changing the temporal delay while the tunneling current is recorded, the evolution of the carriers in time can be studied.

3.3.5 Photoemission sampling of the THz pulse waveform in the STM

The temporal profile of the near field, induced by the THz pulse field when it is coupled to the STM tip, can potentially be measured by taking advantage of the electron photoemission mechanisms described in Section 2.4. The configuration for this measurement is similar to the pump-probe experiment shown in Fig. 3.15a, but in this case, the tip is at least a few hundred nm away from the sample surface. To achieve this, the feedback loop is turned off while the tip is in the tunneling regime, and then it is manually retracted using the STM controller, while monitoring the tip height. When the ultrafast optical pulse illuminates the STM junction with enough power, multiphoton emission of electrons can be triggered, which will closely have the same duration as the ultrafast pulse, and can even be shorter due to the nonlinearity of the multiphoton emission [152]. The electric field of a THz pulse can then modulate the electron emission, which occurs mainly at the tip apex due to the geometrical enhancement of the fields [153]. By changing the temporal delay $\Delta\tau$ between the two pulses while the electron emission current is recorded, one can sample $V_{\mathrm{THz}}(t)$ at different points in time to reconstruct the THz near-field waveform. With this technique, only the waveform and not the amplitude of the electric field is directly obtained, since the THz-induced photoemission current is the quantity being measured and a calibration procedure would be required. However, this technique is becoming a common practice among the THz-STM community [39, 42, 51], because it provides a direct measurement of the THz near-field waveform at the tip, which might not be the same as the waveform measured in free-space. However, some subtleties about this technique are still under discussion since its accuracy might depend on the experimental settings. This technique will be explored in more detail in Chapter 7. An example of this measurement obtained with a gold tip over an Au(111) surface at room temperature is shown in Fig. 3.16, which was taken with an average optical power of $P_{\mathrm{pump,avg}} = 4.6\,\mathrm{mW}$, $E_{\mathrm{THz,pk}} = +400\,\mathrm{V/cm}$ and $V_{\mathrm{DC}} = -1\,\mathrm{V}$.

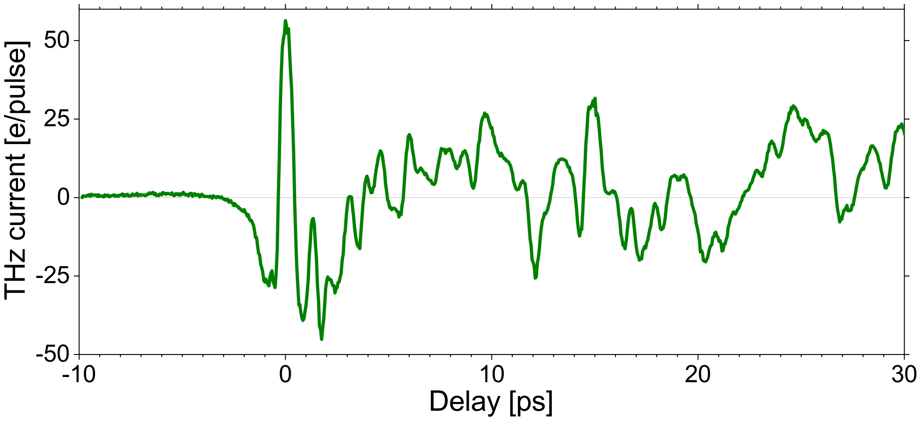

Figure 3.16: The near field waveform of a THz pulse coupled to the STM junction, measured by electron photoemission. An ultrafast optical pulse induces photoemission from the tip, which is then modulated by the electric field of a THz pulse. The temporal delay between the two pulses is varied while the electron emission is recorded to obtain the THz near field waveform. Notice that the y-axis has units of current, not the electric field amplitude. The data was acquired with $V_{\mathrm{DC}} = -1\,\mathrm{V}$, $E_{\mathrm{THz,pk}} = 400\,\mathrm{V/cm}$, $P_{\mathrm{pump,avg}} = 4.6\,\mathrm{mW}$ and with a gold tip $z = 500\,\mathrm{nm}$ away from an Au(111) sample at room temperature.

3.3.6 THz autocorrelation

To determine the temporal resolution of the THz-STM system, an autocorrelation measurement of two THz pulses is made. A high-resistivity silicon wafer, that acts as a beam splitter, is used to separate the THz beam into the two arms of a Michelson interferometer. The mirror of one of the arms is mounted on a motorized linear stage to control the time delay ($\Delta\tau_{\mathrm{THz}}$) between the two THz pulses coming out of the interferometer, as shown in Fig. 3.17. The THz pulses are then guided into the STM chamber to be coupled at the junction. Similarly to previous measurements, once the tip is positioned over a single point on the sample, the tip height will be set by V_{DC} and I_{DC}, when the THz pulses are off. The STM feedback loop is then turned off, the THz pulses are turned on, and the THz-induced current is recorded as $\Delta\tau_{\mathrm{THz}}$ is varied. The temporal width of the THz pulse can be extracted by fitting the data with the convolution of a Gaussian function with itself. Fig. 3.18 shows an autocorrelation measurement performed on Au(111), where the tip height was set with $V_{\mathrm{DC}} = 50\,\mathrm{mV}$, $I_{\mathrm{DC}} = 42\,\mathrm{pA}$, and $E_{\mathrm{THz,pk}} = +260\,\mathrm{V/cm}$. The autocorrelation signal has a full-width-half-maximum (FWHM) of 0.5 ps, and from the fit, a FWHM THz pulse width of 0.35 ps was extracted, which determines the temporal resolution of the system.

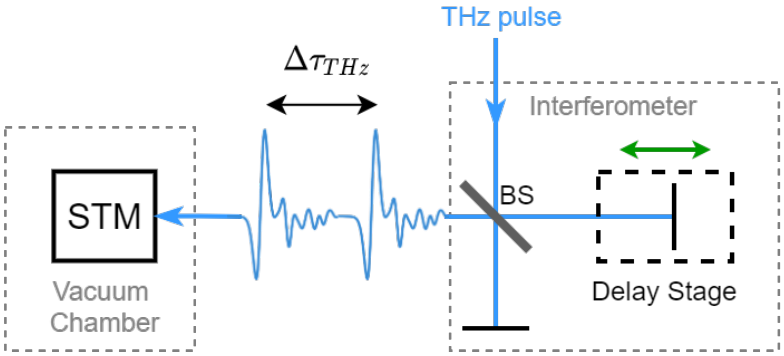

Figure 3.17: Optical setup to perform autocorrelation measurements that consists of a Michelson interferometer, where a high-resistance silicon wafer splits the incoming THz beam into the two arms of the interferometer. By changing the path length of one of the arms, the temporal delay $\Delta\tau_{\mathrm{THz}}$ between the two THz pulses is varied before they couple to the STM tip.

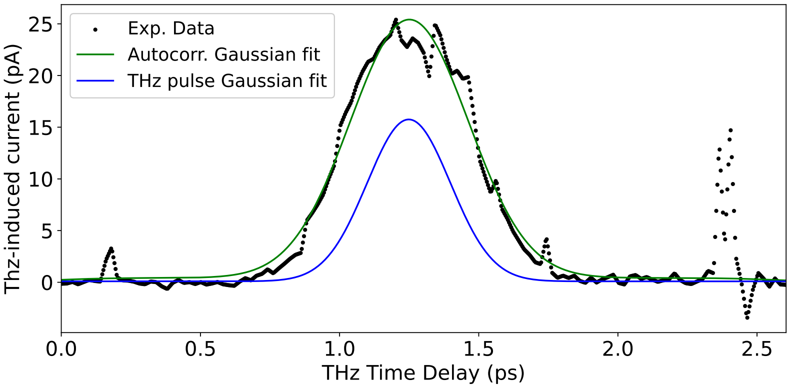

Figure 3.18: Autocorrelation measurement of two THz pulses, where the temporal delay $\Delta\tau_{\mathrm{THz}}$ described in Fig. 3.17 is varied while the THz-induced current is recorded. The experimental data (black dots) is the average of six consecutive measurements where the initial tip height was set with $V_{\mathrm{DC}} = 50\,\mathrm{mV}$, and $I_{\mathrm{DC}} = 42\,\mathrm{pA}$. The THz pulse field at the peak was $E_{\mathrm{THz,pk}} = +260\,\mathrm{V/cm}$. The autocorrelation data fit (green line) was obtained from the convolution of a Gaussian function (blue line) with itself, which presented a FWHM (pulse duration) of 0.35 ps. The current spikes on the sides of the plot were caused by a tip change during one of the measurements.

Chapter 4

Sample preparation and UHV-STM studies of material systems

The preparation procedures of the samples used in the experiments of this work will be described in this chapter. Conventional STM measurements obtained on these samples will also be presented. First, Au(111) will be covered, which was used as a substrate in some cases and as a sample in other cases. Then, carbon allotropes will also be discussed, which include single-walled carbon nanotubes and graphene-like structures. Finally, the three different types of semiconductors that were used in the photoemission experiments will also be covered.

4.1 Au(111)

Thin films of gold were deposited on freshly cleaved Mica grade V1 (Ted Pella, Inc.) substrates with a thermal evaporation system. The Mica was first degassed at 420 °C for at least 8 hrs inside the evaporation vacuum chamber with an average pressure of 5×10^{-7} torr. Maintaining the same temperature, 100 nm of gold was deposited on the Mica substrate at a rate of 0.5 Å/s and under a pressure of 2×10^{-6} torr. The samples were then transferred into the STM chamber, where multiple cycles of ion sputtering and annealing were applied to the gold until the surface was clean and presented large atomically flat areas [154]. For ion sputtering, the vacuum chamber was filled with Argon gas until a pressure of 8×10^{-6} torr was reached. The ion sputtering gun then accelerates the Argon ions towards the sample surface at an incident angle of 45°, with an energy of 0.8 keV for a period of around 20 minutes. To anneal the sample, the backside of the substrate is in contact with a metallic plate that is heated by electron bombardment from a hot thoriated tungsten filament, as shown in Fig. 3.4b. A current of 2.4 A is driven through the filament to induce thermal emission, which is approximately 2 mm away from the metallic plate. A potential difference of $800 - 1000\,\mathrm{V}$ is applied between the filament and the metallic plate to accelerate the emitted electrons towards the latter. Annealing was done in cycles of 40 minutes, and the sample temperature was monitored with a non-contact portable infrared thermometer Cyclops 180L (AMETEK-Land) through one of the windows of the vacuum chamber. If the gold samples are transferred into the STM chamber right after deposition (they are not exposed to air for long periods of time), a couple of 10-minute cycles of ion sputtering and annealing are enough to clean the gold surface. Fig. 4.1 shows photographs of the gold surface before (left) and after (right) a few cycles of ion sputtering and annealing.

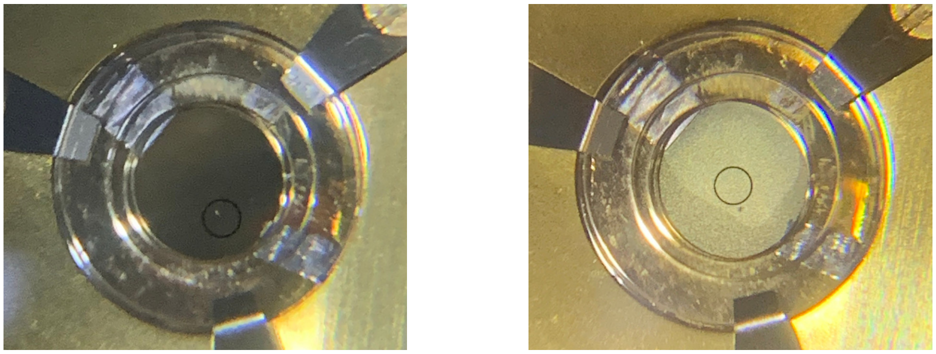

(a) (b)

Figure 4.1: Photograph of the clean Au(111) substrate mounted on the STM sample holder a) before and b) after a few cycles of ion sputtering and annealing in the vacuum chamber.

The appearance of the herringbone reconstruction over regions of hundreds of nm is a good indication of the quality of the Au(111) surface. An STM image of the Au(111) surface with atomically flat areas is shown in Fig. 4.2a. The herringbone reconstruction could be observed in those flat regions (Fig. 4.2b). The tip height profile along the white line from Fig. 4.2b, is presented in Fig. 4.2c. The experimental data points are represented in red. The data was smoothed out by taking the average of 10 adjacent points, which is shown in black, and it served to identify the peaks more easily. A narrow spacing of $2.65 \pm 0.24\,\mathrm{nm}$ between peaks was obtained for the hexagonal close packing (HCP) structure region, while a broad spacing of $3.95 \pm 0.25\,\mathrm{nm}$ was obtained for the face-centered cubic (FCC) structure region. These numbers are comparable to values previously reported (2.5 nm for HCP and 3.8 nm for FCC) [155, 156].

STM spectroscopy was also performed on the Au(111) surface for benchmarking

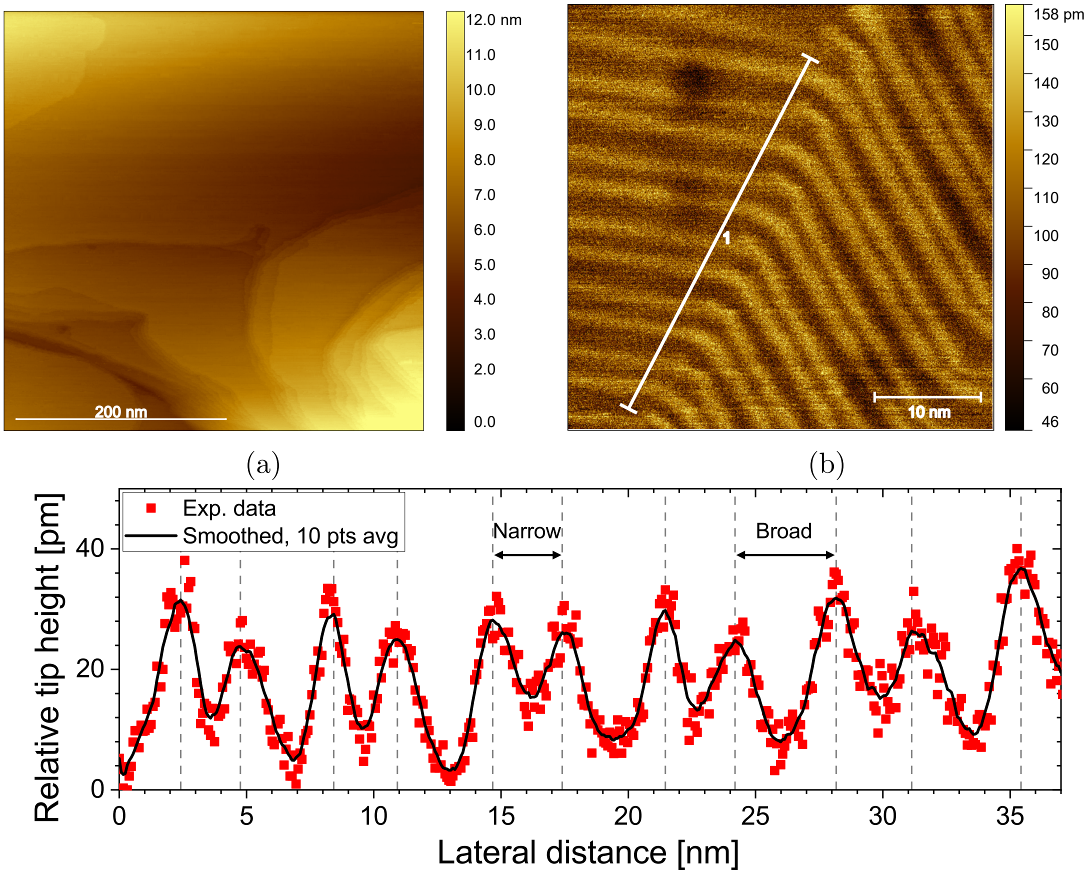

(a)

(b)

(c)

Figure 4.2: STM topographic images of the clean Au(111) surface. a) Image with large atomically flat areas. The window is $400 \times 400\,\mathrm{nm}$ and was acquired with $V_{\mathrm{DC}} = 1.2\,\mathrm{V}$ and $I_{\mathrm{DC}} = 200\,\mathrm{pA}$. b) The herringbone reconstruction. The window is $40 \times 40\,\mathrm{nm}$ and was acquired with $V_{\mathrm{DC}} = 50\,\mathrm{mV}$ and $I_{\mathrm{DC}} = 200\,\mathrm{pA}$. These images were acquired with a W tip at room temperature. c) Tip-height profile over the herringbone structure along the white line shown in (b). The experimental data points are shown in red, and the average of 10 adjacent points is shown as a smooth black solid line. The smoothed line was used to calculate the narrow ($2.65 \pm 0.24\,\mathrm{nm}$) and broad ($3.95 \pm 0.25\,\mathrm{nm}$) peak spacing of the herringbone structure.

purposes. Fig. 4.3a shows the average of multiple I-V curves taken on the Au surface at the hill and the broad valley of the herringbone structure. The $I-V$ curves were taken with a tip–sample separation set by $V_{\mathrm{DC}} = -1\,\mathrm{V}$ and $I_{\mathrm{DC}} = 1\,\mathrm{nA}$. An AC modulation of $10\,\mathrm{mV}$ was superimposed on the bias voltage to simultaneously acquire the dI/dV curve (Fig. 4.3b) by means of lock-in detection, along with the $I-V$ curve. The $(dI/dV)/(I/V)$ spectrum (Fig. 4.3c) is almost identical for the hill and valley of the herringbone structure, except for a slight difference at $-0.6\,\mathrm{V}$. The spectrum matches the results from previous works; it can be observed that it has a shoulder around $-0.4\,\mathrm{V}$ caused by surface states, which has previously been reported [157, 158].

$I-z$ measurements were also taken on the Au surface and are presented on a semilog plot in Fig. 4.3d. The initial tip height was set by different bias voltages and different setpoints, to verify that these parameters do not affect the result. The experimental data points are presented with colored symbols, and the exponential fits, using Eq. 2.1, are shown with solid lines. From the exponential fits, the effective work function, also known as the apparent barrier height, can be extracted. The estimated work function for each case is shown in square brackets in the plot legend. An average work function of $4.80 \pm 0.21\,\mathrm{eV}$ was calculated, which is similar to the values reported previously [159].

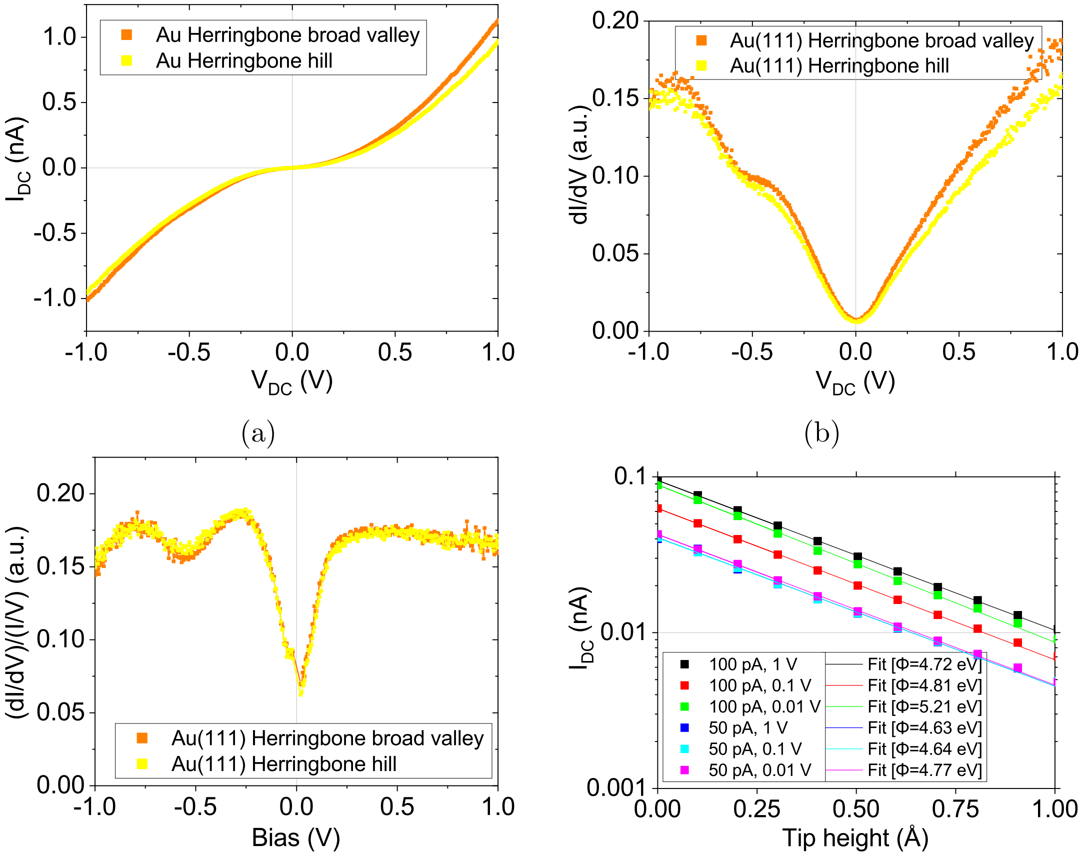

(a) (b)

(c) (d)

Figure 4.3: STS measurements on Au(111). a) $I-V$ curve taken on the Au surface on the hill and on the broad valley of the herringbone structure. The initial tip-sample separation was set by $V_{\mathrm{DC}} = -1\,\mathrm{V}$ and $I_{\mathrm{DC}} = 1\,\mathrm{nA}$. b) dI/dV and c) normalized $(dI/dV)/(I/V)$ spectrum. d)$I-z$ curves in a semilog plot. The initial tip height was set by different bias voltages and setpoints, as described in the plot legend. The experimental data points are presented with colored symbols, whereas the exponential fits are shown with colored continuous lines. The calculated work function Φ for each case is shown in square brackets, and the average was estimated to be $4.80 \pm 0.21\,\mathrm{eV}$.

4.2 Carbon allotropes

Carbon atoms can form stable structures with various atomic configurations called allotropes, which include amorphous carbon, diamond, graphite, graphene and fullerenes. Amorphous carbon is made of free, reactive carbon without a crystalline structure, and with no long-range order. The crystallinity of amorphous carbon can increase when it is treated with heat, which is known as graphitization [160]. On the other hand, diamond presents a 3-dimensional crystal structure, where each atom forms sp^3 bonds with its four nearest neighbors. The strong bonds form a tetrahedron, providing diamond with the highest number of atoms per unit volume, making it the hardest and least compressible material [161]. Graphite is made of carbon atoms covalently bonded and arranged in planar honeycomb layers that are bonded together by van der Waals forces. In 2004, Novoselov [162] demonstrated that a single atomic layer of graphite, also known as graphene, could be obtained by peeling off layers of graphite with Scotch tape. Novoselov was awarded a share of the 2010 Nobel Prize in Physics for this achievement. A strip of graphene less than 100 nm wide is commonly known as a graphene nanoribbon. The fullerenes include buckyballs, carbon nanotubes, nanobuds and nanofibers. Some of these allotropes will be relevant for the work presented here, more specifically, graphene and carbon nanotubes, which will be reviewed in the following sections.

4.2.1 Graphene background

Atomic planes in bulk crystals had been known for a long time, but one-atomic layers of a specific material were unknown; at the time, it was even thought that this configuration was unstable and, therefore, impossible. For this reason, the discovery of graphene became very relevant because it was the first two-dimensional (2D) crystal found [163]. Furthermore, it has been stipulated that graphene nanostructures are stable down to a single benzene ring [164]. An illustration of the graphene structure is presented in Fig. 4.4a. There are different techniques to produce micrometer-sized graphene sheets, such as the known scotch-tape technique [162], ultrasonic cleavage technique [165] , epitaxial growth of graphene on a substrate [166], graphite oxidation [167], and chemical vapor deposition (CVD) [168].

The mechanical and thermal properties of a graphene monolayer are exceptional; it can be stretched by up to 20%, it presents a breaking strength of $\sim 40\,\mathrm{N/m}$, a Young's modulus of 1 TPa [169], which is ~ 2.5 times larger than tungsten's, and it also has a thermal conductivity at room temperature of $5 \times 10^3\,\mathrm{W/mK}$ [170], which is ~ 12 times larger than copper's. However, the electronic properties of graphene are even more interesting. There are 4 aspects that make graphene unique: First, charge carriers traveling in the graphene crystal have no effective mass and mimic relativistic particles, therefore, the theory for Dirac fermions is more suitable to describe them, instead of the Schrodinger equation. Second, electrons propagate in a one-atom-thick layer in graphene, so they can be studied directly by scanning probe techniques. Third, the high quality of the graphene crystal allows electrons to travel distances in the micrometer range without scattering [171, 172]. Fourth, because of the properties mentioned before, quantum effects can survive at room temperature [173].

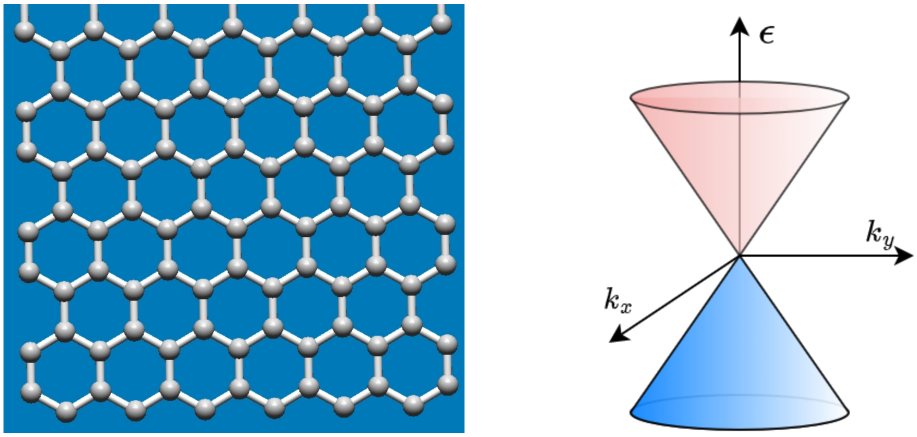

(a) (b)

Figure 4.4: Graphene diagrams. a) Illustration of the atomic structure of graphene, where each sphere represents a carbon atom. The diagram was built with the Nanotube Modeler (JCrystalSoft) software [174]. b) Energy dispersion relation of graphene at the Dirac point.

The advantages in performance provided by graphene make it a good candidate for use in new electronic devices. For example, it has been shown that electrons in graphene show ballistic transport at room temperature, allowing them to travel through a transistor channel 100 nm long in only 0.1 ps [173]. Due to the conic dispersion relation of graphene, shown in Fig. 4.4b, charge carriers can be continuously controlled from electrons to holes with concentrations up to $10^{13}\,\text{cm}^{-2}$, depending on the applied field, which is known as the ambipolar electric field effect [164].

To study graphene, metallic contacts are commonly added, which can alter its electrical properties or induce damage. Contactless methods such as terahertz timedomain spectroscopy (THz-TDS) [175] and time-resolved terahertz spectroscopy (TRTS) [176] have already been used to study graphene properties. Additionally, a method such as THz-STM is ideal for performing less intrusive experiments on graphene at the nanoscale.

4.2.2 Single-walled carbon nanotubes background

A carbon nanotube is technically just a cylinder made of a rolled graphene layer. After Iijima's paper in 1991 [177], carbon nanotubes attracted the attention of many researchers and have been studied extensively ever since then. There are carbon nanotubes made of a single graphene layer, which are known as single-walled carbon nanotubes (SWCNTs), and there are nanotubes with multiple layers arranged concentrically, which are known as multi-walled carbon nanotubes (MWCNTs). Both types present unique properties, but this work will focus on SWCNTs only.

The diameter of SWCNTs can range from 0.4 to 3 nm, and their length is generally in the micrometer range [178]. The diameter, as well as the electronic[179] and optical[180] properties, will be determined by the angle at which the graphene layer is rolled up, which is known as the chiral angle or chirality. The chiral angle can range from 0° to 30°; however, the indices (n, m) are more commonly used to identify the different types of nanotubes. Fig. 4.5a illustrates a honeycomb lattice representing a graphene sheet, where the position of the indices $(n = 6, m = 5)$ is indicated by the blue lines. The chirality α is determined by the angle between the red line that connects the origin to (6,5) and the horizontal axis. The atomic structure corresponding to (6,5) is shown in Fig. 4.5b, which was built with the Nanotube Modeler software [174].

Small variations in chirality can produce a big difference in the nanotube properties. For example, when $|m - n| = 3k$, where k is an integer, the nanotube will present metallic properties; whereas it will behave as a semiconductor when $|m - n| = 3k \pm 1$. If $m = 0$, the nanotube structure is known as zigzag because of the boundary shape of the atoms along the horizontal axis in Fig. 4.5a, and if $m = n$, the nanotube will have an armchair structure [181]. The nanotube diameter d can be determined from the indices (n, m) as [182]

$$d = \frac{a}{\pi}\sqrt{n^2 + nm + m^2}\,, \tag{4.1}$$

where $a = 0.246\,\text{nm}$ is the graphene lattice constant, or alternatively $a = \sqrt{3}a_{\text{cc}}$, where $a_{\text{cc}} = 0.142\,\text{nm}$ is the C-C interatomic distance, as shown in Fig. 4.5a. The tight-binding model has been used to calculate the transition energy of the nanotubes [183], which is the energy difference between the van Hove singularities (Fig. 4.5c). The transition energy dependence on tube diameter is given by

$$\epsilon^{sc,m} = 2i\frac{\gamma_0 a_{\text{cc}}}{d}\,, \tag{4.2}$$

where $\gamma_0 = 2.9\,\text{eV}$ is the nearest neighbor carbon-carbon interaction energy, and $i = 1, 2, 4, 5, ...$ for the transition energies $(\epsilon^{sc}_{11}, \epsilon^{sc}_{22}, \epsilon^{sc}_{33}, \epsilon^{sc}_{44}, ...)$ of a semiconductive

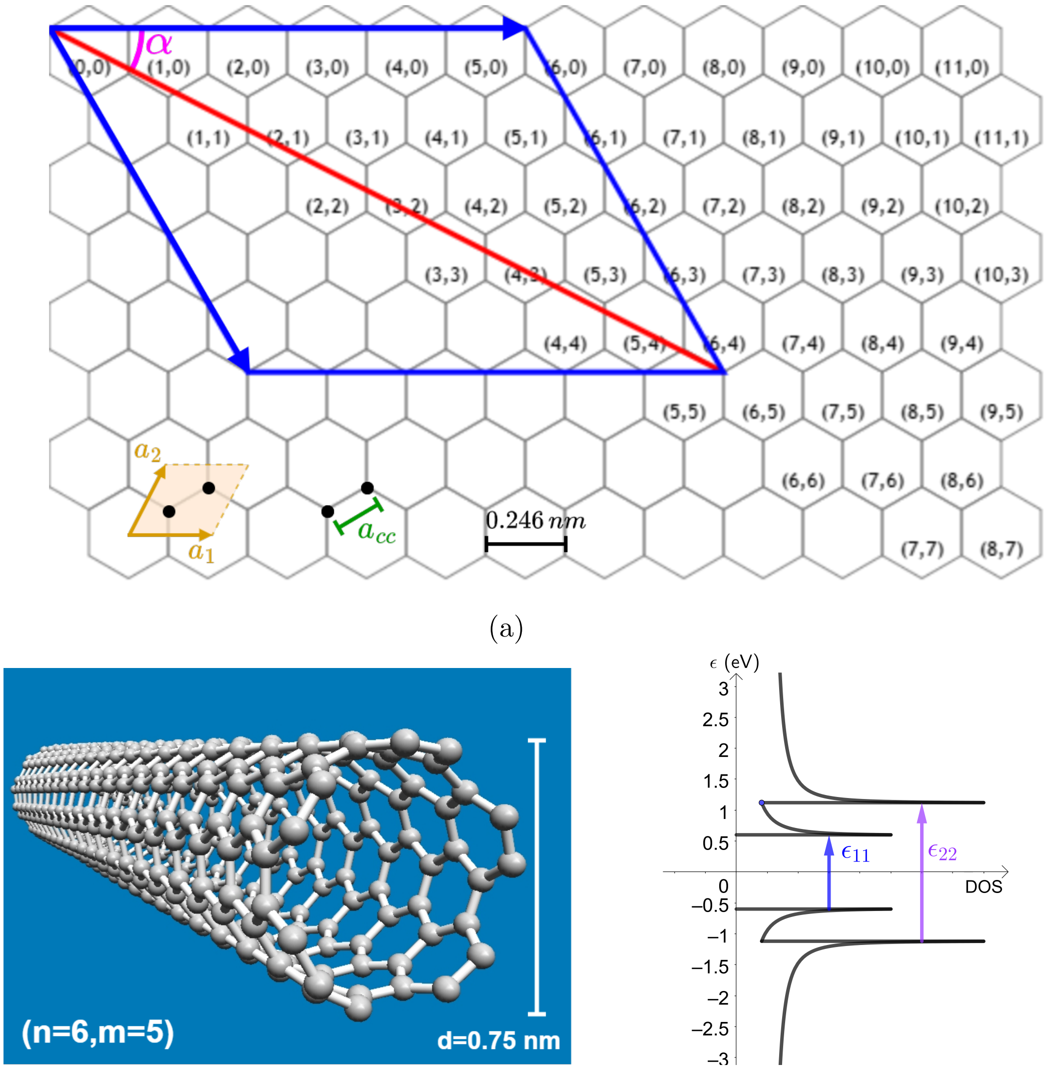

(a)

(b)

(c)

Figure 4.5: SWCNTs diagrams. a) Honeycomb lattice representation of a graphene layer, where the text inside each hexagon shows the position of several nanotube indices. The position of ($n = 6$,$m = 5$) is indicated by the blue lines. The chirality α is determined by the angle between the red line that connects the origin to (6,5) and the horizontal axis, which is the angle at which the graphene layer is rolled up, also known as the chiral angle. The unit cell and the C-C interatomic distance a_{cc} are also shown. b) Atomic structure of a (6,5) SWCNT where each sphere represents a carbon atom. The diagram was built with the Nanotube Modeler (JCrystalSoft) software [174]. c) Energy diagram of a (6,5) SWCNT where the semiconductive energy gaps are $\epsilon_{11} = 1.12\,\mathrm{eV}$ and $\epsilon_{22} = 2.24\,\mathrm{eV}$.

nanotube , and $i = 3, 6$ for the transition energies of a metallic nanotube ($\epsilon_{11}^{m}, \epsilon_{22}^{m}$) [184]. Studies on metallic nanotubes have found outstanding high-field transport properties, with current densities exceeding 10^9 A/cm^2 [185]. The mechanical strength of SWCNTs is exceptional, presenting a Young's modulus around 1 TPa [186, 187], which is 5 times greater than steel. SWCNTs also exhibit high thermal stability, since no structural changes have been detected for heat treatments under vacuum up to temperatures of 1400 °C [188, 189].

4.2.3 SWCNTs samples

Single-walled carbon nanotubes were purchased in powder form (PN:#704113) from Sigma-Aldrich. They were produced by CoMoCAT™ Catalytic Chemical Vapor Deposition, and have $\geq 90\%$ carbon basis ($\geq 70\%$ as carbon nanotubes). Most SWCNTs are expected to have a diameter between $0.7 - 1.3$ nm. According to the supplier, 52% of the nanotubes have a (6,5) chirality, which means that around half of the nanotubes will be semiconductive and they will have a diameter of $d = 0.75$ nm, a first energy gap of $\epsilon_{11} = 1.12$ eV and a second energy gap of $\epsilon_{22} = 2.24$ eV according to Equations (4.1) and (4.2). Special care needs to be taken when handling SWCNTs in powder form; they are very volatile and can easily be released into the air from the handling tools. The SWCNTs toxicity is still under discussion [190, 191], however, you should minimize exposure to nanotubes and avoid ingesting or inhaling them.

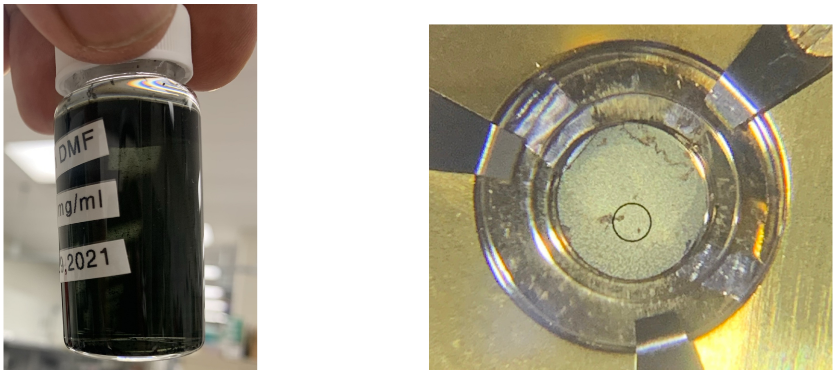

(a) (b)

Figure 4.6: a) Photograph of the solution containing SWCNTs in DMF with a concentration of 0.05 mg/ml. b) Photograph of the Au(111) substrate after the SWCNTs were deposited by the drop casting method.

SWCNTs naturally form bundles due to intertube van der Waals forces [192]. Several solvents can be used to dilute SWCNTs, such as chloroform, toluene, dimethylformamide (DMF), ortho-dichlorobenzene (o-DCB), metadichlorobenzene (m-DCB), monochlorobenzene (MCB), 1,2,4-trichlorobenzene (TCB), 1,2-dicholorethane (DCE), N-methylpyrrolidone (NMP) and others [193–195]. However, DMF has proven to form stable suspensions to dilute or disperse SWCNTs [195]. By mixing 1 mg of SWCNTs and 20 ml of DMF, a solution with a concentration of 0.05 mg/ml was obtained. The solution container was sonicated either for 10 or 30 minutes in a Branson Ultrasonic Cleaner 2510 System that operates at 40 kHz. Right after sonication, the solution (Fig. 4.6a) was then drop casted (5 drops) onto a gold substrate that was previously cleaned by Ar sputtering and annealing cycles. The Au substrate was heated to a temperature slightly above 100 °C inside the vacuum chamber. It was then briefly removed from the chamber to deposit the SWCNTs solution, and immediately placed back into the vacuum chamber. The DMF solvent evaporates in seconds once the solution is deposited on the sample, leaving only the nanotubes on the surface. Small dark regions can occasionally be observed on the gold surface with the naked eye due to the accumulation of SWCNTs clusters, as shown in Fig. 4.6b.

STM images of the SWCNTs deposited on the Au substrate are shown in Fig. 4.7. When the solution was sonicated for 10 minutes or less, the SWCNTs were not effectively dispersed, which means that there were either large empty areas on the Au surface where it was difficult to find any nanotubes, or regions with big clusters of nanotubes that were very unstable to perform any measurements on them. Fig. 4.7a shows one of the rare cases when a few single nanotubes were found on the surface. When the sonication time was increased to 30 minutes, the dispersion of the solution improved and the nanotubes could be found more easily on the gold surface. However, in this case, unexpected irregular features were found on the surface in addition to the nanotubes, which are pointed out by white arrows in Fig. 4.7b. These features were found on the sample before and after 3 cycles of annealing at 430 °C for 10 min. A more detailed study of these unexpected features is presented in Section 4.2.4.

To rule out the possibility that these features were produced by contaminants at some point during the preparation process, multiple samples were prepared from scratch. The preparation procedure was technically the same for all of them, but freshly deposited gold substrates and new SWCNTs solutions were made. The unidentified features were found on all the samples that were sonicated for 30 minutes; furthermore, increasing the amount of solution deposited clearly showed an increase in the presence of these irregular features on the gold surface, as shown in Fig. 4.8.

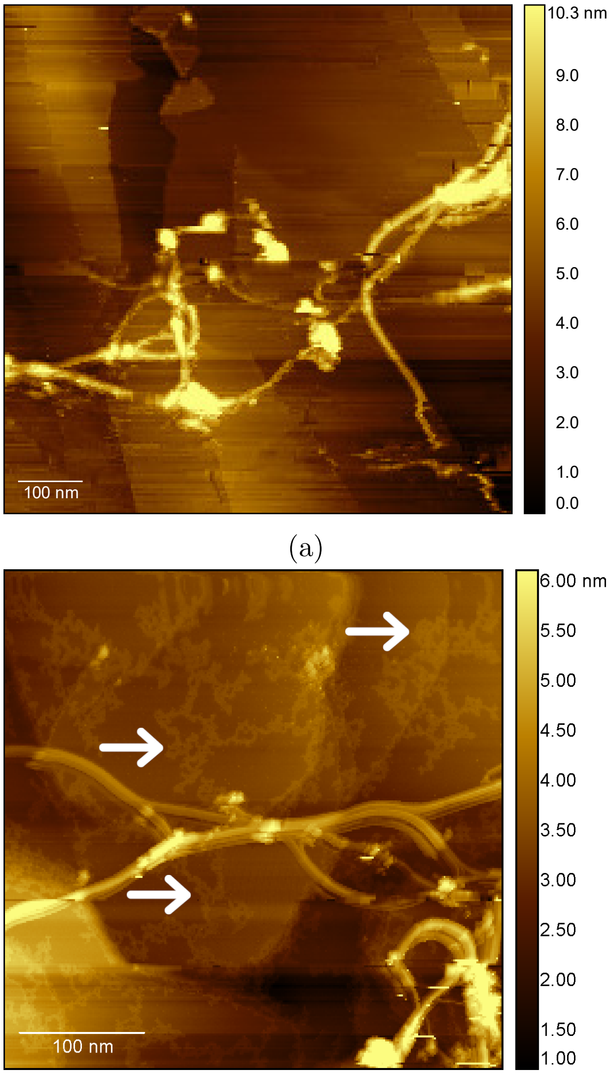

(a)

(b)

Figure 4.7: Topographic images of SWCNTs deposited by drop casting (5 drops) on the Au(111) substrate. SWCNTs were diluted on DMF and sonicated for a) 10 minutes and b) 30 minutes. The images were acquired with (a) $V_{\mathrm{DC}} = 1.2\,\mathrm{V}$ and $I_{\mathrm{DC}} = 22\,\mathrm{pA}$ and (b) $V_{\mathrm{DC}} = 3.5\,\mathrm{V}$ and $I_{\mathrm{DC}} = 10\,\mathrm{pA}$. Image (b) presents unexpected irregular features on the Au surface, which are pointed out by white arrows. Image taken with a W tip at room temperature.

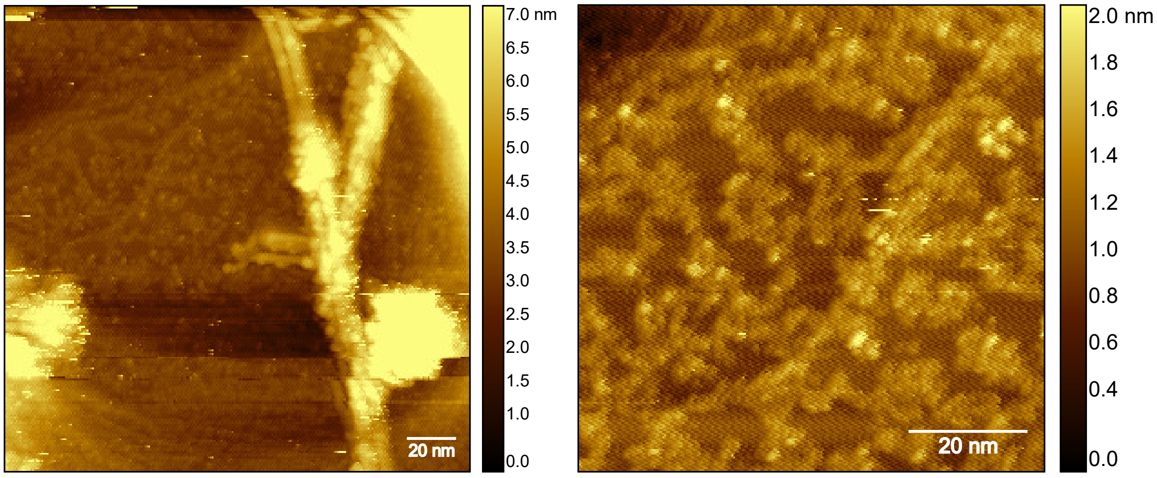

(a) (b)

Figure 4.8: Topographic images of SWCNTs deposited by drop casting on an Au(111) substrate. The solution of SWCNTs in DMF was sonicated for 30 minutes. By depositing 8 drops of solution instead of 5 (Fig. 4.7b), the Au surface area was almost fully covered by these unexpected irregular features. The sample with the SWCNTs underwent 3 cycles of annealing at 430 °C for 10 min. Images were acquired with $V_{\mathrm{DC}} = 3.5\,\mathrm{V}$, $I_{\mathrm{DC}} = 60\,\mathrm{pA}$ and a W tip at room temperature.

4.2.4 Graphene-like structures on Au(111)

To understand what the unidentified features found in Fig. 4.7b are, we can first look at the different processes that can alter and damage the structure of the SWCNTs. For example, carbon nanotubes can be unzipped in a controllable manner to form uniform graphene nanoribbons using a solution-based oxidative process [196]. Another example is when the applied shear force from the cavitation process induced by sonication not only helps to debundle and disperse the nanotubes, but also induces defects and nanotubes scission [197]. When a cavitation bubble collapses in the vicinity of a nanotube, the nanotube itself and the surrounding liquid will flow at a different velocity; the drag force on the nanotube surface can be strong enough for a scission [198]. Experiments on carbon fibers found that the strain rate around cavitation bubbles is $\sim 10^{10}\,\mathrm{s}^{-1}$, which was calculated to be enough to scission SWCNTs (having 30 GPa tensile strength) down to a terminal length of 13 nm [198]. The sonication process is not standardized since it depends on solvent parameters such as vapor pressure, viscosity, and surface tension, and also on sonication parameters such as frequency, intensity, and time [199], so it is possible that long sonication times in our setup could damage the SWCNTs.

Raman spectroscopy is commonly used to characterize the structure of SWCNTs. The Raman spectra show two main peaks, one at $1350\,\mathrm{cm}^{-1}$, which is known as defect-induced disorder mode (D band) and is related to carbon atoms with structural defects, and the second peak at $1580\,\mathrm{cm}^{-1}$, which is known as the tangential mode (G band) and is related to the carbon atoms in-plane vibrational motion. The ratio between the two peak intensities I_D/I_G provides an estimate of the defects site content on the nanotubes structure. It has been shown that, in general, longer sonication times lead to an increasing I_D/I_G ratio due to progressive damage and the formation of structural defects on the nanotubes surface [199–201]. Furthermore, structural modifications have been observed on TEM micrographs, where the nanotubes presented waviness and amorphous carbon on the surface [200]. Raman spectroscopy was not performed on the SWCNT solutions used in this work, so the number of defects was not monitored before and after the sonication. However, these previous studies support the hypothesis that during the sonication process, the SWCNTs were broken down into smaller nanotubes and because of the creation of surface defects, they could also potentially be broken down into graphene pieces or amorphous carbon. This could be the source of the atoms that formed the unidentified features on the Au surface (Fig. 4.9a). A second alternative would be that the carbon atoms come from the raw SWCNTs powder itself, since the manufacturer specifies that it contains a $\geq 90\%$ carbon basis from which $\geq 70\%$ has the form of nanotubes, which means that the difference would probably be in the form of amorphous carbon. If that was the case, the dispersion of amorphous carbon in the solution would increase with the sonication time, which could also explain the increase in the number of features found in Fig. 4.8. Unfortunately, these arguments are not conclusive enough to determine the origin of the atoms that form those features, and detailed experiments would be required to clarify this question. However, they strongly suggest that the unidentified features are formed by carbon atoms.

If we continue under the assumption that these features are made of carbon atoms, then we can look at previous studies in which graphene has been formed on the Au(111) surface using carbon sources. The growth of graphene on an Au(111) substrate was first achieved using a technique known as ethylene irradiation, which is based on the thermal decomposition of low-energy ethylene ions which are irradiated on the surface of a hot metal. The substrate is required to be at 800 °C during irradiation, and it is further annealed at up to 950 °C after the deposition to form a graphene monolayer [202]. A following work [203], which used an electron beam evaporator to deposit carbon on the Au(111) surface at 950 °C, found that graphene islands were formed with dendritic shapes. The graphene islands were found at the bottom of surface depressions, because at that temperature, Au is displaced as the graphene is formed. In contrast, when the substrate temperature was not as high

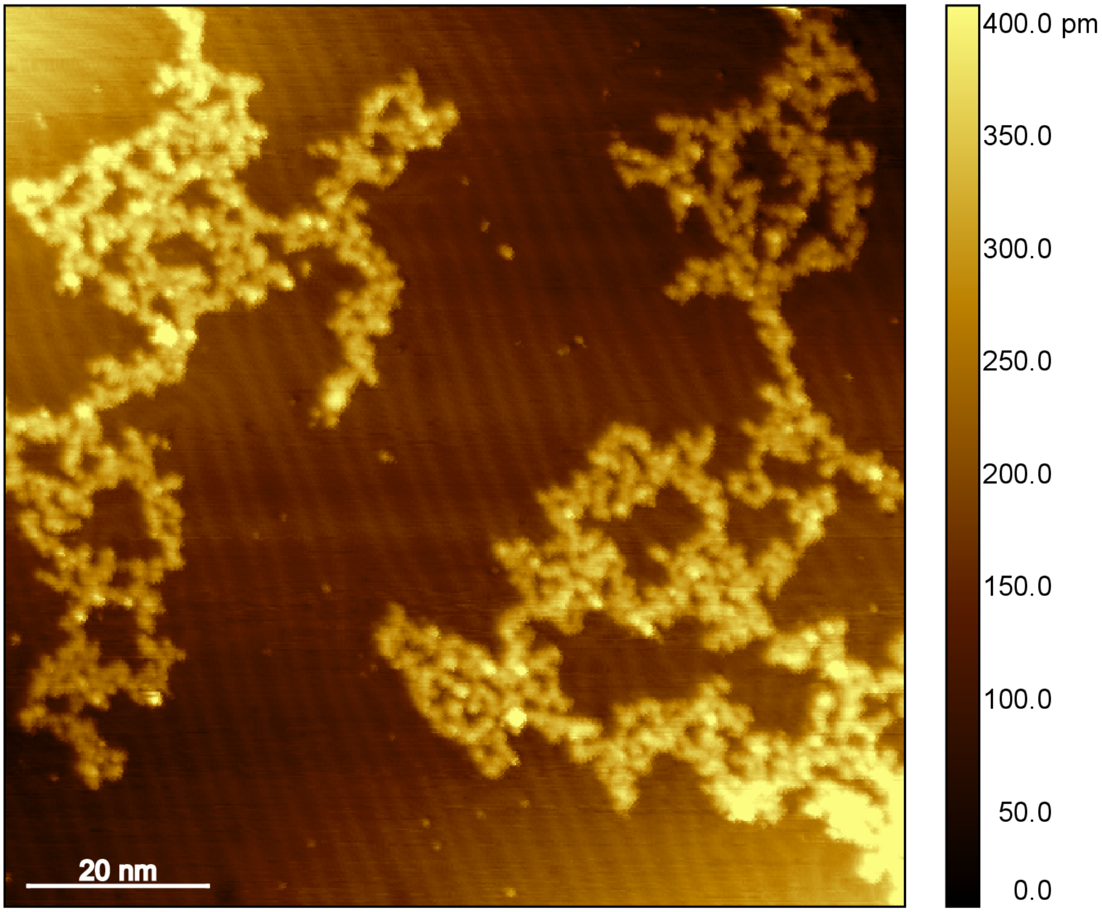

(a)

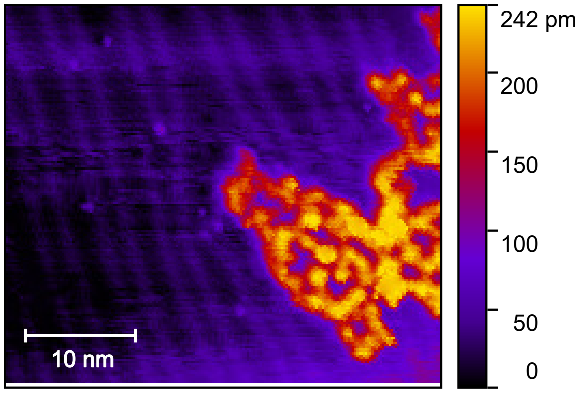

(b)

Figure 4.9: a) Topographic image of graphene dendritic islands on the Au(111) substrate. The solution of SWCNTs in DMF was sonicated for 30 minutes and 5 drops were deposited on the Au substrate. The sample underwent 3 cycles of annealing at 430 °C for 10 min after the deposition. The 100 × 100 nm window was acquired with $V_{\mathrm{DC}} = 0.1\,\mathrm{V}$, $I_{\mathrm{DC}} = 50\,\mathrm{pA}$ and a W tip at 120 K. b) Zoomed-in window showing how the herringbone structure underneath the graphene islands is distorted, implying that the interaction with the Au substrate is not negligible.

(550 °C) during the carbon deposition, the graphene dendritic islands were more likely found at the Au step edges or pinned by defects. The Au mobility is reduced by the lower temperature, allowing it to remain unchanged during the deposition. However, substrate temperatures below 550 °C did not form graphene islands, but unordered carbonaceous features [204]. Additionally, it has been shown that, under continuous deposition, the dendritic islands join together to form a single monolayer of graphene, which can be clearly observed in a movie made by low-energy electron microscopy that can be found in the supplementary information of Ref. [205]. During the deposition process, the graphene islands nucleated at the step edges are found to grow more rapidly than the ones on the Au terraces, similar to what is shown in Fig. 4.10a. It should be highlighted that even after the single continuous film was formed, there was no evidence of a second graphene layer. All these studies only found one-atom-thick graphene sheets.

The unidentified features in our samples were also found forming single atomic layers; and the STM images presented in Figs. 4.9a and 4.10, are visually very similar, for example, to Fig. 3b from Ref. [204], Fig. 1a from Ref. [205], Fig. 1a from Ref. [206] and Fig. 12a from Ref. [207], which further suggests that they are, in fact, dendritic islands of graphene. A geometric analysis of these graphene-like features was done using STM topographic images. In Fig. 4.10b, a single step of the Au substrate can be identified by the color difference between the left and right sides of the image. The graphene-like features on the gold substrate are also visible in this image with a brighter color. The line profile along the path marked with the white line is shown in Fig. 4.10c. By comparing the tip height values of the immediate points on both sides of the step edge, a value of 2.17 ± 0.07 Å was extracted for the atomic step height of Au, which is lower but comparable to the value of 2.35 Å reported before [208]. For the case of the graphene, an average height of 1.71 ± 0.11 Å was calculated. In graphite, the interplanar distance between layers is 3.35 Å, which is an estimate for the π-electron cloud thickness around the carbon atoms [209], and this number is usually given for the graphene monolayer thickness. However, previous STM studies of graphene on metals have reported atomic height values of 1.5 Å , 1.45 Å and ~ 1.3 Å for the case of Cu, Ru and Au substrates, respectively [210–212], which differ because of variations in carbon bonding with each metal. One also has to remember that the topography measured by the STM depends on both geometric and electronic factors. And, even though the graphene step height of ~ 1.7 Å, experimentally measured here, is higher than the examples just mentioned, this value was consistently found throughout this work, even when various tips and samples from different batches were used. Multiple attempts were made to acquire an STM image with atomic resolution, which would

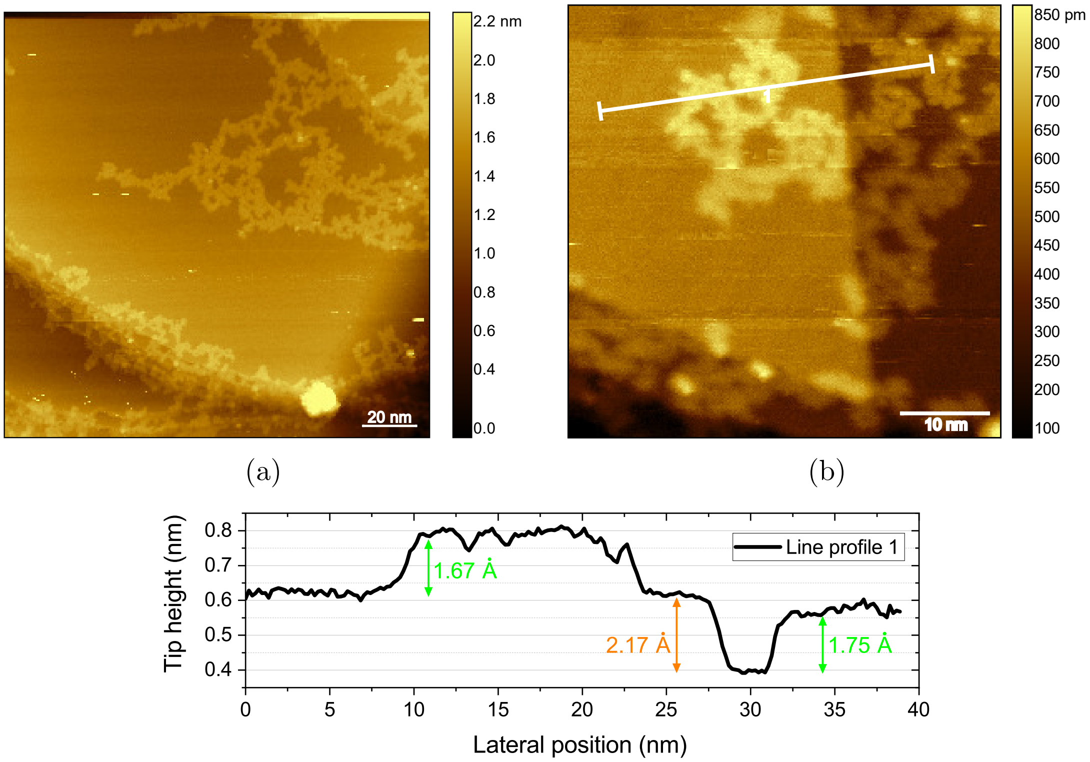

(a)

(b)

(c)

Figure 4.10: Topographic images of graphene dendritic islands on Au(111) substrate. a) The formation of graphene islands is favored at the Au step edges as compared with the Au terraces. The 160 × 160 nm window was acquired with $V_{\mathrm{DC}} = 3\,\mathrm{V}$ and $I_{\mathrm{DC}} = 50\,\mathrm{pA}$ b) A single layer is formed even when there is an atomic step on the Au substrate. The 50×50 nm window was acquired with $V_{\mathrm{DC}} = 1\,\mathrm{V}$ and $I_{\mathrm{DC}} = 50\,\mathrm{pA}$. c) Line profile along the path marked with a white line in b). An atomic step height of 2.17 Å and 1.71 Å was calculated for the Au and graphene, respectively. The solution of SWCNTs in DMF was sonicated for 30 minutes and 5 drops were deposited on the Au substrate. The sample underwent 3 cycles of annealing at 430 °C for 10 min after the deposition. The images were taken with a W tip at room temperature.

help to conclusively identify the atomic structure of the carbon atoms, but due to equipment limitations and instabilities, this could not be achieved. However, there seems to be enough evidence to assume that these features are graphene islands, and they will be referred to as such from now on.

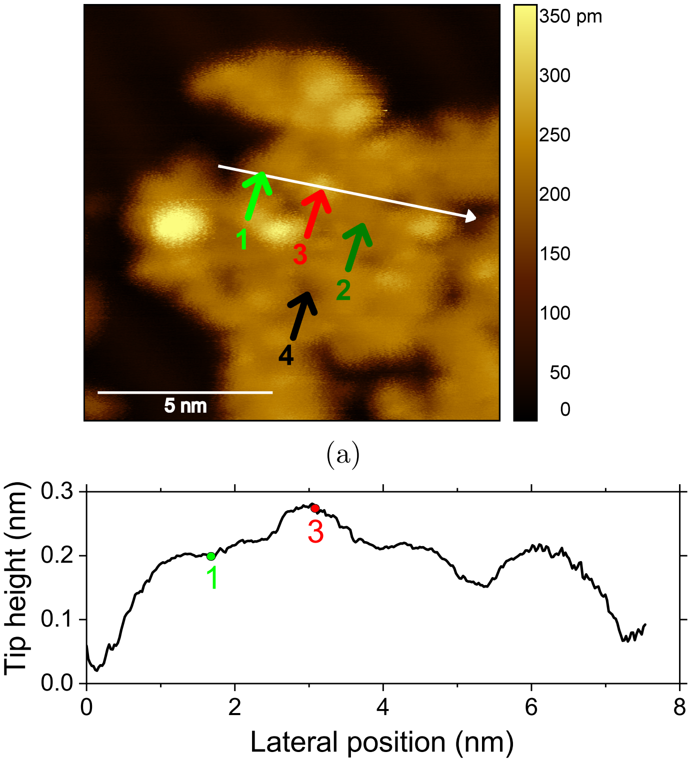

(a)

(b)

Figure 4.11: Structural analysis of graphene island. a) The 12 × 12 nm topographic image was acquired with $V_{\mathrm{DC}} = -1\,\mathrm{V}$, $I_{\mathrm{DC}} = 1\,\mathrm{nA}$ and a W tip at 120 K. Arrows 1 and 2 mark points on the flat monolayer graphene island, while arrows 3 and 4 mark points on structural defects found as bright and dark spots, respectively. b) Line profile along the white path marked in (a), showing that the height difference at point 3 is less than 1 Å and does not correspond to a second atomic layer. The solution of SWCNTs in DMF was sonicated for 30 minutes and 5 drops were deposited on the Au substrate. The sample underwent 3 cycles of annealing at 430 °C for 10 min after the deposition.

From Fig. 4.11a, one can see that bright and dark spots are present on the graphene islands. The line profile along the path marked with a white arrow (Fig. 4.11b) shows that the bright spots are less than 1 Å in height, which does not correspond to a second atom on top of the graphene layer, and is presumably produced by a structural defect on the graphene. STM spectroscopy measurements provided additional information about the graphene islands and their bright and dark spots. Figs. 4.12a to 4.12c, respectively, show the $I - V$, dI/dV and the normalized $(dI/dV)/(I/V)$ curves measured on the different points marked by the arrows in Fig. 4.11a. $I - V$ and dI/dV curves were acquired simultaneously, and each line contains the average of a set of 4 consecutive measurements. The curves obtained in the Au substrate are also shown (in orange) for comparison. Points 1 and 2 (in green) correspond to a single graphene layer, Point 3 (in red) and Point 4 (in black) mark the bright and dark spots on the graphene structure, respectively.

The dI/dV curves of graphene (green) presented in Fig. 4.12b are consistent with previously reported measurements of graphene on metals [202, 210, 213–217]. Ideal free-standing graphene would have a v-shaped density of states. When graphene is adsorbed on a metal, the charge transfer due to their difference in work function and their chemical interaction will induce charge doping in graphene. The doping level strongly depends on the adsorption distance. As a result of doping, the Fermi level of graphene will shift with respect to the Dirac point, which is reflected in the graphene density of states. In the case of an Au substrate, the graphene will be p-doped, and the energy shift is theoretically expected to be $0.03\,\mathrm{eV}$ for an equilibrium separation distance of $3.31\,\text{Å}$ [218]. Experimentally, the Fermi level shift has been identified in the dI/dV plots as a dip in the curve [219], which marks the position of the Dirac point. The doping level has been found to vary locally, and the Fermi level shift measured experimentally ranges between $0.25 - 0.55\,\mathrm{eV}$ at different points on a single graphene flake [215], which can be thought of as a well-formed defect-free graphene island. Au is considered to have a weak interaction with graphene, compared to other metals, in fact, a previous work [212] showed that the presence of graphene flakes did not affect the herringbone reconstruction of the Au substrate, which translates into quasi-free-standing graphene.

The $(dI/dV)/(I/V)$ plot probes the electrons tunneling from the occupied states of the sample (tip) to the unoccupied states of the tip (sample) when $V_{\mathrm{DC}} < 0$ ($V_{\mathrm{DC}} > 0$), as illustrated in Fig. 4.12d. Due to an asymmetry in the tunneling spectra, when V_{DC} is negative (positive), the DOS of the tip (sample) dominates [4]. This explains why all the curves present a similar pattern on the left side of the plot, making it difficult to identify the spectra of the sample in that range, since the DOS of the tip dominates. However, different features of the sample DOS can be identified on the right side of the plot. The $(dI/dV)/(I/V)$ curves of the graphene island (green) present a maxima followed by a dip at around $0.75\,\mathrm{eV}$, which can be interpreted as the graphene level shift caused by the graphene doping. This value is higher compared to the shift observed in graphene flakes ($0.25 - 0.55\,\mathrm{eV}$), which means that the graphene dendritic islands experience a higher doping and a stronger interaction with Au than the flakes. This can be confirmed by Fig. 4.9b, where the herringbone structure underneath the graphene islands is distorted in several regions. From this, we can speculate that the stronger interaction of the graphene islands with Au might be caused by defects and carbon dangling bonds at the graphene boundaries as a result of the irregular structure of these dendritic islands.

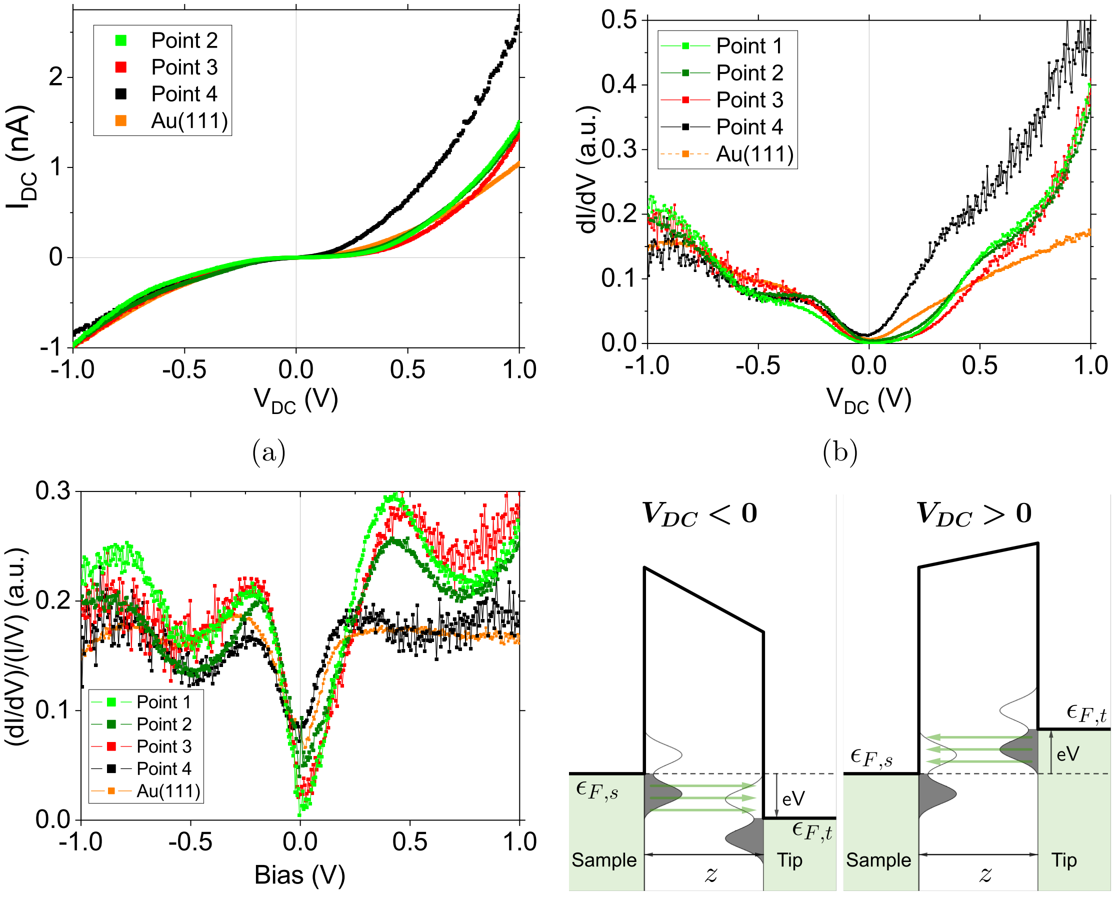

(a) (b)

(c) (d)

Figure 4.12: Spectroscopy measurements on the graphene islands. a) $I - V$, b)dI/dV and c) normalized $(dI/dV)/(I/V)$ taken with a W tip at the points marked in Fig. 4.11a. Each curve line shown is the average of 4 data sets. Measurements were acquired simultaneously with an initial tip height set by $V_{\mathrm{DC}} = -1\,\mathrm{V}$ and $I_{\mathrm{DC}} = 1\,\mathrm{nA}$. Measurements on the Au(111) substrate are also shown for comparison. d) Energy diagram of the STM junction to illustrate the tunneling current from the occupied states of the sample (tip) to the unoccupied states of the tip (sample) when $V_{\mathrm{DC}} < 0$ ($V_{\mathrm{DC}} > 0$).

The $(dI/dV)/(I/V)$ curve of Point 3 (red) follows the same pattern as the graphene islands (green), which implies that it is most likely a structural defect in the arrangement of the carbon atoms and not an atomic dopant caused by a different element.

Atomic vacancies can appear as a protrusion due to dangling bonds with a larger density of states. When a single carbon atom is missing, the three closest atoms will have a dangling bond each, and sometimes two of them are joined to form a pentagon, leaving one of them unsaturated [220]. This reconstruction can also modify the adsorption distance with the Au substrate [213]. A topographic image with a scaled diagram of the graphene structure with a single vacancy defect is shown in Fig. 4.13. This type of vacancy defect is the most probable cause for the bright spots on the graphene islands. The defect at point 4 (black) is found as a valley on the topography. Its $(dI/dV)/(I/V)$ spectra, closely follows the same pattern as the gold substrate, suggesting that several atoms are missing in the graphene sheet, creating a hole and giving access to the gold substrate. A scaled diagram of the graphene structure with a hexagonal ring missing has been superimposed on the topographic image in Fig. 4.13, to show that the dark spots on the graphene islands could be explained by missing graphene atoms.

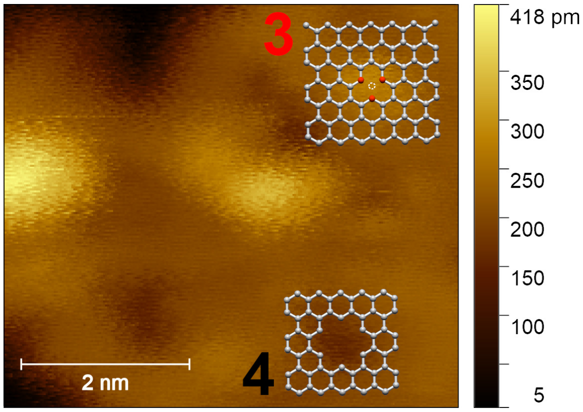

Figure 4.13: Structural analysis of graphene island defects. Zoomed-in image of Fig. 4.11a that shows the defects from points 3 and 4, with a superimposed real scale schematic of the graphene structure and the proposed defect type. The image was acquired with $V_{\mathrm{DC}} = -1\,\mathrm{V}$, $I_{\mathrm{DC}} = 1\,\mathrm{nA}$ and a W tip at 120 K.

4.3 Gallium Arsenide (110)

To perform STM scans on GaAs, the samples need to be heavily doped to increase their conductivity. Two different samples of GaAs were studied: an n-type Si-doped GaAs(110) sample with a carrier concentration of $3 \times 10^{18}\,\mathrm{cm}^{-3}$ and 0.35 mm thick, and a p-type Zn-doped GaAs(110) sample with a carrier concentration of $3 \times 10^{18}\,\mathrm{cm}^{-3}$ and 0.35 mm thick. A Poisson solver, that evaluates the potential distribution of the STM junction called SEMITIP, was used to calculate and illustrate the energy diagrams for these two GaAs samples (Figs. 4.14a and 4.14b). These diagrams will be used for the analysis of the photoemission experiments presented in Chapter 8. SEMITIP is a powerful tool that helps visualize the conditions at the STM junction and study how they evolve when different variables are modified. It is built with the Fortran programming language, but I developed a Matlab interface to facilitate its usage. The Matlab code and the instructions to use the software are presented in Appendix A.

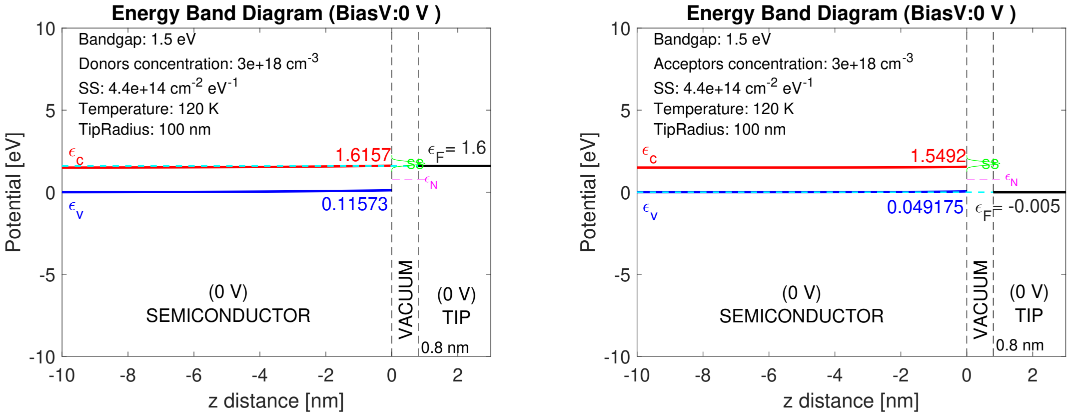

(a) Energy diagram for n-type GaAs.

(b) Energy diagram for p-type GaAs.

Figure 4.14: Energy diagram of the a) n-type and b) p-type GaAs samples. The values for the energy bands and the Fermi level, for these samples, were calculated with the SEMITIP software.

The samples were obtained from GaAs(100) wafers that were cut into slices to be vertically mounted in a special sample holder for cleaving. The cleavage planes of a (100) GaAs wafer [221] are shown in Fig. 4.15a. To set a preferential direction for the cleaving, a scriber tool with a diamond tip was used to scratch a line along the surface of GaAs. The sample was mechanically cleaved inside the STM, in vacuum, at low temperature (110 K), to expose a clean and atomically flat surface, in this case, the (110) face of the crystal. A picture of the cleaved sample with the STM tip in the tunneling regime is shown in Fig. 4.15b.

For GaAs, different features can be observed from the STM topographic images depending on the bias voltage, as shown in Figs. 4.16a to 4.16d. In general, a positive (negative) bias will probe the gallium (arsenide) atoms. Dopant atoms are also reflected on the STM images. For this work, the individual features of the surface are not relevant, because a large area will be illuminated for the photoemission experiments; therefore, the overall state of the surface is more important. Both the n-type and p-type GaAs samples presented a surface roughness of only a few tens of

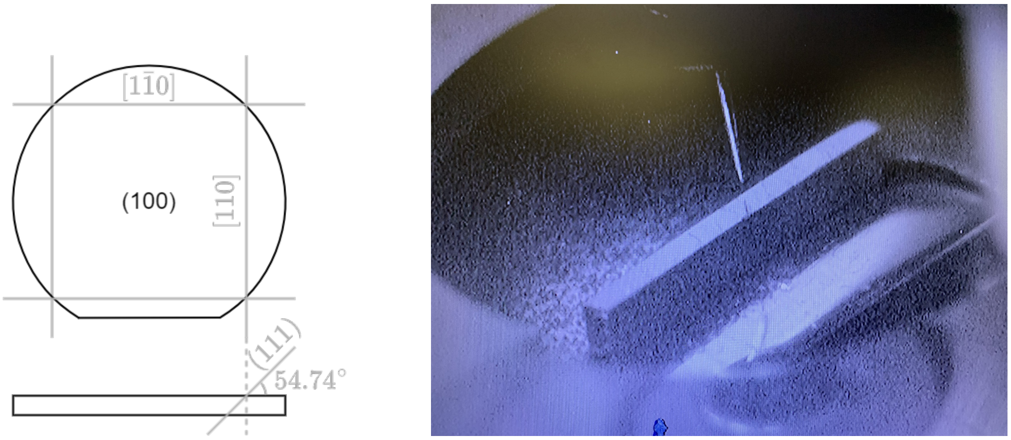

(a) Cleavage planes of (100)-plane GaAs.

(b) Photograph of the STM tip over the freshly cleaved (110) face of the GaAs sample.

Figure 4.15: The cleaved GaAs(110) sample. a) Cleavage planes and b) a photograph of a freshly cleaved sample.

picometers over areas of hundreds of nanometers, which provided a flat surface for the experiments.

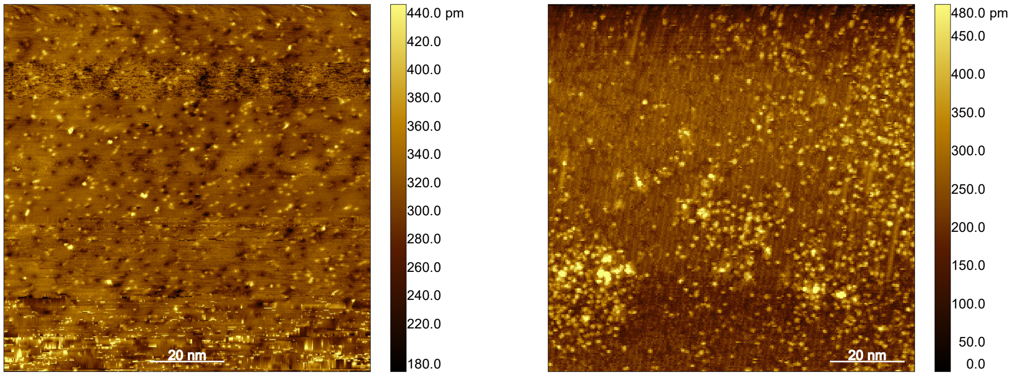

(a) Topography of n-type GaAs(110). Acquired with $V_{\mathrm{DC}} = +3\,\mathrm{V}$.

(b) Topography of n-type GaAs(110). Acquired with $V_{\mathrm{DC}} = -3\,\mathrm{V}$.

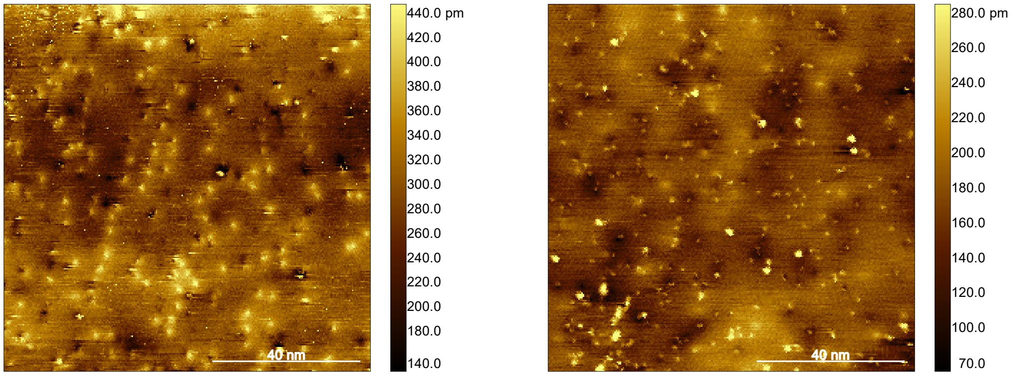

(c) Topography of p-type GaAs(110). Acquired with $V_{\mathrm{DC}} = +1.5\,\mathrm{V}$.

(d) Topography of p-type GaAs(110). Acquired with $V_{\mathrm{DC}} = -1.5\,\mathrm{V}$.

Figure 4.16: Topographic STM images of the GaAs surfaces studied here. Images were acquired in constant current mode with a W tip at 110 K. The images size is 100 nm × 100 nm, and the current setpoint used was $I_{\mathrm{DC}} = 10\,\mathrm{pA}$ for all images.

4.4 Gallium Nitride

A p-type Zn-doped GaN sample with a carrier concentration of $\sim 3 \times 10^{17}\,\mathrm{cm}^{-3}$ was provided by Andreas Zeidler from the Technische Universität München. Using molecular-beam epitaxy, 360 nm of GaN was deposited on top of 16 nm of AlN on a sapphire substrate. Gold contacts were also deposited at the 4 corners of the sample, on top of GaN, to ensure good electrical conductivity for the STM bias connection.

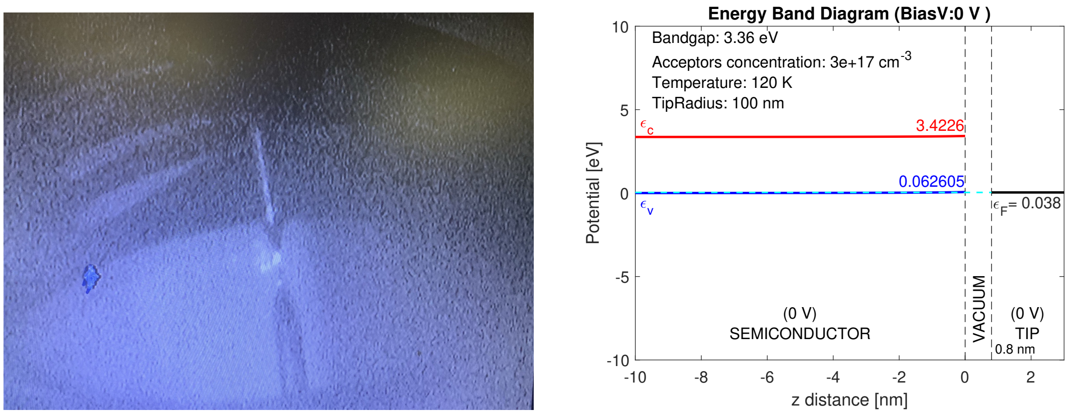

(a) Photograph of the GaN p-type sample.

(b) Energy diagram for p-type GaN.

Figure 4.17: The GaN sample. a) Photograph of the STM tip in tunneling range on the surface of the sample. b) Energy diagram of the GaN sample where the values for the energy bands and the Fermi level were calculated with the SEMITIP software.

This sample was not cleaved, and the surface had to be cleaned. Ion sputtering and annealing are commonly used techniques to clean the surface of GaN in situ [222, 223], because it oxidizes and gets contaminated when exposed to air. The GaN sample used here was degassed at 610 °C for 24 hrs inside vacuum with an average pressure of 2×10^{-8} torr, to remove most of the contaminants from the surface. The sample was heated by thermal contact with a metallic plate that was placed underneath the sapphire substrate and was heated by electron bombardment from a hot thoriated tungsten filament. Nitrogen is preferably used to sputter GaN to reduce nitrogen surface depletion [222], however, our sputtering system can only use Ar. Since the GaN surface looked clean after the annealing procedure, ion sputtering was not performed on this sample. A photograph of the GaN mounted on the STM sample holder is shown in Fig. 4.17a, and the energy diagram with the values calculated from the SEMITIP program is shown in Fig. 4.17b.

For the case of GaN, the surface presents granular islands a few nanometers wide (Fig. 4.18), similar to what has been previously observed on a similar sample [224]. The surface features are comparable for positive and negative bias, and the surface

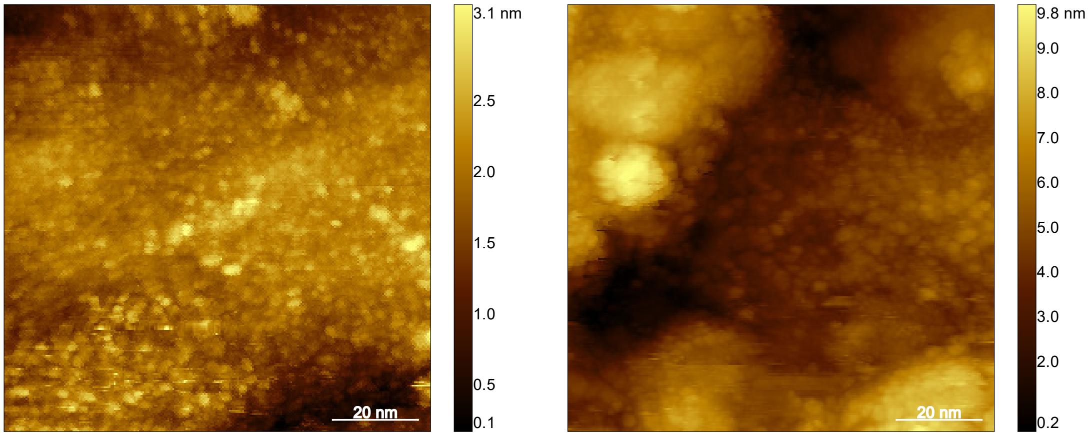

(a) Topography of p-type GaN. Acquired with $V_{\mathrm{DC}} = +3\,\mathrm{V}$.

(b) Topography of p-type GaN. Acquired with $V_{\mathrm{DC}} = -1.5\,\mathrm{V}$.

Figure 4.18: Topographic STM images of the GaN surface. The $100\,\mathrm{nm} \times 100\,\mathrm{nm}$ images were acquired with $I_{\mathrm{DC}} = 10\,\mathrm{pA}$ and a W tip at 120 K.

presented a roughness of a few hundreds of picometers. The lack of an atomically flat surface can be a disadvantage when GaN is used as a substrate.

Chapter 5

THz-STM on metals

Metals are one of the key components of any electronic device built today. Metals are commonly used as contacts and transmission lines, and they are fundamental to transport charge in electronic devices. Metals are well understood and they offer a simple material that can be used to understand and characterize the transient currents induced in a THz-STM system [41]. In this chapter, the surface of Au(111) was studied to establish a benchmark of the THz-STM system, and the results are compared with those obtained on Cu(111).

5.1 Au(111)

The Au(111) surface, which is well known for its remarkable surface reconstruction, is commonly the substrate of choice for many experiments. For this work, Au(111) was used as an electrode for the photoemission experiments, as the substrate for SWCNTs and graphene islands, and it was also used to characterize our THz-STM system, which was done as follows. The $I_{\mathrm{THz}} - E_{\mathrm{THz,pk}}$ measurement can be used to calibrate the lock-in output signal of the THz-induced current channel. When the STM feedback loop is kept on during the $I_{\mathrm{THz}} - E_{\mathrm{THz,pk}}$ acquisition, the tip height will be adjusted for the given setpoint, given that $I_{\mathrm{total}} = I_{\mathrm{DC}} + I_{\mathrm{THz}}$. As $E_{\mathrm{THz,pk}}$ increases, the contribution from I_{THz} will increase. If the current setpoint is large, such that $I_{\mathrm{DC}} > I_{\mathrm{THz}}$ at all times, then the tip height will almost remain constant and the $I_{\mathrm{THz}} - E_{\mathrm{THz,pk}}$ curves will be similar to when the feedback loop is off. However, if the current setpoint is very low, the contribution from I_{THz}, as $E_{\mathrm{THz,pk}}$ increases, will approach and eventually equal the setpoint, which will force the tip to retract to keep a constant current. This will be reflected as a saturation on the $I_{\mathrm{THz}} - E_{\mathrm{THz,pk}}$ curve, as shown by the orange line in Fig. 5.1a. This plot shows the lock-in output signal for the THz channel ($A_{\mathrm{THz,lockin-out}}$) as a function of $E_{\mathrm{THz,pk}}$, where multiple current setpoints were used to show the saturation effect. For the case of a 2 pA setpoint, the $I_{\mathrm{THz}} - E_{\mathrm{THz,pk}}$ curve approaches a lock-in signal amplitude of $A_{\mathrm{THz,lockin-out}} = 0.277\,\mathrm{V}$ at high fields. It can be estimated from this curve that, when the setpoint is 2 pA, a field of $E_{\mathrm{THz,pk}} = 400\,\mathrm{V/cm}$ is enough to generate $I_{\mathrm{THz}} \approx 2\,\mathrm{pA}$, which means that the system is THz-driven for $E_{\mathrm{THz,pk}} > 400\,\mathrm{V/cm}$. From Eq. 2.18, we calculate $N_{\mathrm{e/pulse}} = 100\,\mathrm{e/pulse}$ for an average current setpoint of 2 pA, where a 50 % duty cycle was included for the THz modulation. Therefore, using Eq. 3.2, with a lock-in sensitivity of 50 mV, a laser repetition rate of 250 kHz, and inverse gains of $K_1 = 1.7\,\mathrm{nA/V}$,$K_2 = 0.96$ and $K_3 = 2.13$ gives a correction factor Z_{exp} as follows

$$Z_{\mathrm{exp}} = \frac{(100\,\mathrm{e/pulse})(1.602 \times 10^{-19}\mathrm{C/e})(250 \times 10^{3}\,\mathrm{pulses/s})}{(1.7\,\mathrm{nA/V})(0.96)(2.13)(0.05\,\mathrm{V})(\frac{0.277\,\mathrm{V}}{10\,\mathrm{V}})} = 0.832\ . \tag{5.1}$$

This value of $Z_{\mathrm{exp}} = 0.832$ was then used to obtain the total scaling factor to convert the lock-in output signal to the number of electrons per pulse as

$$\begin{aligned} N_{\mathrm{e/pulse}} &= \left(\frac{4\,\mu\mathrm{s/pulse}}{1.602 \times 10^{-19}\mathrm{C}}\right)(0.832)(1.7\,\mathrm{nA/V})(0.96)(2.13)(0.05\,\mathrm{V})\left(\frac{A_{\mathrm{THz,lockin-out}}}{10\,\mathrm{V}}\right) \\ &= (361\,\mathrm{e/V})(A_{\mathrm{THz,lockin-out}})\ . \end{aligned} \tag{5.2}$$

The $I_{\mathrm{THz}} - E_{\mathrm{THz,pk}}$ plots with the calibrated vertical axis are shown in Fig. 5.1b. The retraction of the tip as $E_{\mathrm{THz,pk}}$ increases is also shown in Fig. 5.1c. Once the THz channel was calibrated, regular $I_{\mathrm{THz}} - E_{\mathrm{THz,pk}}$ measurements, with the STM feedback loop off, were performed on the Au(111) surface with a tungsten tip, as shown in Fig. 5.2a. The initial tip height was set by $I_{\mathrm{DC}} = 5\,\mathrm{pA}$ and three different bias voltages: 10 mV, 100 mV and 1 V. The lower the bias voltage, the closer the tip is to the sample surface, which translates into a larger I_{THz} for a given $E_{\mathrm{THz,pk}}$. Although, the I_{THz} difference between the 100 mV and 1 V cases is hardly noticeable in this plot. The I_{THz} onset, determined when the signal rises above the noise floor (2 e/pulse), was found to be around 160 V/cm, for the three cases.

A second set of data is presented in Fig. 5.2b, where a different tungsten tip was used. Absolute I_{THz} is shown for positive and negative $E_{\mathrm{THz,pk}}$ values, and in this case, the onset occurs at $E_{\mathrm{THz,pk}} = -100\,\mathrm{V/cm}$ and $E_{\mathrm{THz,pk}} = +120\,\mathrm{V/cm}$. The slight variation of the onset, as compared with the previous dataset, can be caused by a THz field coupling efficiency difference from tip to tip, which depends on their shape.

As mentioned before, for a current setpoint of 2 pA and $E_{\mathrm{THz,pk}} > 400\,\mathrm{V/cm}$, the STM operates in THz-driven mode, where most of the tunneling current is

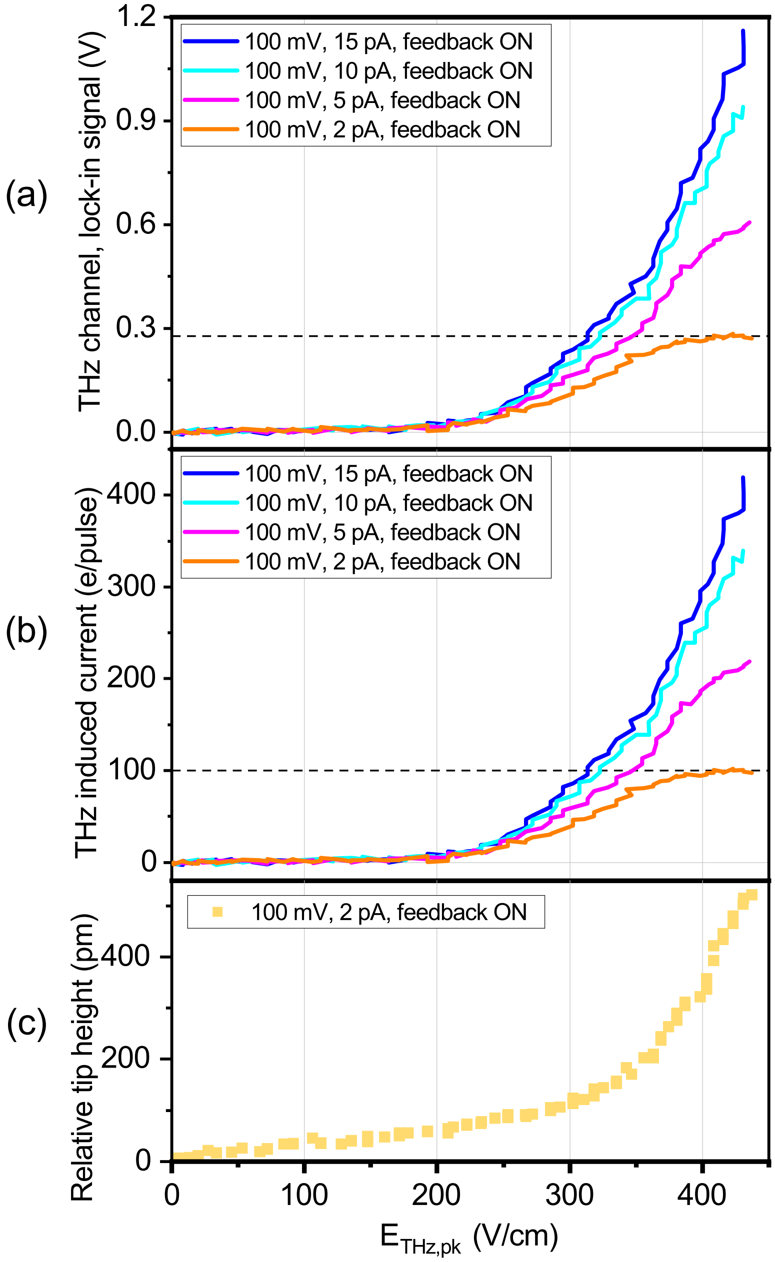

Figure 5.1: $I_{\mathrm{THz}} - E_{\mathrm{THz,pk}}$ curves that were used to calibrate the lock-in output signal of the THz-induced current channel. The data was acquired with the STM feedback loop on and different current setpoints. The vertical axis shows a) the raw signal from the lock-in output and b) the actual number of tunneling electrons after the calibration. c) Relative tip height for the case of $I_{\mathrm{DC}} = 2\,\mathrm{pA}$. Measurements were acquired with a W tip on Au(111) at room temperature.

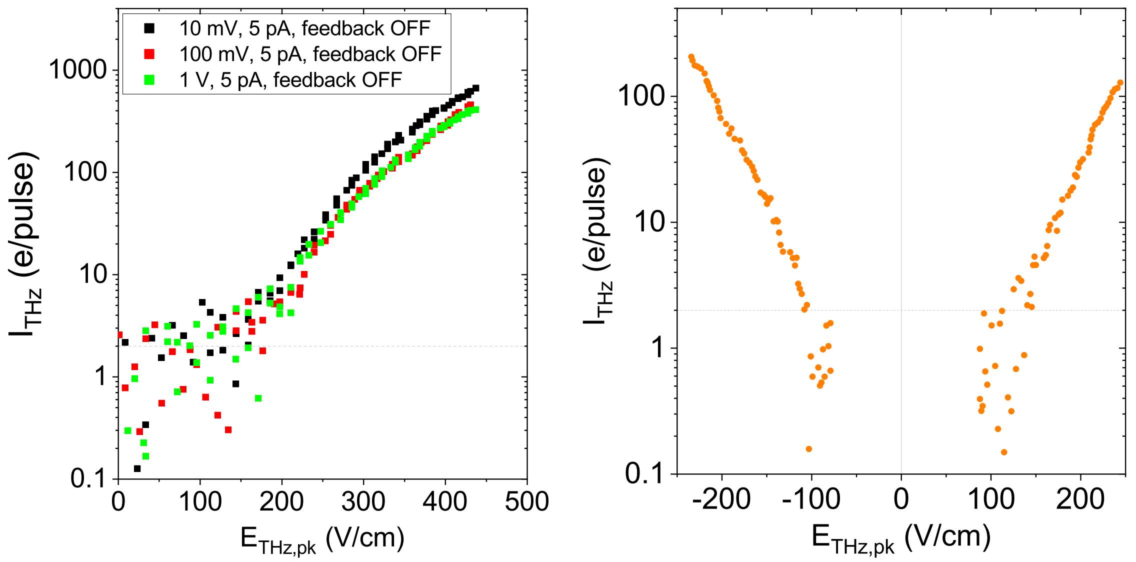

(a)

(b)

Figure 5.2: $I_{\mathrm{THz}} - E_{\mathrm{THz,pk}}$ curves that were acquired on Au(111) with a W tip and the STM feedback loop off. a) The initial tip height was set by $I_{\mathrm{DC}} = 5\,\mathrm{pA}$ and three different V_{DC} values. Lower V_{DC} means the tip is closer to the surface, which translates into a higher I_{THz} for a given $E_{\mathrm{THz,pk}}$. The I_{THz} onset was found to be around 160 V/cm. b) A set of data from a second W tip, showing the absolute I_{THz} where the initial tip height was set by $V_{\mathrm{DC}} = +100\,\mathrm{mV}$ and $I_{\mathrm{DC}} = 50\,\mathrm{pA}$. In this case, the onset occurs at $E_{\mathrm{THz,pk}} = -100\,\mathrm{V/cm}$ and $E_{\mathrm{THz,pk}} = +120\,\mathrm{V/cm}$. The onset difference with a) is caused by the difference in tip coupling efficiency. The onsets were estimated at the point where the signal rises above the noise floor (2 e/pulse) marked with a dashed line.

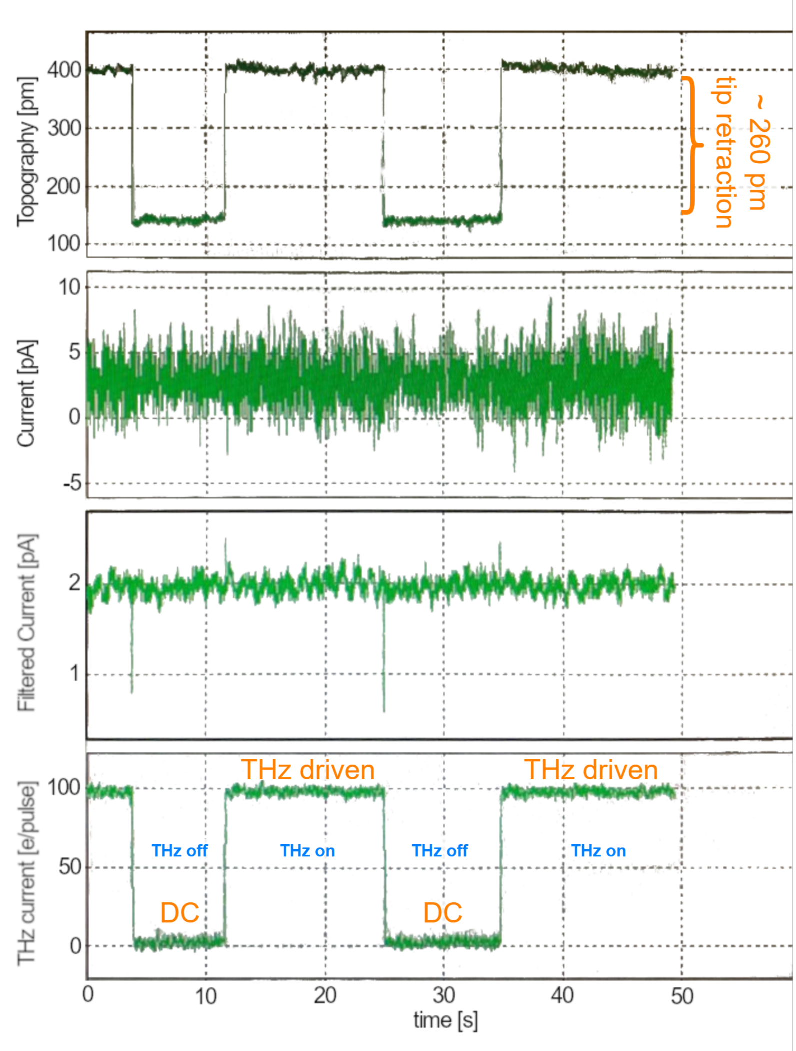

Figure 5.3: The transition between conventional STM DC mode and THz-driven mode. The topography (tip height), the tunneling current, the low-pass filtered tunneling current, and the THz-induced current channels are recorded simultaneously as a function of time. Measurements were taken with $V_{\mathrm{DC}} = 10\,\mathrm{mV}$ and $I_{\mathrm{DC}} = 2\,\mathrm{pA}$. The generation of THz pulses was turned on and off, with $E_{\mathrm{THz,pk}} = 437\,\mathrm{V/cm}$. When the THz pulses were turned on, the tip retracted $\sim 260\,\mathrm{pm}$, which translates into a reduction of the DC current of almost 400 times.

produced by the THz electric fields. Fig. 5.3 shows the transition between this mode of operation and the conventional DC mode with $V_{\mathrm{DC}} = 10\,\mathrm{mV}$. The topography (tip height), the tunneling current, the low-pass filtered tunneling current, and the THz-induced current channels are recorded simultaneously as a function of time, while the generation of THz pulses is turned on and off, with an amplitude at the peak of $E_{\mathrm{THz,pk}} = 437\,\mathrm{V/cm}$. The total tunneling current remains constant throughout the measurement, but I_{THz} goes from 0 to 100 e/pulse, which corresponds to 2 pA. When the THz pulses are on, the tip retracts $\sim 260\,\mathrm{pm}$ to satisfy the current setpoint, due to the additional contribution of I_{THz}. It should be noted that transient I_{THz} currents are estimated to reach peak magnitudes of hundreds of microamperes or even milliamperes over a few hundreds of femtoseconds [37]. The reduction of DC current due to a tip retraction of 260 pm can be estimated using Eq. 2.1, with $\Phi_{\mathrm{Au}} = 4.8\,\mathrm{eV}$ as follows

$$\frac{T(z=0)}{T(z=0.26\,\mathrm{nm})} = \frac{1}{\exp(-2(0.26)\sqrt{\frac{2m}{\hbar}(4.8)})} = 334\,. \tag{5.3}$$

A tip retraction of $\sim 260\,\mathrm{pm}$ translates into a reduction of DC current of over 300 times, confirming that the STM was entirely operating in THz-driven mode.

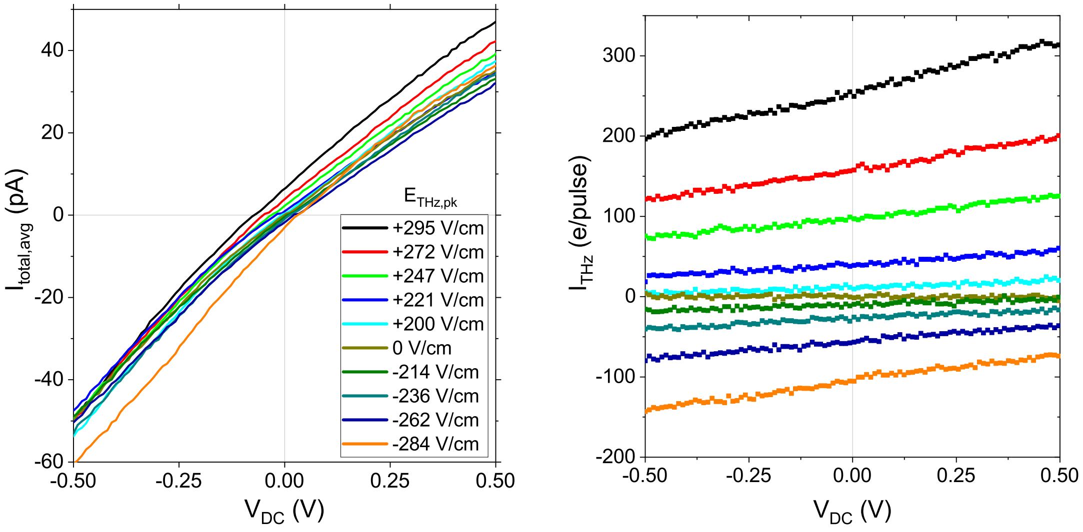

(a) (b)

Figure 5.4: a) $I-V$ curves and b) $I_{\mathrm{THz}}-V$ curves, acquired simultaneously on the Au(111) surface for positive and negative $E_{\mathrm{THz,pk}}$ values. The tip height was set by $V_{\mathrm{DC}} = -0.5\,\mathrm{V}$ and $I_{\mathrm{DC}} = 50\,\mathrm{pA}$. The contribution of I_{THz} shifts the $I-V$ curves up (down) when the THz pulse peak is positive (negative). Measurements were acquired with a W tip at 120 K

To study the sample response in the presence of THz fields, $I-V$ curves (Fig. 5.4a) and $I_{\mathrm{THz}}-V$ curves (Fig. 5.4b) were acquired simultaneously on the Au(111) surface for positive and negative $E_{\mathrm{THz,pk}}$ values. The tip height was set with $V_{\mathrm{DC}} = -0.5\,\mathrm{V}$ and $I_{\mathrm{DC}} = 50\,\mathrm{pA}$. When the feedback loop is turned off by the STM controller to start the data acquisition, small random variations in tip height shift the initial point of the curves, causing the overlap and crossover of some of the $I-V$ curves; but a general trend can be observed: A positive (negative) $E_{\mathrm{THz,pk}}$ shifts the $I-V$ curve up (down) due to the small contribution of I_{THz} to the total tunneling current. The $I_{\mathrm{THz}}-V$ curves clearly show how the I_{THz} contribution changes with $E_{\mathrm{THz,pk}}$. Technically, V_{DC} shifts the voltage window accessed by the transient THz voltage to the sides of the $I-V$ curve (see Fig. 2.13a). When the THz fields are small, they oscillate in a small voltage window and the I_{THz} slope is small. However, as $E_{\mathrm{THz,pk}}$ increases, the voltage window is larger, and the positive (negative) part of the THz pulse will reach the nonlinear region of the $I_{\mathrm{THz}}-V$ curve when V_{DC} is positive (negative), which increases the slope of I_{THz}. The nonlinear region of the $I-V$ curve is more evident in Fig. 4.3a. The $I_{\mathrm{THz}}-V$ curve provides an estimate of the expected I_{THz} contribution to the total tunneling current depending on the operating parameters V_{DC} and $E_{\mathrm{THz,pk}}$.

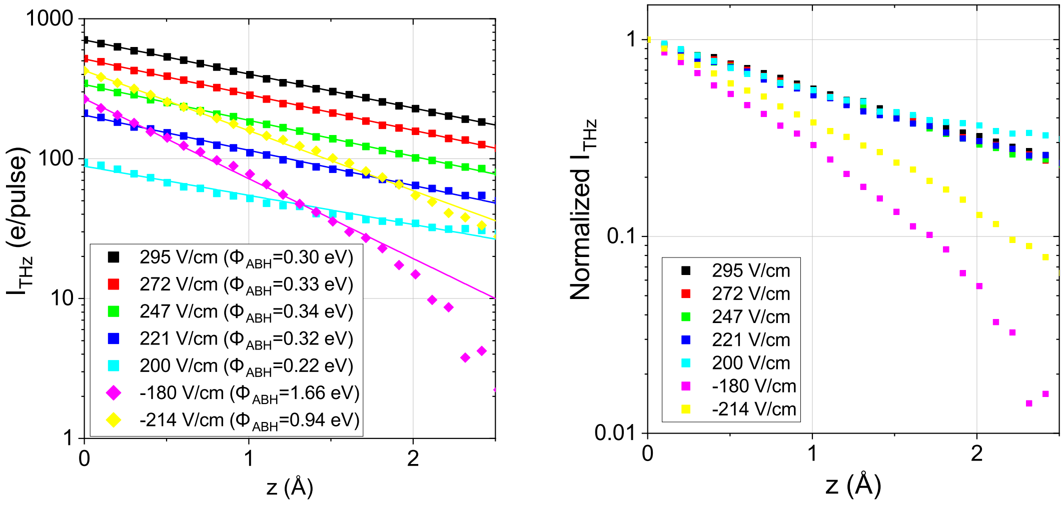

(a) (b)

Figure 5.5: $I_{\mathrm{THz}}-z$ measurements on Au(111) a) $I_{\mathrm{THz}}-z$ curves, acquired by lock-in detection for positive and negative $E_{\mathrm{THz,pk}}$ values. The initial tip height was set by $V_{\mathrm{DC}} = +5\,\mathrm{mV}$ and $I_{\mathrm{DC}} = 50\,\mathrm{pA}$. The experimental data is shown with colored squares, and it was fitted by single exponential functions, which are shown with colored solid lines. The presence of the THz pulse fields lowers the apparent barrier height at the junction. The calculated ABH for each case, obtained from the fits, is presented within brackets in the legend box. b) Normalized $I_{\mathrm{THz}}-z$ data from (a).

To study the apparent barrier height Φ_{ABH} of the Au(111) surface when the THz pulse field is present, $I - z$ and $I_{\mathrm{THz}} - z$ curves were obtained simultaneously with an initial tip height set by $V_{\mathrm{DC}} = +5\,\mathrm{mV}$ and $I_{\mathrm{DC}} = 50\,\mathrm{pA}$. In Fig. 5.5a, I_{THz} clearly shows an exponential decay with distance, and a reduced apparent barrier height can be noted by the low slope. The experimental data shown with colored squares was fitted with a single exponential of the form of Eq. 2.1, which is presented with colored solid lines. When $E_{\mathrm{THz,pk}}$ was positive, the calculated ABH was almost constant at around 0.3 eV, independent of the peak field amplitude. This can be clearly observed in Fig. 5.5b, where the $I_{\mathrm{THz}} - z$ curves have been normalized. These low ABH values agree with those calculated in previous works [37, 41]. When $E_{\mathrm{THz,pk}}$ was negative, the ABH was found to be 1.66 eV and 0.94 eV for $E_{\mathrm{THz,pk}} = -180\,\mathrm{V/cm}$ and $E_{\mathrm{THz,pk}} = -214\,\mathrm{V/cm}$, respectively.

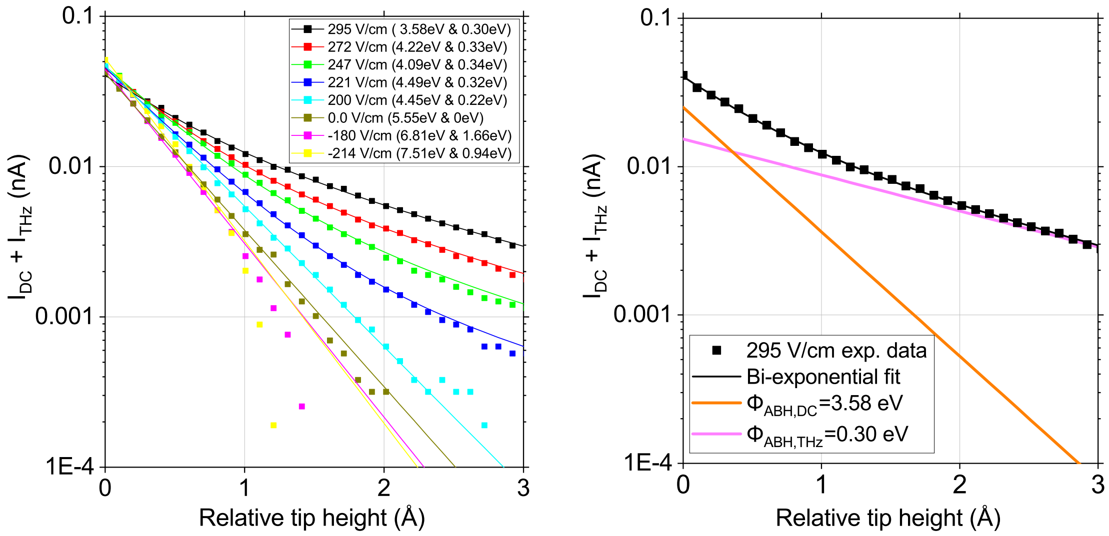

(a) (b)

Figure 5.6: $I - z$ measurements on Au(111) in the presence of THz fields. $I = I_{\mathrm{DC}} + I_{\mathrm{THz}}$. a) $I - z$ curves taken with an initial tip height set by $V_{\mathrm{DC}} = +5\,\mathrm{mV}$ and $I_{\mathrm{DC}} = 50\,\mathrm{pA}$, for positive and negative $E_{\mathrm{THz,pk}}$ values. The experimental data is shown with colored squares, and it was fitted with bi-exponential functions, which are shown with colored solid lines. b) Case with $E_{\mathrm{THz,pk}} = 295\,\mathrm{V/cm}$ where the bi-exponential behavior can be observed.

Looking at the $I - z$ curves shown in Fig. 5.6a, it was obvious that they do not follow a straight line as expected for a single exponential decay. It was assumed that these curves actually followed a bi-exponential behavior described by the following function

$$I = A_{\mathrm{DC}} \exp\left(-2 * 5.1\sqrt{\Phi_{\mathrm{ABH,DC}}}z\right) + A_{\mathrm{THz}} \exp\left(-2 * 5.1\sqrt{\Phi_{\mathrm{ABH,THz}}}z\right), \tag{5.4}$$

where the second exponential function would follow the $I_{\mathrm{THz}} - z$ curves of Fig. 5.5a; hence, $\Phi_{\mathrm{ABH,THz}}$ was fixed with the values shown in that Figure.

$E_{\mathrm{THz,pk}}$ [V/cm]	A_{DC} [nA]	$\Phi_{\mathrm{ABH,DC}}$ [eV]	A_{THz} [nA]	$\Phi_{\mathrm{ABH,THz}}$ [eV]
295	0.0251	3.58	0.0154	0.30*
272	0.0338	4.23	0.0109	0.33*
247	0.0398	4.09	0.0068	0.34*
221	0.0424	4.49	0.0032	0.32*
200	0.0468	4.45	2.9E-16	0.22*
0	0.0418	5.55	0*	0*
-180	0.0442	6.81	5.6E-19	1.66*
-214	0.0524	7.51	4E-20	0.94*

Table 5.1: Resulting values for the parameters used to fit the data in Fig. 5.6a. A bi-exponential function given by Eq. 5.4 was used. *These numbers were fixed and taken from Fig. 5.5a.

In Fig. 5.6a, the experimental data is shown with colored squares, the bi-exponential fits are presented with solid lines, and the resulting values for the fit parameters are shown in Table 5.1. As a general trend, $\Phi_{\mathrm{ABH,DC}}$ decreases as the positive $E_{\mathrm{THz,pk}}$ field increases, and conversely, it increases as the negative $E_{\mathrm{THz,pk}}$ field increases. To illustrate the contribution of the two exponentials, the case where $E_{\mathrm{THz,pk}} = 295\,\mathrm{V/cm}$ is shown in Fig. 5.6b. The idea that the contribution of the $I_{\mathrm{THz}} - z$ is simply embedded in the $I - z$ curve is supported by the fact that the A_{THz} values obtained from the fits are very close to the actual current amplitudes measured experimentally. For example, when $E_{\mathrm{THz,pk}} = 295\,\mathrm{V/cm}$, the initial I_{THz} would be given by $A_{\mathrm{THz}} = 15.4\,\mathrm{pA}$, which is the point where the pink line crosses the vertical axis in Fig. 5.6b. This corresponds to $I_{\mathrm{THz}} \approx 770\,\mathrm{e/pulse}$, which is very close to the point where the black line crosses the vertical axis in Fig. 5.5a. Moreover, the accuracy of the fits with the experimental data in Fig. 5.6a further supports this approach. The ABH dependence on $E_{\mathrm{THz,pk}}$ is presented in Fig. 5.7. $\Phi_{\mathrm{ABH,DC}}$ and $\Phi_{\mathrm{ABH,THz}}$ are shown in black and red, respectively. The estimated THz onsets of $\pm 160\,\mathrm{V/cm}$ are marked by dashed vertical lines. The top axis shows the calculated transient bias voltage peak $V_{\mathrm{THz,pk}}$ at the junction, which was obtained with $E_{\mathrm{THz,pk}}$ and the scaling factor of $1/45\,\mathrm{cm}$ from previous works [37, 41], which corresponds to a field enhancement factor of $F \approx 2.2 \times 10^5$.

The $I_{\mathrm{THz}} - E_{\mathrm{THz,pk}}$ curves from Fig. 5.2a, can also be analyzed with the Fowler-Nordheim theory, which states that field emission would appear as a straight line in a plot of $\ln(J/E^2)$ versus $1/E$ (see Section 2.4.1.2). Fig. 5.8 presents that data in the form of $\ln(I_{\mathrm{THz}}/V_{\mathrm{THz,pk}}^2)$ versus $1/V_{\mathrm{THz,pk}}$. Since the work function of the tip

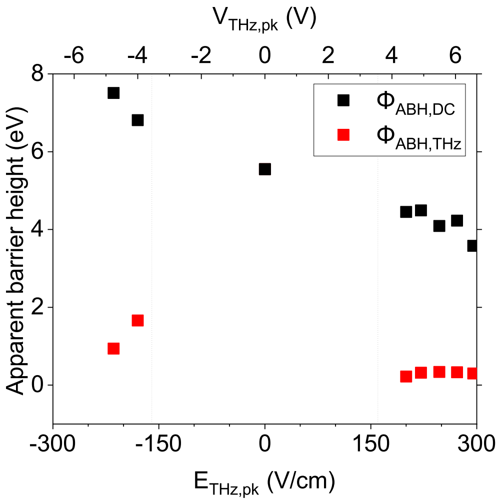

Figure 5.7: Apparent barrier height as a function of THz pulse peak electric field. $\Phi_{\mathrm{ABH,DC}}$ and $\Phi_{\mathrm{ABH,THz}}$ are shown in black and red, respectively. $\Phi_{\mathrm{ABH,DC}}$ decreases (increases) when the positive (negative) THz peak field amplitude is increased. The top axis shows the equivalent transient bias voltage peak calculated with a scaling factor of 1/45 cm.

and sample is $\sim 5\,\mathrm{eV}$, the point where $V_{\mathrm{THz,pk}} = 5\,\mathrm{V}$ ($E_{\mathrm{THz,pk}} = 225\,\mathrm{V/cm}$) has been marked with a vertical gray dashed line. This point seems to agree with the threshold where the system transitions from a straight line corresponding to the field emission regime into the direct tunneling regime, which is the middle part. A vertical gray solid line marks the I_{THz} onset at $E_{\mathrm{THz,pk}} = 160\,\mathrm{V/cm}$, therefore, data on the right of this line corresponds to the noise floor. This plot shows that field emission occurred on the Au(111) sample and the tunneling regime was accessible when $E_{\mathrm{THz,pk}} < 225\,\mathrm{V/cm}$.

Finally, THz-STM imaging on the Au surface was explored. The herringbone reconstruction is one of the characteristic features of the Au(111) surface. Fig. 5.9 shows the topography channel (left) and the I_{THz} channel (right), which were acquired simultaneously for a 30 nm x 30 nm window scan, with $E_{\mathrm{THz,pk}} = +295\,\mathrm{V/cm}$ (top) and $E_{\mathrm{THz,pk}} = -214\,\mathrm{V/cm}$ (bottom). An inverse pattern of the Herringbone reconstruction can be observed in the THz-STM images (right). The top right image presents good spatial resolution even when $E_{\mathrm{THz,pk}} = +295\,\mathrm{V/cm}$ is larger than the threshold of 225 V/cm previously found for the field emission regime. The line profiles, along the white path marked in the top images, are presented in Fig. 5.10, where the black line and the left axis correspond to the topography, and the red line and the right axis correspond to I_{THz}. It should be noted that the line profiles are the opposite of each other, which means that I_{THz} decreases when the tip retracts and increases when the tip gets closer to the surface. The tip height difference between the hills and the deep

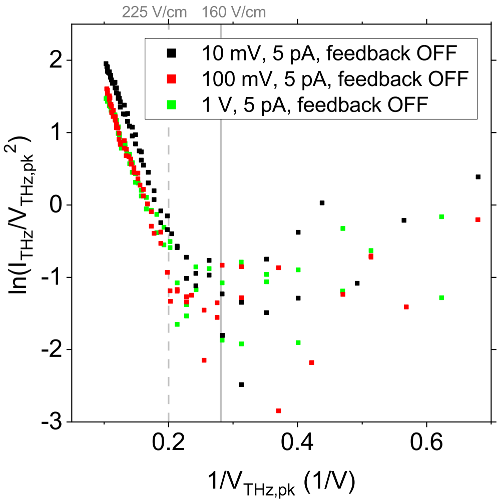

Figure 5.8: Fowler-Nordheim theory applied to the Au(111) sample measurements. The $I_{\mathrm{THz}} - E_{\mathrm{THz,pk}}$ curves from Fig. 5.2a are presented in the form of $\ln\left(I_{\mathrm{THz}}/V^2_{\mathrm{THz,pk}}\right)$ versus $1/V_{\mathrm{THz,pk}}$. The linear trend on the left side indicates the field emission regime. The vertical gray dashed line indicates the threshold ($V_{\mathrm{THz,pk}} = 5\,\mathrm{V}$) where the system transitions from the field emission regime into the direct tunneling regime.

valleys is on average 17 pm. This number is smaller than the one obtained in Fig. 4.2c because of a smoothing effect from a larger tip height caused by the presence of the THz fields. Using the plots in Fig. 5.5b as reference, we find that a tip retraction of 17 pm translates into an I_{THz} reduction of 0.91 when $E_{\mathrm{THz,pk}} = +295\,\mathrm{V/cm}$. From Fig. 5.10 we see that there is a change of $\sim$ 10 e/pulse between the hills and the deep valleys, which corresponds to an I_{THz} reduction of 0.95. This suggests that the herringbone structure that appears in the THz-STM image is most likely produced by variations in the tip height, and not by variations of the DOS from the crystal structure. This is supported by the fact that the $(dI/dV)/(I/V)$ curves on Au(111) didn't show any difference between the HCP and FCC regions of the herringbone reconstruction. The same inverting effect occurs for the point defects along the Au surface. The protrusions shown as bright spots on the topography appear as dark spots on the THz-STM image, and vice versa for the depressions.

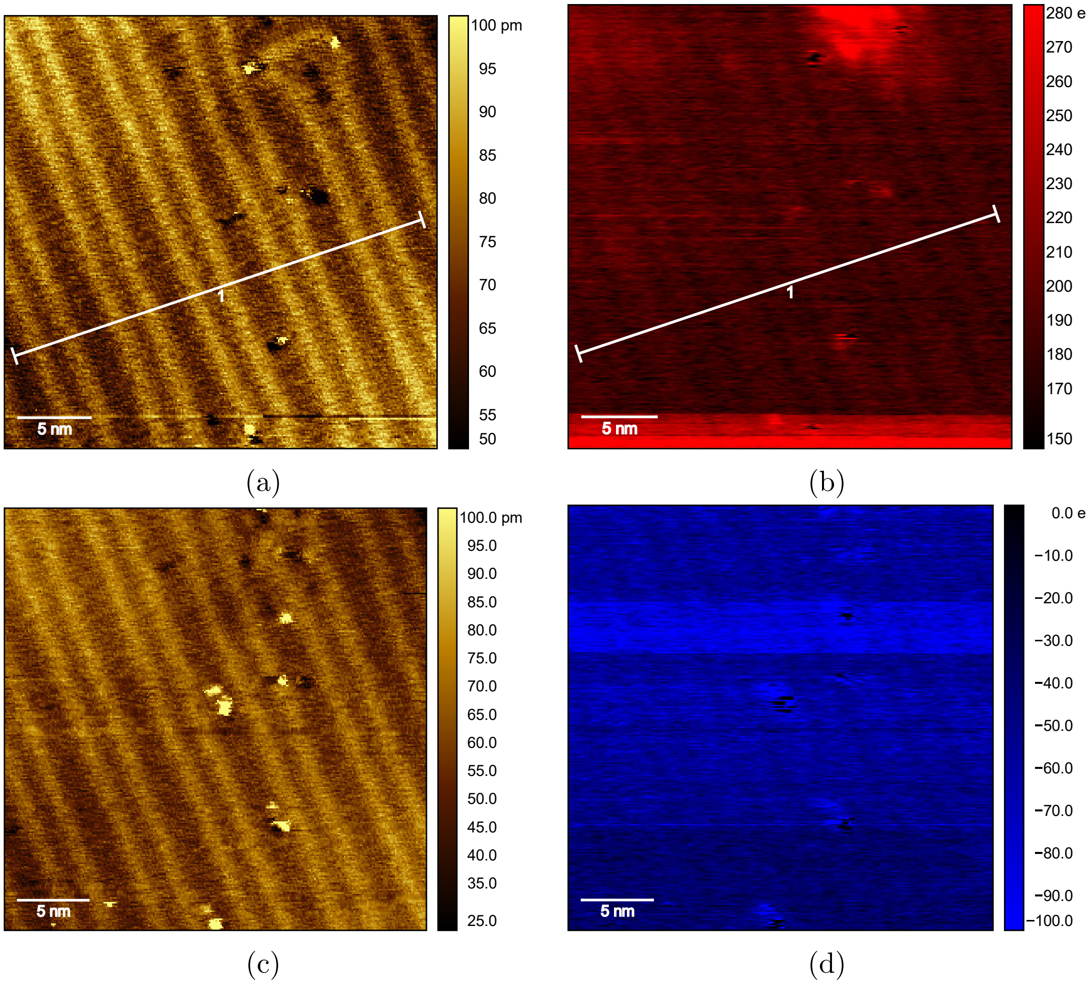

Figure 5.9: THz-STM analysis of the herringbone reconstruction in Au(111). Images of the topography channel (left) and I_{THz} channel (right) were acquired simultaneously for a 30 nm x 30 nm window scan, with $E_{\mathrm{THz,pk}} = +295\,\mathrm{V/cm}$ (top) and $E_{\mathrm{THz,pk}} = -214\,\mathrm{V/cm}$ (bottom). An inverse image of the Herringbone reconstruction can be observed in the THz-STM images (right).

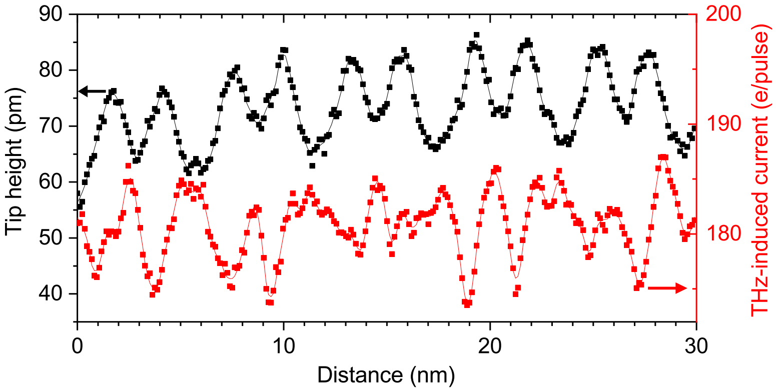

Figure 5.10: Line profile along the paths marked in white on Figs. 5.9a and 5.9b. The black line and the left axis correspond to the topography, and the red line and the right axis correspond to I_{THz}. The line profiles are opposite to each other, which means that I_{THz} increases (decreases) when the tip gets closer (retracts).

5.2 Cu(111)

The surface of Cu(111) was also studied with the THz-STM system and the results were recently published by Luo [41]. Some of the measurements will be presented here for comparison with the Au(111) data discussed in the previous section. First, in Fig. 5.11a, the $I_{\mathrm{THz}} - E_{\mathrm{THz,pk}}$ curve on Cu(111) is shown. Cu presents I_{THz} onsets at +360 V/cm and −315 V/cm, which is larger than the onset on Au (∼ 160 V/cm). The DOS of Cu(111) is similar to that of Au(111) and even rises earlier at lower energies [225–227], therefore, the late THz onset on Cu is potentially caused by a coupling efficiency difference from the tips. Nonetheless, both metals show a comparable I_{THz} increase of around two orders of magnitude after the first 250 V/cm increment on $E_{\mathrm{THz,pk}}$.

Then, in Fig. 5.11b, multiple $I_{\mathrm{DC}} - z$ and $I_{\mathrm{THz}} - z$ measurements were taken on Cu(111) in the absence and presence of THz pulses. When there is no THz field, the DC bias voltage could be increased up to a point around 6 V, where the measurements became unstable, because damage could be induced in the sample by the high fields. On the other hand, when the THz fields were present, a stable $I_{\mathrm{THz}} - z$ measurement could not be obtained with a THz peak field lower than 360 V/cm (which corresponds to $V_{\mathrm{THz,pk}} \approx 8$ V), because the current signal was comparable to the preamp noise (∼ 2 e/pulse). The initial tip-sample distance was reduced in an attempt to increase the I_{THz} current or reduce the $E_{\mathrm{THz,pk}}$ onset, but the larger local electric fields occasionally induced field-enhanced diffusion and the large tunneling currents sporadically induced local sublimation on the sample surface, which translated into

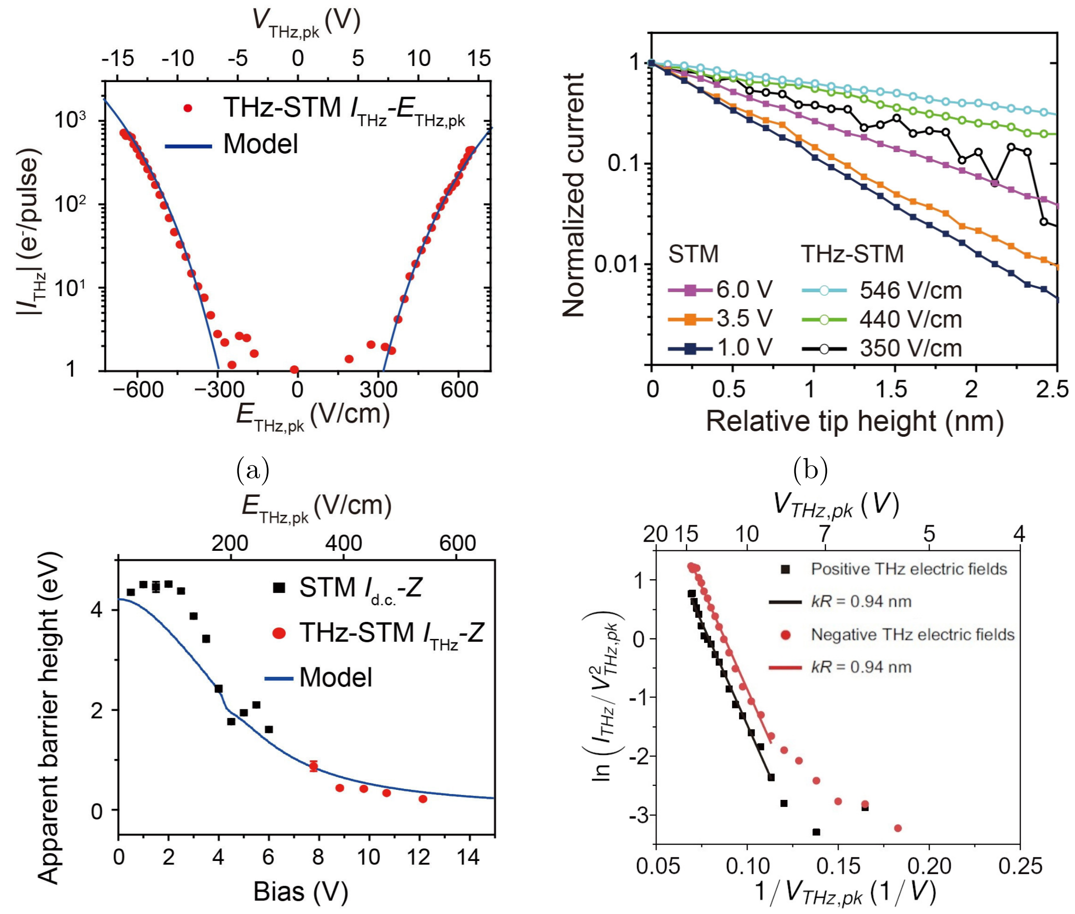

(a) (b)

(c) (d)

Figure 5.11: THz spectroscopy measurements on Cu(111) with a W tip at 100 K. a) Experimental (red dots) and simulated (blue solid line) $I_{\mathrm{THz}} - E_{\mathrm{THz,pk}}$ curves. The tip height was set by $V_{\mathrm{DC}} = 1\,\mathrm{V}$ and $I_{\mathrm{DC}} = 20\,\mathrm{pA}$. It was acquired with feedback loop off and $V_{\mathrm{DC}} = 0.1\,\mathrm{V}$. b) Experimental $I_{\mathrm{DC}} - z$ and $I_{\mathrm{THz}} - z$ curves that were acquired with an initial tip height set by $I_{\mathrm{DC}} = 50\,\mathrm{pA}$, $V_{\mathrm{DC}} = 0.1\,\mathrm{V}$, and $E_{\mathrm{THz,pk}} = 0$. c) Calculated ABH obtained from the $I_{\mathrm{DC}} - z$ and $I_{\mathrm{THz}} - z$ curves shown in (b). Values from STM (black dots), THz-STM (red dots) and simulation (blue solid line) are shown. d) Comparison of $I_{\mathrm{THz}} - E_{\mathrm{THz,pk}}$ with Fowler-Nordheim theory by plotting $\ln(I_{\mathrm{THz}}/V^2_{\mathrm{THz,pk}})$ versus $1/V_{\mathrm{THz,pk}}$. *Reprinted from ref. [41].*

unstable measurements. Fig. 5.11c shows the ABH calculated for each of the stable $I_{\mathrm{DC}} - z$ (black squares) and $I_{\mathrm{THz}} - z$ (red squares) measurements as a function of V_{DC} (bottom axis) and $E_{\mathrm{THz,pk}}$ (top axis). The scaling factor of $1/45\,\mathrm{cm}$ was used. In the absence of THz fields, the STM operates in the tunneling regime and the ABH is close to the workfunction of Cu(111) $\Phi_{\mathrm{Cu}} = 4.94\,\mathrm{eV}$ [228] when $V_{\mathrm{DC}} = 0\,\mathrm{V}$. As V_{DC} increases ABH is reduced until field emission would occur. In the presence of THz fields, the amplitude of the transient voltage $V_{\mathrm{THz,pk}}$ stays above the sample and tip work function ($\sim 5\,\mathrm{eV}$), and it reduces ABH considerably, which suggests that the STM actually operates in the field emission regime. This argument was supported by the Fowler-Nordheim theory, when $\ln\left(I_{\mathrm{THz}}/V_{\mathrm{THz,pk}}^2\right)$ was plotted versus $1/V_{\mathrm{THz,pk}}$, in Fig. 5.11d. A linear behavior was observed, which confirmed that the THz-STM system was operating in the field emission regime. The tunneling regime was not accessible in this case because $E_{\mathrm{THz,pk}} < 360\,\mathrm{V/cm}$ did not produce a measurable I_{THz} signal as mentioned above.

Chapter 6

THz-STM on SWCNTs and graphene islands

One of the main advantages of the THz-STM system is its capability to perform temporally resolved contactless experiments with subnanometer spatial resolution. Therefore, this technique is ideal for studying nanostructures and their properties. Structures at the nanoscale behave differently than what we are used to at the macroscale; their properties change mainly due to electron confinement. This is what motivated the study of SWCNTs, which are quasi-one-dimensional structures with unique properties, and the graphene dendritic islands, which could present two-dimensional crystal properties. The SWCNTs and the graphene islands were deposited on an Au(111) substrate, and they were studied under the THz-STM system.

6.1 THz-STM on SWCNTs and graphene islands

The first step on a THz-STM is to use the $I_{\mathrm{THz}} - E_{\mathrm{THz,pk}}$ plot to determine what THz field amplitude is needed to see a contrast between the sample and the substrate in a THz-STM image. Fig. 6.1 shows the $I_{\mathrm{THz}} - E_{\mathrm{THz,pk}}$ curves on the graphene islands and the Au(111) substrate. These plots can be compared with the corresponding $I - V$ curves taken on Au(111) and graphene islands presented in Fig. 3.10. From the $I_{\mathrm{THz}} - E_{\mathrm{THz,pk}}$ curves, one can see that, for example, $E_{\mathrm{THz,pk}} = +200\,\mathrm{V/cm}$ would induce a larger $+I_{\mathrm{THz}}$ on graphene, but $E_{\mathrm{THz,pk}} = -200\,\mathrm{V/cm}$ would actually induce a smaller $-I_{\mathrm{THz}}$, compared to the substrate signal. Therefore, this field amplitude can provide good contrast for THz-STM imaging. The $I_{\mathrm{THz}} - E_{\mathrm{THz,pk}}$ curves on SWCNTs are not included in this plot because the nanotubes suffered damaged during the measurements, which will be shown below.

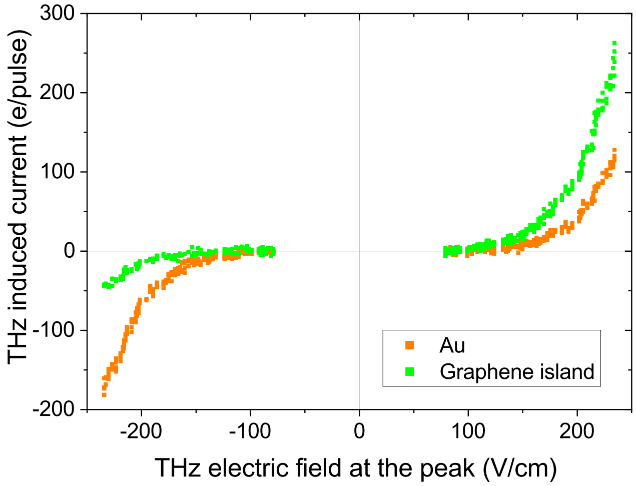

Figure 6.1: I_{THz} as a function of $E_{\mathrm{THz,pk}}$. The data was acquired with the feedback loop off, and an initial tip height set by $V_{\mathrm{DC}} = +100\,\mathrm{mV}$ and $I_{\mathrm{DC}} = 50\,\mathrm{pA}$ for both cases.

The dependence of the THz-induced current on V_{DC} and $E_{\mathrm{THz,pk}}$ is illustrated in Fig. 6.2, where four sequential STM (left) and THz-STM (right) images were taken over a SWCNT resting on graphene islands on an Au(111) substrate. Each image shows one of the possible combinations with $V_{\mathrm{DC}} = \pm 300\,\mathrm{mV}$ and $E_{\mathrm{THz,pk}} = \pm 200\,\mathrm{V/cm}$. The current setpoint was 10 pA. In the THz-STM images, one can see that when $E_{\mathrm{THz,pk}}$ is positive (top and bottom), the largest $+I_{\mathrm{THz}}$ signal is induced on the nanotube, then the graphene islands appear dimmer, and the Au(111) substrate is the darkest, which is what the $I_{\mathrm{THz}} - E_{\mathrm{THz,pk}}$ plot predicted. For the case when $E_{\mathrm{THz,pk}}$ is negative, $-I_{\mathrm{THz}}$ on the substrate and the graphene islands is almost null, and the only negative THz-induced current is generated on small regions of the nanotube surface.

It can be noted from the STM images sequence (Figs. 6.2a, 6.2c, 6.2e and 6.2g) that the SWCNT starts as a regular continuous wire, but it gradually suffers damage after each image is taken, which is induced by the THz fields during the scanning. This was a recurrent problem when a THz-STM measurement was performed on a SWCNT, which restricted the accuracy and reliability of these measurements. Sometimes, the THz fields also pushed the nanotubes away, as can be seen in Fig. 6.3, where a cluster of three nanotubes was moved and bent away while an $I_{\mathrm{THz}} - V$ measurement was being performed on this cluster. A possible solution to this problem would be to reduce the $E_{\mathrm{THz,pk}}$ field amplitude to minimize or eliminate the structural damage on the nanotubes; however, it could not be reduced any further in our setup because the minimum detectable THz-induced current was limited by the noise floor.

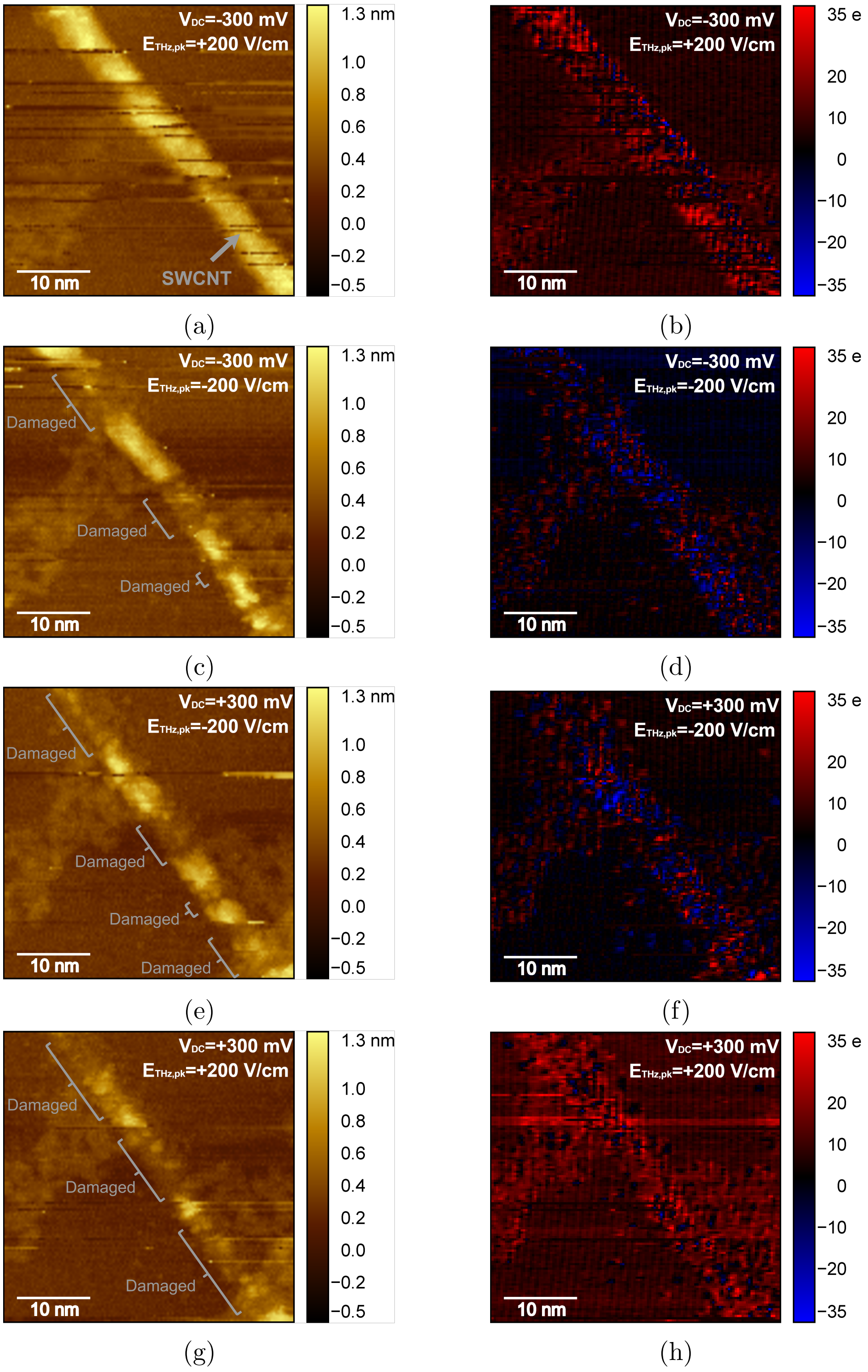

(a) (b) (c) (d) (e) (f) (g) (h)

Figure 6.2: Sequential STM (left) and THz-STM (right) images of a SWCNT resting on graphene islands on an Au(111) substrate. The current setpoint was $I_{\mathrm{DC}} = 10\,\mathrm{pA}$, and the V_{DC} and $E_{\mathrm{THz,pk}}$ values are shown in each image. Gradual damage to the SWCNT due to the THz fields was observed after each image was taken.

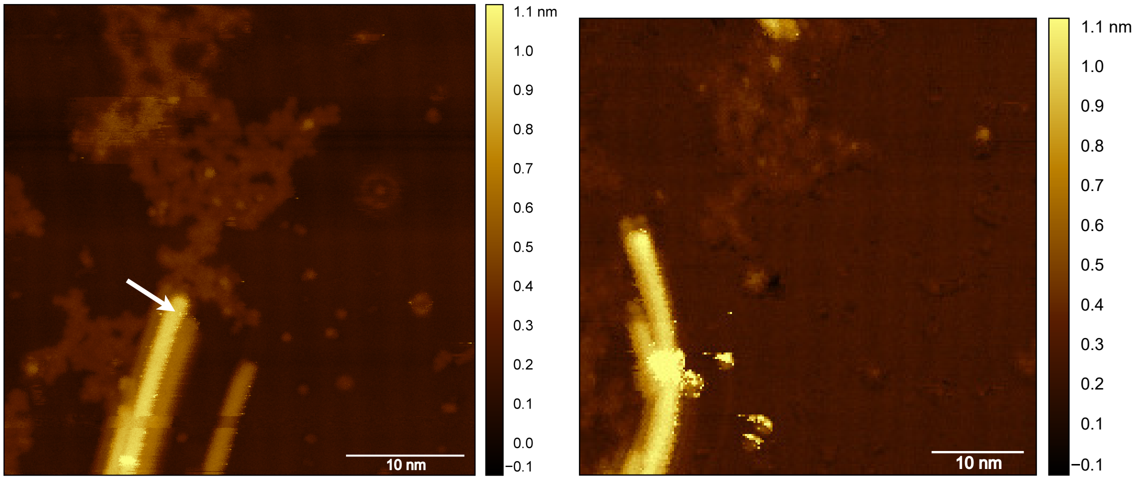

(a) (b)

Figure 6.3: Topographic images of a cluster with three nanotubes a) before and b) after being pushed and bent away by the THz fields, when an $I_{\mathrm{THz}} - V$ measurement was performed on the cluster. A white arrow marks the point where the measurement was being taken. Images were acquired with $V_{\mathrm{DC}} = -2\,\mathrm{V}$ and $I_{\mathrm{DC}} = 50\,\mathrm{pA}$.

The structure of the graphene islands, on the other hand, remained undisturbed during the experiments. The binding energy per carbon atom in SWCNTs ranges between $6.8 - 7.3\,\mathrm{eV}$ [229], and in graphene, it ranges between $7 - 8.2\,\mathrm{eV}$ depending on the number of carbon atoms [230]. Therefore, the damage threshold of the nanotubes is lower. More importantly, the larger surface area of the graphene islands in contact with the substrate compared to that of the nanotubes might explain the stability difference under the THz pulse fields.

This realization led to focusing the efforts on the graphene islands instead of the SWCNTs. First, the spatial resolution of the I_{THz} signal for different tip heights was studied by varying the STM current setpoint. Fig. 6.4 shows four STM (left) and THz-STM (right) images that were acquired on a graphene island with $E_{\mathrm{THz,pk}} = 247\,\mathrm{V/cm}$, $V_{\mathrm{DC}} = +10\,\mathrm{mV}$ and a current setpoint of 2 pA, 5 pA, 10 pA and 15 pA, respectively from top to bottom. The higher the setpoint, the closer the tip is to the sample surface. This can be noted by the increase in the I_{THz} signal as the setpoint increases and the tip gets closer, while all the other parameters remain fixed.

The features in the THz-STM images closely follow the topographic images. A spatial analysis is presented in Fig. 6.5, where the resolution of the two extreme cases (setpoints of 15 pA and 2 pA) is compared. In the THz-STM images (Figs. 6.5a and 6.5b), a small intermediate I_{THz} range was highlighted in white (24 ± 1 e/pulse and 11.9 ± 0.2 e/pulse), roughly marking the boundaries of the graphene island structure. This contour pattern was then superimposed on the topographic images (Figs. 6.5c

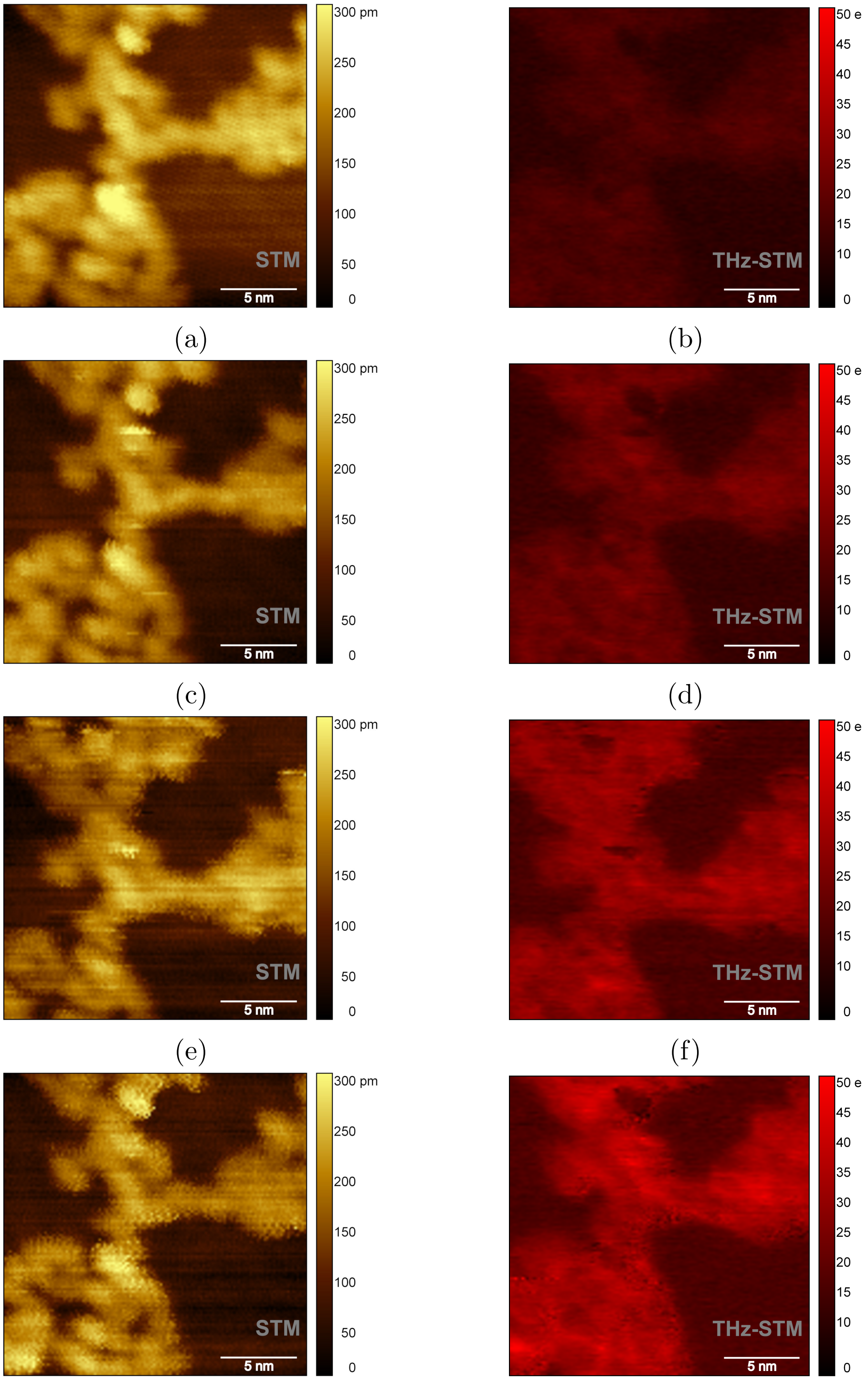

(a) (b) (c) (d) (e) (f) (g) (h)

Figure 6.4: STM (left) and THz-STM (right) images of a graphene island on Au(111) at 120 K. Each pair of images was acquired simultaneously with $E_{\mathrm{THz,pk}} = 247\,\mathrm{V/cm}$, $V_{\mathrm{DC}} = +10\,\mathrm{mV}$ and a current setpoint of 2 pA, 5 pA, 10 pA and 15 pA, respectively, from top to bottom. The I_{THz} signal increases as the W tip gets closer to the sample surface. Sample preparation: A solution of SWCNTs in DMF with (0.05 mg/ml) was sonicated for 30 min. Five drops of the solution were deposited on Au(111), and then received 3 cycles of annealing at 430 °C for 10 min in vacuum.

and 6.5d), and it can be noted that they match almost perfectly. Two main differences between the STM and THz-STM images have been pointed out with green arrows. Difference number 1 shows a small protrusion on the topography that appears as a flat region on the THz-STM image. Difference number 2, shows a similar protrusion on the topography where the I_{THz} signal is actually suppressed. These are probably two different types of structural defects on the graphene island, such as the examples shown in Fig. 4.13 that were discussed in Section 4.2.4, but unfortunately, atomic resolution could not be obtained to properly identify these defects. However, this highlights an advantage of the THz-STM technique to identify specific features which would not be possible by looking at the topography alone. Finally, a comparison of the contour patterns for the two cases is shown in Fig. 6.5e. The similarity of the two patterns indicates that the THz-STM spatial resolution remained technically the same, at least within the tip height range of these experiments (using 2 pA and 15 pA).

A following experiment on the graphene islands is presented in Fig. 6.6, where two pairs of STM (left) and THz-STM (right) images are shown, which were acquired simultaneously with $I_{\mathrm{DC}} = 50\,\mathrm{pA}$, $V_{\mathrm{DC}} = (-)+100\,\mathrm{mV}$ and $E_{\mathrm{THz,pk}} = (-)+200\,\mathrm{V/cm}$. Multiple tip changes occurred during the acquisition of the top images. This can be observed by horizontal striking lines of different brightness in the topography image, and especially by a black fringe at the bottom of Fig. 6.6a, where the tip lost a bunch of atoms from the apex, which forced the tip to move a few nanometers closer for the rest of the scanning. The data points in that region are out of the colorbar scale range selected here, but computational corrections can be applied to the image to fix this issue. The corresponding THz-STM image (Fig. 6.6b), on the other hand, does not depend on the absolute tip height distance and clearly shows the features in that region without any image correction. However, one can see that the I_{THz} signal from the substrate varies when there is a tip change, which is reflected by horizontal blue fringes of different brightness. Since I_{THz} does not depend on the absolute tip height, this suggests that each reconstruction of the atoms at the apex of the tip produces a slightly different field enhancement at the junction. This would make the estimation of the exact field enhancement for a tip very difficult, because tip changes randomly occur during the STM measurements and the spontaneous reconstruction of the tip apex cannot be controlled.

As mentioned before, specific structural defects in the dendritic graphene islands can appear as a protrusion in the STM image, but they actually suppress the I_{THz} signal and appear as dark spots on the THz-STM image. Multiple points where this occurred are marked with white circles on Figs. 6.6c and 6.6d. The suggested

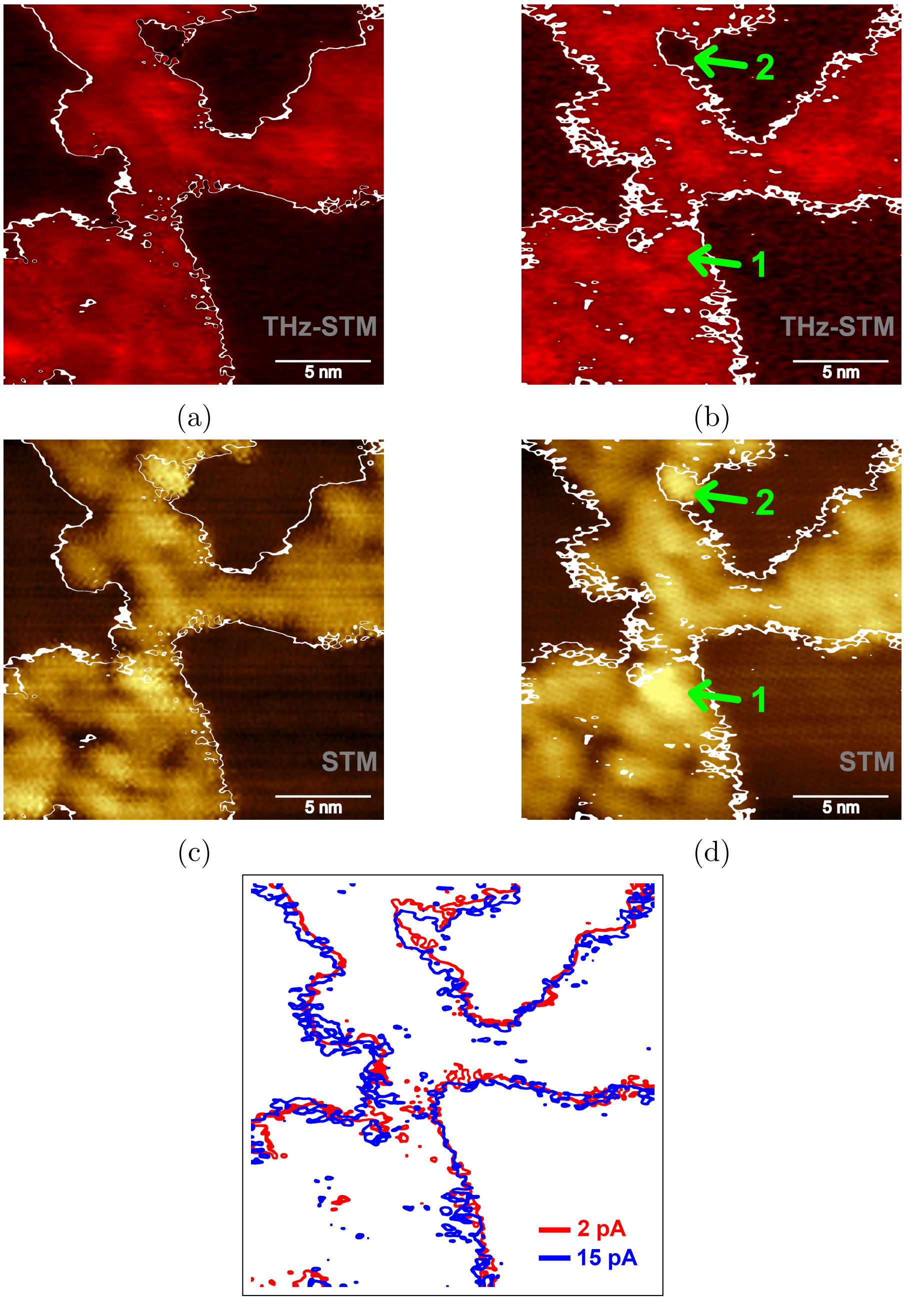

(a) (b) (c) (d) (e)

Figure 6.5: Spatial analysis of the two extreme cases presented in Fig. 6.5. The THz-STM (top) and STM (middle) images were acquired with $E_{\mathrm{THz,pk}} = 247\,\mathrm{V/cm}$, $V_{\mathrm{DC}} = +10\,\mathrm{mV}$ and a current setpoint of 15 pA (left) and 2 pA (right). A specific I_{THz} range was highlighted in white on the THz-STM images, which roughly marks the graphene island boundary. This contour pattern was then superimposed on the topographic images for comparison. Green arrows point out two of the main differences between the images, marked as 1 and 2. A comparison of the contour patterns for the two cases (bottom) indicates that the THz-STM spatial resolution does not change within the tip height range of these experiments.

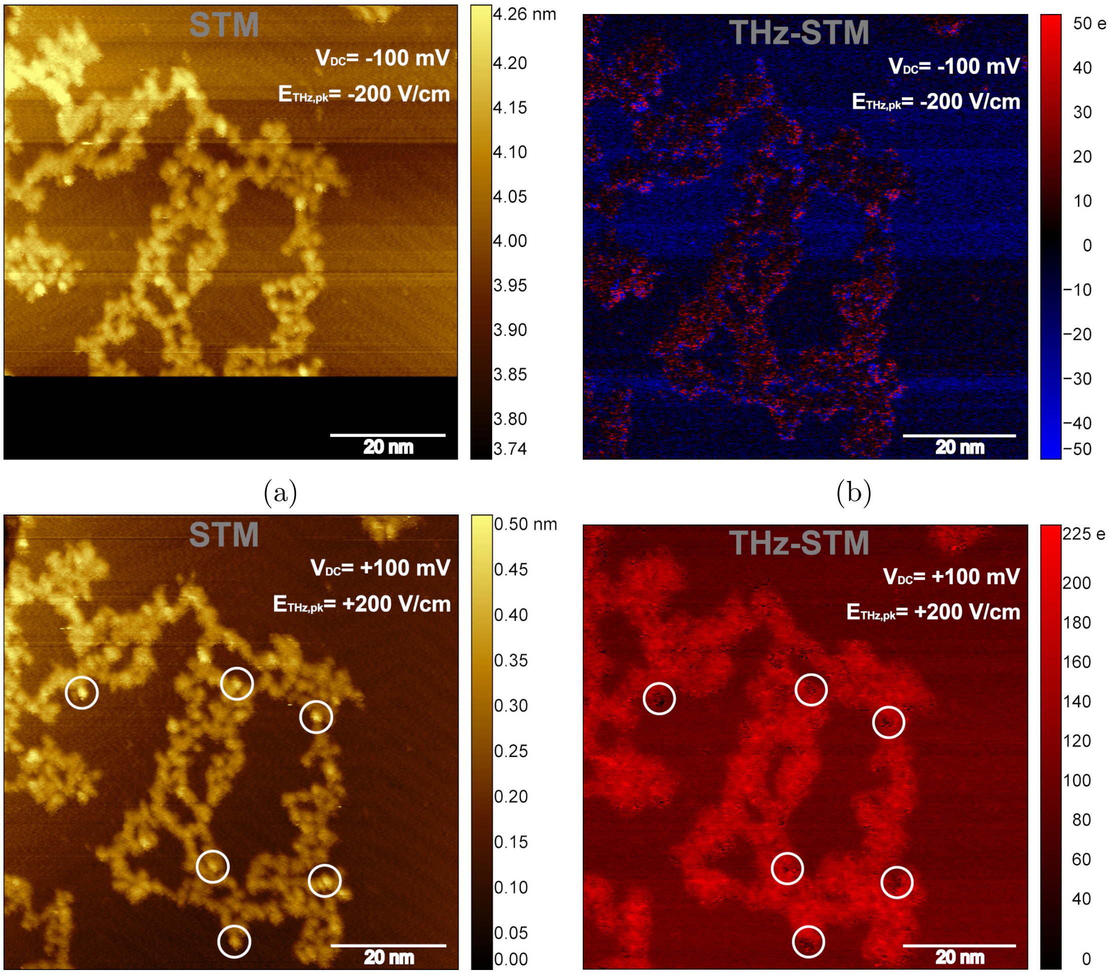

(a) (b)

(c) (d)

Figure 6.6: STM (left) and THz-STM (right) images of a dendritic graphene island on an Au(111) substrate. The images were acquired with $I_{\mathrm{DC}} = 50\,\mathrm{pA}$, $V_{\mathrm{DC}} = (-) + 100\,\mathrm{mV}$ and $E_{\mathrm{THz,pk}} = (-) + 200\,\mathrm{V/cm}$. Multiple tip changes occurred during the image acquisition. The blue horizontal fringes with different brightness, in the THz-STM image, suggest a variation in the field enhancement after each tip apex reconstruction. Multiple points where the structural defects suppressed the I_{THz} signal are circled on the bottom images.

explanation for these features will be described here. A protrusion in the topography image can be caused for example by a missing atom in the graphene structure, as was shown in Fig. 4.13. The missing carbon atom will produce dangling bonds on the surrounding atoms, which modifies the LDOS but not the vertical position of the atoms. The change in LDOS makes the tip retract during the scan, which is shown as a protrusion in the topography image. However, this does not appear in the THz image because V_{THz} oscillates over a large voltage window and might average out this change in the LDOS. Furthermore, when the tip retracts over the defect, the THz-induced current decreases, which is shown as a depression in the THz image.

6.2 Optical pump-THz probe on a SWCNT

At one point during this work, an optical pump-THz probe experiment was attempted on a SWCNT to study its carrier dynamics. Although it was not successful, it helped identify an underlying problem in the system. The experiment was performed as follows, the amplitude of the THz field was set to be very close to the I_{THz} onset of the substrate, in this case $E_{\mathrm{THz,pk}} = +247\,\mathrm{V/cm}$. Fig. 3.1 shows the optical setup that modifies the temporal delay ($\Delta\tau$) between an ultrafast optical pump pulse and the THz pulse, with a motorized delay stage. To find the delay ($\Delta\tau_0$) where the optical pump pulse overlapped in time with the THz pulse peak at the junction, I_{THz} was monitored while $\Delta\tau$ was swept. This measurement was performed with the tip on the Au(111) substrate and on a SWCNT, as shown in Fig. 6.7. On the left side of the plot, the optical pump pulse arrives before the THz pulse; and the right side of the plot shows when the THz pulse arrives first.

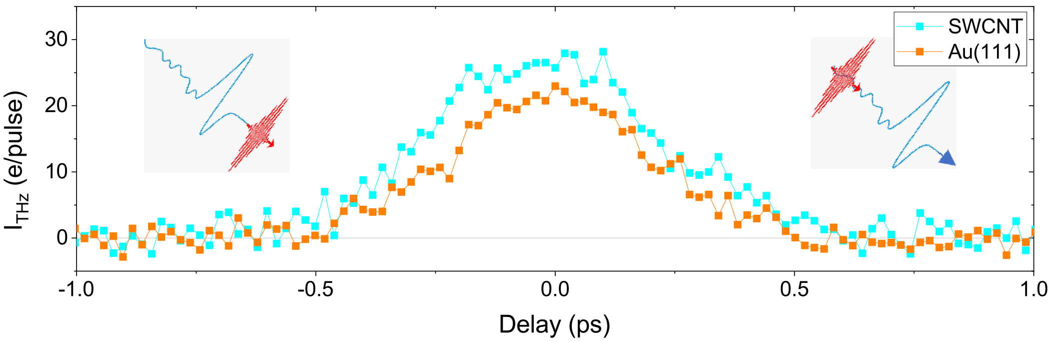

Figure 6.7: I_{THz} as a function of time delay $\Delta\tau$ between the optical pump pulse and the THz pulse. Measurement was acquired with the STM tip on top of a SWCNT and on Au(111), with $I_{\mathrm{DC}} = 5\,\mathrm{pA}$, $V_{\mathrm{DC}} = +1.5\,\mathrm{V}$, $E_{\mathrm{THz,pk}} = +247\,\mathrm{V/cm}$, $P_{\mathrm{pump,avg}} = 12\,\mathrm{mW}$ and a p-polarized pump beam.

The fact that the pump-probe signal increased evenly on the SWCNT and substrate suggested that some other mechanism might have been at play. This was confirmed by monitoring the tunneling current over time on the Au surface, with the optical pump beam on and the THz beam off, as shown in Fig. 6.8a. At time 0 s, $V_{\mathrm{DC}} = +3\,\mathrm{V}$, $P_{\mathrm{pump,avg}} = 12\,\mathrm{mW}$, the current setpoint was +5 pA and the feedback loop was turned off to keep the tip height fixed. With these settings, I_{DC} stayed around 5 pA as expected. The data points above 10 pA are just current spikes produced by sudden tip changes. Then V_{DC} was gradually decreased to 0 V from time 6 s to 8 s. In the absence of V_{DC}, a negative current of −38 pA was produced solely by the optical pump laser pulses, which meant that electrons were being photoemitted from the sample to the tip. This photoemission current would be modulated by the THz fields when they are present; therefore, the recorded I_{THz} signal during a pump-probe experiment contains both the actual pump-probe tunneling current and this unwanted photoemission current, which made it impossible to isolate the tunneling current.

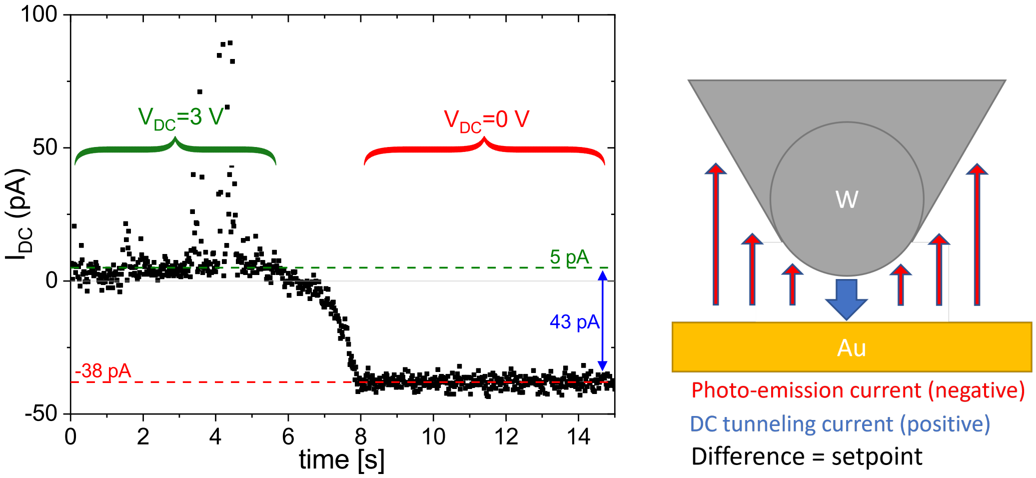

(a) (b)

Figure 6.8: Photoemission current induced by the optical pump pulses with a W tip on the Au(111) surface. a) STM DC current as a function of time with a starting point set by $I_{\mathrm{DC}} = 5\,\mathrm{pA}$, $V_{\mathrm{DC}} = 3\,\mathrm{V}$, $P_{\mathrm{pump,avg}} = 12\,\mathrm{mW}$, THz pulses off and the feedback loop is turned off at time 0 s. At around 6 s, V_{DC} was gradually decreased to 0 V. A photoemission current of −38 pA was found in the absence of V_{DC}. b) STM junction diagram illustrating the competition between tunneling (blue) and photoemission (red) currents.

As illustrated in Fig. 6.8b, when the STM was operating with a positive V_{DC}, optical pump pulses and with the feedback loop on, the positive tunneling DC current and the negative photoemission current competed with each other to reach the defined current setpoint, which in this case forced the tip to get closer to the sample to produce a larger tunneling current. Smaller distances can produce a large transient THz field that can easily damage the sample. On the other hand, if the current setpoint was set to be negative such as $-5\,\mathrm{pA}$, for example, that would force the tip to fully retract, since the photoemission current ($-38\,\mathrm{pA}$) would be larger than the setpoint at all tip heights. A negative set point higher than the photoemission current would be required to perform an experiment but the undesired photoemission from the sample would always be present. The average optical pump power was reduced in an attempt to minimize the photoemission from the sample, but the tunneling I_{THz} pump-probe signal could not be found. An alternative approach could be to reduce the sample area being illuminated by the optical pump pulses and concentrate the beam at the junction; however, our beam spot size was already at its best and was limited by the setup arrangement. Therefore, the remaining option was to investigate this photoemission current at the junction to find a way to eliminate it from the substrate. This would enable the recording of the tunneling I_{THz} pump-probe signal from the sample in question on its own. The study of photoemission currents from metal substrates at the STM junction is presented in Chapter 7, and an alternative substrate candidate for pump-probe experiments using semiconductors to suppress sample photoemission is presented in Chapter 8.

Chapter 7

Photoemission from metals in STM

The STM offers the flexibility to perform a variety of electro-optic experiments. One example is the electron emission induced by ultrafast optical pulses illuminating the STM junction. This electron emission can additionally be modulated by the electric field of a single-cycle THz pulse [51], as stated in Section 3.3.5. The photoelectric emission is sometimes undesirable for optical pump-THz probe STM experiments, as was found in Section 6.2. However, it also provides a way to measure the THz near-fields at the apex of an STM tip, which is becoming a common practice among the THz-STM community [39, 42, 51]. Nonetheless, some aspects of this experimental technique are still unclear and need further investigation.

7.1 Photoemission from a gold tip on a gold substrate

A gold tip on a gold sample is one of the simplest configurations to perform experiments in the STM, and it served as the basis to study photoemission. First, the photoemission current dependence on bias voltage, $I_{\mathrm{PE,DC}} - V_{\mathrm{DC}}$ curve, was obtained with the tip 500 nm away from the sample, and an 800 nm optical pump beam polarized perpendicular to the tip axis, with 9 mW of average power and centered at the STM junction. The STM feedback loop was off and the bias voltage was varied from -8 to 8 V, as shown in Fig. 7.1a. The photoemission current is mostly positive, which means that electrons flow from the tip to the sample, even in the absence of a DC bias voltage. This is expected because of the confinement and enhancement of the optical field at the tip apex, which produces larger photoemission currents compared to the flat surface of the substrate [231]. This fact is explained by the energy diagram in Fig. 7.1b, where the potential barrier at the Au-vacuum interface is shown for $P_{\mathrm{pump,avg}} = 9\,\mathrm{mW}$, a laser repetition rate of $f_{\mathrm{rep}} = 250\,\mathrm{kHz}$, a pulse temporal width of

$t_{\text{pump}} = 70\,\text{fs}$, and a beam spot diameter of $216\,\mu\text{m}$. The potential barrier is calculated for three different cases: in the absence of electric fields (gray), which is the reference case; with the incident field amplitude $E_{\text{pump,pk}}$ (orange), which is the case of the sample surface; and with the enhanced field $E_{\text{pump,pk,enh}}$ (red), which is the case of the tip apex with an enhancement factor of 15 [103, 105, 232, 233]. Even though the potential barrier is lowered considerably, it is not enough to induce field emission. The electron emission mechanism will be explored later, however, the energy diagram illustrates how electron emission would be favored at the tip apex, even in the absence of V_{DC}.

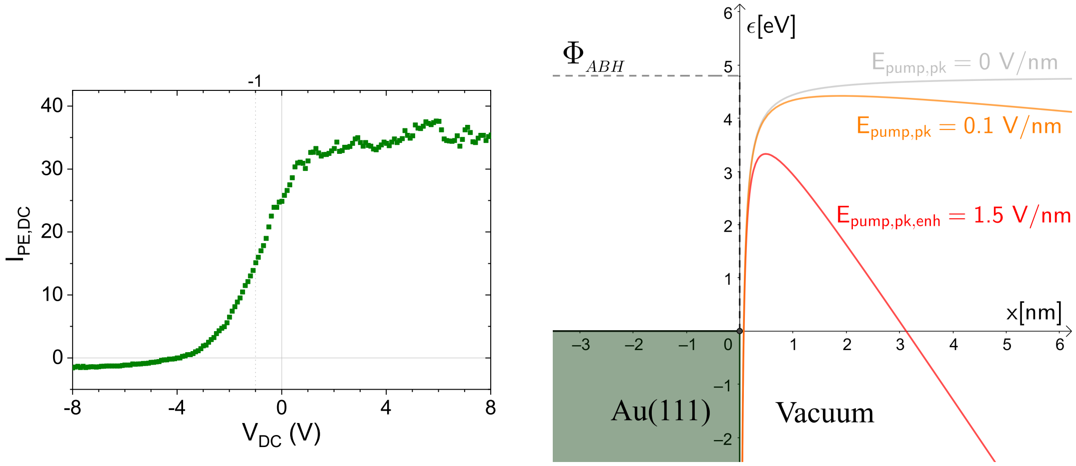

(a) (b)

Figure 7.1: Electron emission at the STM junction with a gold tip on an Au(111) surface. a) $I_{\text{PE,DC}} - V_{\text{DC}}$ curve acquired with the tip 500 nm away from the sample, $E_{\text{THz,pk}} = 0\,\text{V/cm}$ and the 800 nm optical pump beam ($P_{\text{pump,avg}} = 9\,\text{mW}$) centered at the STM junction with a polarization perpendicular to the tip axis. A linear region can be found from $-3\,\text{V}$ to $+1\,\text{V}$. b) Energy diagram that illustrates the reduced potential barrier at the tip apex (red) compared to the Au(111) surface (orange). Potential barrier calculated with $P_{\text{pump,avg}} = 9\,\text{mW}$, $f_{\text{rep}} = 250\,\text{kHz}$, $t_{\text{pump}} = 70\,\text{fs}$, a beam spot diameter of $216\,\mu\text{m}$, and an enhancement factor of 15 at the tip apex.

A photoemission $I_{\text{PE,DC}} - V_{\text{DC}}$ curve, similar to Fig. 7.1a, was taken by Yoshida [39] with a PtIr-coated tungsten tip $1\,\mu\text{m}$ away from HOPG, where the photoemission is mostly positive. On the left side of our plot, the photoemission from the tip is suppressed by the negative voltage, and even a small negative photoemission from the sample was recorded when $V_{\text{DC}} < -4\,\text{V}$. On the right side, $I_{\text{PE,DC}}$ seems to reach a saturation level, which is caused by a lensing phenomenon where V_{DC} is large enough to capture all the electrons emitted away from the tip [234]. The region between $-3\,\text{V}$ and $+1\,\text{V}$ shows a linear response and presents a large change in $I_{\text{PE,DC}}$ for a given voltage change, which is desired to sample the THz waveform using the photoemission technique. A bias voltage of $-1\,\text{V}$, which is close to the center of this region, was set to sample the THz waveform.

The THz beam was then centered at the STM junction with an electric field of $E_{\text{THz,pk}} = 400\,\text{V/cm}$ at the pulse peak. The THz-induced photoemission current $I_{\text{PE,THz}}$ as a function of delay time $\Delta\tau$ between the optical pump pulse and the THz pulse, is shown in green in Fig. 7.2. The bias voltage was set to $V_{\text{DC}} = -1\,\text{V}$, expecting that the transient V_{THz} modulation would vary within a linear region of the $I_{\text{PE,DC}} - V_{\text{DC}}$ curve. This way, $I_{\text{PE,THz}}$ can potentially provide a measurement of the near-field waveform at the tip apex. The THz pulse electric field waveform obtained by EOS outside the chamber is also shown in red; even though their amplitude and units are different, both signals have been normalized here for comparison. The spectral content of both waveforms is also presented in Fig. 7.3.

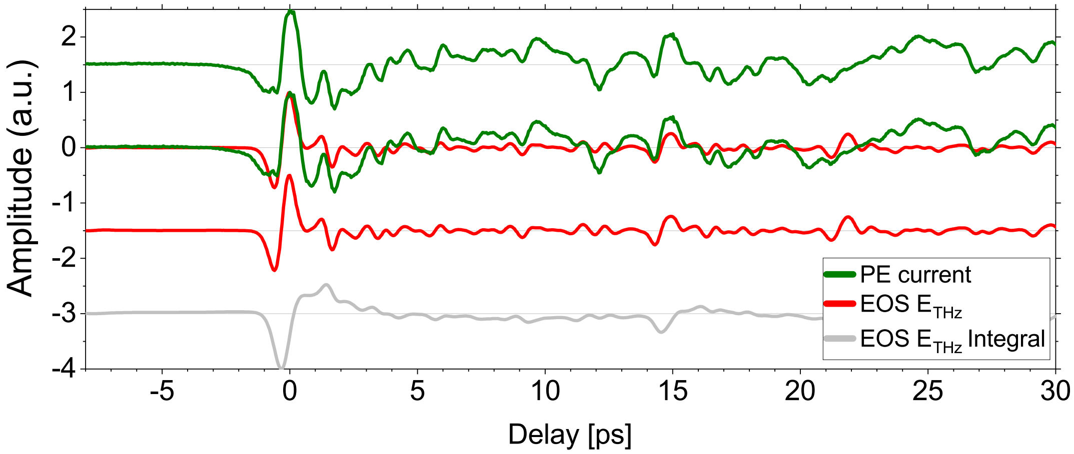

Figure 7.2: Normalized THz-induced photoemission current $I_{\text{PE,THz}}$ (green) as a function of delay time $\Delta\tau$ between the optical pump pulse and the THz pulse. The data was acquired with $z = 500\,\text{nm}$, $V_{\text{DC}} = -1\,\text{V}$, $E_{\text{THz,pk}} = 400\,\text{V/cm}$, $P_{\text{pump,avg}} = 4.6\,\text{mW}$ and with a gold tip on an Au(111) sample at room temperature. The PE waveform is assumed to be the near field at the tip apex. The THz pulse measured by EOS is also shown in red, which is assumed to be the far field. The two waveforms are shown overlapped in the middle for an easy comparison with each other. The integral of the EOS waveform (gray) is also shown at the bottom.

One can clearly see that the two waveforms are different. It has previously been assumed [37, 41] that the near-field waveform at the tip apex was similar to the one measured in free-space by EOS. However, antenna coupling theory predicts that the induced current at the junction would be proportional to the integral of the incident electric field [115], but integrating the EOS waveform does not reproduce the $I_{\text{PE,THz}}$ waveform, as shown in Fig. 7.2. Finite element analysis simulations have also been

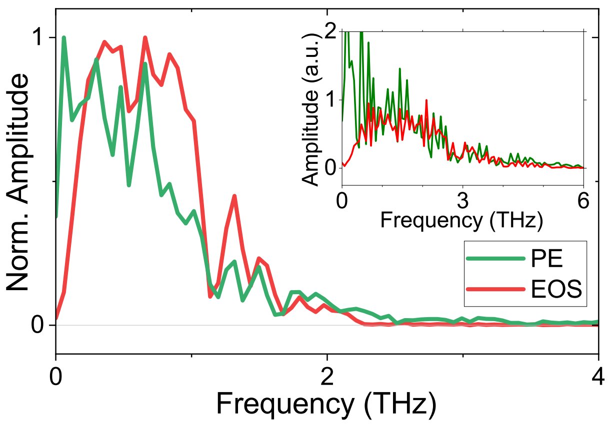

Figure 7.3: The spectral content of the PE and EOS waveforms shown in Fig.7.2, where only the data below 12 ps was used to exclude the reflections. The spectrum of the full waveforms is shown in the inset.

performed [33] to explore what the near-field waveform would be. However, there are many variables at play and this is still a research field under investigation.

One variable that can change the photoemission waveform is the position of the optical pump beam. Fig. 7.4 shows a set of waveforms obtained with a tip height of $z = 400\,\mathrm{nm}$, $V_{\mathrm{DC}} = 8\,\mathrm{V}$, $E_{\mathrm{THz,pk}} = -330\,\mathrm{V/cm}$ and $P_{\mathrm{pump,avg}} = 4\,\mathrm{mW}$; where the pump beam was initially positioned at the center of the STM junction and then incrementally moved up along the tip shaft for each measurement. It has previously been shown that photoemission from a tip illuminated with ultrafast laser pulses occurs mainly at the tip apex [153]. When the pump beam is at the junction, the $I_{\mathrm{PE,THz}}$ waveform resembles a single-cycle THz pulse, but as it moves up the tip axis, the signal is almost completely suppressed at a point in the middle of the shank of the tip. A possible explanation is that the tip does not have any discontinuities in the middle of the shank to generate surface plasmons that would travel to the tip apex to induce electron emission. The signal then reappears as the pump beam reaches the tip cusp, where the pump beam can presumably generate plasmons, but its waveform has been drastically modified, and it even seems to be inverted. As the pump beam moves up the shaft, the waveforms present a small shift in time, which could be the time it takes for the plasmon to travel from the illumination point to the tip apex. A temporal delay of $\sim 1.7\,\mathrm{ps}$ was estimated between the first and last waveform, as pointed out with black arrows in Fig. 7.4. The total distance from the highest point on the tip shaft to the junction was roughly estimated to be $\sim 0.5\,\mathrm{mm}$ using the picture on the right as reference. This results in a velocity of $0.98\,c$, which agrees reasonably well with a plasmon group velocity on gold, which has been measured to be 0.95 c [235]. Finally, when the pump beam is far away from the tip apex and cusp, the $I_{\mathrm{PE,THz}}$ signal vanishes, as expected. In this example, the pump beam spot size is large (216 μm) and it was moved long distances, but the position of the pump beam will be critical when the spot size is small, since a slight variation in position can have a large impact on the measured waveform.

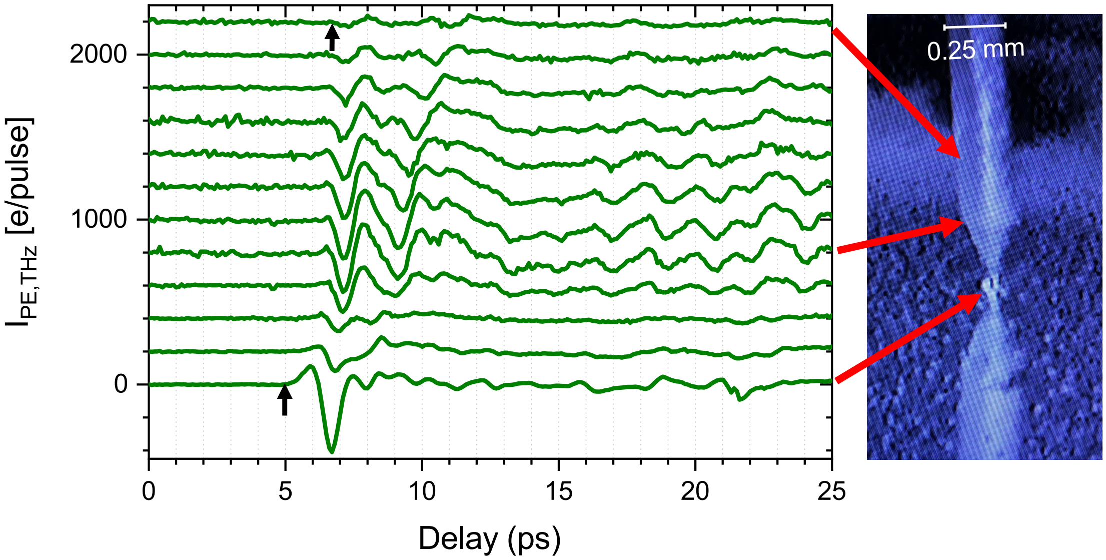

Figure 7.4: $I_{\mathrm{PE,THz}}$ as a function of delay time $\Delta\tau$ with the pump beam at different positions along the vertical axis of the tip shaft. The waveforms were acquired with a gold tip on an Au(111) substrate, $z = 400\,\mathrm{nm}$, $V_{\mathrm{DC}} = 8\,\mathrm{V}$, $E_{\mathrm{THz,pk}} = -330\,\mathrm{V/cm}$ and $P_{\mathrm{pump,avg}} = 4\,\mathrm{mW}$. A photograph of the STM tip is shown on the right for reference.

It should be noted that for this experiment, $V_{\mathrm{DC}} = 8\,\mathrm{V}$, which marks a region in the $I_{\mathrm{PE,DC}} - V_{\mathrm{DC}}$ curve where $I_{\mathrm{PE,DC}}$ is supposed to be saturated, and a modulation of V_{DC} should not produce a change in $I_{\mathrm{PE,DC}}$. However, the modulation induced by V_{THz} did produce an $I_{\mathrm{PE,THz}}$ current that mapped out the temporal profile of the THz fields. This suggests that the transient photoemission currents do not strictly follow the static $I_{\mathrm{PE,DC}} - V_{\mathrm{DC}}$ curve acquired with V_{DC}. A THz field assisted photoemission $I_{\mathrm{PE,THz}} - V_{\mathrm{DC}}$ curve can be obtained by setting the temporal delay at $\Delta\tau_0$ and sweeping V_{DC}. However, the tilt of the potential barrier in vacuum depends on the amplitude of the THz fields, and the $I_{\mathrm{PE,THz}} - V_{\mathrm{DC}}$ curves would be different for different $E_{\mathrm{THz,pk}}$ values. This approach could not be generalized and would depend on the $E_{\mathrm{THz,pk}}$ and $P_{\mathrm{pump,avg}}$ values, on a case-by-case basis. Nevertheless, it will be shown later that this approach is not accurate either. Therefore, an $I - V$ curve to describe the photoemission transient response is still not fully defined and requires more detailed investigation.

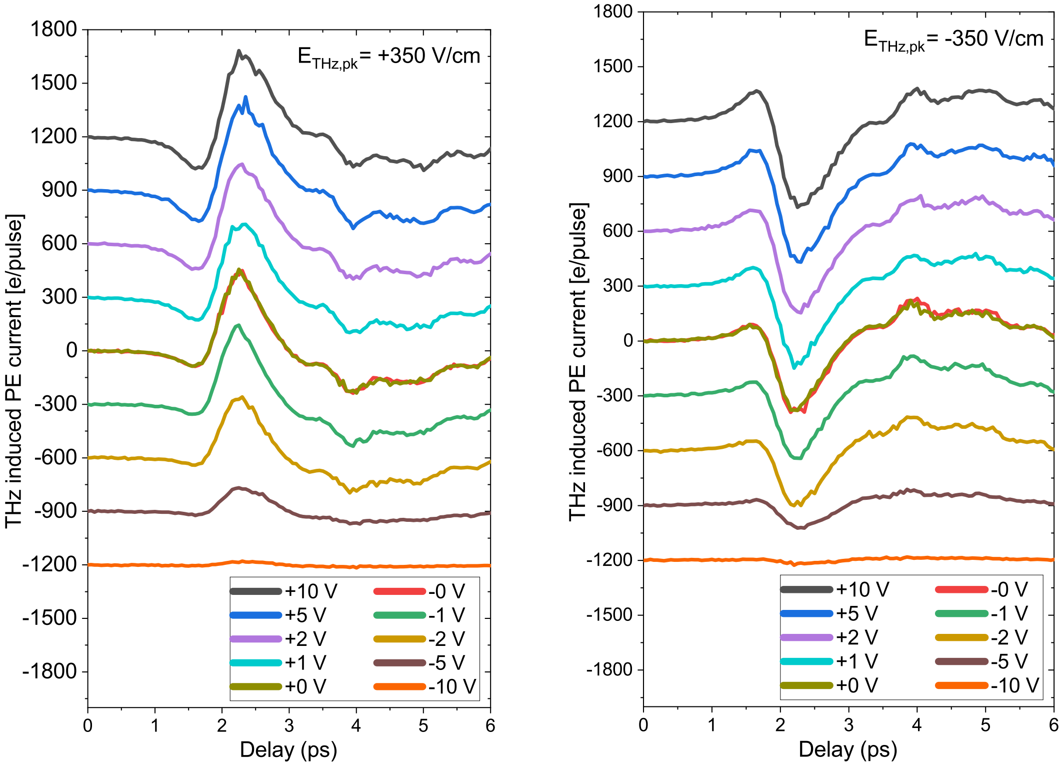

(a) (b)

Figure 7.5: Photoemission waveforms obtained at different V_{DC} values, with an Au tip on an Au(111) substrate, where $z = 500\,\mathrm{nm}$ and $P_{\mathrm{pump,avg}} = 14.6\,\mathrm{mW}$ with the pump beam linearly polarized perpendicular to the tip axis. The two plots show the cases where a) $E_{\mathrm{THz,pk}} = +350\,\mathrm{V/cm}$ and b) $E_{\mathrm{THz,pk}} = -350\,\mathrm{V/cm}$. Both $+0\,\mathrm{V}$ and $-0\,\mathrm{V}$ are plotted just to confirm they are the same when the STM controller switches the polarity of V_{DC}.

Another variable that can change the photoemission waveform is the bias voltage V_{DC}. Fig. 7.5 shows two sets of waveforms obtained with an Au tip on an Au(111) substrate, where $z = 500\,\mathrm{nm}$, $P_{\mathrm{pump,avg}} = 14.6\,\mathrm{mW}$ and the pump beam linear polarization was perpendicular to the tip axis. The left and right plots show the cases where $E_{\mathrm{THz,pk}}$ was $+350\,\mathrm{V/cm}$ and $-350\,\mathrm{V/cm}$, respectively. As V_{DC} becomes negative, it filters out the electrons photoemitted from the tip with lower energy. As it gets more negative, the $I_{\mathrm{PE,THz}}$ waveform amplitude becomes smaller and some of the fine features get lost. This suggests that a more accurate representation of the THz near fields at the tip apex will be obtained when V_{DC} is more positive, which suppresses the sample current and favors the one from the tip. V_{DC} should at least be higher than the maximum modulation amplitude of V_{THz}. But one also has to verify that the $I_{\mathrm{PE,THz}}$ response to V_{THz}, using a specific V_{DC} voltage, is linear within the V_{THz} amplitude range. A new way to find the linear regimes of the photoemission response to the THz fields is needed, because, as mentioned before, it is not correlated to the $I_{\mathrm{PE,DC}} - V_{\mathrm{DC}}$ curve, and it will be demonstrated below that it is not correlated to $I_{\mathrm{PE,THz}} - V_{\mathrm{DC}}$ either.

From the two sets of data, the absolute peak amplitude of the waveforms was extracted and plotted as a function of V_{DC}, which is shown in Fig. 7.6a. The two cases, $+350\,\mathrm{V/cm}$ and $-350\,\mathrm{V/cm}$, produce very similar waveform peak amplitudes within the -10 to $10\,\mathrm{V}$ range, except for a few points where the positive $E_{\mathrm{THz,pk}}$ generates a slightly larger peak amplitude. A normalized version of this data is shown in Fig. 7.6b. In addition to those points, a normalized $I_{\mathrm{PE,DC}} - V_{\mathrm{DC}}$ and $I_{\mathrm{PE,THz}} - V_{\mathrm{DC}}$ curves have been superimposed to show that the waveform peak amplitude points do not follow these curves either. These curves were acquired on a different day with $z = 500\,\mathrm{nm}$, $P_{\mathrm{pump,avg}} = 9\,\mathrm{mW}$, $E_{\mathrm{THz,pk}} = -360\,\mathrm{V/cm}$ and with the pump and THz beams positioned at the junction. The THz-induced photoemission current dependence on V_{DC} has not been fully characterized and requires further investigation.

Even though $I_{\mathrm{PE}} - V_{\mathrm{DC}}$ curves cannot predict $I_{\mathrm{PE,THz}}$ directly, they can still be useful to examine the photoemission currents, in the absence of a THz pulse, to identify the underlying mechanisms producing it. Fig. 7.7a shows multiple $I_{\mathrm{PE,DC}} - V_{\mathrm{DC}}$ curves that were acquired at different optical pump powers, using a gold tip $500\,\mathrm{nm}$ away from the Au(111) substrate. All curves present the same saturation mentioned before, which occurs when the positive V_{DC} is large enough to capture all electrons emitted from the tip. To study the I_{PE} dependence on pump power, the average of the three closest points to $-9\,\mathrm{V}$, $-6\,\mathrm{V}$, $-3\,\mathrm{V}$, $0\,\mathrm{V}$, $3\,\mathrm{V}$, $6\,\mathrm{V}$ and $9\,\mathrm{V}$, were extracted from each measurement and are presented with square symbols in a logarithmic plot in Fig. 7.7b.

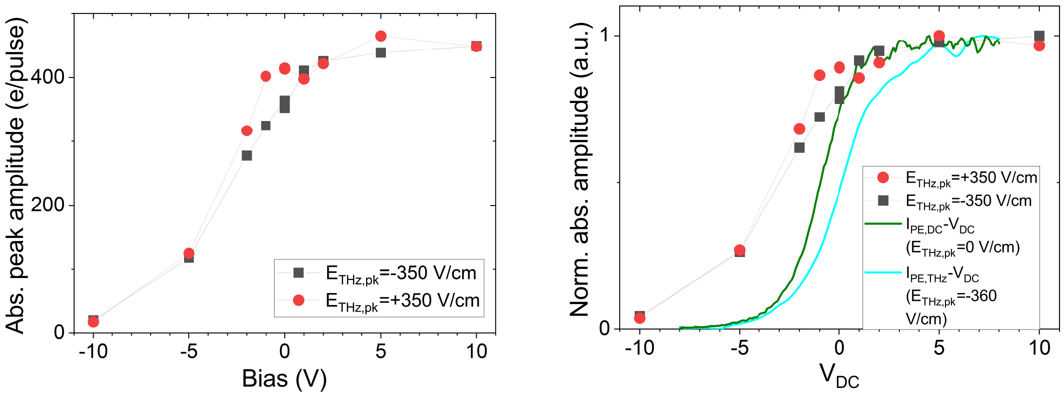

(a) (b)

Figure 7.6: a) Absolute peak amplitude of the waveforms from Fig. 7.5, as a function of V_{DC}. The squares and circles represent $E_{\mathrm{THz,pk}} = -350\,\mathrm{V/cm}$ and $E_{\mathrm{THz,pk}} = +350\,\mathrm{V/cm}$, respectively. b) Normalized data from (a) compared with normalized $I_{\mathrm{PE,DC}} - V_{\mathrm{DC}}$ (green solid line) and $I_{\mathrm{PE,THz}} - V_{\mathrm{DC}}$ (blue solid line) curves.

From the electron emission mechanisms mentioned in Section 2.4.1, we can immediately disregard the field emission caused by the DC bias fields, because the effective electric field at the tip apex from a few volts of V_{DC}, would be negligible when the tip is 500 nm away from the sample. And we can also discard the direct photoelectric emission, since the photon energy of the pump (1.55 eV) is smaller than the work function of gold ($\sim$ 5 eV). Therefore, thermionic emission, optical field emission, and multiphoton photoemission are the remaining possible candidates. In Fig. 7.7c, the data for the case when $V_{\mathrm{DC}} = 0\,\mathrm{V}$, was fitted with the current density equations of these three mechanisms, which as a function of average pump power P_{avg} have the form

$$J \propto A_{\mathrm{TE}}(P_{\mathrm{avg}})^2 \exp\left(\frac{-B_{\mathrm{TE}}}{P_{\mathrm{avg}}}\right), \tag{7.1}$$

$$J \propto A_{\mathrm{FE}} P_{\mathrm{avg}} \exp\left(\frac{-B_{\mathrm{FE}}}{\sqrt{P_{\mathrm{avg}}}}\right), \tag{7.2}$$

$$J \propto A_{\mathrm{MPP}}(P_{\mathrm{avg}})^n, \tag{7.3}$$

respectively, for thermionic emission, optical field emission and multiphoton photoemission, where the following substitutions were made: $T \propto \epsilon_{\mathrm{pulse}} \propto P_{\mathrm{avg}}$, $E \propto E_{\mathrm{pk}} \propto \sqrt{P_{\mathrm{avg}}}$ and $I_{\mathrm{pk}} \propto P_{\mathrm{avg}}$, where T is temperature, $\epsilon_{\mathrm{pulse}}$ is pump pulse energy, E is electric field, E_{pk} is peak electric field, and I_{pk} is peak intensity. To support the analysis, the typical experimental parameters used in our experiments are presented in Table 7.1, where a laser repetition rate of $f_{\text{rep}} = 250\,\text{kHz}$, a pulse temporal width of $t_{\text{pump}} = 70\,\text{fs}$, and a beam spot diameter of $216\,\mu\text{m}$ were used for the calculations.

Average power [mW] P_{avg}	1	5	10	20	40
Energy per pulse [nJ] $\epsilon_{\text{pulse}} = \dfrac{P_{\text{avg}}}{f_{\text{rep}}}$	4	20	40	80	160
Peak power [W] $P_{\text{pk}} = \dfrac{\epsilon_{\text{pulse}}}{t_{\text{pump}}}$	5.7×10^4	2.9×10^5	5.7×10^5	1.1×10^6	2.3×10^6
Peak intensity [W/cm^2] $I_{\text{pk}} = \dfrac{P_{\text{pk}}}{A_{\text{area}}}$	1.6×10^8	7.8×10^8	16×10^8	3.1×10^9	6.2×10^9
Peak electric field [V/nm] $E_{\text{pk}} = \sqrt{\dfrac{2I_{\text{pk}}}{\varepsilon_0 c}}$	0.03	0.08	0.11	0.15	0.22
Fluence [mJ/cm^2] $H = \dfrac{\epsilon_{\text{pulse}}}{A_{\text{area}}}$	1.1	5.5	10.9	22	43.7

Table 7.1: Table with typical values of the optical excitation used for the experiments.

Electrons gain energy when an incident laser pulse is incident on a material, and their energy is redistributed via electron-electron and electron-phonon scattering on a $10 - 100\,\text{fs}$ time scale, to form a Fermi-Dirac distribution [47]. Thermionic emission occurs when electrons at the high energy tail of this electron distribution overcome the potential barrier and are emitted into vacuum. Since the time duration of the pump pulse is 70 fs, the Fermi-Dirac distribution could be formed within this time, and thermionic emission could potentially occur. However, in a theoretical work [236], the threshold for thermionic emission in a 100 nm Au film has been estimated to occur at a fluence of $100\,\text{mJ/cm}^2$ for 100 fs pulses. The effect of thermionic emission has also been observed experimentally from nanometric tips at peak intensities of $10^{11}\,\text{W/cm}^2$[47]. When these numbers are compared with the values in Table 7.1, one can conclude that thermionic emission from the laser intensities in our experiments

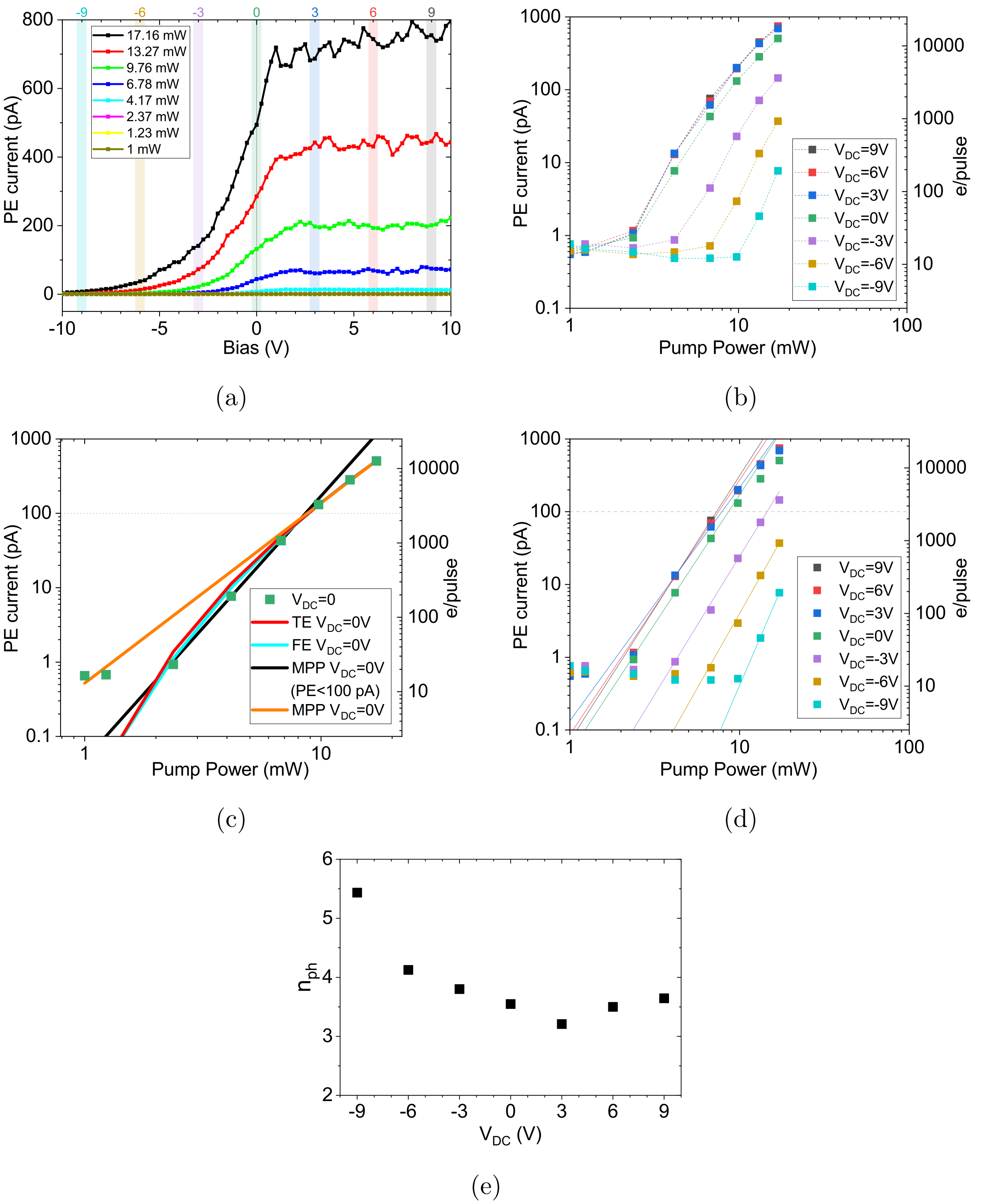

Figure 7.7: a) $I_{\mathrm{PE,DC}} - V_{\mathrm{DC}}$ curves, acquired at different excitation pump powers, with an Au tip 500 nm away from the Au(111) substrate. b) From each measurement, the average of the three closest points to -9 V, -6 V, -3 V, 0 V, 3 V, 6 V and 9 V, was extracted and is presented with square symbols as a function of pump power. c) The case when $V_{\mathrm{DC}} = 0$ V is shown as an example, to fit the experimental data with the current density equations (Eqs. (7.1) to (7.3)) of thermionic emission (TE), optical field emission (FE) and multiphoton photoemission(MPP). The fit parameters are A_{TE}, B_{TE}, A_{FE}, B_{FE} and A_{MPP}, respectively. d) MPP fits (solid lines) to the experimental data (squares) from (b). e) Number of photons n_{ph}, nonlinearity extracted from the MPP fits in (d) as a function of V_{DC}.

would not be probable. Furthermore, the thermionic emission fit in Fig. 7.7c would require temperatures of $25,000 - 180,000\,\mathrm{K}$ which are too high compared to electron temperatures reported previously in similar experiments. Therefore, thermionic emission will be omitted as a possible mechanism in our experiments.

For optical field emission to occur, peak electric fields of $\sim 5\,\mathrm{V/nm}$ are typically required, but only $0.22\,\mathrm{V/nm}$ fields are reached from the optical excitation with $P_{\mathrm{pump,avg}} = 40\,\mathrm{mW}$. We can also consider the field enhancement at the tip apex which is typically ~ 15 [103, 105, 232, 233]. Optical field emission is usually identified when the Keldysh parameter is smaller than unity. The Keldysh parameter as a function of $P_{\mathrm{pump,avg}}$ with a field enhancement of 15 (Fig. 7.8) indicates that field emission would not occur even with $P_{\mathrm{pump,avg}} = 80\,\mathrm{mW}$. Furthermore, even though the optical field emission fit in Fig. 7.7c seems to fit the data well, the fit parameter values required for this fit are not close to the actual experimental parameters and are unrealistic. Therefore, optical field emission will also be omitted as the main emission mechanism in our experiments, even though the pump pulse fields lower the potential barrier considerably, as shown in Fig. 7.1b.

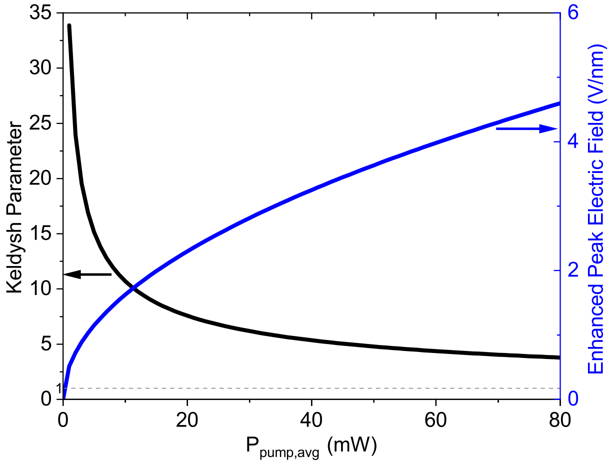

Figure 7.8: Keldysh parameter (left-black axis) and enhanced peak electric field (right-blue axis) as a function of $P_{\mathrm{pump,avg}}$ calculated with $f_{\mathrm{rep}} = 250\,\mathrm{kHz}$, $t_{\mathrm{pump}} = 70\,\mathrm{fs}$, a beam spot diameter of $216\,\mu\mathrm{m}$, and an enhancement factor of 15.

Multiphoton remained as the main mechanism of electron emission; however, one can see in Fig. 7.7c that the data does not completely follow the straight line expected from the multiphoton nonlinearity. It was found that in all cases, the data starts to deviate from a straight line when $I_{\mathrm{PE,DC}}$ exceeds $\sim 100\,\mathrm{pA}$, which can be observed in Fig. 7.7d. This can be attributed to space charge effects. For currents of more than one electron per pulse, space charge effects will take place, however, due to the experimental setup geometry, these effects are not observable here until currents of 100 pA are reached, which translates into 2500 electrons/pulse. In our STM, the sample, the sample holder and the sample stage are all connected to the same potential, therefore, space charge effects need to be large enough to deviate electrons from being collected by the sample stage to be noticeable. Additionally, one can see that in the saturation region of the black curve in Fig. 7.7a, the collected PE current slightly increases as the positive V_{DC} increases, because a more positive potential can collect more of the electrons that were deviated by space charge. This only becomes noticeable when the $I_{\mathrm{PE,DC}}$ is large, which agrees with space charge effects. Therefore, only data where $I_{\mathrm{PE,DC}} < 100\,\mathrm{pA}$ was used to produce the fits shown in Fig. 7.7d. The slope of these fits is an indication of the number of photons (n_{ph}) being absorbed to produce the electron emission, which is plotted as a function of V_{DC} in Fig. 7.7e. The work function of gold is $\sim 5\,\mathrm{eV}$, which would require the energy of 3.2 (1.55 eV) photons to overcome the potential barrier, which is consistent with this plot. The value of n_{ph} technically remains the same for positive values of V_{DC}, but increases when V_{DC} is negative. Electrons emitted into vacuum from the tip via MPP have an energy distribution [153]. A negative potential at the sample will only allow electrons with higher energies to be collected. Higher energy means those electrons absorbed a higher number of photons, which explains the increase of n_{ph} when V_{DC} is negative. Similar results have been previously reported from a tungsten tip [237].

7.2 Photoemission from a tungsten tip on a gold substrate

STM gold tips offer a large field enhancement, good electrical properties, and are ideal for ambient STM studies, since they do not oxidize when exposed to air. Unfortunately, they are soft and get structurally modified or damaged very easily. Tungsten tips, on the other hand, have great strength and good electrical and thermal conductivity. Tungsten is the pure metal with the highest melting point (3422 °C) and the lowest thermal expansion coefficient ($4.5 \times 10^{-6}\,\mathrm{K}^{-1}$ at 25 °C) [238], which makes them ideal for STM studies in general, as long as they are performed in vacuum. The same set of measurements acquired with a gold tip in the previous section were also performed with a tungsten tip to compare their photoemission currents. These 2 sets of measurements were acquired with only one day difference, therefore, the sample and the equipment settings were all the same, the STM tip was the only thing that was replaced.

A set of $I_{\mathrm{PE,DC}}-V_{\mathrm{DC}}$ curves was first obtained (Fig.7.9a) from a tungsten tip 500 nm away from the Au(111) surface at different pump power values. It can be immediately noticed that the negative photoemission (electrons emitted from the sample) when V_{DC} is negative has almost the same magnitude as the positive photoemission current (electrons emitted from the tip) when V_{DC} is positive. A similar-looking $I_{\mathrm{PE,DC}} - V_{\mathrm{DC}}$ curve, taken with a tungsten tip $1\,\mu$m away from a silver sample, was presented by Muller [42], where it was stated that the negative photoemission current is present because the sample is also photoexcited by the ultrafast pulses. The fact that this plot differs from the one reported by Yoshida [39] already shows the variation of these measurements reported in the literature, which cannot be directly compared one to one and should be used with care since they strongly depend on the experimental settings.

One can first compare the magnitude of the photoemission currents from the tungsten tip (Fig.7.9a) and the gold tip (Fig.7.7a), for the case when $V_{\mathrm{DC}} = 10\,\mathrm{V}$ and $P_{\mathrm{pump,avg}} \approx 17\,\mathrm{mW}$. The emission from the gold tip is 2 orders of magnitude larger. Gold tips have a field enhancement at the apex around 4 times larger than tungsten [103, 105], which does not explain the 2 orders of magnitude difference observed. However, a thin layer of a few nm thick oxide is always formed on the surface of the tungsten tips during the etching process. This layer is mainly tungsten trioxide (WO_3) which is typically removed by heating the tip via electron bombardment. Due to the field enhancement at the apex of the tip, this technique mainly heats and removes the WO_3 from the apex, leaving the rest of the tip surface covered with oxide. WO_3 has an indirect bandgap that has experimentally been measured to be between 2.5 and 3.2 eV [239, 240], which would reduce the multiphoton emission from the oxide area. Therefore, the positive photoemission from the tungsten tip (Fig. 7.9a) is being produced mainly from a small region at the apex of the tip, which would explain why it is 2 orders of magnitude smaller than gold. A smaller beam spot size that only illuminates the clean region of the tungsten tip apex would be required to properly compare one to one the photoemission from the W and Au tips.

The fact that the photoemission from the tungsten tip is small, in this case, allows us to observe that there is also a photoemission contribution from the sample, which can be observed as V_{DC} goes negative. Similar to the previous section, the $I_{\mathrm{PE,DC}} - V_{\mathrm{DC}}$ curves for different excitation pump powers are plotted in Fig. 7.9b. The case where $V_{\mathrm{DC}} = 0\,\mathrm{V}$, was used as reference to fit the data with the multiphoton, thermionic, and field emission equations (Fig. 7.9c), where multiphoton emission gives the most accurate fit. The multiphoton fits for all the data points are presented in Fig. 7.9d. It should be noted that space charge effects were not observed in these measurements, because the $I_{\mathrm{PE,DC}}$ magnitude remained below 100 pA, even at the highest excitation

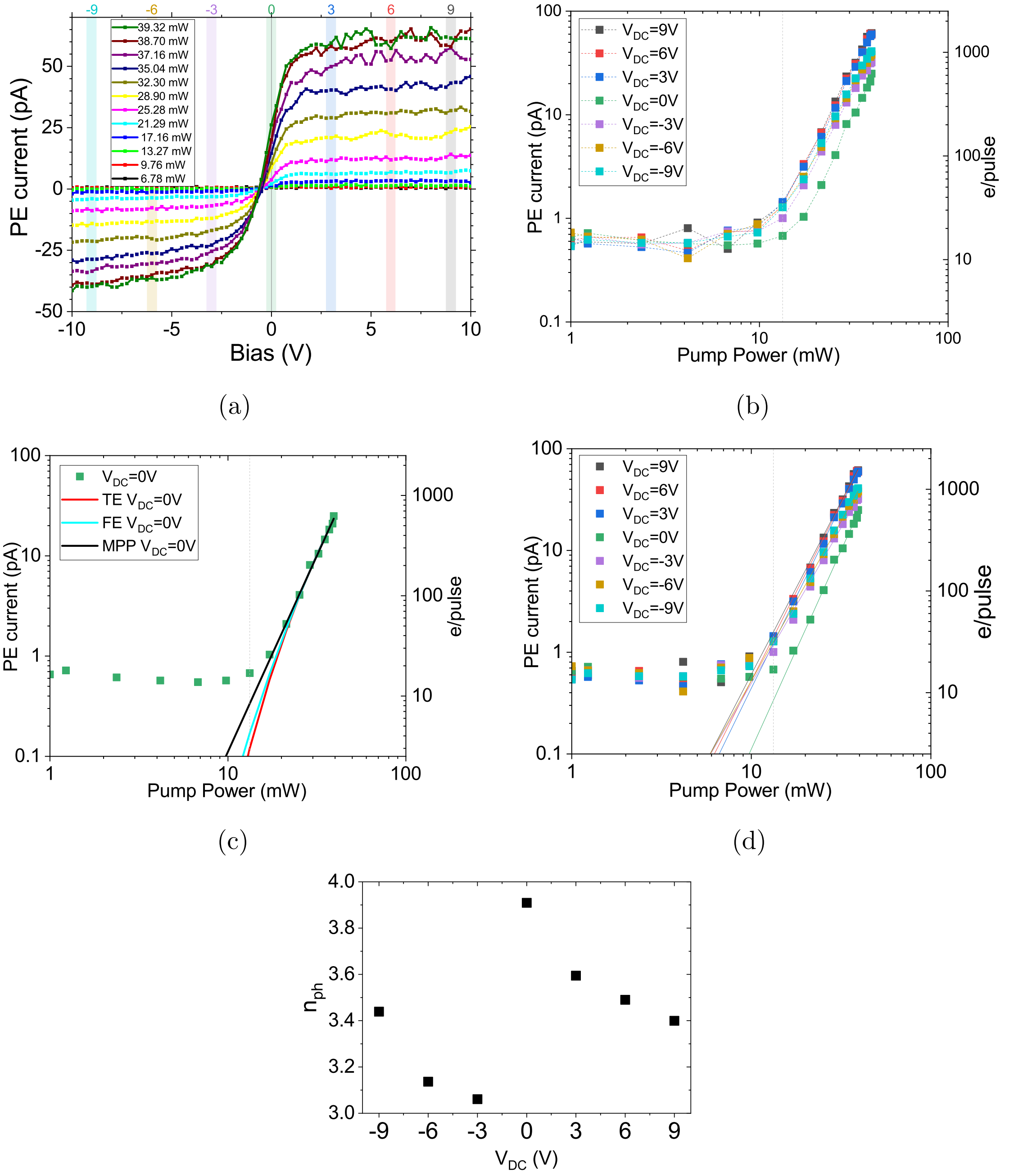

(a)

(b)

(c)

(d)

(e)

Figure 7.9: a) $I_{\mathrm{PE,DC}} - V_{\mathrm{DC}}$ curves, acquired at different excitation pump powers, with a W tip 500 nm away from the Au(111) substrate. b) The average of the three closest points to −9 V, −6 V, −3 V, 0 V, 3 V, 6 V and 9 V, was extracted, and is presented with square symbols as a function of pump power. c) The case when $V_{\mathrm{DC}} = 0\,\mathrm{V}$ is shown as an example, to fit the experimental data with the current density equations of thermionic emission (TE), optical field emission (FE) and multiphoton photoemission(MPP). d) MPP fits (solid lines) to the experimental data (squares) from (b). e) Number of photons n_{ph} nonlinearity extracted from the MPP fits in (d) as a function of V_{DC}.

power. The n_{ph} values extracted from the fits are shown in Fig. 7.9e. There are two different trends for n_{ph}, one where the photoemission from the tip dominates ($V_{\mathrm{DC}} > -0.5\,\mathrm{V}$) and one where the sample photoemission dominates ($V_{\mathrm{DC}} < -0.5\,\mathrm{V}$).

In Fig. 7.9a, for the case when $P_{\mathrm{pump,avg}} \approx 17\,\mathrm{mW}$ and $V_{\mathrm{DC}} = -10\,\mathrm{V}$, the PE current from the sample is $\sim 1\,\mathrm{pA}$. It should also be present in the experiments with the Au tip, since the sample was the same. However, in that case, it is imperceptible because it is buried by the large photoemission from the tip. As discussed in Section 6.2, the sample photoemission is a problem for optical pump-THz probe experiments because the substrate contribution will interfere with the desired measurement. Additionally, in order to study the THz near-field waveforms using the photoemission technique, we want to make sure that the photoemission current measured by the system is being produced mainly, if not uniquely, by the tip. Even though, a low excitation regime is preferred to avoid space charge dynamics from large photocurrents that can broaden the near-field waveforms [42, 47], reducing the optical pump power did not eliminate the sample contribution in our case. An alternative solution is to use a substrate material that does not photoemit when illuminated with optical laser pulses, which is an option that will be explored in the following section.

Chapter 8

Photoemission from semiconductors in STM

Semiconductors are extensively studied in academia and widely used in industry because they are an essential component of electronic devices. Their electrical properties make them suitable for STM studies, and as shown in this chapter, the semiconductor bandgap, if chosen properly, offers the possibility to suppress the multiphoton photoemission from its surface. To achieve this, the semiconductor Fermi level should lie below or as close as possible to the valence band, and its bandgap should be as large as possible. This will increase the energy required to reach the vacuum level from the Fermi level, and can reduce the light absorption depending on the illumination wavelength.

One example of a semiconductor that meets these requirements is highly p-doped GaN. It has a bandgap of 3.4 eV and an electron affinity of 4.1 eV, which adds up to a work function from the valence band of around 7.5 eV [241]. Fig. 8.1 shows the energy diagram of the STM junction with a W tip and a p-doped GaN sample being illuminated with 800 nm pulses. For illustration purposes, the case when four photons are absorbed is presented. When $V_{\mathrm{DC}} <= 0\,\mathrm{V}$, the potential barrier prevents any photoemission current. However, a positive V_{DC} can lower the barrier enough to allow the photoemission from the tip only. The photoemission from the sample is suppressed or minimized in all cases. A set of photoemission measurements was performed on a p-doped GaN sample to confirm these claims, and two more semiconductive samples were used as a reference, an n-type Si-doped GaAs(110) and a p-type Zn-doped GaAs(110), whose bandgap (1.42 eV) is smaller than the excitation photon energy (1.55 eV) and has an electron affinity of 4.07 eV [242]. The same W tip was used for all the measurements on these semiconductive samples.

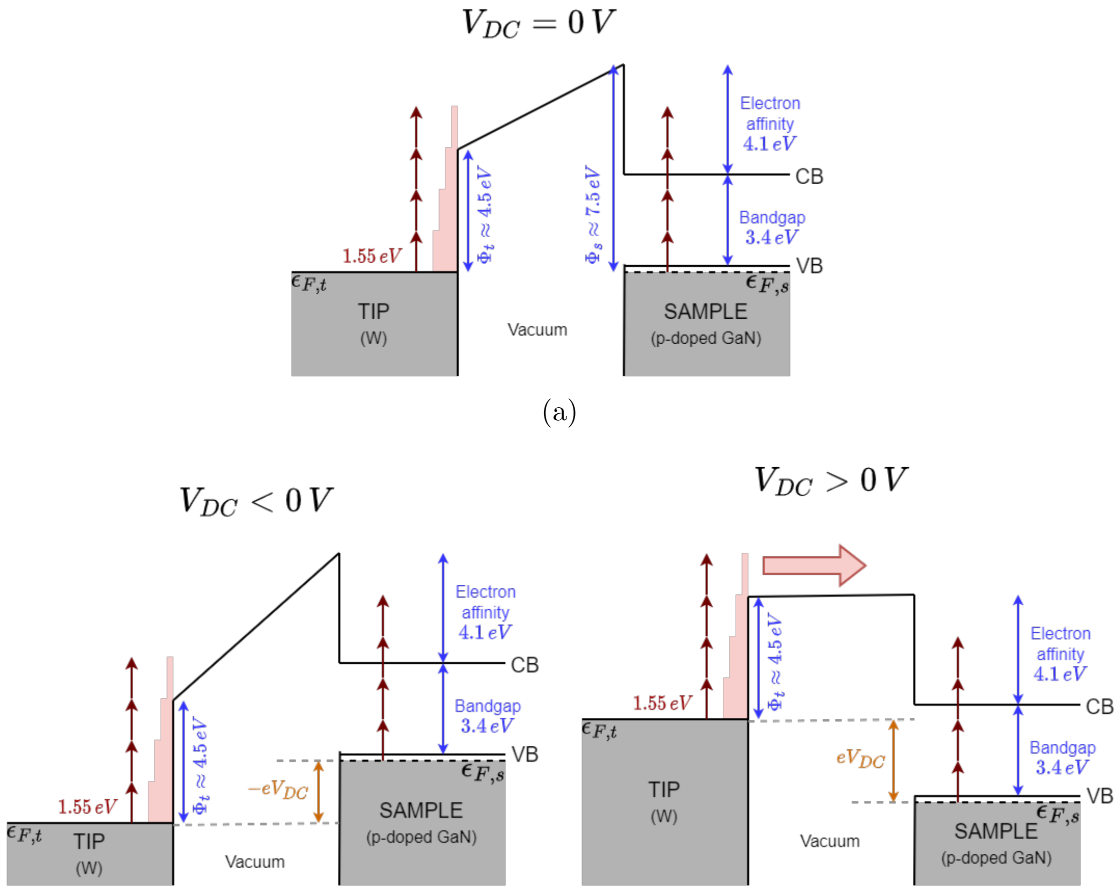

(a)

(b)

(c)

Figure 8.1: Energy diagram of the STM junction with a W tip and a wide bandgap semiconductor, in this case, p-doped GaN being illuminated with 800 nm pulses. The absorption of four photons is shown for illustration purposes. When a) $V_{\text{DC}} = 0\,\text{V}$ and b) $V_{\text{DC}} < 0\,\text{V}$, the potential barrier prevents any photoemission current. c) A positive V_{DC} can lower the barrier enough to allow the photoemission from the tip only. And the sample photoemission is suppressed or minimized in all cases.

8.1 Photoemission bias dependence

The first set of measurements was aimed at studying the bias dependence of the photoemission current at the STM junction. Photographs of the setup are presented in Fig.8.2a (GaAs) and Fig. 8.2b (GaN). Fig. 8.2c shows the $I_{\mathrm{PE,DC}} - V_{\mathrm{DC}}$ curves of the three semiconductor samples (GaAs n-type, GaAs p-type, and GaN p-type) using the exact same W tip. The curves were acquired at room temperature (297 K) and 120 K, with $z \approx 500\,\mathrm{nm}$, $P_{\mathrm{pump,avg}} = 26\,\mathrm{mW}$ and the pump beam was focused at the junction with polarization parallel (p) and perpendicular (s) to the tip axis (Fig. 8.2e). The first thing to note in this plot is the fact that there is no photoemission from the GaN sample, independent of the temperature or the pump beam polarization, which confirms that the multiphoton photoemission has been suppressed. And the second thing is the fact that there is no photoemission from the tip. It was found that by moving the pump beam just slightly above the junction, a photoemission current from the tip was immediately detected. This suggests that a larger surface area of the tip needed to be illuminated to induce a detectable photoemission current with these experimental settings.

8.1.1 GaN

The p-type Zn-doped GaN sample did not produce a photoemission current even with an average pump power of 26 mW (Fig. 8.2d). A photoemission current from the W tip was not detected either, even though the pump beam was centered at the junction. The pump beam was minimally moved upwards as to detect a small photoemission signal from the tip, which is shown in Fig. 8.3a as a function of V_{DC}, and was measured with $z \approx 500\,\mathrm{nm}$ and $P_{\mathrm{pump,avg}} = 26\,\mathrm{mW}$. Interestingly, in this case, only the s-polarized excitation induced PE from the tip, which is counterintuitive. The p-polarized fields are expected to be confined and enhanced at the apex. However, there is evidence [243, 244] that the absorption of s-polarized light can be enhanced by resonant excitations that depend on the ratio between the laser wavelength and the tip dimensions, which could explain why only s-polarized light induces photoemission in Fig. 8.3a. The $I_{\mathrm{PE,DC}}$ dependency on the linear polarization angle of the pump beam is presented in Fig. 8.3b, where the s-polarized light dominates the photoemission and a positive V_{DC} increases the photoemission current as compared with $V_{\mathrm{DC}} = 0\,\mathrm{V}$.

A PE THz waveform could not be detected with such small PE currents, therefore, the pump beam was slightly moved up from the junction again, and the PE THz waveform shown in Fig. 8.3c was acquired with $z \approx 500\,\mathrm{nm}$, $V_{\mathrm{DC}} = 10\,\mathrm{V}$, $E_{\mathrm{THz,pk}} = -295\,\mathrm{V/cm}$, $P_{\mathrm{pump,avg}} = 26\,\mathrm{mW}$ and an s-polarized pump beam. This waveform,

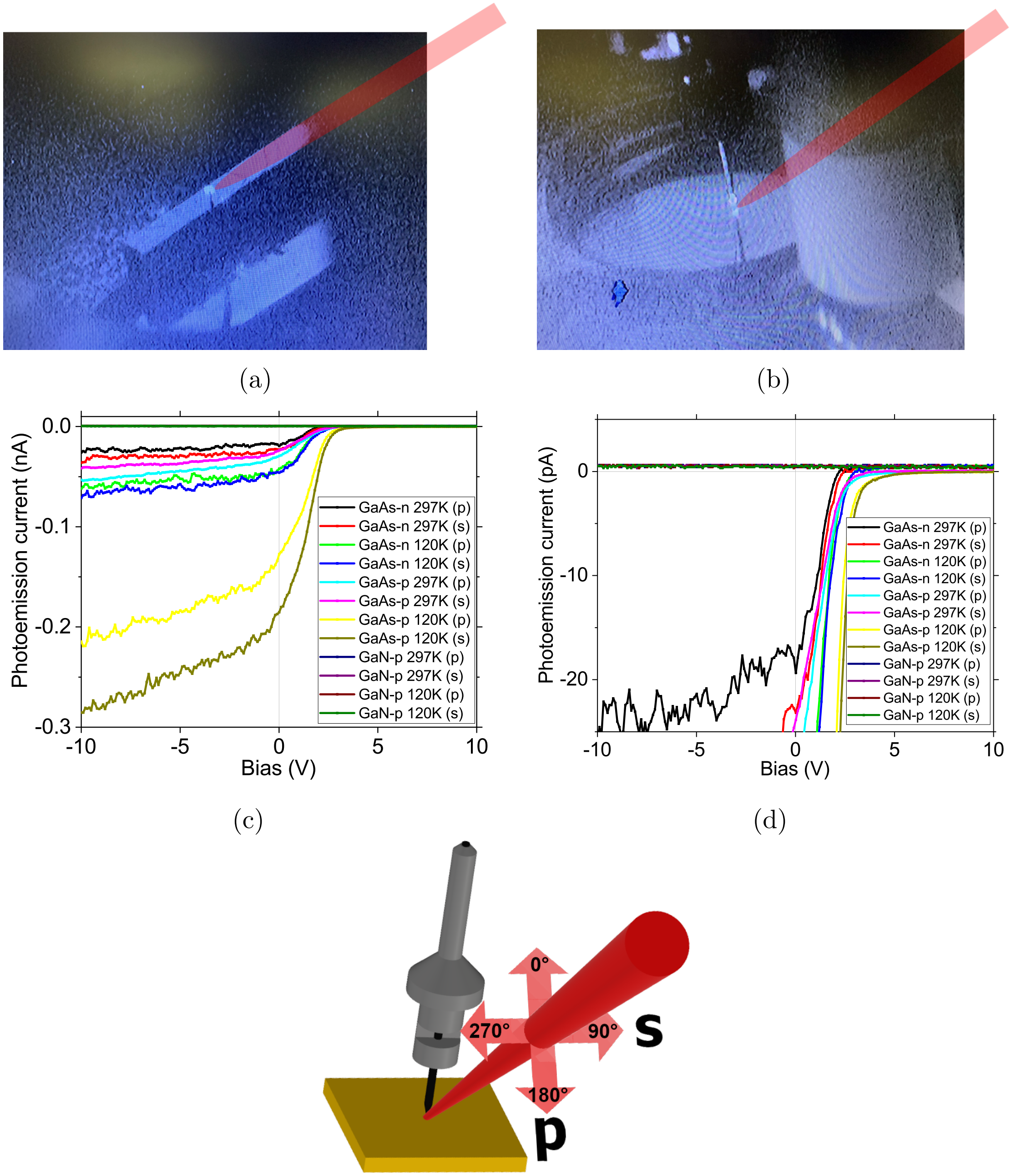
(a)
(b)
(c)
(d)
(e)

Figure 8.2: Photographs of the STM setup for the a) cleaved GaAs and b) GaN samples. c) $I_{\mathrm{PE,DC}} - V_{\mathrm{DC}}$ curves from the n-type GaAs, p-type GaAs and p-type GaN using a W tip. d) Zoomed-in plot of (c) that highligths the photoemission absence from the GaN sample. Curves were acquired at room temperature (297 K) and 120 K, with $z \approx 500\,\mathrm{nm}$, $P_{\mathrm{pump,avg}} = 26\,\mathrm{mW}$ and the pump beam was focused at the junction with polarization parallel (p) and perpendicular (s) to the tip axis. e) Diagram to illustrate the linear polarization angle of the pump beam.

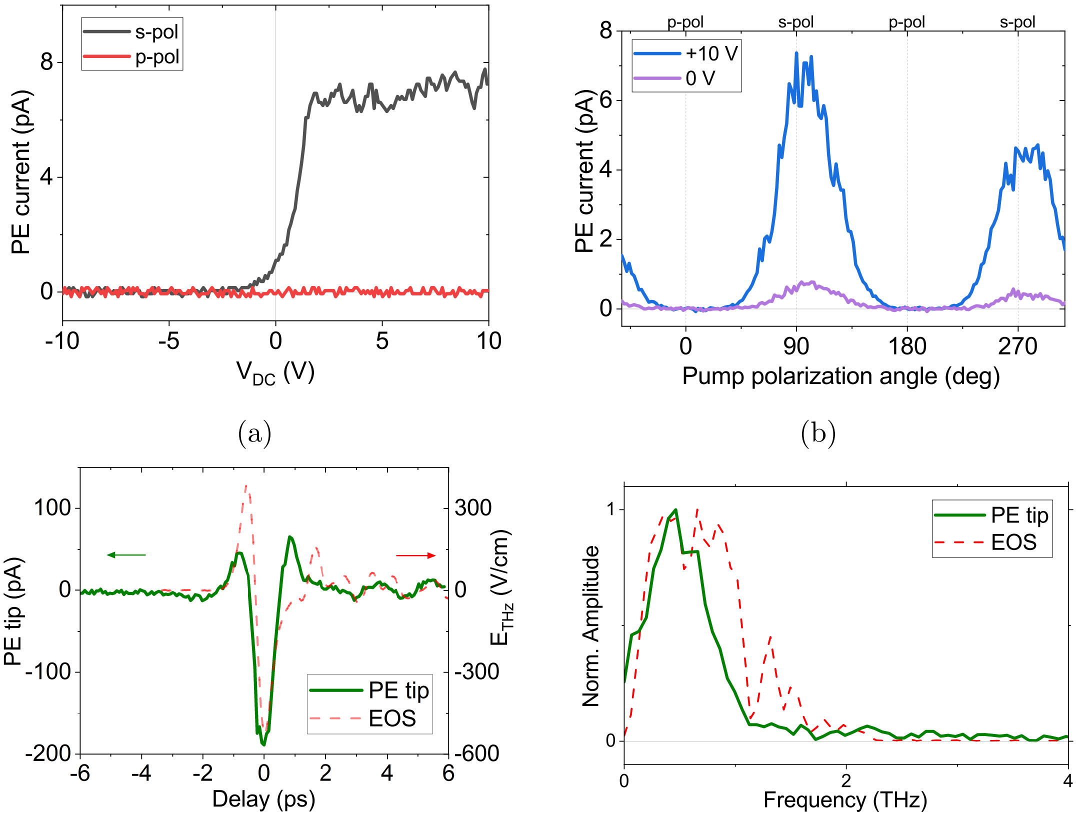

(a) (b)

(c) (d)

Figure 8.3: Photoemission current from the tip as a function of a) V_{DC} and b) pump polarization angle. The data was acquired on the p-type GaN sample with $z \approx 500\,\mathrm{nm}$ and $P_{\mathrm{pump,avg}} = 26\,\mathrm{mW}$. c) Photoemission waveform of the THz near-field at the tip apex (green), with $E_{\mathrm{THz,pk}} = -295\,\mathrm{V/cm}$ and an s-polarized pump beam. The THz pulse waveform measured by EOS, from Fig. 7.2, is also shown (red dashed line), and it was inverted for comparison. d) Frequency content of the PE waveform (solid green) compared with the EOS spectrum (red dashed line) from Fig. 7.3.

which is purely photoemission from the tip, resembles a single-cycle THz pulse. The EOS waveform (from Fig. 7.3), which represents the THz far field, is also shown with a dashed red line for comparison. A phase shift between the near (PE) and far (EOS) fields can be observed in Fig. 8.3c, which has been found to be caused by coupling variations due to the shape of the tips [36]. The frequency content of both waveforms is also shown in Fig. 8.3d, where the PE presents a reduction of the high frequencies, which is characteristic of the antenna coupling. A similar low-pass filter effect has also been explained by delayed photoemission currents in the STM produced by hot thermal electrons [47]. This result again confirms that the far and near-fields are usually different; nevertheless, this photoemission technique can be used to measure the effective THz near-field waveform at the tip apex.

8.2 Photoemission power dependence

Although it was confirmed that the photoemission was suppressed from the GaN sample, the PE current from the GaAs samples was studied for completeness. The energy diagrams of the semiconducting samples are presented in Fig. 8.4, to illustrate the number of photons required to induce MPP in each case. Electrons need to gain the energy difference from the Fermi level ϵ_{F} to the vacuum level to be emitted from the surface. According to these diagrams, electrons require the energy of $n_{\mathrm{ph}} = 2.5$ photons for n-type GaAs, $n_{\mathrm{ph}} = 3.5$ for p-type GaAs, and $n_{\mathrm{ph}} = 4.8$ for p-type GaN.

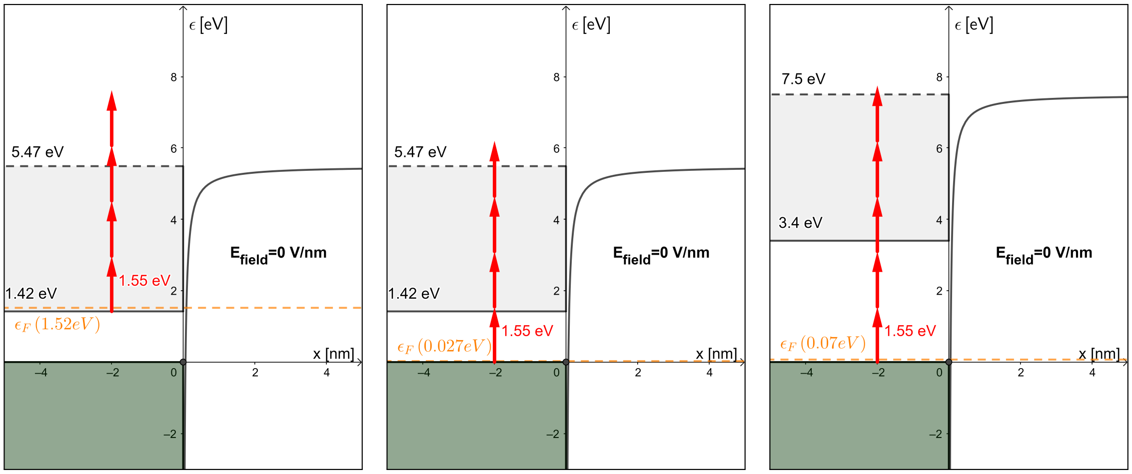

(a) n-type GaAs (b) p-type GaAs (c) p-type GaN

Figure 8.4: Energy diagrams illustrating the number of photons required to induce multiphoton photoemission from a) n-type GaAs, b) p-type GaAs, and c) p-type GaN.

The dependence of $I_{\mathrm{PE,DC}}$ on pump power, for GaAs, is shown in Fig. 8.5, where the W tip was $z = 500\,\mathrm{nm}$ away from the surface. The data was acquired with $V_{\mathrm{DC}} = -10, 0, 10\,\mathrm{V}$, and at two different temperatures, 297 K and 120 K, with s and p polarized pump beams. Only the data for the s-polarized beam is plotted here for visualization clarity, but the results for a p-polarized beam were similar. The overlap of data points indicates that a negative V_{DC} had almost no effect on the results.

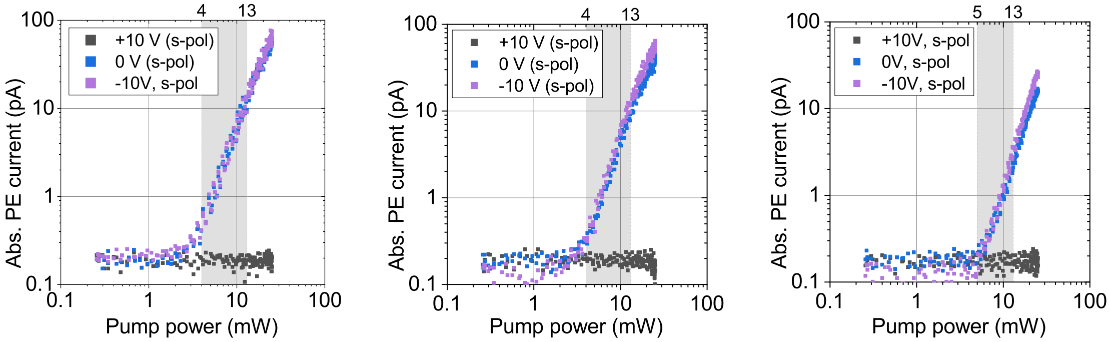

(a) n-type GaAs at 120 K (b) n-type GaAs at 297 K (c) p-type GaAs at 297 K

Figure 8.5: Photoemission current from the GaAs samples as a function of pump power, with $z = 500\,\mathrm{nm}$, $V_{\mathrm{DC}} = -10, 0, 10\,\mathrm{V}$ and an s-polarized pump beam. Two regimes were identified, one below and one above 13 mW.

All data was fitted with the current density equation for MPP, and it was found that the slope in the logarithmic plot slightly changed around 13 mW, which seems to divide two different regimes. This change cannot be attributed to space charge effects, since the total PE current remained below 100 pA, which was the threshold found in Section 7.1 for our experimental setup. Furthermore, the threshold is given by a specific pump power, not a PE current amplitude. A possible explanation will be explored below. The data was analyzed separately for the regions below and above $P_{\mathrm{pump,avg}} = 13\,\mathrm{mW}$. Fig. 8.6 shows one example, for the case of n-type GaAs at 297 K, with $V_{\mathrm{DC}} = 0\,\mathrm{V}$ and an s-polarized pump beam, where the data was fitted separately in these two regions labeled as low-power and high-power.

The extracted values of n_{ph} for each region and each case are presented in Fig. 8.7. These values suggest that at low power (Fig. 8.7a), most of the photoemitted electrons come from the top of the valence band. Electrons need $n_{\mathrm{ph}} \approx 3.5$ to be emitted from the top of the valence band and $n_{\mathrm{ph}} \approx 2.6$ to be emitted from the bottom of the conduction band. Photoexcited electrons from the valence band can also thermalize to the bottom of the conduction band, from where they can absorb multiple photons to be emitted. The thermalization of hot electrons is expected to take $10 - 100\,\mathrm{fs}$ [47], which can occur within the time duration of the excitation pulse (70 fs). As the pump power increases and more electrons are moved into the conduction band, the

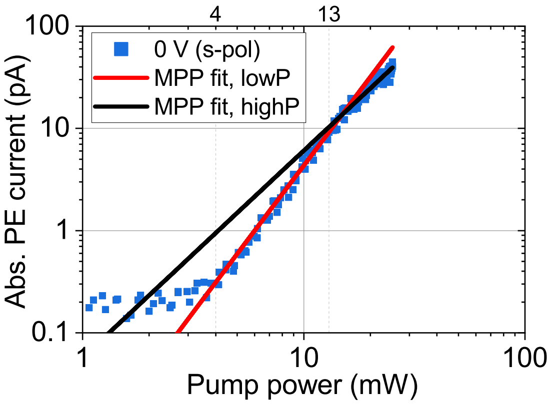

Figure 8.6: Photoemission current from the n-type GaAs sample as a function of pump power, with $z = 500\,\mathrm{nm}$, $V_{\mathrm{DC}} = 0\,\mathrm{V}$ and an s-polarized pump beam. The MPP equation was used to fit the data for both regimes, below and above $P_{\mathrm{pump,avg}} = 13\,\mathrm{mW}$.

photoemission from the bottom of this band seems to take over and dominate, which is reflected in lower n_{ph} values (Fig. 8.7b). Additionally, the values of n_{ph} for p-type GaAs were found to be higher than those for n-type GaAs, mainly due to the position of the Fermi energy.

It can be concluded that photoemission from semiconductors, such as GaAs, is also induced by multiphoton processes when it is excited with low peak intensities, such as those achieved in our setup. However, the emission response will directly depend on the energetic landscape of the sample used, and it can even be completely suppressed by a wide bandgap semiconductor such as a highly doped p-type GaN.

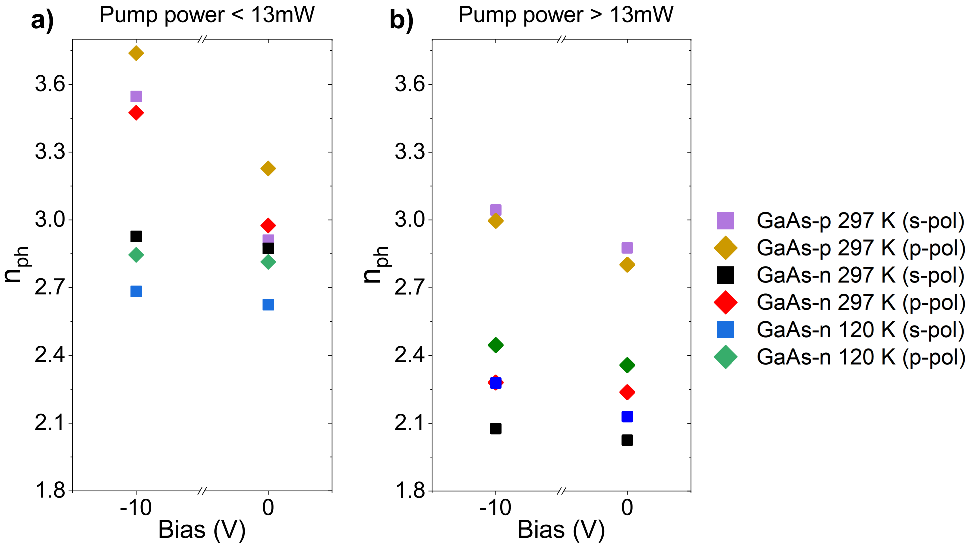

Figure 8.7: Number of photons n_{ph} extracted from the MPP fits to the PE current data with the GaAs samples. The a) low power and b) high power regimes are presented separately.

8.3 Suppressing sample photoemission for pump-probe experiments

Once it was confirmed that the photoemission from the STM sample could be suppressed using p-type GaN, the next step was to attempt a pump-probe experiment in the STM using it as a substrate. The GaN sample was taken out of the vacuum chamber only for a few minutes to deposit the SWCNTs solution on its surface by the drop casting method, and it was immediately brought back into vacuum to minimize its exposure to air. Then, the sample was annealed at 600 °C for 24 hrs. Fig. 8.8 shows STM images of the p-type GaN surface before (left) and after (right) the SWCNTs deposition, with a window size of 400×400 nm and $1.2 \times 1.2\,\mu$m, respectively.

A PE THz waveform that was acquired after the SWCNTs deposition, is compared with the one obtained before the deposition in Fig. 8.9a. It was acquired with $z \approx 500$ nm, $V_{\mathrm{DC}} = 10$ V, $P_{\mathrm{pump,avg}} = 26$ mW and $E_{\mathrm{THz,pk}} = 295$ V/cm. The similarity of the two waveforms confirms that the photoemission was not affected by the changes in the sample since it was mainly produced at the tip apex. The tip was then brought into the tunneling regime, and it was positioned on top of a nanotube. An optical-pump THz-probe waveform was obtained with the feedback loop off, $V_{\mathrm{DC}} = 0$ V, $P_{\mathrm{pump,avg}} = 26$ mW and $E_{\mathrm{THz,pk}} = 295$ V/cm, which is shown in Fig. 8.9b. The amplitude of the signal was only a few electrons per pulse, and it resembles the THz near-field waveform that was acquired with the PE technique, which suggests that

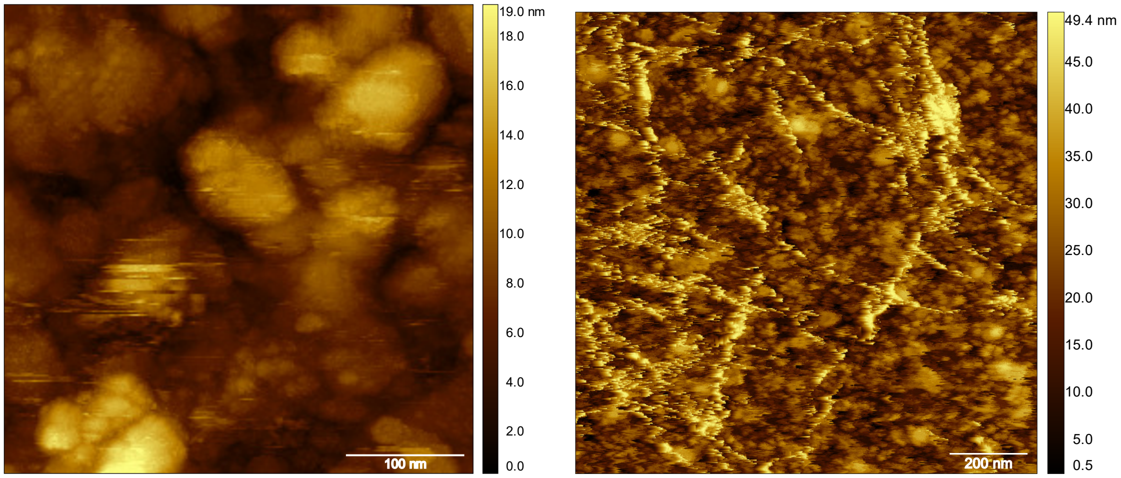

(a) (b)

Figure 8.8: STM images of the p-type GaN sample a) before and b) after the deposition of SWCNTs by drop casting. The window size is 400 × 400 nm and 1.2 × 1.2 μm, respectively. Images were acquired with a) $V_{\mathrm{DC}} = -1.5\,\mathrm{V}$ and $I_{\mathrm{DC}} = 10\,\mathrm{pA}$, and b) $V_{\mathrm{DC}} = -0.5\,\mathrm{V}$ and $I_{\mathrm{DC}} = 100\,\mathrm{pA}$.

this is still a PE signal from the tip and not the actual pump-probe signal from the nanotube. A negative V_{DC} would have ensured that the measured signal was from the nanotube.

Pump-probe imaging was attempted on the nanotubes with no success. Unfortunately, the nanotubes suffered an unexpected deterioration, probably caused by the nanotubes reacting with the GaN substrate to form GaN–SWCNT composites [245]. The deterioration can be observed in Fig. 8.10, where STM images of the SWCNTs that were acquired soon after the deposition (left) and a few weeks later (right) are presented. The degradation of the nanotubes precluded the execution of any further experiments. The p-type GaN sample was custom-made and not easily obtained commercially, therefore, it could take a long time to acquire a new sample. However, it served the purpose of proving that the THz near-field at the tip apex can be accurately measured in an STM setup when the photoemission from the sample is suppressed using a p-doped wide bandgap semiconductor.

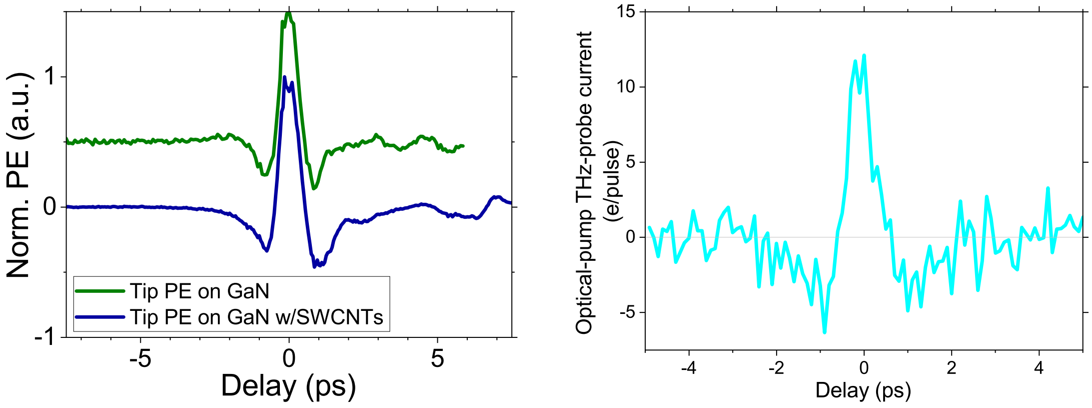

(a) (b)

Figure 8.9: THz waveforms on GaN with SWCNTs. a) Normalized PE waveforms, acquired with the tip 500 nm away from the GaN surface before (green) and after (blue) the deposition of SWCNTs. The green waveform is shifted for clarity. b) Optical-pump THz-probe waveform with the tip tunneling on top of a nanotube. Experimental settings for both cases: $V_{\mathrm{DC}} = 10\,\mathrm{V}$, $P_{\mathrm{pump,avg}} = 26\,\mathrm{mW}$ and $E_{\mathrm{THz,pk}} = 295\,\mathrm{V/cm}$.

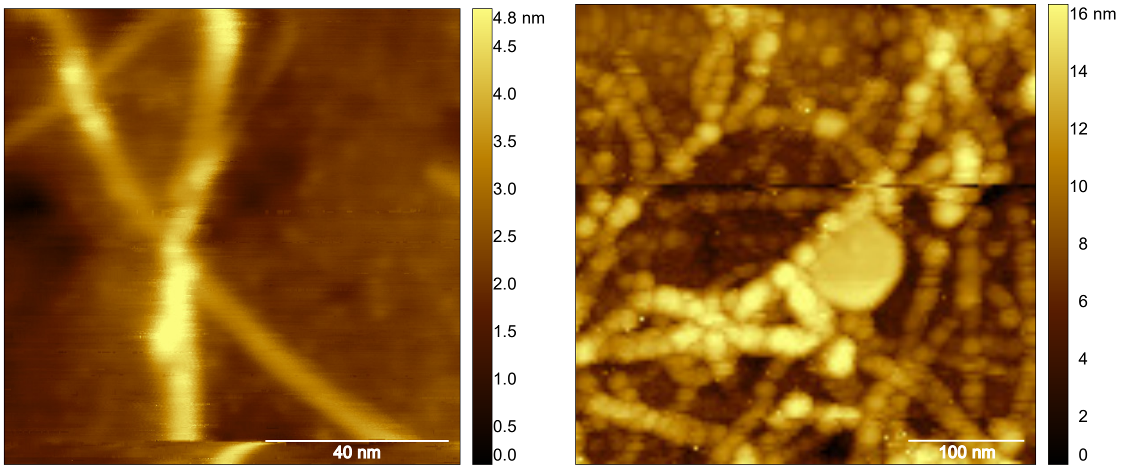

(a) (b)

Figure 8.10: Deterioration of the nanotubes. STM images of the GaN surface were taken a) after the SWCNTs deposition and b) a few weeks later. Images were acquired with $I_{\mathrm{DC}} = 100\,\mathrm{pA}$ and, a) $V_{\mathrm{DC}} = 10\,\mathrm{V}$ and b) $V_{\mathrm{DC}} = -10\,\mathrm{V}$.

Chapter 9

Ultrafast laser-induced thermal effects

Thermal changes will occur in the STM when the junction is illuminated with ultrafast 800 nm laser pulses. The resulting thermal expansion of the tip and sample can have a large impact on the experimental measurements when the STM is operating in the tunneling regime, where a subnanometer separation at the junction is typically required. This motivated the study of the thermal expansion of the W tip, the Au(111) substrate and the semiconductor samples discussed in Chapter 8.

9.1 Laser-induced thermal expansion in the STM

To study thermal expansion in the STM as a whole, the tip was first brought into a tunneling distance from the Au(111) surface by setting $V_{\mathrm{DC}} = 3\,\mathrm{V}$ and $I_{\mathrm{DC}} = 10\,\mathrm{pA}$, with the feedback loop on. The optical pump beam is centered at the junction with an initial pump power of $P_{\mathrm{pump,avg}} = 0.35\,\mathrm{mW}$, which was chosen randomly as a reference. The system is left at rest until the system is thermally stable, which occurs when the tip height is constant over time. This can take minutes or hours, depending on the materials being studied. Once the tip height is stable, the pump power is increased by 0.35 mW, which takes only a fraction of a second, but the tip height presents a gradual change that occurs in a much longer timescale. The change in tip height was monitored during the first 6 min, as shown in Fig. 9.1, where the case of a W tip on an Au(111) surface is shown. The expansion induced by increasing the pump power will force the tip to retract, in order to maintain a constant current. The recovering case, where the pump power was reduced from 0.7 to 0.35 mW, was also monitored to study the material contraction. The average pump power was limited to a maximum of 0.7 mW, which ensures that only the thermal expansion of the materials affects the STM junction, since photoemission was found to be triggered at $\sim 4\,\mathrm{mW}$ and does not contribute to the tunneling current.

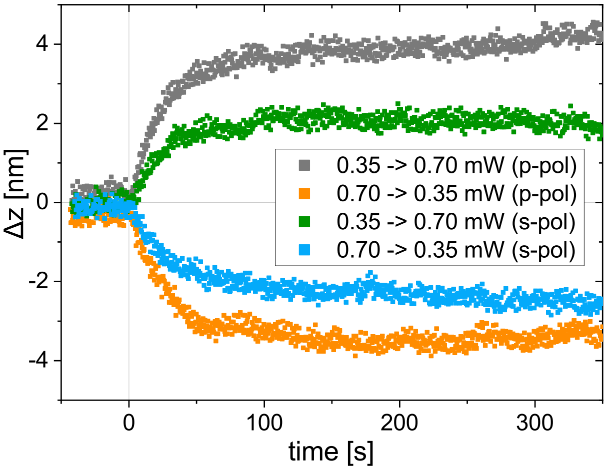

Figure 9.1: Relative tip height as a function of time (squares), after a laser pump power variation of $\pm 35\,\mathrm{mW}$, with a p and s-polarized beam. This change reflects the thermal expansion of the STM system, including the W tip and the Au(111) surface at room temperature.

The same experiment was performed on the following samples: Au(111), n-type GaAs, p-type GaAs and p-type GaN; and the change in tip height was recorded with a p and s-polarized pump beam, and at two different temperatures, 293 K and 120 K. Two additional experiments were performed: one where the pump beam was only illuminating the tip shaft, and one where it was only illuminating the side wall of the n-type GaAs wafer, as shown in Fig. 9.2. These two cases served to measure the thermal expansion of the tip and sample independently.

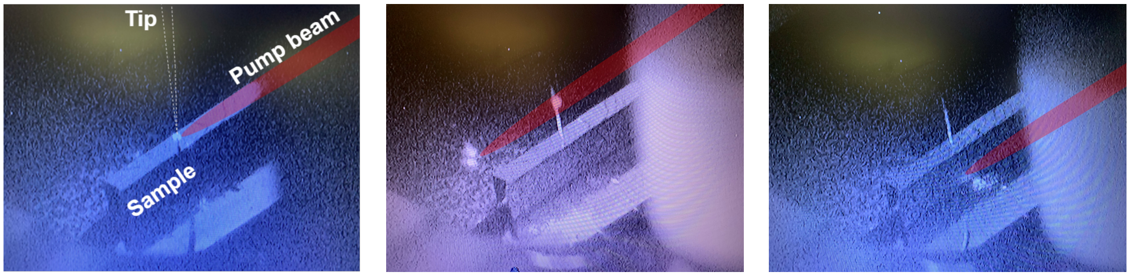

(a) (b) (c)

Figure 9.2: Photographs of the STM setup for the experiments on thermal effects with an n-type GaAs sample. The excitation pump beam was positioned a) at the STM junction, b) at the shaft of the tip and c) at the side wall of the semiconductor crystal.

Fig. 9.3 shows how the tip height changed over time for all the samples. The tip height change is different for a p and s-polarized pump beam due to a different absorption ratio of the incident radiation (Eqs. 9.4 and 9.5), which will be discussed later. Additionally, several aspects can be noted from these plots. First, only in a few cases, the tip height was constant 6 min after the pump power was changed, even though the power difference was small (0.35 mW). This waiting time should be taken into account for the sampling time on experiments involving pump power variations. Second, the total thermal expansion was considerable even for such a small power change. After 6 min, the total thermal expansion on the GaAs samples ranged from a couple of nanometers to ~ 40 nm, which is significant for STM experiments. Even Au(111), which has high reflectivity and a low absorption ratio, presented a thermal expansion of a couple of nanometers. The only exception was the p-type GaN sample, which expanded less than half a nanometer, as it is technically transparent to 800 nm light. This again supports the proposition that p-doped wide bandgap semiconductors are good candidates to be used as substrates when 800 nm ultrafast lasers are used to optically excite the samples, since they can minimize thermal effects. The GaN sample also presented a unique feature, once the expansion/contraction reached a maximum, at around 100 s, the tip height slowly moved back towards its original position. This thermal relaxation could only be appreciated on GaN, and it presents an interesting phenomenon to be studied in the future.

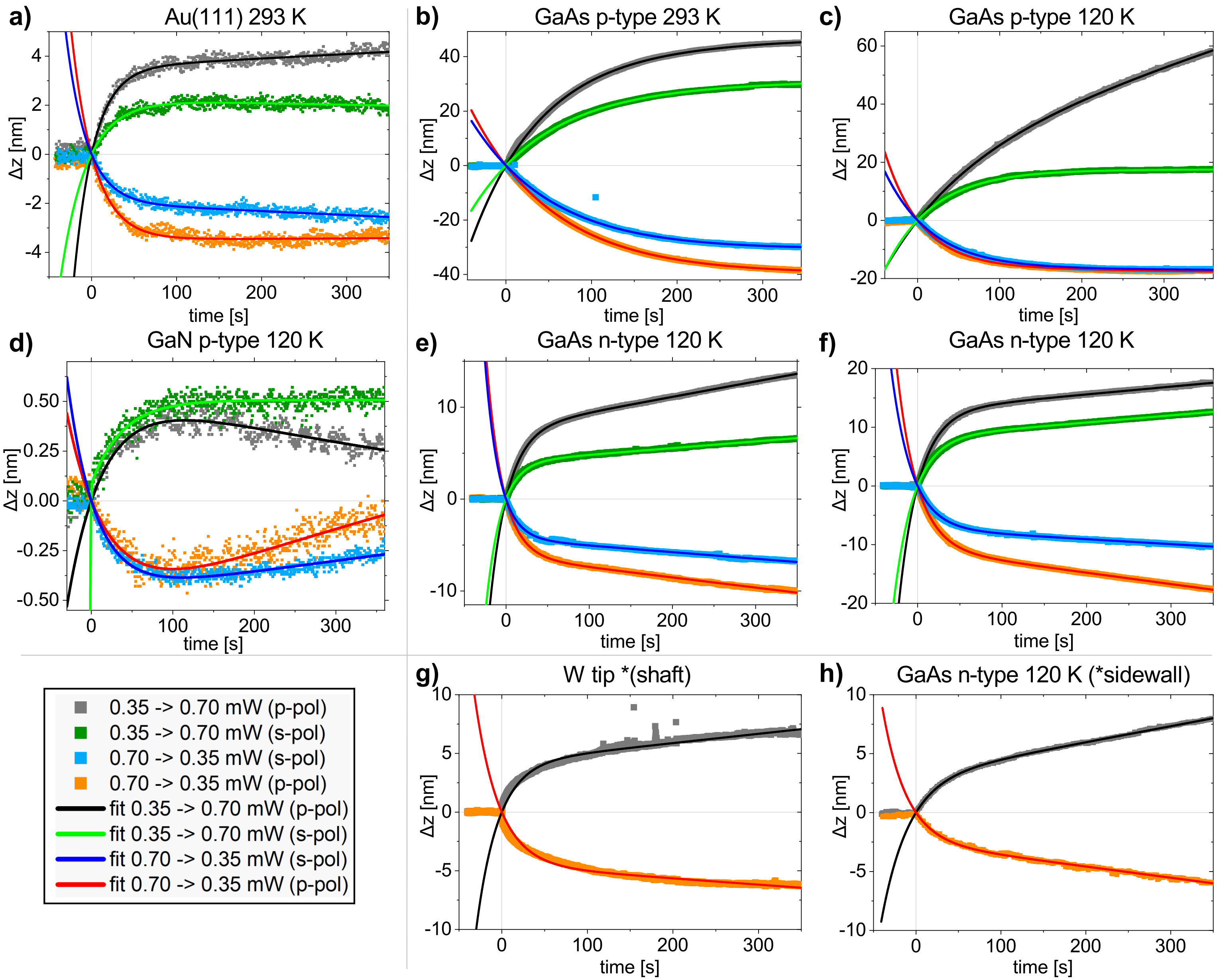

Figure 9.3: Plots of the tip height Δz as a function of time, which correlates with the total thermal change of the STM system caused by a pump beam power change of $\pm 0.35\,\text{mW}$. Measurements taken with the pump beam centered at the junction with a W tip on a) Au(111) at 293 K, b) GaAs p-type at 293 K, c) GaAs p-type at 120 K, d) GaN p-type at 120 K, e) GaAs n-type at 120 K, and f) GaAs n-type at 120 K. Additionally, the pump beam was positioned at g) the tip shaft and h) the GaAs n-type sample sidewall at 120 K. Experimental data is shown with colored squares, and the solid lines show the exponential fits.

			Pump beam p-polarized						Pump beam s-polarized					
			0.35 mW ↑			0.35 mW ↓			0.35 mW ↑			0.35 mW ↓		
	Sample	Temp. [K]	A_z [nm]	τ [s]	k [pm]	A_z [nm]	τ [s]	k [pm]	A_z [nm]	τ [s]	k [pm]	A_z [nm]	τ [s]	k [pm]
at junction	Au	293	3.54	23.5	1.8	-3.50	26.8	0.2	2.21	30.6	-0.6	-2.0	23.5	-1.6
	GaAs p-type	293	43.4	82.7	7.5	-39.7	97.8	0.1	28.7	90.0	5.9	-31.4	95.4	1.8
	GaAs p-type	120	26.1*	98.4*	92.0*	-16.1	44.6	-4.3	17.4	58.8	0.4	-16.4	56.8	-1.6
	GaAs n-type	120	12.9	24.0	13.3	-10.9	24.0	-19.4	8.4	23.6	12.1	-7.4	24.1	-8.4
	GaAs n-type	120	7.8	21.7	16.8	-6.3	19.4	-11.1	4.1	18.0	7.3	-4.3	17.0	-7.2
	GaN p-type	120	0.52	40.4	-0.7	-0.53	45.0	1.3	0.48	28.0	0.1	-0.47	34.7	0.5
at W tip	GaAs n-type	120	4.3	25.3	7.9	-4.6	28.0	-5.3	N/A	N/A	N/A	N/A	N/A	N/A
at sample	GaAs n-type	120	3.2	31.4	13.6	-2.7	27.7	-9.5	N/A	N/A	N/A	N/A	N/A	N/A

Table 9.1: Fit parameters extracted from the plots in Fig. 9.3. An exponential plus a linear term of the form of Eq. 9.2 was used. *This data set differs considerably from the rest due to unknown reasons.

The STM tip expanded a few nanometers for the case when the pump beam illuminated its shaft, as shown in Fig. 9.3 (bottom center). However, the total expansion of the tip and the GaN sample combined, when the pump beam was at the junction, was only 0.5 nm. This shows that the tip expands at least one order of magnitude less when the laser beam is at the junction, mainly because of a drastic reduction of the tip surface area being illuminated. This aspect will be explored in Section 9.2. For the case where only the side wall of the sample wafer was illuminated (bottom right), the thermal expansion was slightly lower than when the beam was at the junction, mainly because the pump beam was illuminating a region $\sim 0.5\,\mathrm{mm}$ away from the junction, where the heat is transferred horizontally and vertically along the crystal. This confirms that the expansion of the sample is the main concern, regarding thermal effects, when an ultrafast laser beam is used for STM experiments, since the tungsten tip expansion is small in comparison.

The analysis of the plots in Fig. 9.3 was performed as follows. The thermal expansion over time of an STM tip [246] and a crystal lattice [247] has been previously described by an exponential of the form

$$\Delta Z = A_z(1 - \exp(-t/\tau))\,, \tag{9.1}$$

where A_z represents the maximum value of the thermal expansion at long times and τ is the time constant. Therefore, the experimental data was initially fitted with a dual exponential of this form, assuming that it could contain the contributions from the tip and sample, since both are being illuminated when the excitation beam is centered at the junction. However, it was found that the time constant for the second exponential was really large in many cases, suggesting that, instead of a second exponential, a linear term should be included to represent the cumulative heating of the elements over time. This again suggests that the tip expansion is negligible compared to the sample expansion which is the one that dominates. Therefore, the data was fitted with an equation of the form

$$\Delta Z = A_z(1 - \exp(-t/\tau)) + kt\,, \tag{9.2}$$

where the linear term k was added to account for the continuous heating up of the sample and sample holder due to the absorption of multiple laser pulses over time. The exponential plus the linear term fits are shown with colored solid lines in Fig. 9.3. Table 9.1 summarizes the numerical values obtained for A_z, τ, and k in all different cases. The absolute value of these parameters is also presented in Fig. 9.4. The thermal expansion constant A_z shows values from a few nm to tens of nm, which are considerable for STM measurements. The time constant values of tens of seconds show that long waiting times are required between measurements every time the pump power changes. The linear term k values of a few pm are small and might only be important for high-accuracy measurements.

A deeper analysis would be required to estimate the exact values expected from these experiments, since there are unknown variables, such as the actual volume of material being heated in each case which depends on the sample geometry, or the relative position of the pump beam, which complicates the analysis. However, a simple approach can also provide insight into this data. For example, the one-dimensional thermal expansion is described by

$$\Delta L = \alpha(\Delta T)L = \alpha \left(\frac{Q}{mC}\right) L \,, \tag{9.3}$$

where α is the linear expansion coefficient, ΔT is the temperature change, L is the length of the material, Q is the energy absorbed, m is the material mass, and C is the specific heat capacity. Table 9.2 summarizes some of these parameters for the different materials.

Material	Temp. K	n real	κ imag.	Thermal exp. coeff. 10^{-6}K^{-1}	Thermal conductivity $\text{Wm}^{-1}\text{K}^{-1}$	Specific heat cap. $\text{Jg}^{-1}\text{K}^{-1}$
Au	293	0.188 [248]	5.39 [248]	14.2	318	0.126
GaAs p-type	293	3.68 [249]	0.089 [249]	5.5* [250]	49 [251]	0.327
GaAs p-type	120	3.68 [249]	0.089 [249]	2.5* [250]	125 [251]	0.327
GaAs n-type	120	3.68 [249]	0.089 [249]	2.5* [250]	125 [251]	0.327
GaN undoped autodoped	120	2.346 [249]	0 [249]	1.0 [252]	110** [253]	0.49
W	293	3.56 [248]	2.73 [248]	4.5 [238]	173	0.134

Table 9.2: Thermal-related properties of materials. *Values for an undoped sample. **Values for a $3 \times 10^{17}\,\text{cm}^{-1}$ n-doping concentration.

We can assume that the incident energy Q_{inc} on all samples is the same; however, the absorbed energy Q will be different for each case. The incident beam can be reflected, transmitted or absorbed by the material. The reflectance R, transmittance T and absorptance A follow the equation $R + T + A = 1$. The reflectance can be

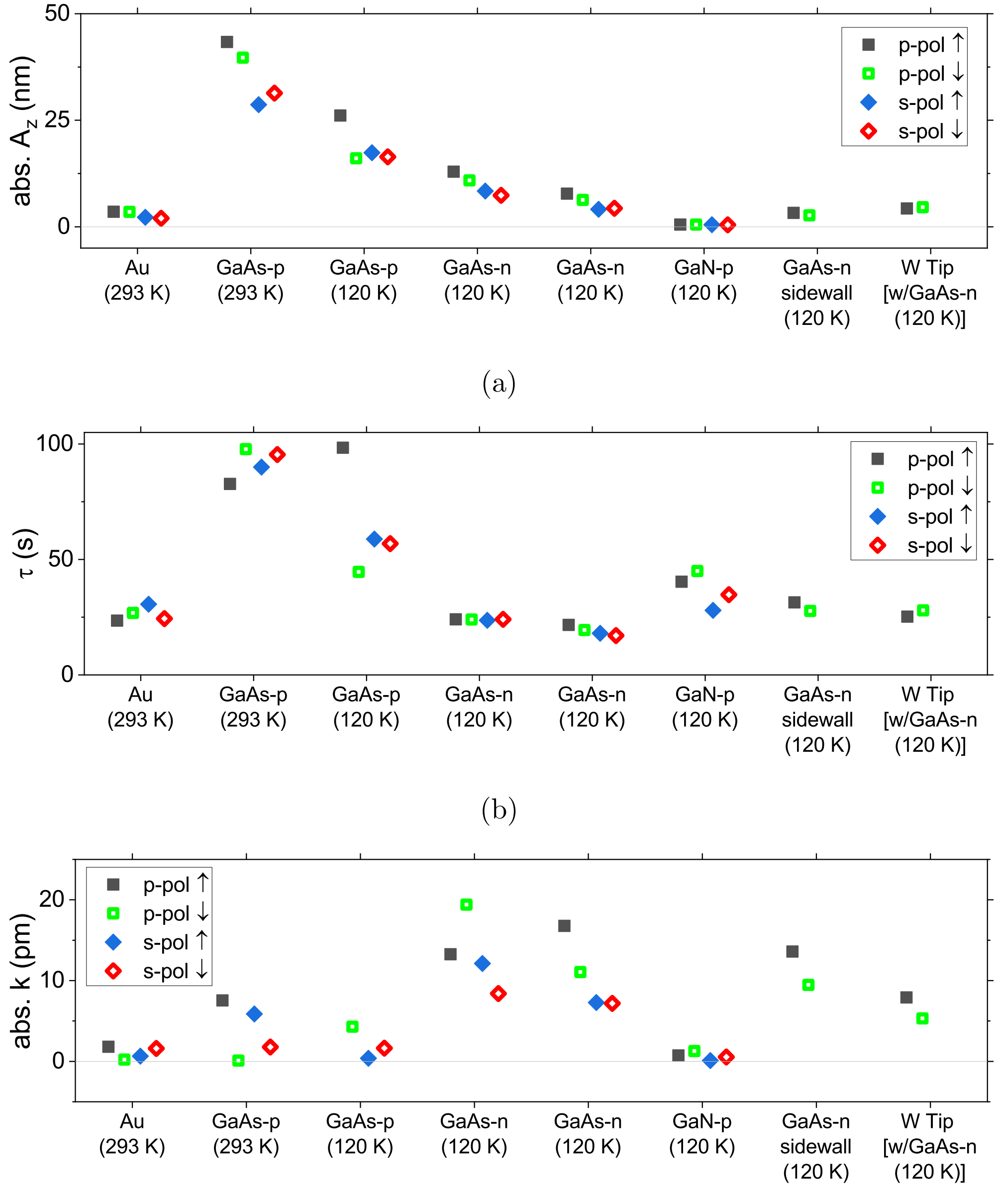

(a)

(b)

(c)

Figure 9.4: Numerical values obtained from the fits to the experimental data for a) $/A_z/$, b) τ, and c) $/k/$.

calculated using Fresnel equations

$$R_s = \left| \frac{n_1 \cos\theta_i - n_2 \sqrt{1 - \left(\frac{n_1}{n_2}\sin\theta_i\right)^2}}{n_1 \cos\theta_i + n_2 \sqrt{1 - \left(\frac{n_1}{n_2}\sin\theta_i\right)^2}} \right|^2 , \tag{9.4}$$

$$R_p = \left| \frac{n_1 \sqrt{1 - \left(\frac{n_1}{n_2}\sin\theta_i\right)^2} - n_2 \cos\theta_i}{n_1 \sqrt{1 - \left(\frac{n_1}{n_2}\sin\theta_i\right)^2} + n_2 \cos\theta_i} \right|^2 , \tag{9.5}$$

where n_1 and n_2 are the complex refractive indices of the two mediums at the interface, and θ_i is the incidence angle. The reflectance of the different samples was calculated for a 50° incidence angle, an 800 nm wavelength, and a p and s-polarized pump beam. The transmittance of the samples is null because they are thick enough to absorb the full intensity entering the sample, and the absorptance can be directly calculated as $A = 1 - R$. The GaN sample is the only exception since it does not absorb the 800 nm radiation. The results are presented in Table 9.3. The actual energy absorbed in each case can then be calculated as $Q = AQ_{\text{inc}}$.

	Au		GaAs		GaN		W		GaAs sidewall	
	p-pol	s-pol	p-pol	s-pol	p-pol	s-pol	p-pol	s-pol	p-pol	s-pol
Reflectance	0.963	0.985	0.173	0.486	0.053	0.303	0.923	0.967	0.233	0.424
Absorptance	0.037	0.015	0.828	0.514	0	0	0.077	0.033	0.767	0.576

Table 9.3: Reflectance R and absorptance A of the samples for a 50° incidence angle, 800 nm wavelength, and a p and s-polarized beam. The W tip and GaAs sidewall cases had an incidence angle of 40°.

If we assume that the mass and length are the same for all samples, we can set $Q_{\text{inc}}L/m = 1$, and Eq. 9.3 reduces to $\Delta L = \alpha \left(\frac{A}{C}\right)$. The relative expansion using the reduced formula was estimated for each case with the values from Tables 9.2 and 9.3, and the results are presented in Fig. 9.5.

Despite the simplicity of this approach, the estimated relative expansion from this plot presents some similarities with Fig. 9.4a, showing that this technique has the potential to study the thermal changes of samples in situ with the STM. It provides the means to measure and quantify the thermal expansion/contraction from different samples when an ultrafast 800 nm laser is involved, and can be used to identify materials that minimize the thermal changes. In this case, p-type GaN was

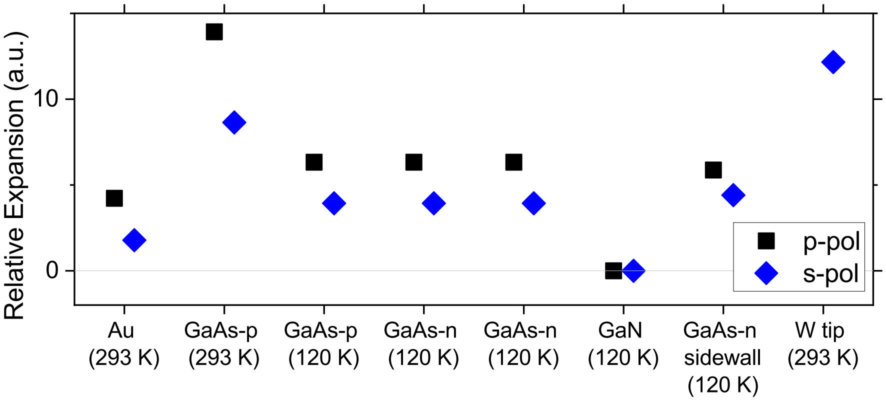

Figure 9.5: Relative thermal expansion of different materials calculated with Eq. 9.3 and the values from Tables 9.2 and 9.3. The x-axis was adjusted to match that of Fig. 9.4a for comparison.

the material least affected by laser power changes, which suggests that wide bandgap semiconductors would be ideal to be used as substrates for this type of experiments. Furthermore, time constants of tens of seconds and up to $\sim 100\,\mathrm{s}$ were measured in these experiments. These time constants are critical to consider for the sampling time used in experiments where the beam power is varied.

9.2 Laser-induced thermal expansion of the tip

The thermal expansion of the tip can also be analyzed when the pump beam is centered on its shaft, which is illustrated in Fig.9.6a (case A). The effective power incident on the tip shaft can be calculated as the integral in spherical coordinates of the incident beam intensity, which is described by a Gaussian distribution as follows

$$P_{\text{inc}} = \int_0^{\theta'} \int_0^{r'} I_0 \left(\frac{w_0}{w(z)}\right)^2 \exp\left(\frac{-2r^2}{w(z)^2}\right) r dr d\theta \,, \tag{9.6}$$

where r is the radial distance from the beam axis, $w(z)$ is the beam radius at a distance z from the focus, $w_0 = w(0)$ is the beam waist radius, $I_0 = 2P_0/(\pi w_0^2)$ is the intensity at the center of the beam, and P_0 is the total beam power. Assuming that the tip shaft is at the focal point of the beam, one can evaluate the integral of Eq. 9.6 with $w(z) = w_0 = 108\,\mu\mathrm{m}$ (our beam spot diameter was $216\,\mu\mathrm{m}$) to obtain an expression for the incident power as a function of radius r' and angular range θ' as follows

$$P(r', \theta') = \frac{\theta'}{2\pi} \left[1 - \exp\left(\frac{-2(r')^2}{w_0^2}\right)\right] P_0 \,. \tag{9.7}$$

To calculate the incident power on the tip shaft, one can use $r' = 125\,\mu\text{m}$ and $\theta' = 2\pi$, since the diameter of the tip shaft is 0.25 mm and the illuminated area covers a full circle. Therefore, $P_{\text{inc}} = 0.93P_0$. When the pump beam is centered at the tip apex, the angular range is reduced, since only a portion of a circle is being illuminated (Fig.9.6a, case B). Using an optical image of the tip apex with a magnification of 80x (Fig.9.6b), the conical angle of the tip shape was estimated to be 10°. The incident power when the beam is at the junction can then be calculated with $r' = 125\,\mu\text{m}$ and $\theta' = \pi/18$, and the result is $P_{\text{inc}} = \frac{1}{36}0.93P_0$, which is 36 times less than when the tip shaft is illuminated directly.

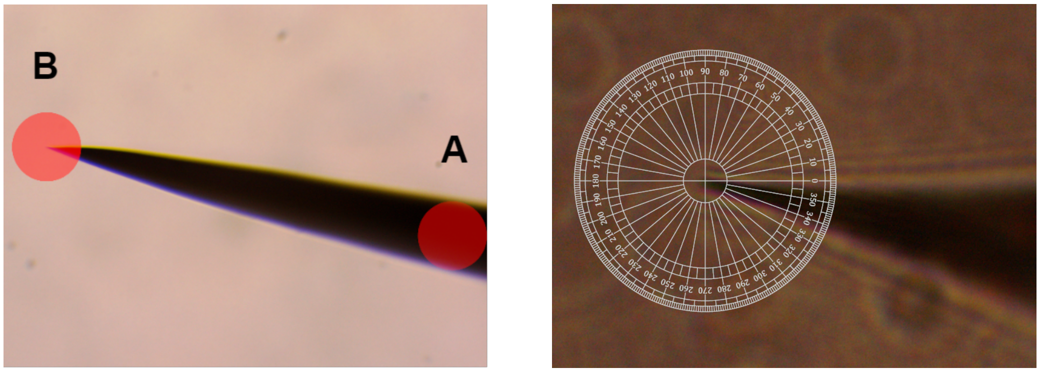

(a) (b)

Figure 9.6: Photographs of a tungsten tip from an optical microscope. a) Two points on the tip are highlighted, where the pump beam is illuminating the tip shaft (A) and the tip apex (B). b) A zoomed-in image of the tip apex where the angle of the conic shape can be measured.

The incident energy would be 36 times smaller for case B, however, the temperature change induced by each unit of absorbed energy will differ for the two cases due to geometrical differences. For example, the thermal dissipation in case B would be lower because of the reduced volume surrounding the tip apex, which translates into higher temperatures. A proper simulation with Finite Element Analysis (FEA) would be required to accurately compare the two cases. Nevertheless, the total expansion for case A in Fig. 9.3 (bottom center) was $\sim 6.5\,\text{nm}$, but the combined expansion of the tip and GaN for case B (middle left) was less than $\sim 0.5\,\text{nm}$, which is at least 10 times smaller. This estimate, combined with the results from the previous section, suggests that the thermal expansion of W tips, induced by laser heating in STM experiments, is small when the laser beam is focused at the junction; and the main concern should be the thermal expansion of the sample in question.

Chapter 10

Home-built ambient THz-STM system

Reliable STM systems can be found commercially available for a variety of applications, however, the acquisition cost can be an entry barrier for some research groups who would like to try and test these systems in new experimental setups. A possible solution is to build the STM in-house, which can greatly reduce the cost. Even though the performance of a home-built STM might not be the best, it can be a first step to test new ideas. Furthermore, a home-built STM can be designed having in mind the needs and limitations of a specific application, which facilitates its integration with other systems. This reasoning motivated the construction of an ambient STM to study the coupling of THz pulses on STM tips, which is the project that will be discussed in this chapter.

10.1 Design and construction

A simple setup was built to study how the THz pulses are coupled to the STM tip. The goal was to study the THz-induced current when different tips were illuminated with THz pulses under different conditions. To control the tip-sample distance, a linear micrometer positioner was used for the coarse approach in combination with a linear piezo stage for the fine approach, as shown in Fig. 10.1. However, the capabilities of this setup were limited and considerable vibrational noise and thermal drifts were observed. For these reasons, the project evolved into the design and construction of a fully functional STM that would be more stable, and that could be easily integrated with an optical setup to perform THz-STM studies under ambient conditions.

A custom STM can provide more stable tip-sample distances if it is built with a robust structure to reduce high-frequency vibrations and a damping system to

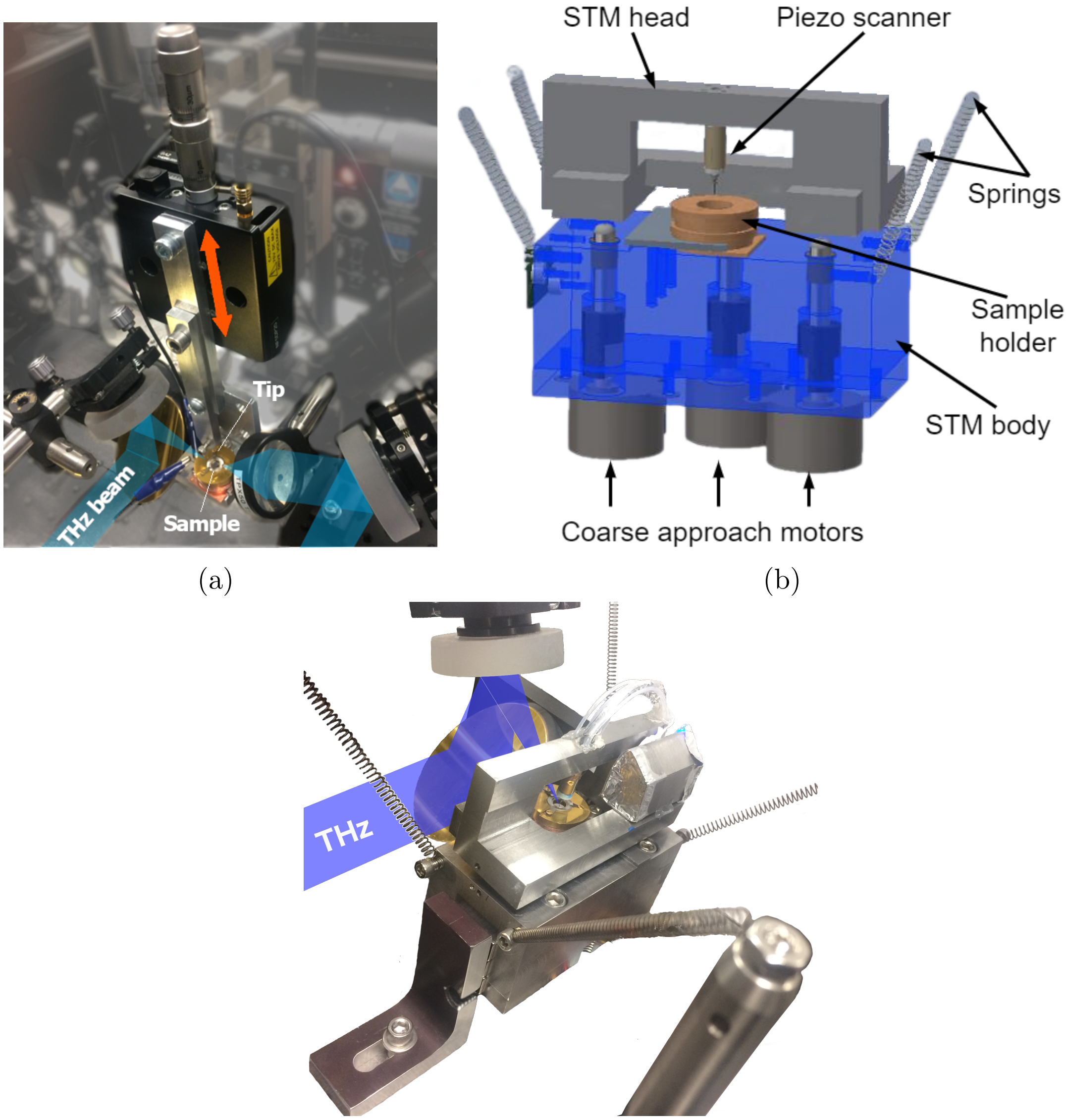

(a) (b)

(c)

Figure 10.1: Initial setups that were used to study the coupling of THz pulses onto the STM tip. a) Photograph of the initial setup with a piezo stage for a linear approach mechanism. b) CAD model of the first version of the ambient STM showing the main parts of the system. c) Photograph of the fully functional STM.

reduce low-frequency vibrations. Additionally, the thermal drift can also be reduced by selecting the proper materials for its construction. The STM head was designed to provide easy access to the STM junction from two opposite sides, as shown in Fig. 10.1c. Having a clear space around the junction gives easy access to illuminate the tunnel junction with free-space-propagating radiation, for example, to perform pump-probe experiments. Additionally, the scattered radiation or the photoluminescence from the STM junction at different angles can also be collected.

A simplified schematic of the electronics used to control the STM is presented in Fig. 10.2. The microcontroller printed circuit board (PCB), the preamp PCB, and the basic software with a user interface to operate the STM, were purchased from Daniel Berard, a physics PhD student at McGill University (Montreal) at the time.

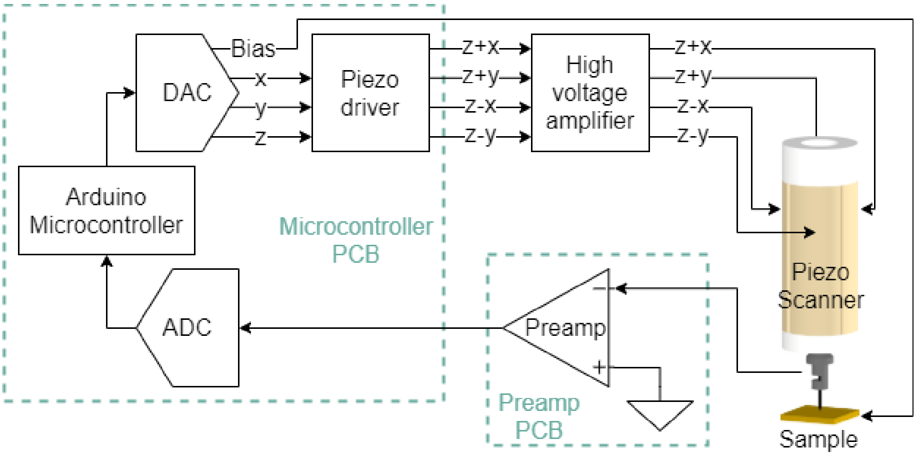

Figure 10.2: Simplified schematic of the electronics used in the ambient STM.

The microcontroller is a Teensy 3.2, a 32bit Arduino-compatible microcontroller that operates at 72 MHz. It controls the position of the piezo scanner and its output goes into a digital-to-analog converter (DAC), which is a DAC8814 4-channel 16-bit multiplying DAC. The use of sigma-delta modulation increases the effective resolution of the DAC to 20-bit. The signals then go into a piezo driver that converts the signals from Cartesian coordinates into four $1V$ signals for each one of the piezo scanner electrodes. These 4 signals are then amplified 250 times by a TD250 six-channel amplifier (PiezoDrive) before they go into the piezo scanner. The piezo scanner was built in the lab with a piezo radial tube (Boston Piezo-Optics Inc.) made of PZT-5A. It has an outer diameter of 0.250 in, a wall thickness of 0.025 in and a length of 0.5 in. The piezo tube has electroless nickel electrodes; one internal, which is connected to ground, and 4 external, which are connected to the high-voltage signals that control the displacement of the piezo scanner. The coupling pieces, used to attach the piezo scanner to the STM head frame and to retain the tip-holder, were machined out of glass-mica ceramic rods, also known as Macor. This material presents a thermal expansion similar to that of PZT-5A which helps minimize the thermal drift at the junction[254].

An estimation for the axial and lateral displacement of a piezo tube, respectively, is given by

$$\Delta L_{\text{axial}} = d_{31(\text{GS})}\frac{l}{t}V\,, \tag{10.1}$$

$$\Delta L_{\text{lateral}} = 0.9 d_{31(\text{GS})}\frac{l^2}{(ID+t)t}V\,, \tag{10.2}$$

where l is the tube length, t is the wall thickness, ID is the internal diameter of the tube, V is the voltage applied to the electrodes, and $d_{31(\text{GS})}$ is the transverse piezoelectric deformation coefficient ($d_{31(\text{GS})} = -171\,\text{pm/V}$ for PZT-5A).

The HV amplifier (PiezoDrive TD250-SGL) can supply up to ±250 V which translates into a vertical range of 1.7 μm and a horizontal range of 3.4 μm, from a total potential difference of 500 V. Dividing these numbers by the resolution of the DAC gives a minimum step size of 1.6 pm and 3.2 pm in the vertical and horizontal axis, respectively.

The STM tip-holder is electrically connected to the preamp with an ultra-miniature coaxial cable type SC (Lake Shore Cryotronics, Inc. LSCC-SC-25). The Teflon outer jacket of this cable was stripped off to make it more flexible, and the cable was kept as short as possible to reduce its capacitance. The coax shield helps to reduce any pickup noise from the environment, since this part of the circuit is the most sensitive. The preamp PCB has an OPA124 low-noise precision difet operational amplifier connected as a current-to-voltage converter. It can measure a minimum current of 1 pA and can handle a maximum current of ±10 nA, with a bandwidth of 32 kHz. Feedback resistors of 100 MΩ and 1 GΩ are used to set the current-to-voltage gain at 10^8 and 10^9, respectively. The tunneling current signal from the preamp then goes into a LTC2326-16 16-bit pseudo-differential analog-to-digital converter (ADC) and then into the microcontroller to be used as reference for the feedback loop.

The body of the STM and the frame for the STM head were machined out of 17-4 PH Stainless Steel. The coarse approach of the tip to the sample is achieved with motor-controlled ultra-fine-thread thumb screws that provide a vertical range of 5 mm and a step size of 61 nm. New routines and functionalities had to be implemented into the original software to perform basic STS measurements such as $I-V$ and $I-z$ curves, which provided a fully functional STM.

This first version of the STM (Fig. 10.1c) was able to acquire topographic images

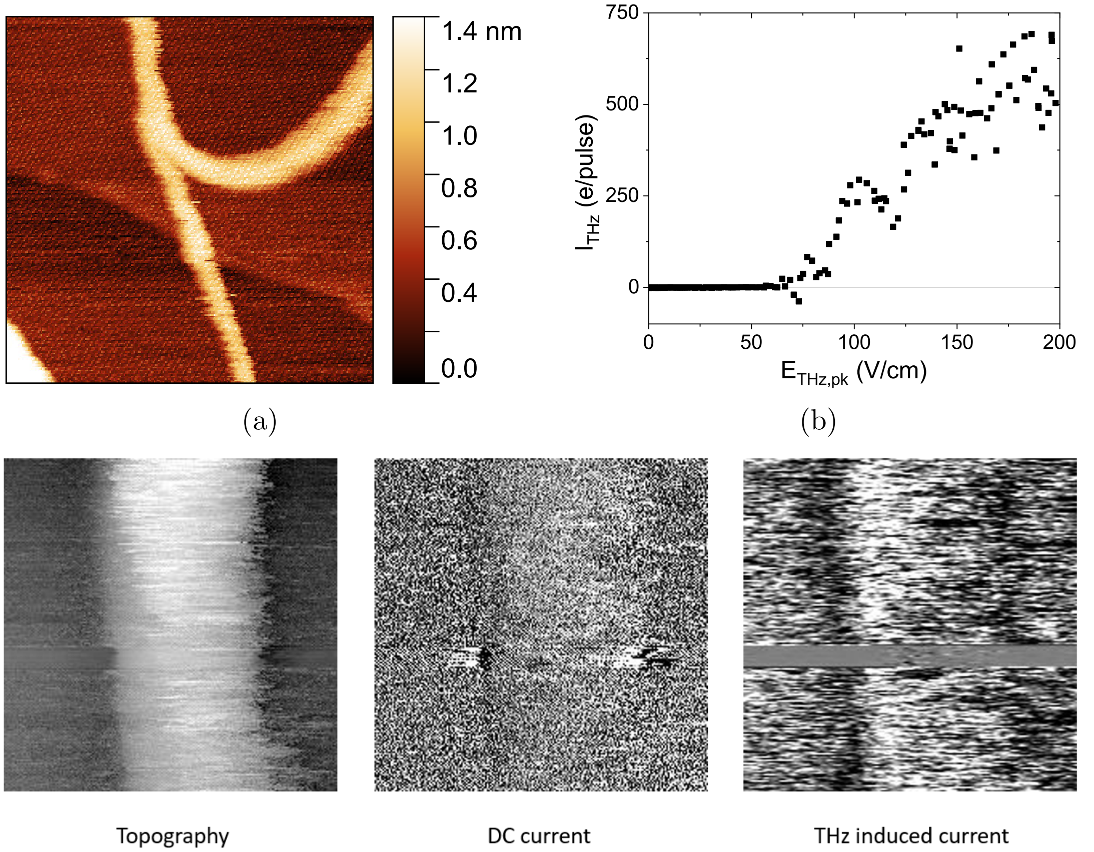

(a) (b)

(c)

Figure 10.3: STM and STS preliminary results from nanotubes on an HOPG substrate, with the first version of the ambient STM. a) STM image of a single nanotube over an atomic step of HOPG. b) Experimental data for an $I_{\mathrm{THz}} - E_{\mathrm{THz}}$ curve on HOPG with a gold tip. c) THz-STM imaging of a SWCNT on HOPG.

with sub-nanometer resolution, such as Fig. 10.3a where a single carbon nanotube and a single step in the HOPG are shown. Free-space propagating THz pulses were also successfully coupled to the STM junction and $I_{\text{THz}} - E_{\text{THz}}$ curves on the HOPG substrate were acquired by lock-in detection (Fig. 10.3b). Furthermore, a THz-STM image of a SWCNT was successfully obtained, as shown in Fig. 10.3c. The topography, the DC current, and the THz-induced current are presented from left to right, respectively. The topography follows the contour of the nanotube, while the DC current channel is technically plain, which indicates that the noise level is the same on the nanotube and the substrate. The last image on the right shows a contrast in the THz-induced current between the nanotube and the substrate. This contrast does not appear in the DC current channel, proving that the signal is actually induced by the THz pulses and not caused by random noise. Moreover, there is a gray fringe in the middle of the THz-STM image where the generation of THz pulses was turned off, which eliminated the THz-induced signal from both the nanotube and the substrate. Although these were just preliminary results, they proved that THz-STM experiments were possible with this system. Unfortunately, this version of the STM could not be properly calibrated because images with atomic resolution could not be obtained due to vibrational and electrical noise in the system, which led to a redesign of the STM.

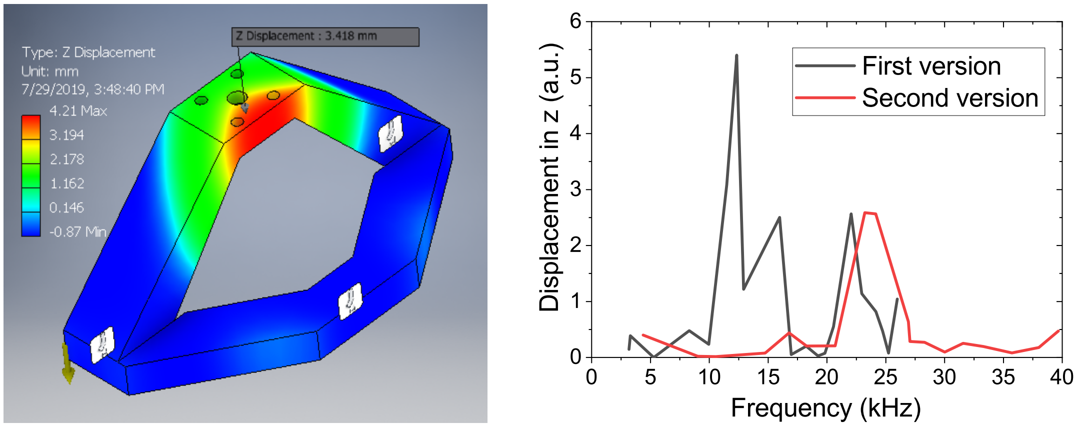

(a)

(b)

Figure 10.4: Redesign of the STM head using finite-element analysis simulations that helped to reduce vibrational modes and to improve the STM performance. a) Finite-element analysis simulation to improve the STM head design. b) Comparison of the vertical displacement of the piezo scanner due to structural vibrational modes on the two STM head designs.

A second version of the ambient STM head was designed using finite-element analysis simulations (Autodesk Inventor 2019) to reduce vibrations on the piezo

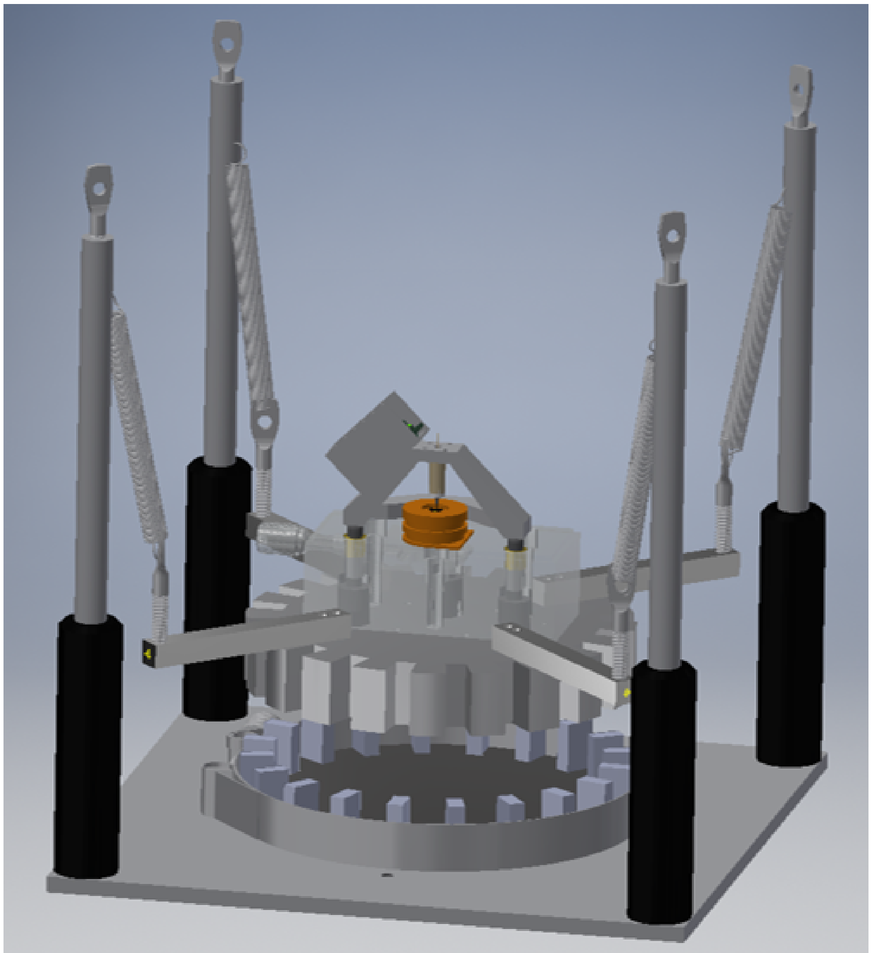

Figure 10.5: Final ambient STM design. The STM core is suspended on springs, and the bottom part forms a vibration damping system based on eddy currents. The STM core is lifted vertically in the image to clearly show the parts of the vibration damping system.

scanner (Fig. 10.4a). This new structural design suppressed the vibrational modes between 10 and 17 kHz, and moved the main peak to a higher frequency (∼ 24 kHz), as shown in Fig. 10.4b. Additionally, to minimize low-frequency vibrations, longer stainless steel springs were used, and a vibration isolation system, based on eddy currents damping, was also integrated into the system, as shown in Fig. 10.5. This new ambient STM system had better performance and was successfully calibrated using topographic images of HOPG with atomic resolution (Fig. 10.6a). A THz beam and a 800 nm pump beam were simultaneously coupled to the STM junction to perform pump-probe experiments. This provided the capability to perform electron photoemission experiments to study the THz near-field waveform at the tip under ambient conditions. In Fig. 10.6b, an example of a THz waveform that was acquired using this technique is presented. This result demonstrated that the custom-built STM was also capable of performing ultrafast pump-probe experiments.

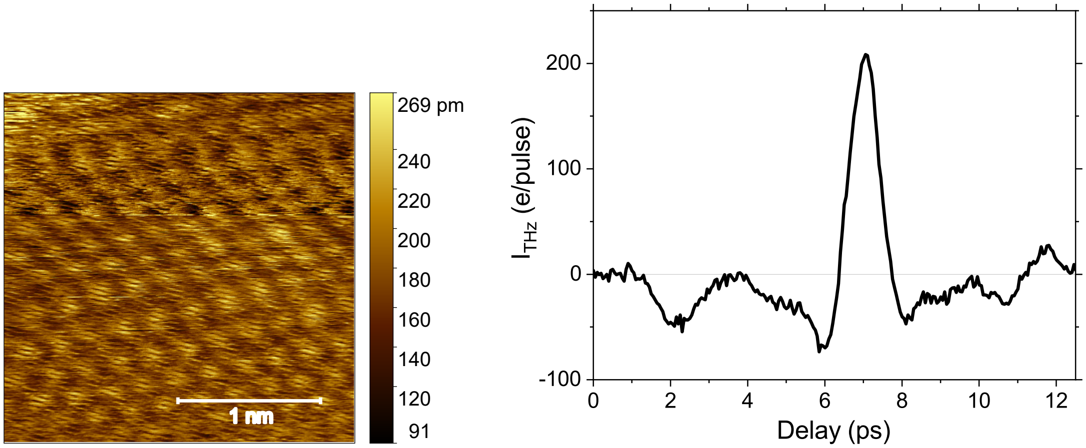

(a)

(b)

Figure 10.6: Experimental results acquired with the second version of the ambient STM system. a) STM image of HOPG with atomic resolution, acquired with $V_DC =$ 0.2 V, $I_{\mathrm{DC}} = 1$ nA and a gold tip. b) THz-induced photoemission current as a function of optical-pump THz-probe delay time. The THz near field waveform was acquired with $V_{\mathrm{DC}} = 4$ V, $E_{\mathrm{THz,pk}} = 480$ V/cm, $P_{\mathrm{pump,avg}} = 95$ mW and a gold tip ∼ 500 nm away from an HOPG sample.

The ambient THz-STM was designed to be flexible and portable in order to be used in different experimental and optical setups. It was built using primarily off-the-shelf components, and its design provides rapid tip and sample turnaround times. The STM system has proven to be useful and has already been used by Christina Strilets to study Au nanoislands on an HOPG substrate (Fig. 10.7), among other samples. The ambient STM is currently being integrated to work with a mode-locked Coherent Mira system that provides 800 nm pulses with 1.3 W of power at a repetition rate of

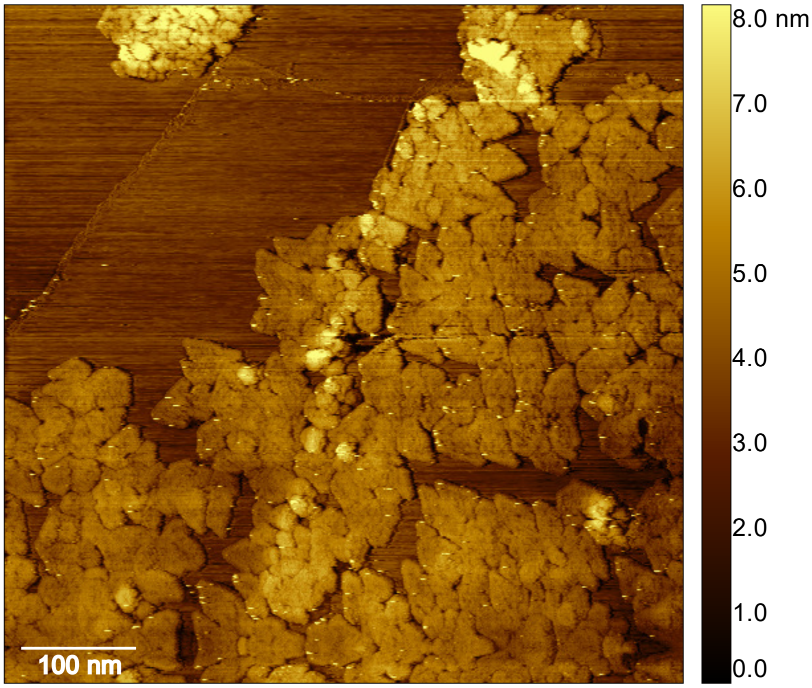

Figure 10.7: STM image of 2 nm of Au deposited on HOPG imaged with a PtIr tip under ambient conditions. The image is 600 nm × 600 nm and was acquired with $V_{\mathrm{DC}} = 1\,\mathrm{V}$ and $I_{\mathrm{DC}} = 800\,\mathrm{pA}$. The image was taken by Christina Strilets.

76 MHz, which would improve the signal-to-noise ratio for the THz-STM system. At this point, the ambient STM is capable of performing all the conventional STM measurements, but more importantly, it has proven to be a useful tool for studying the coupling of THz pulses on the STM junction and for performing photoemission experiments.

Chapter 11

Conclusions and future outlook

This thesis has reported the study of metals and nanostructures with a recently developed technique that uses single-cycle terahertz pulses coupled to the tip of a scanning tunneling microscope (THz-STM) to perform imaging and spectroscopic measurements. Contributions to system characterization and understanding of THz-STM as a research tool have also been presented, and an STM has been specially designed, built and tested to be used for THz-STM experiments in ambient conditions. A wide bandgap semiconductor has been proposed as a substrate candidate suitable for pump-probe experiments after studying the electron photoemission and the thermal expansion of metals and semiconductors in the STM induced by ultrafast near-infrared laser pulses. The required conditions to adequately measure the THz pulse near field waveform at the apex of the STM tip using the photoemission technique have also been discussed.

First, using a gold tip on an Au(111) sample, the amplitude of the THz-induced current signal in the system was experimentally calibrated as described in Chapter 5. The calibration was performed by monitoring the THz-induced current channel as a function of peak amplitude of the THz pulse electric field while the STM was operating in the tunneling regime with the feedback loop on, and a small current setpoint of 2 pA. As the peak electric field increases, the STM tip retracts while the contribution of the THz-induced current to the total current increases until it finally reaches the current setpoint previously defined, which provided the calibration of the system. This also demonstrated the transition between the conventional STM DC mode and the THz-driven mode. The analysis of the total current and the THz-induced current as a function of tip-sample distance showed that the apparent barrier height experienced by the DC fields and the THz fields is different, since the total current could be accurately described with a bi-exponential function. The experimental results obtained on the Au(111) and Cu(111) samples agree with the fact that the large transient THz-induced voltages and the reduced apparent barrier heights mainly produce transient tunneling currents in the field emission regime.

THz-STM studies on single-walled carbon nanotubes deposited on an Au(111) substrate were limited by their damage threshold under the THz fields in our system. However, on the same sample, graphene dendritic islands were identified and investigated in Chapter 6. The same spatial resolution was observed from the contour of graphene islands in STM and THz-STM images. These measurements also showed that structural defects in the dendritic graphene islands, which have been attributed to missing carbon atoms, did not follow the same profile in the THz-STM images as the topography. And an attempt to perform an optical pump-terahertz probe experiment on a single-walled carbon nanotube revealed an undesired electron emission from the sample substrate.

The electron photoemission in the STM was then investigated in Chapter 7 with a gold tip and an Au(111) sample. In this configuration, electron emission from the tip dominates when the optical pump beam is centered at the junction due to the enhancement and confinement of the fields at the tip apex. The electron emission was determined to be caused mainly by multiphoton photoemission. Replacing the gold tip with a tungsten tip, which has a smaller enhancement factor, made the photoemission from the sample more evident. The near field THz pulse waveform measured with the photoemission technique in the STM presented high sensitivity to the position of the optical pump beam and was also affected by the bias voltage and the photoemission from the sample. A high positive bias voltage ensured that only the photoemission from the tip was measured, which would follow the THz near field at the apex. However, eliminating the photoemission from the sample would be preferred, since that would also facilitate the execution of pump-probe experiments.

The study of photoemission from n-type Si-doped GaAs(110), p-type Zn-doped GaAs(110) and p-type Zn-doped GaN samples, in Chapter 8, revealed that a wide bandgap semiconductor with a high work function, such as highly doped p-type GaN, does not produce a photoemission current under illumination of 800 nm laser pulses. Furthermore, measurements of thermal expansion in the STM showed that the GaN sample presented the least thermal expansion. Lack of an atomically flat surface, potential reactivity with other materials, and difficulty to produce and acquire the samples, were some of the disadvantages found for the GaN substrate. However, accurate waveforms of the THz near fields using the photoemission technique were successfully acquired using the p-type GaN sample as a substrate, which makes it a potential candidate for future THz-STM experiments. Finally, in Chapter 10, the design, construction and calibration of an ambient STM specifically developed to be used in THz-STM experiments was presented. The home-built microscope proved its capability to perform as a conventional STM, and preliminary results from THz-STM experiments have also been presented.

Many aspects of the experiments presented here could be further improved. For example, the STM temperature could be decreased to a few K with the use of liquid helium, which would reduce thermal noise and would improve the stability of nanostructures, and the performance of the system in general, during the experiments. The beam spot size of the optical pump beam could be reduced to achieve higher peak intensities and to reduce the area being illuminated at the junction. The beam alignment could also be more accurate with the use of mirrors with positioning actuators that are remotely controlled. The signal-to-noise ratio would be improved with a pulsed laser operating in the MHz range. Regarding the research field in general, several different avenues can be further explored. The application of THz-STM imaging to identify surface features or defects that are not distinguishable in the topographic images has great potential. The accurate control of electron photoemission from a tip and the subsequent manipulation of the electron bunch with a THz pulse field is a technique that can be applied in a transmission electron microscope, which can achieve a higher spatial resolution than the STM. Finding an alternative wide bandgap semiconductor that could be used as a substrate but does not have the disadvantages mentioned for the GaN sample, would definitely impact the performance of pump-probe experiments and would facilitate the measurement of the THz near field waveform with the photoemission technique. And eventually, the study of carrier dynamics in individual nanostructures with high spatial and temporal resolution should be achievable in the THz-STM system.

Bibliography

[1] B. Voigtländer, *Scanning Probe Microscopy*. Springer Berlin Heidelberg, 2015. Available: https://doi.org/10.1007/978-3-662-45240-0.

[2] G. Binnig, H. Rohrer, C. Gerber, and E. Weibel, "Tunneling through a controllable vacuum gap", *Applied Physics Letters*, vol. 40, no. 2, pp. 178–180, 1982. Available: https://doi.org/10.1063/1.92999.

[3] G. Binnig, H. Rohrer, C. Gerber, and E. Weibel, "7x7 reconstruction on si(111) resolved in real space", *Physical Review Letters*, vol. 50, no. 2, pp. 120–123, Jan. 1983. Available: https://doi.org/10.1103/physrevlett.50.120.

[4] C. J. Chen, *Introduction to Scanning Tunneling Microscopy*. Oxford University Press, Sep. 2007. Available: https://doi.org/10.1093/acprof:oso/9780199211500.001.0001.

[5] G. Binnig, C. F. Quate, and C. Gerber, "Atomic force microscope", *Physical Review Letters*, vol. 56, no. 9, pp. 930–933, Mar. 1986. Available: https://doi.org/10.1103/physrevlett.56.930.

[6] C. Böhm, "Electric force microscopy: Gigahertz and nanometer measurement tool", *Microelectronic Engineering*, vol. 31, no. 1-4, pp. 171–179, Feb. 1996. Available: https://doi.org/10.1016/0167-9317(95)00340-1.

[7] Y. Martin and H. K. Wickramasinghe, "Magnetic imaging by "force microscopy" with 1000 Å resolution", *Applied Physics Letters*, vol. 50, no. 20, pp. 1455–1457, May 1987. Available: https://doi.org/10.1063/1.97800.

[8] D. Rugar *et al.*, "Magnetic force microscopy: General principles and application to longitudinal recording media", *Journal of Applied Physics*, vol. 68, no. 3, pp. 1169–1183, Aug. 1990. Available: https://doi.org/10.1063/1.346713.

[9] D. W. Pohl, W. Denk, and M. Lanz, "Optical stethoscopy: Image recording with resolution $\lambda/20$", *Applied Physics Letters*, vol. 44, no. 7, pp. 651–653, Apr. 1984. Available: https://doi.org/10.1063/1.94865.

[10] U. Dürig, D. W. Pohl, and F. Rohner, "Near-field optical-scanning microscopy", *Journal of Applied Physics*, vol. 59, no. 10, pp. 3318–3327, May 1986. Available: https://doi.org/10.1063/1.336848.

[11] H. Fattahi *et al.*, "Third-generation femtosecond technology", *Optica*, vol. 1, no. 1, p. 45, Jul. 2014. Available: https://doi.org/10.1364/optica.1.000045.

[12] P. Jepsen, D. Cooke, and M. Koch, "Terahertz spectroscopy and imaging - modern techniques and applications", *Laser & Photonics Reviews*, vol. 5, no. 1, pp. 124–166, Oct. 2010. Available: https://doi.org/10.1002/lpor.201000011.

[13] R. A. Lewis, "A review of terahertz sources", *Journal of Physics D: Applied Physics*, vol. 47, no. 37, p. 374 001, Aug. 2014. Available: https://doi.org/10.1088/0022-3727/47/37/374001.

[14] R. A. Lewis, "A review of terahertz detectors", *Journal of Physics D: Applied Physics*, vol. 52, no. 43, p. 433 001, Aug. 2019. Available: https://doi.org/10.1088/1361-6463/ab31d5.

[15] J. R. Knab, A. J. L. Adam, E. Shaner, H. J. A. J. Starmans, and P. C. M. Planken, "Terahertz near-field spectroscopy of filled subwavelength sized apertures in thin metal films", *Optics Express*, vol. 21, no. 1, p. 1101, Jan. 2013. Available: https://doi.org/10.1364/oe.21.001101.

[16] O. Mitrofanov *et al.*, "Terahertz pulse propagation through small apertures", *Applied Physics Letters*, vol. 79, no. 7, pp. 907–909, Aug. 2001. Available: https://doi.org/10.1063/1.1392303.

[17] A. J. Macfaden, J. L. Reno, I. Brener, and O. Mitrofanov, "$3\,\mu m$ Aperture probes for near-field terahertz transmission microscopy", *Applied Physics Letters*, vol. 104, no. 1, p. 011 110, Jan. 2014. Available: https://doi.org/10.1063/1.4861621.

[18] T. Kiwa, M. Tonouchi, M. Yamashita, and K. Kawase, "Laser terahertz-emission microscope for inspecting electrical faults in integrated circuits", *Optics Letters*, vol. 28, no. 21, p. 2058, Nov. 2003. Available: https://doi.org/10.1364/ol.28.002058.

[19] M. Wächter, M. Nagel, and H. Kurz, "Tapered photoconductive terahertz field probe tip with subwavelength spatial resolution", *Applied Physics Letters*, vol. 95, no. 4, p. 041 112, Jul. 2009. Available: https://doi.org/10.1063/1.3189702.

[20] N. C. J. van der Valk and P. C. M. Planken, "Electro-optic detection of subwavelength terahertz spot sizes in the near field of a metal tip", *Applied Physics Letters*, vol. 81, no. 9, pp. 1558–1560, Aug. 2002. Available: https://doi.org/10.1063/1.1503404.

[21] A. J. L. Adam *et al.*, "Advanced terahertz electric near-field measurements at sub-wavelength diameter metallic apertures", *Optics Express*, vol. 16, no. 10, p. 7407, May 2008. Available: https://doi.org/10.1364/oe.16.007407.

[22] F. Blanchard and K. Tanaka, "Improving time and space resolution in electro-optic sampling for near-field terahertz imaging", *Optics Letters*, vol. 41, no. 20, p. 4645, Oct. 2016. Available: https://doi.org/10.1364/ol.41.004645.

[23] T. L. Cocker, V. Jelic, R. Hillenbrand, and F. A. Hegmann, "Nanoscale terahertz scanning probe microscopy", *Nature Photonics*, vol. 15, no. 8, pp. 558–569, Jul. 2021. Available: https://doi.org/10.1038/s41566-021-00835-6.

[24] F. Keilmann and R. Hillenbrand, “Near-field microscopy by elastic light scattering from a tip”, *Philosophical Transactions of the Royal Society of London. Series A: Mathematical, Physical and Engineering Sciences*, vol. 362, no. 1817, D. Richards and A. Zayats, Eds., pp. 787–805, Apr. 2004. Available: https://doi.org/10.1098/rsta.2003.1347.

[25] X. Chen *et al.*, “Modern scattering-type scanning near-field optical microscopy for advanced material research”, *Advanced Materials*, vol. 31, no. 24, p. 1 804 774, Apr. 2019. Available: https://doi.org/10.1002/adma.201804774.

[26] G. Keiser and P. Klarskov, “Terahertz field confinement in nonlinear metamaterials and near-field imaging”, *Photonics*, vol. 6, no. 1, p. 22, Feb. 2019. Available: https://doi.org/10.3390/photonics6010022.

[27] S. Kawata and Y. Inouye, “Scanning probe optical microscopy using a metallic probe tip”, *Ultramicroscopy*, vol. 57, no. 2-3, pp. 313–317, Feb. 1995. Available: https://doi.org/10.1016/0304-3991(94)00159-k.

[28] F. Zenhausern, Y. Martin, and H. K. Wickramasinghe, “Scanning interferometric apertureless microscopy: Optical imaging at 10 angstrom resolution”, *Science*, vol. 269, no. 5227, pp. 1083–1085, Aug. 1995. Available: https://doi.org/10.1126/science.269.5227.1083.

[29] H.-T. Chen, R. Kersting, and G. C. Cho, “Terahertz imaging with nanometer resolution”, *Applied Physics Letters*, vol. 83, no. 15, pp. 3009–3011, Oct. 2003. Available: https://doi.org/10.1063/1.1616668.

[30] H.-G. von Ribbeck *et al.*, “Spectroscopic THz near-field microscope”, *Optics Express*, vol. 16, no. 5, p. 3430, 2008. Available: https://doi.org/10.1364/oe.16.003430.

[31] P. Klarskov, H. Kim, V. L. Colvin, and D. M. Mittleman, “Nanoscale laser terahertz emission microscopy”, *ACS Photonics*, vol. 4, no. 11, pp. 2676–2680, Oct. 2017. Available: https://doi.org/10.1021/acsphotonics.7b00870.

[32] T. L. Cocker *et al.*, “An ultrafast terahertz scanning tunnelling microscope”, *Nature Photonics*, vol. 7, no. 8, pp. 620–625, Jul. 2013. Available: https://doi.org/10.1038/nphoton.2013.151.

[33] P. Nguyen, “Coupling terahertz pulses to a scanning tunneling microscope”, *Physics in Canada*, vol. 71, pp. 157–160, Oct. 2015. Available: https://pic-pac.cap.ca/index.php/Issues/showpdf/article/v71n3.0-a2434.pdf.

[34] K. Yoshioka *et al.*, “Real-space coherent manipulation of electrons in a single tunnel junction by single-cycle terahertz electric fields”, *Nature Photonics*, vol. 10, no. 12, pp. 762–765, Nov. 2016. Available: https://doi.org/10.1038/nphoton.2016.205.

[35] T. L. Cocker, D. Peller, P. Yu, J. Repp, and R. Huber, “Tracking the ultrafast motion of a single molecule by femtosecond orbital imaging”, *Nature*, vol. 539, no. 7628, pp. 263–267, Nov. 2016. Available: https://doi.org/10.1038/nature19816.

[36] K. Yoshioka *et al.*, "Tailoring single-cycle near field in a tunnel junction with carrier-envelope phase-controlled terahertz electric fields", *Nano Letters*, vol. 18, no. 8, pp. 5198–5204, Jul. 2018. Available: https://doi.org/10.1021/acs.nanolett.8b02161.

[37] V. Jelic *et al.*, "Ultrafast terahertz control of extreme tunnel currents through single atoms on a silicon surface", *Nature Physics*, vol. 13, no. 6, pp. 591–598, Feb. 2017. Available: https://doi.org/10.1038/nphys4047.

[38] Y. Tian, F. Yang, C. Guo, and Y. Jiang, "Recent advances in ultrafast time-resolved scanning tunneling microscopy", *Surface Review and Letters*, vol. 25, no. Supp01, p. 1 841 003, Dec. 2018. Available: https://doi.org/10.1142/s0218625x18410032.

[39] S. Yoshida *et al.*, "Subcycle transient scanning tunneling spectroscopy with visualization of enhanced terahertz near field", *ACS Photonics*, vol. 6, no. 6, pp. 1356–1364, May 2019. Available: https://doi.org/10.1021/acsphotonics.9b00266.

[40] D. Peller *et al.*, "Sub-cycle atomic-scale forces coherently control a single-molecule switch", *Nature*, vol. 585, no. 7823, pp. 58–62, Sep. 2020. Available: https://doi.org/10.1038/s41586-020-2620-2.

[41] Y. Luo *et al.*, "Nanoscale terahertz STM imaging of a metal surface", *Physical Review B*, vol. 102, no. 20, Nov. 2020. Available: https://doi.org/10.1103/physrevb.102.205417.

[42] M. Müller, N. M. Sabanés, T. Kampfrath, and M. Wolf, "Phase-resolved detection of ultrabroadband THz pulses inside a scanning tunneling microscope junction", *ACS Photonics*, vol. 7, no. 8, pp. 2046–2055, Jul. 2020. Available: https://doi.org/10.1021/acsphotonics.0c00386.

[43] K. Kimura *et al.*, "Terahertz-field-driven scanning tunneling luminescence spectroscopy", *ACS Photonics*, vol. 8, no. 4, pp. 982–987, Jan. 2021. Available: https://doi.org/10.1021/acsphotonics.0c01755.

[44] S. Yoshida *et al.*, "Terahertz scanning tunneling microscopy for visualizing ultrafast electron motion in nanoscale potential variations", *ACS Photonics*, vol. 8, no. 1, pp. 315–323, Jan. 2021. Available: https://doi.org/10.1021/acsphotonics.0c01572.

[45] S. E. Ammerman *et al.*, "Lightwave-driven scanning tunnelling spectroscopy of atomically precise graphene nanoribbons", *Nature Communications*, vol. 12, no. 1, Nov. 2021. Available: https://doi.org/10.1038/s41467-021-26656-3.

[46] S. E. Ammerman, Y. Wei, N. Everett, V. Jelic, and T. L. Cocker, "Algorithm for subcycle terahertz scanning tunneling spectroscopy", *Physical Review B*, vol. 105, no. 11, Mar. 2022. Available: https://doi.org/10.1103/physrevb.105.115427.

[47] N. M. Sabanés, F. Krecinic, T. Kumagai, F. Schulz, M. Wolf, and M. Müller, "Femtosecond thermal and nonthermal hot electron tunneling inside a photoexcited tunnel junction", *ACS Nano*, vol. 16, no. 9, pp. 14 479–14 489, Aug. 2022. Available: https://doi.org/10.1021/acsnano.2c04846.

[48] S. Chen, W. Shi, and W. Ho, "Single-molecule continuous-wave terahertz rectification spectroscopy and microscopy", *Nano Letters*, vol. 23, no. 7, pp. 2915–2920, Mar. 2023. Available: https://doi.org/10.1021/acs.nanolett.3c00271.

[49] H.-J. Güntherodt and R. Wiesendanger, Eds., *Scanning Tunneling Microscopy I*. Springer Berlin Heidelberg, 1992. Available: https://doi.org/10.1007/978-3-642-97343-7.

[50] D. Peller *et al.*, "Quantitative sampling of atomic-scale electromagnetic waveforms", *Nature Photonics*, vol. 15, no. 2, pp. 143–147, Nov. 2020. Available: https://doi.org/10.1038/s41566-020-00720-8.

[51] L. Wimmer, G. Herink, D. R. Solli, S. V. Yalunin, K. E. Echternkamp, and C. Ropers, "Terahertz control of nanotip photoemission", *Nature Physics*, vol. 10, no. 6, pp. 432–436, May 2014. Available: https://doi.org/10.1038/nphys2974.

[52] G. Binnig and H. Rohrer, "Scanning tunneling microscopy—from birth to adolescence", vol. 59, no. 3, pp. 615–625, Jul. 1987. Available: https://doi.org/10.1103/revmodphys.59.615.

[53] C. J. Chen, "Origin of atomic resolution on metal surfaces in scanning tunneling microscopy", vol. 65, no. 4, pp. 448–451, Jul. 1990. Available: https://doi.org/10.1103/physrevlett.65.448.

[54] D. R. Vij, Ed., *Handbook of Applied Solid State Spectroscopy*. Springer US, 2006. Available: https://doi.org/10.1007/0-387-37590-2.

[55] D. J. Griffiths and D. F. Schroeter, *Introduction to Quantum Mechanics*. Cambridge University Press, Aug. 2018. Available: https://doi.org/10.1017/9781316995433.

[56] J. G. Simmons, "Generalized formula for the electric tunnel effect between similar electrodes separated by a thin insulating film", *Journal of Applied Physics*, vol. 34, no. 6, pp. 1793–1803, Jun. 1963. Available: https://doi.org/10.1063/1.1702682.

[57] I. Bâldea and H. Köppel, "Transition voltage spectroscopy in vacuum break junction: The standard tunneling barrier model and beyond", *physica status solidi (b)*, vol. 249, no. 9, pp. 1791–1804, May 2012. Available: https://doi.org/10.1002/pssb.201248034.

[58] L. E. C. van de Leemput and H van Kempen, "Scanning tunnelling microscopy", vol. 55, no. 8, pp. 1165–1240, Aug. 1992. Available: https://doi.org/10.1088/0034-4885/55/8/002.

[59] J. Bardeen, "Tunnelling from a many-particle point of view", *Physical Review Letters*, vol. 6, no. 2, pp. 57–59, Jan. 1961. Available: https://doi.org/10.1103/physrevlett.6.57.

[60] J. Tersoff and D. R. Hamann, “Theory and application for the scanning tunneling microscope”, vol. 50, no. 25, pp. 1998–2001, Jun. 1983. Available: https://doi.org/10.1103/physrevlett.50.1998.

[61] A. D. Gottlieb and L. Wesoloski, “Bardeen’s tunnelling theory as applied to scanning tunnelling microscopy: A technical guide to the traditional interpretation”, vol. 17, no. 8, R57–R65, Mar. 2006. Available: https://doi.org/10.1088/0957-4484/17/8/r01.

[62] J. M. Blanco, F. Flores, and R. Pérez, “STM-theory: Image potential, chemistry and surface relaxation”, *Progress in Surface Science*, vol. 81, no. 10-12, pp. 403–443, Jan. 2006. Available: https://doi.org/10.1016/j.progsurf.2006.07.004.

[63] H. J. Zandvliet and A. van Houselt, “Scanning tunneling spectroscopy”, vol. 2, no. 1, pp. 37–55, Jul. 2009. Available: https://doi.org/10.1146/annurev-anchem-060908-155213.

[64] J. Tersoff and D. R. Hamann, “Theory of the scanning tunneling microscope”, vol. 31, no. 2, pp. 805–813, Jan. 1985. Available: https://doi.org/10.1103/physrevb.31.805.

[65] J. P. Gordon, H. J. Zeiger, and C. H. Townes, “Molecular microwave oscillator and new hyperfine structure in the microwave spectrum of NH3”, vol. 95, no. 1, pp. 282–284, Jul. 1954. Available: https://doi.org/10.1103/physrev.95.282.

[66] J. Hecht, “Beam: The race to make the laser”, *Optics and Photonics News*, vol. 16, no. 7, p. 24, Jul. 2005. Available: https://doi.org/10.1364/opn.16.7.000024.

[67] W. Koechner, *Solid-State Laser Engineering*. Springer New York, 1976. Available: https://doi.org/10.1007/978-1-4757-8519-7.

[68] D. Strickland and G. Mourou, “Compression of amplified chirped optical pulses”, vol. 56, no. 3, pp. 219–221, Dec. 1985. Available: https://doi.org/10.1016/0030-4018(85)90120-8.

[69] P. Maine, D. Strickland, P. Bado, M. Pessot, and G. Mourou, “Generation of ultrahigh peak power pulses by chirped pulse amplification”, vol. 24, no. 2, pp. 398–403, Feb. 1988. Available: https://doi.org/10.1109/3.137.

[70] E. Treacy, “Optical pulse compression with diffraction gratings”, vol. 5, no. 9, pp. 454–458, Sep. 1969. Available: https://doi.org/10.1109/jqe.1969.1076303.

[71] O. E. Martinez, J. P. Gordon, and R. L. Fork, “Negative group-velocity dispersion using refraction”, vol. 1, no. 10, p. 1003, Oct. 1984. Available: https://doi.org/10.1364/josaa.1.001003.

[72] D. E. Spence, P. N. Kean, and W. Sibbett, “60-fsec pulse generation from a self-mode-locked ti:sapphire laser”, vol. 16, no. 1, p. 42, Jan. 1991. Available: https://doi.org/10.1364/ol.16.000042.

[73] Y.-S. Lee, *Principles of Terahertz Science and Technology*. Springer US, 2009. Available: https://doi.org/10.1007/978-0-387-09540-0.

[74] S. Backus, C. G. Durfee, M. M. Murnane, and H. C. Kapteyn, “High power ultrafast lasers”, vol. 69, no. 3, pp. 1207–1223, Mar. 1998. Available: https://doi.org/10.1063/1.1148795.

[75] N. E. Tielking and R. R. Jones, “Coherent population transfer among rydberg states by subpicosecond, half-cycle pulses”, vol. 52, no. 2, pp. 1371–1381, Aug. 1995. Available: https://doi.org/10.1103/physreva.52.1371.

[76] J. Ahn, D. N. Hutchinson, C. Rangan, and P. H. Bucksbaum, “Quantum phase retrieval of a rydberg wave packet using a half-cycle pulse”, vol. 86, no. 7, pp. 1179–1182, Feb. 2001. Available: https://doi.org/10.1103/physrevlett.86.1179.

[77] K. B. Nordstrom *et al.*, “Excitonic dynamical franz-keldysh effect”, *Physical Review Letters*, vol. 81, no. 2, pp. 457–460, Jul. 1998. Available: https://doi.org/10.1103/physrevlett.81.457.

[78] S. G. Carter *et al.*, “Quantum coherence in an optical modulator”, *Science*, vol. 310, no. 5748, pp. 651–653, Oct. 2005. Available: https://doi.org/10.1126/science.1116195.

[79] B. E. Cole, J. B. Williams, B. T. King, M. S. Sherwin, and C. R. Stanley, “Coherent manipulation of semiconductor quantum bits with terahertz radiation”, *Nature*, vol. 410, no. 6824, pp. 60–63, Mar. 2001. Available: https://doi.org/10.1038/35065032.

[80] M. Schall, M. Walther, and P. U. Jepsen, “Fundamental and second-order phonon processes in CdTe and ZnTe”, vol. 64, no. 9, Aug. 2001. Available: https://doi.org/10.1103/physrevb.64.094301.

[81] M. Rini *et al.*, “Control of the electronic phase of a manganite by mode-selective vibrational excitation”, *Nature*, vol. 449, no. 7158, pp. 72–74, Sep. 2007. Available: https://doi.org/10.1038/nature06119.

[82] A. D. Jameson *et al.*, “Transient optical response of quantum well excitons to intense narrowband terahertz pulses”, *Applied Physics Letters*, vol. 95, no. 20, p. 201 107, Nov. 2009. Available: https://doi.org/10.1063/1.3265735.

[83] H. Harde, S. Keiding, and D. Grischkowsky, “THz commensurate echoes: Periodic rephasing of molecular transitions in free-induction decay”, vol. 66, no. 14, pp. 1834–1837, Apr. 1991. Available: https://doi.org/10.1103/physrevlett.66.1834.

[84] D. N. Purschke *et al.*, “Ultrafast photoconductivity and terahertz vibrational dynamics in double-helix SnIP nanowires”, *Advanced Materials*, vol. 33, no. 34, p. 2 100 978, Jul. 2021. Available: https://doi.org/10.1002/adma.202100978.

[85] M. Leahy-Hoppa, M. Fitch, X. Zheng, L. Hayden, and R. Osiander, “Wideband terahertz spectroscopy of explosives”, *Chemical Physics Letters*, vol. 434, no. 4-6, pp. 227–230, Feb. 2007. Available: https://doi.org/10.1016/j.cplett.2006.12.015.

[86] J. F. Federici *et al.*, “THz imaging and sensing for security applications - explosives, weapons and drugs”, *Semiconductor Science and Technology*, vol. 20, no. 7, S266–S280, Jun. 2005. Available: https://doi.org/10.1088/0268-1242/20/7/018.

[87] D. H. Auston and P. R. Smith, “Generation and detection of millimeter waves by picosecond photoconductivity”, vol. 43, no. 7, pp. 631–633, Oct. 1983. Available: https://doi.org/10.1063/1.94468.

[88] D. H. Auston, K. P. Cheung, and P. R. Smith, “Picosecond photoconducting hertzian dipoles”, vol. 45, no. 3, pp. 284–286, Aug. 1984. Available: https://doi.org/10.1063/1.95174.

[89] E. Castro-Camus and M. Alfaro, “Photoconductive devices for terahertz pulsed spectroscopy: A review [invited]”, vol. 4, no. 3, A36, Jun. 2016. Available: https://doi.org/10.1364/prj.4.000a36.

[90] R. Bogue, “Sensing with terahertz radiation: A review of recent progress”, vol. 38, no. 2, pp. 216–222, Mar. 2018. Available: https://doi.org/10.1108/sr-10-2017-0221.

[91] D. R. Bacon, J. Madéo, and K. M. Dani, “Photoconductive emitters for pulsed terahertz generation”, vol. 23, no. 6, p. 064 001, Apr. 2021. Available: https://doi.org/10.1088/2040-8986/abf6ba.

[92] D. Auston and M. Nuss, “Electrooptical generation and detection of femtosecond electrical transients”, vol. 24, no. 2, pp. 184–197, Feb. 1988. Available: https://doi.org/10.1109/3.114.

[93] A. Ibrahim, D. Férachou, G. Sharma, K. Singh, M. Kirouac-Turmel, and T. Ozaki, “Ultra-high dynamic range electro-optic sampling for detecting millimeter and sub-millimeter radiation”, *Scientific Reports*, vol. 6, no. 1, Mar. 2016. Available: https://doi.org/10.1038/srep23107.

[94] R. J. Hamers and D. G. Cahill, “Ultrafast time resolution in scanned probe microscopies”, vol. 57, no. 19, pp. 2031–2033, Nov. 1990. Available: https://doi.org/10.1063/1.103997.

[95] S. Weiss, D. Botkin, D. F. Ogletree, M. Salmeron, and D. S. Chemla, “The ultrafast response of a scanning tunneling microscope”, vol. 188, no. 1, pp. 343–359, Mar. 1995. Available: https://doi.org/10.1002/pssb.2221880132.

[96] R. H. M. Groeneveld and H. van Kempen, “The capacitive origin of the picosecond electrical transients detected by a photoconductively gated scanning tunneling microscope”, vol. 69, no. 15, pp. 2294–2296, Oct. 1996. Available: https://doi.org/10.1063/1.117538.

[97] M. Freeman, A. Elezzabi, G. Steeves, and G. Nunes, “Ultrafast time resolution in scanning tunneling microscopy”, vol. 386, no. 1-3, pp. 290–300, Oct. 1997. Available: https://doi.org/10.1016/s0039-6028(97)00306-3.

[98] M. J. Feldstein, P. Vöhringer, W. Wang, and N. F. Scherer, “Femtosecond optical spectroscopy and scanning probe microscopy”, vol. 100, no. 12, pp. 4739–4748, Jan. 1996. Available: https://doi.org/10.1021/jp9517918.

[99] N. N. Khusnatdinov, T. J. Nagle, and G. Nunes, “Ultrafast scanning tunneling microscopy with 1 nm resolution”, vol. 77, no. 26, pp. 4434–4436, Dec. 2000. Available: https://doi.org/10.1063/1.1336817.

[100] V. Gerstner, A. Knoll, W. Pfeiffer, A. Thon, and G. Gerber, “Femtosecond laser assisted scanning tunneling microscopy”, vol. 88, no. 8, p. 4851, 2000. Available: https://doi.org/10.1063/1.1290706.

[101] O. Takeuchi, R. Morita, M. Yamashita, and H. Shigekawa, “Development of time-resolved scanning tunneling microscopy in femtosecond range”, vol. 41, no. Part 1, No. 7B, pp. 4994–4997, Jul. 2002. Available: https://doi.org/10.1143/jjap.41.4994.

[102] Y. Terada, M. Aoyama, H. Kondo, A. Taninaka, O. Takeuchi, and H. Shigekawa, “Ultrafast photoinduced carrier dynamics in GaNAs probed using femtosecond time-resolved scanning tunnelling microscopy”, vol. 18, no. 4, p. 044 028, Dec. 2006. Available: https://doi.org/10.1088/0957-4484/18/4/044028.

[103] N. Behr and M. B. Raschke, “Optical antenna properties of scanning probe tips: plasmonic light scattering, tip-sample coupling, and near-field enhancement”, *The Journal of Physical Chemistry C*, vol. 112, no. 10, pp. 3766–3773, Mar. 2008. Available: https://doi.org/10.1021/jp7098009.

[104] W. Zhang, X. Cui, and O. J. F. Martin, “Local field enhancement of an infinite conical metal tip illuminated by a focused beam”, *Journal of Raman Spectroscopy*, vol. 40, no. 10, pp. 1338–1342, Sep. 2009. Available: https://doi.org/10.1002/jrs.2439.

[105] S. Thomas, G. Wachter, C. Lemell, J. Burgdörfer, and P. Hommelhoff, “Large optical field enhancement for nanotips with large opening angles”, *New Journal of Physics*, vol. 17, no. 6, p. 063 010, Jun. 2015. Available: https://doi.org/10.1088/1367-2630/17/6/063010.

[106] M. Walther, G. S. Chambers, Z. Liu, M. R. Freeman, and F. A. Hegmann, “Emission and detection of terahertz pulses from a metal-tip antenna”, *Journal of the Optical Society of America B*, vol. 22, no. 11, p. 2357, Nov. 2005. Available: https://doi.org/10.1364/josab.22.002357.

[107] L. Novotny and B. Hecht, “Near-field optical probes”, in *Principles of Nano-Optics*, Cambridge University Press, 2012, pp. 173–224. Available: https://doi.org/10.1017/cbo9780511813535.007.

[108] C. A. Balanis, Ed., *Modern Antenna Handbook*. Wiley, Nov. 2007. Available: https://doi.org/10.1002/9780470294154.

[109] T. Taubner, R. Hillenbrand, and F. Keilmann, "Performance of visible and mid-infrared scattering-type near-field optical microscopes", *Journal of Microscopy*, vol. 210, no. 3, pp. 311–314, Jun. 2003. Available: https://doi.org/10.1046/j.1365-2818.2003.01164.x.

[110] C. Girard, C. Joachim, and S. Gauthier, "The physics of the near-field", *Reports on Progress in Physics*, vol. 63, no. 6, pp. 893–938, May 2000. Available: https://doi.org/10.1088/0034-4885/63/6/202.

[111] E. G. Bortchagovsky, "Simple modeling of the ratio of fields at a tip and at contacting surface", *Nanospectroscopy*, vol. 2, no. 1, Jan. 2016. Available: https://doi.org/10.1515/nansp-2016-0002.

[112] E. Bortchagovsky, "Simple modeling of the ratio of fields at a tip and a contacting surface with external illumination", *Journal of Nanotechnology*, vol. 2018, pp. 1–6, Aug. 2018. Available: https://doi.org/10.1155/2018/3898524.

[113] A. J. Adam, N. C. van der Valk, and P. C. Planken, "Measurement and calculation of the near field of a terahertz apertureless scanning optical microscope", *Journal of the Optical Society of America B*, vol. 24, no. 5, p. 1080, Apr. 2007. Available: https://doi.org/10.1364/josab.24.001080.

[114] P. C. M. Planken and N. C. J. van der Valk, "Spot-size reduction in terahertz apertureless near-field imaging", *Optics Letters*, vol. 29, no. 19, p. 2306, Oct. 2004. Available: https://doi.org/10.1364/ol.29.002306.

[115] K. Wang, D. M. Mittleman, N. C. J. van der Valk, and P. C. M. Planken, "Antenna effects in terahertz apertureless near-field optical microscopy", *Applied Physics Letters*, vol. 85, no. 14, pp. 2715–2717, Oct. 2004. Available: https://doi.org/10.1063/1.1797554.

[116] J. Houard, L. Arnoldi, A. Ayoub, A. Hideur, and A. Vella, "Nanotip response to monocycle terahertz pulses", *Applied Physics Letters*, vol. 117, no. 15, p. 151 105, Oct. 2020. Available: https://doi.org/10.1063/5.0022182.

[117] V. Jelic, "Imaging ultrafast dynamics on the atomic scale with a terahertz scanning tunneling microscope", Ph.D. dissertation, University of Alberta, 2019. Available: https://era.library.ualberta.ca/items/718be8a4-d91e-4bd0-bac0-b0360ba711ea.

[118] C. Crowell, "The richardson constant for thermionic emission in schottky barrier diodes", *Solid-State Electronics*, vol. 8, no. 4, pp. 395–399, Apr. 1965. Available: https://doi.org/10.1016/0038-1101(65)90116-4.

[119] "Electron emission in intense electric fields", *Proceedings of the Royal Society of London. Series A, Containing Papers of a Mathematical and Physical Character*, vol. 119, no. 781, pp. 173–181, May 1928. Available: https://doi.org/10.1098/rspa.1928.0091.

[120] G. N. Fursey, "Deviations from the fowler–nordheim theory and peculiarities of field electron emission from small-scale objects", *Journal of Vacuum Science & Technology B*, vol. 16, no. 2, p. 910, Mar. 1998. Available: https://doi.org/10.1116/1.589929.

[121] P. Cutler, J. He, J. Miller, N. Miskovsky, B. Weiss, and T. Sullivan, "Theory of electron emission in high fields from atomically sharp emitters: Validity of the fowler-nordheim equation", *Progress in Surface Science*, vol. 42, no. 1-4, pp. 169–185, Jan. 1993. Available: https://doi.org/10.1016/0079-6816(93)90068-7.

[122] A Modinos, "Field, thermionic, and secondary electron emission spectroscopy", Jan. 1984. Available: https://www.osti.gov/biblio/5110755.

[123] W. E. Spicer, "Photoemissive, photoconductive, and optical absorption studies of alkali-antimony compounds", *Physical Review*, vol. 112, no. 1, pp. 114–122, Oct. 1958. Available: https://doi.org/10.1103/physrev.112.114.

[124] C. N. Berglund and W. E. Spicer, "Photoemission studies of copper and silver: Theory", *Physical Review*, vol. 136, no. 4A, A1030–A1044, Nov. 1964. Available: https://doi.org/10.1103/physrev.136.a1030.

[125] W. F. Krolikowski and W. E. Spicer, "Photoemission studies of the noble metals. i. copper", *Physical Review*, vol. 185, no. 3, pp. 882–900, Sep. 1969. Available: https://doi.org/10.1103/physrev.185.882.

[126] W. F. Krolikowski and W. E. Spicer, "Photoemission studies of the noble metals. II. gold", *Physical Review B*, vol. 1, no. 2, pp. 478–487, Jan. 1970. Available: https://doi.org/10.1103/physrevb.1.478.

[127] R. H. Fowler, "The analysis of photoelectric sensitivity curves for clean metals at various temperatures", *Physical Review*, vol. 38, no. 1, pp. 45–56, Jul. 1931. Available: https://doi.org/10.1103/physrev.38.45.

[128] L. A. DuBridge, "A further experimental test of fowler's theory of photoelectric emission", *Physical Review*, vol. 39, no. 1, pp. 108–118, Jan. 1932. Available: https://doi.org/10.1103/physrev.39.108.

[129] L. A. DuBridge, "Theory of the energy distribution of photoelectrons", *Physical Review*, vol. 43, no. 9, pp. 727–741, May 1933. Available: https://doi.org/10.1103/physrev.43.727.

[130] Y. Zhou and P. Zhang, "A quantum model for photoemission from metal surfaces and its comparison with the three-step model and fowler–DuBridge model", *Journal of Applied Physics*, vol. 127, no. 16, p. 164 903, Apr. 2020. Available: https://doi.org/10.1063/5.0004140.

[131] K. L. Jensen, "Electron emission physics", in *Electron Emission Physics*, Elsevier, 2007, pp. 147–279. Available: https://doi.org/10.1016/s1076-5670(07)49003-6.

[132] L. V. Keldysh, "Ionization in the field of a strong electromagnetic wave", *Zh. Eksperim. i Teor. Fiz.*, vol. Vol: 47, Nov. 1964. Available: https://www.osti.gov/biblio/4662394.

[133] G Mainfray and G Manus, "Multiphoton ionization of atoms", *Reports on Progress in Physics*, vol. 54, no. 10, pp. 1333–1372, Oct. 1991. Available: https://doi.org/10.1088/0034-4885/54/10/002.

[134] B. D. Guenther, *Encyclopedia of modern optics*. Amsterdam: Elsevier Science Direct Academic Press, 2005.

[135] G. S. He, "Multi-photon excitation based nonlinear optical effects and applications", in *Progress in Optics*, Elsevier, 2019, pp. 155–278. Available: https://doi.org/10.1016/bs.po.2019.01.001.

[136] J. P. Girardeau-Montaut and C. Girardeau-Montaut, "Theory of ultrashort nonlinear multiphoton photoelectric emission from metals", *Physical Review B*, vol. 51, no. 19, pp. 13 560–13 567, May 1995. Available: https://doi.org/10.1103/physrevb.51.13560.

[137] J. H. Bechtel, W. L. Smith, and N. Bloembergen, "Two-photon photoemission from metals induced by picosecond laser pulses", *Physical Review B*, vol. 15, no. 10, pp. 4557–4563, May 1977. Available: https://doi.org/10.1103/physrevb.15.4557.

[138] E. M. Brunkow, "Investigations of novel sources of spin-polarized electrons", English, Copyright - Database copyright ProQuest LLC; ProQuest does not claim copyright in the individual underlying works; Last updated - 2021-05-26, Ph.D. dissertation, 2018, p. 148. Available: https://digitalcommons.unl.edu/physicsdiss/43/.

[139] P. Dombi *et al.*, "Strong-field nano-optics", *Reviews of Modern Physics*, vol. 92, no. 2, Jun. 2020. Available: https://doi.org/10.1103/revmodphys.92.025003.

[140] M. J. G. Lee, "Field emission of hot electrons from tungsten", *Physical Review Letters*, vol. 30, no. 24, pp. 1193–1196, Jun. 1973. Available: https://doi.org/10.1103/physrevlett.30.1193.

[141] M. Pant and L. K. Ang, "Ultrafast laser-induced electron emission from multiphoton to optical tunneling", *Physical Review B*, vol. 86, no. 4, Jul. 2012. Available: https://doi.org/10.1103/physrevb.86.045423.

[142] L. K. Ang and M. Pant, "Generalized model for ultrafast laser induced electron emission from a metal tip", *Physics of Plasmas*, vol. 20, no. 5, p. 056 705, May 2013. Available: https://doi.org/10.1063/1.4803086.

[143] A. Dreyhaupt, S. Winnerl, T. Dekorsy, and M. Helm, "High-intensity terahertz radiation from a microstructured large-area photoconductor", *Applied Physics Letters*, vol. 86, no. 12, p. 121 114, Mar. 2005. Available: https://doi.org/10.1063/1.1891304.

[144] M. Beck *et al.*, "Impulsive terahertz radiation with high electric fields from an amplifier-driven large-area photoconductive antenna", *Optics Express*, vol. 18, no. 9, p. 9251, Apr. 2010. Available: https://doi.org/10.1364/oe.18.009251.

[145] B. Ren, G. Picardi, and B. Pettinger, "Preparation of gold tips suitable for tip-enhanced raman spectroscopy and light emission by electrochemical etching", *Review of Scientific Instruments*, vol. 75, no. 4, pp. 837–841, Apr. 2004. Available: https://doi.org/10.1063/1.1688442.

[146] J. P. Ibe *et al.*, "On the electrochemical etching of tips for scanning tunneling microscopy", *Journal of Vacuum Science & Technology A*, vol. 8, no. 4, pp. 3570–3575, Jul. 1990. Available: https://doi.org/10.1116/1.576509.

[147] J. Garnaes, F. Kragh, K. A. Mo/rch, and A. R. Thölén, "Transmission electron microscopy of scanning tunneling tips", *Journal of Vacuum Science & Technology A*, vol. 8, no. 1, pp. 441–444, Jan. 1990. Available: https://doi.org/10.1116/1.576417.

[148] I. Ekvall, E. Wahlström, D. Claesson, H. Olin, and E. Olsson, "Preparation and characterization of electrochemically etched w tips for STM", *Measurement Science and Technology*, vol. 10, no. 1, pp. 11–18, Jan. 1999. Available: https://doi.org/10.1088/0957-0233/10/1/006.

[149] L. Ottaviano, L. Lozzi, and S. Santucci, "Scanning auger microscopy study of w tips for scanning tunneling microscopy", *Review of Scientific Instruments*, vol. 74, no. 7, pp. 3368–3378, Jul. 2003. Available: https://doi.org/10.1063/1.1581392.

[150] S. Ernst, S. Wirth, M. Rams, V. Dolocan, and F. Steglich, "Tip preparation for usage in an ultra-low temperature UHV scanning tunneling microscope", *Science and Technology of Advanced Materials*, vol. 8, no. 5, pp. 347–351, Jan. 2007. Available: https://doi.org/10.1016/j.stam.2007.05.008.

[151] A. P. Janssen and J. P. Jones, "The sharpening of field emitter tips by ion sputtering", *Journal of Physics D: Applied Physics*, vol. 4, no. 1, pp. 118–123, Jan. 1971. Available: https://doi.org/10.1088/0022-3727/4/1/316.

[152] S. Meier, T. Higuchi, M. Nutz, A. Högele, and P. Hommelhoff, "High spatial coherence in multiphoton-photoemitted electron beams", *Applied Physics Letters*, vol. 113, no. 14, p. 143 101, Oct. 2018. Available: https://doi.org/10.1063/1.5045282.

[153] C. Ropers, D. R. Solli, C. P. Schulz, C. Lienau, and T. Elsaesser, "Localized multiphoton emission of femtosecond electron pulses from metal nanotips", *Physical Review Letters*, vol. 98, no. 4, Jan. 2007. Available: https://doi.org/10.1103/physrevlett.98.043907.

[154] R. G. Musket, W. McLean, C. A. Colemenares, and W. J. Siekhaus, "Atomically clean surfaces of elemental solids", in Springer US, 2002, pp. 63–143. Available: https://doi.org/10.1007/0-306-46913-8_4.

[155] J. V. Barth, H. Brune, G. Ertl, and R. J. Behm, “Scanning tunneling microscopy observations on the reconstructed au(111) surface: Atomic structure, long-range superstructure, rotational domains, and surface defects”, *Physical Review B*, vol. 42, no. 15, pp. 9307–9318, Nov. 1990. Available: https://doi.org/10.1103/physrevb.42.9307.

[156] K. Schouteden, P. Lievens, and C. V. Haesendonck, “Fourier-transform scanning tunneling microscopy investigation of the energy versus wave vector dispersion of electrons at the au(111) surface”, *Physical Review B*, vol. 79, no. 19, May 2009. Available: https://doi.org/10.1103/physrevb.79.195409.

[157] T. Andreev, I. Barke, and H. Hövel, “Adsorbed rare-gas layers on au(111): shift of the shockley surface state studied with ultraviolet photoelectron spectroscopy and scanning tunneling spectroscopy”, vol. 70, no. 20, Nov. 2004. Available: https://doi.org/10.1103/physrevb.70.205426.

[158] S. Kawai *et al.*, “Atomically controlled substitutional boron-doping of graphene nanoribbons”, vol. 6, no. 1, Aug. 2015. Available: https://doi.org/10.1038/ncomms9098.

[159] W. Sachtler, G. Dorgelo, and A. Holscher, “The work function of gold”, vol. 5, no. 2, pp. 221–229, Oct. 1966. Available: https://doi.org/10.1016/0039-6028(66)90083-5.

[160] D. D. L. Chung, “Review graphite”, vol. 37, no. 8, pp. 1475–1489, 2002. Available: https://doi.org/10.1023/a:1014915307738.

[161] N. Savvides and T. Bell, “Hardness and elastic modulus of diamond and diamond-like carbon films”, *Thin Solid Films*, vol. 228, no. 1-2, pp. 289–292, May 1993. Available: https://doi.org/10.1016/0040-6090(93)90618-y.

[162] K. S. Novoselov *et al.*, “Electric field effect in atomically thin carbon films”, vol. 306, no. 5696, pp. 666–669, Oct. 2004. Available: https://doi.org/10.1126/science.1102896.

[163] K. S. Novoselov, V. I. Fal′ko, L. Colombo, P. R. Gellert, M. G. Schwab, and K. Kim, “A roadmap for graphene”, vol. 490, no. 7419, pp. 192–200, Oct. 2012. Available: https://doi.org/10.1038/nature11458.

[164] A. K. Geim and K. S. Novoselov, “The rise of graphene”, vol. 6, no. 3, pp. 183–191, Mar. 2007. Available: https://doi.org/10.1038/nmat1849.

[165] Y. Hernandez *et al.*, “High-yield production of graphene by liquid-phase exfoliation of graphite”, vol. 3, no. 9, pp. 563–568, Aug. 2008. Available: https://doi.org/10.1038/nnano.2008.215.

[166] C. Oshima and A. Nagashima, “Ultra-thin epitaxial films of graphite and hexagonal boron nitride on solid surfaces”, vol. 9, no. 1, pp. 1–20, Jan. 1997. Available: https://doi.org/10.1088/0953-8984/9/1/004.

[167] S. Stankovich *et al.*, “Synthesis of graphene-based nanosheets via chemical reduction of exfoliated graphite oxide”, vol. 45, no. 7, pp. 1558–1565, Jun. 2007. Available: https://doi.org/10.1016/j.carbon.2007.02.034.

[168] A. Reina *et al.*, "Large area, few-layer graphene films on arbitrary substrates by chemical vapor deposition", vol. 9, no. 1, pp. 30–35, Jan. 2009. Available: https://doi.org/10.1021/nl801827v.

[169] C. Lee, X. Wei, J. W. Kysar, and J. Hone, "Measurement of the elastic properties and intrinsic strength of monolayer graphene", *Science*, vol. 321, no. 5887, pp. 385–388, Jul. 2008. Available: https://doi.org/10.1126/science.1157996.

[170] A. A. Balandin *et al.*, "Superior thermal conductivity of single-layer graphene", *Nano Letters*, vol. 8, no. 3, pp. 902–907, Feb. 2008. Available: https://doi.org/10.1021/nl0731872.

[171] K. I. Bolotin, K. J. Sikes, J. Hone, H. L. Stormer, and P. Kim, "Temperature-dependent transport in suspended graphene", *Physical Review Letters*, vol. 101, no. 9, Aug. 2008. Available: https://doi.org/10.1103/physrevlett.101.096802.

[172] A. S. Mayorov *et al.*, "Micrometer-scale ballistic transport in encapsulated graphene at room temperature", *Nano Letters*, vol. 11, no. 6, pp. 2396–2399, May 2011. Available: https://doi.org/10.1021/nl200758b.

[173] A. K. Geim, "Graphene: Status and prospects", vol. 324, no. 5934, pp. 1530–1534, Jun. 2009. Available: https://doi.org/10.1126/science.1158877.

[174] JCrystalSoft, *Nanotube modeler*, version 1.8.0, Oct. 1, 2010. Available: http://www.jcrystal.com/products/wincnt/.

[175] P. Bøggild *et al.*, "Mapping the electrical properties of large-area graphene", *2D Materials*, vol. 4, no. 4, p. 042 003, Sep. 2017. Available: https://doi.org/10.1088/2053-1583/aa8683.

[176] S. A. Jensen *et al.*, "Ultrafast photoconductivity of graphene nanoribbons and carbon nanotubes", *Nano Letters*, vol. 13, no. 12, pp. 5925–5930, Nov. 2013. Available: https://doi.org/10.1021/nl402978s.

[177] S. Iijima, "Helical microtubules of graphitic carbon", vol. 354, no. 6348, pp. 56–58, Nov. 1991. Available: https://doi.org/10.1038/354056a0.

[178] R. Shoukat and M. I. Khan, "Carbon nanotubes: A review on properties, synthesis methods and applications in micro and nanotechnology", Jan. 2021. Available: https://doi.org/10.1007/s00542-021-05211-6.

[179] T. W. Odom, J.-L. Huang, P. Kim, and C. M. Lieber, "Atomic structure and electronic properties of single-walled carbon nanotubes", vol. 391, no. 6662, pp. 62–64, Jan. 1998. Available: https://doi.org/10.1038/34145.

[180] S. M. Bachilo, M. S. Strano, C. Kittrell, R. H. Hauge, R. E. Smalley, and R. B. Weisman, "Structure-assigned optical spectra of single-walled carbon nanotubes", vol. 298, no. 5602, pp. 2361–2366, Dec. 2002. Available: https://doi.org/10.1126/science.1078727.

[181] S. Rathinavel, K. Priyadharshini, and D. Panda, “A review on carbon nanotube: An overview of synthesis, properties, functionalization, characterization, and the application”, vol. 268, p. 115 095, Jun. 2021. Available: https://doi.org/10.1016/j.mseb.2021.115095.

[182] R Saito, G Dresselhaus, and M. Dresselhaus, “Physical properties of carbon nanotubes. 1998”, *Imperial College, London*, 2007.

[183] G. R. A. Jamal and S. M. Mominuzzaman, “Universal empirical formula for optical transition energies of semiconducting single-walled carbon nanotubes”, *AIP Advances*, vol. 6, no. 1, p. 015 012, Jan. 2016. Available: https://doi.org/10.1063/1.4940761.

[184] A. Roch *et al.*, “Optical absorption spectroscopy and properties of single walled carbon nanotubes at high temperature”, vol. 197, pp. 182–187, Nov. 2014. Available: https://doi.org/10.1016/j.synthmet.2014.09.016.

[185] Z. Yao, C. L. Kane, and C. Dekker, “High-field electrical transport in single-wall carbon nanotubes”, vol. 84, no. 13, pp. 2941–2944, Mar. 2000. Available: https://doi.org/10.1103/physrevlett.84.2941.

[186] J. P. Lu, “Elastic properties of carbon nanotubes and nanoropes”, *Physical Review Letters*, vol. 79, no. 7, pp. 1297–1300, Aug. 1997. Available: https://doi.org/10.1103/physrevlett.79.1297.

[187] K. Tserpes and P. Papanikos, “Finite element modeling of single-walled carbon nanotubes”, *Composites Part B: Engineering*, vol. 36, no. 5, pp. 468–477, Jul. 2005. Available: https://doi.org/10.1016/j.compositesb.2004.10.003.

[188] M. Yudasaka, T. Ichihashi, D. Kasuya, H. Kataura, and S. Iijima, “Structure changes of single-wall carbon nanotubes and single-wall carbon nanohorns caused by heat treatment”, *Carbon*, vol. 41, no. 6, pp. 1273–1280, 2003. Available: https://doi.org/10.1016/s0008-6223(03)00076-9.

[189] P. Nikolaev, A. Thess, A. G. Rinzler, D. T. Colbert, and R. E. Smalley, “Diameter doubling of single-wall nanotubes”, *Chemical Physics Letters*, vol. 266, no. 5-6, pp. 422–426, Mar. 1997. Available: https://doi.org/10.1016/s0009-2614(97)00053-5.

[190] T. Jiang *et al.*, “Toxicity of single-walled carbon nanotubes (SWCNTs): Effect of lengths, functional groups and electronic structures revealed by a quantitative toxicogenomics assay”, vol. 7, no. 5, pp. 1348–1364, 2020. Available: https://doi.org/10.1039/d0en00230e.

[191] G. A. Timerbulatova and L. M. Fatkhutdinova, “Assessment of the toxicity of single-wall carbon nanotubes using different types of cell cultures: Review of the current state of knowledge”, vol. 13, no. 5-6, pp. 240–245, May 2018. Available: https://doi.org/10.1134/s1995078018030187.

[192] A. M. Rao *et al.*, “Effect of van der waals interactions on the raman modes in single walled carbon nanotubes”, *Physical Review Letters*, vol. 86, no. 17, pp. 3895–3898, Apr. 2001. Available: https://doi.org/10.1103/physrevlett.86.3895.

[193] Q. Cheng, S. Debnath, E. Gregan, and H. J. Byrne, “Effect of solvent solubility parameters on the dispersion of single-walled carbon nanotubes”, *The Journal of Physical Chemistry C*, vol. 112, no. 51, pp. 20 154–20 158, Nov. 2008. Available: https://doi.org/10.1021/jp8067188.

[194] Q. Cheng, S. Debnath, L. O’Neill, T. G. Hedderman, E. Gregan, and H. J. Byrne, “Systematic study of the dispersion of SWNTs in organic solvents”, vol. 114, no. 11, pp. 4857–4863, Mar. 2010. Available: https://doi.org/10.1021/jp911202d.

[195] K. D. Ausman, R. Piner, O. Lourie, R. S. Ruoff, and M. Korobov, “Organic solvent dispersions of single-walled carbon nanotubes: toward solutions of pristine nanotubes”, *The Journal of Physical Chemistry B*, vol. 104, no. 38, pp. 8911–8915, Sep. 2000. Available: https://doi.org/10.1021/jp002555m.

[196] D. V. Kosynkin *et al.*, “Longitudinal unzipping of carbon nanotubes to form graphene nanoribbons”, vol. 458, no. 7240, pp. 872–876, Apr. 2009. Available: https://doi.org/10.1038/nature07872.

[197] F. Hennrich *et al.*, “The mechanism of cavitation-induced scission of single-walled carbon nanotubes”, *The Journal of Physical Chemistry B*, vol. 111, no. 8, pp. 1932–1937, Feb. 2007. Available: https://doi.org/10.1021/jp065262n.

[198] A. Lucas, C. Zakri, M. Maugey, M. Pasquali, P. van der Schoot, and P. Poulin, “Kinetics of nanotube and microfiber scission under sonication”, *The Journal of Physical Chemistry C*, vol. 113, no. 48, pp. 20 599–20 605, Nov. 2009. Available: https://doi.org/10.1021/jp906296y.

[199] Q. Cheng, S. Debnath, E. Gregan, and H. J. Byrne, “Ultrasound-assisted SWNTs dispersion: Effects of sonication parameters and solvent properties”, *The Journal of Physical Chemistry C*, vol. 114, no. 19, pp. 8821–8827, Apr. 2010. Available: https://doi.org/10.1021/jp101431h.

[200] R. Arrigo, R. Teresi, C. Gambarotti, F. Parisi, G. Lazzara, and N. Dintcheva, “Sonication-induced modification of carbon nanotubes: Effect on the rheological and thermo-oxidative behaviour of polymer-based nanocomposites”, *Materials*, vol. 11, no. 3, p. 383, Mar. 2018. Available: https://doi.org/10.3390/ma11030383.

[201] S. D. Bergin, Z. Sun, P. Streich, J. Hamilton, and J. N. Coleman, “New solvents for nanotubes: Approaching the dispersibility of surfactants”, *The Journal of Physical Chemistry C*, vol. 114, no. 1, pp. 231–237, Dec. 2009. Available: https://doi.org/10.1021/jp908923m.

[202] A. J. Martínez-Galera, I. Brihuega, and J. M. Gómez-Rodríguez, "Ethylene irradiation: A new route to grow graphene on low reactivity metals", vol. 11, no. 9, pp. 3576–3580, Aug. 2011. Available: https://doi.org/10.1021/nl201281m.

[203] S. Nie, N. C. Bartelt, J. M. Wofford, O. D. Dubon, K. F. McCarty, and K. Thürmer, "Scanning tunneling microscopy study of graphene on au(111): Growth mechanisms and substrate interactions", vol. 85, no. 20, May 2012. Available: https://doi.org/10.1103/physrevb.85.205406.

[204] I. Hernández-Rodríguez, J. M. García, J. A. Martín-Gago, P. L. de Andrés, and J. Méndez, "Graphene growth on pt(111) and au(111) using a MBE carbon solid-source", vol. 57, pp. 58–62, Aug. 2015. Available: https://doi.org/10.1016/j.diamond.2015.03.004.

[205] J. M. Wofford *et al.*, "Extraordinary epitaxial alignment of graphene islands on au(111)", vol. 14, no. 5, p. 053 008, May 2012. Available: https://doi.org/10.1088/1367-2630/14/5/053008.

[206] D. Tomer, S. Rajput, L. J. Hudy, C. H. Li, and L. Li, "Intrinsic inhomogeneity in barrier height at monolayer graphene/SiC schottky junction", *Applied Physics Letters*, vol. 105, no. 2, p. 021 607, Jul. 2014. Available: https://doi.org/10.1063/1.4890405.

[207] M. Shekhirev and A. Sinitskii, "Solution synthesis of atomically precise graphene nanoribbons", *Physical Sciences Reviews*, vol. 2, no. 5, May 2017. Available: https://doi.org/10.1515/psr-2016-0108.

[208] J. Engbæk, J. Schiøtz, B. Dahl-Madsen, and S. Horch, "Atomic structure of screw dislocations intersecting the Au(111) surface: A combined scanning tunneling microscopy and molecular dynamics study", *Physical Review B*, vol. 74, no. 19, Nov. 2006. Available: https://doi.org/10.1103/physrevb.74.195434.

[209] P. C. E. M. S. Dresselhaus G. Dresselhaus, *Science of Fullerenes and Carbon Nanotubes*. Elsevier, 1996. Available: https://doi.org/10.1016/b978-0-12-221820-0.x5000-x.

[210] B Borca *et al.*, "Periodically modulated geometric and electronic structure of graphene on ru(0 0 0 1)", *Semiconductor Science and Technology*, vol. 25, no. 3, p. 034 001, Feb. 2010. Available: https://doi.org/10.1088/0268-1242/25/3/034001.

[211] L. Zhao *et al.*, "Influence of copper crystal surface on the CVD growth of large area monolayer graphene", *Solid State Communications*, vol. 151, no. 7, pp. 509–513, Apr. 2011. Available: https://doi.org/10.1016/j.ssc.2011.01.014.

[212] P. Leicht *et al.*, "In situ fabrication of quasi-free-standing epitaxial graphene nanoflakes on gold", *ACS Nano*, vol. 8, no. 4, pp. 3735–3742, Apr. 2014. Available: https://doi.org/10.1021/nn500396c.

[213] M. M. Ugeda *et al.*, "Point defects on graphene on metals", *Physical Review Letters*, vol. 107, no. 11, Sep. 2011. Available: https://doi.org/10.1103/physrevlett.107.116803.

[214] J. Tesch *et al.*, "Structural and electronic properties of graphene nanoflakes on au(111) and ag(111)", *Scientific Reports*, vol. 6, no. 1, Mar. 2016. Available: https://doi.org/10.1038/srep23439.

[215] J. Sławińska, I. Wlasny, P. Dabrowski, Z. Klusek, and I. Zasada, "Doping domains in graphene on gold substrates: First-principles and scanning tunneling spectroscopy studies", *Physical Review B*, vol. 85, no. 23, Jun. 2012. Available: https://doi.org/10.1103/physrevb.85.235430.

[216] B. Kiraly, E. V. Iski, A. J. Mannix, B. L. Fisher, M. C. Hersam, and N. P. Guisinger, "Solid-source growth and atomic-scale characterization of graphene on ag(111)", *Nature Communications*, vol. 4, no. 1, Nov. 2013. Available: https://doi.org/10.1038/ncomms3804.

[217] L. Gao, J. R. Guest, and N. P. Guisinger, "Epitaxial graphene on cu(111)", *Nano Letters*, vol. 10, no. 9, pp. 3512–3516, Aug. 2010. Available: https://doi.org/10.1021/nl1016706.

[218] G. Giovannetti, P. A. Khomyakov, G. Brocks, V. M. Karpan, J. van den Brink, and P. J. Kelly, "Doping graphene with metal contacts", *Physical Review Letters*, vol. 101, no. 2, Jul. 2008. Available: https://doi.org/10.1103/physrevlett.101.026803.

[219] Z. Klusek *et al.*, "Graphene on gold: Electron density of states studies by scanning tunneling spectroscopy", *Applied Physics Letters*, vol. 95, no. 11, p. 113 114, Sep. 2009. Available: https://doi.org/10.1063/1.3231440.

[220] S. Li, M. Liu, and X. Qiu, "Scanning probe microscopy of topological structure induced electronic states of graphene", *Small Methods*, vol. 4, no. 3, p. 1 900 683, Jan. 2020. Available: https://doi.org/10.1002/smtd.201900683.

[221] W.-S. Lei, A. Kumar, and R. Yalamanchili, "Die singulation technologies for advanced packaging: A critical review", *Journal of Vacuum Science & Technology B*, vol. 30, no. 4, p. 040 801, Jul. 2012. Available: https://doi.org/10.1116/1.3700230.

[222] R. Hunt *et al.*, "Electronic structure, surface composition and long-range order in GaN", vol. 185, no. 1-4, pp. 415–421, Apr. 1993. Available: https://doi.org/10.1016/0921-4526(93)90271-7.

[223] C. Schulz *et al.*, "Oxide removal from GaN(0001) surfaces", vol. 6, no. S2, S305–S308, Feb. 2009. Available: https://doi.org/10.1002/pssc.200880845.

[224] S. Gangopadhyay, T. Schmidt, S. Einfeldt, T. Yamaguchi, D. Hommel, and J. Falta, "Growth and formation of InGaN and GaN nano-structures studied by STM", *e-Journal of Surface Science and Nanotechnology*, vol. 4, pp. 90–95, 2006. Available: https://doi.org/10.1380/ejssnt.2006.90.

[225] P. Quaino, E. Santos, G. Soldano, and W. Schmickler, “Recent progress in hydrogen electrocatalysis”, *Advances in Physical Chemistry*, vol. 2011, pp. 1–14, Jun. 2011. Available: https://doi.org/10.1155/2011/851640.

[226] Y.-X. Xu, X.-R. Cao, L.-H. Xu, J.-H. Zhang, S.-Q. Wu, and Z.-Z. Zhu, “Electronic properties of vanadium atoms adsorption on clean and graphene-covered cu(111) surface”, *Nanoscale Research Letters*, vol. 13, no. 1, Jul. 2018. Available: https://doi.org/10.1186/s11671-018-2605-3.

[227] S. Venkatachalam and T. Jacob, “Hydrogen adsorption on pd-containing au(111) bimetallic surfaces”, *Physical Chemistry Chemical Physics*, vol. 11, no. 17, p. 3263, 2009. Available: https://doi.org/10.1039/b900250b.

[228] P. O. Gartland, S. Berge, and B. J. Slagsvold, “Photoelectric work function of a copper single crystal for the (100), (110), (111), and (112) faces”, *Physical Review Letters*, vol. 28, no. 12, pp. 738–739, Mar. 1972. Available: https://doi.org/10.1103/physrevlett.28.738.

[229] K. R. Rodriguez, M. A. Malone, W. A. Nanney, C. J. A. Maddux, J. V. Coe, and H. L. Martínez, “Generalizing thermodynamic properties of bulk single-walled carbon nanotubes”, *AIP Advances*, vol. 4, no. 12, p. 127 149, Dec. 2014. Available: https://doi.org/10.1063/1.4905263.

[230] B. D. Oli, C. Bhattarai, B. Nepal, and N. P. Adhikari, “First-principles study of adsorption of alkali metals (li, na, k) on graphene”, in *Springer Proceedings in Physics*, Springer Berlin Heidelberg, 2013, pp. 515–529. Available: https://doi.org/10.1007/978-3-642-34216-5_51.

[231] T. Higuchi, L. Maisenbacher, A. Liehl, P. Dombi, and P. Hommelhoff, “A nanoscale vacuum-tube diode triggered by few-cycle laser pulses”, *Applied Physics Letters*, vol. 106, no. 5, p. 051 109, Feb. 2015. Available: https://doi.org/10.1063/1.4907607.

[232] C. Ropers, C. C. Neacsu, M. B. Raschke, M. Albrecht, C. Lienau, and T. Elsaesser, “Light confinement at ultrasharp metallic tips”, *Japanese Journal of Applied Physics*, vol. 47, no. 7, pp. 6051–6054, Jul. 2008. Available: https://doi.org/10.1143/jjap.47.6051.

[233] C. C. Neacsu, G. A. Steudle, and M. B. Raschke, “Plasmonic light scattering from nanoscopic metal tips”, *Applied Physics B*, vol. 80, no. 3, pp. 295–300, Mar. 2005. Available: https://doi.org/10.1007/s00340-005-1748-y.

[234] S. M. Gray, “Photoemission with the STM”, *Journal of Electron Spectroscopy and Related Phenomena*, vol. 109, no. 1-2, pp. 183–196, Aug. 2000. Available: https://doi.org/10.1016/s0368-2048(00)00116-x.

[235] Y. Gong, A. G. Joly, D. Hu, P. Z. El-Khoury, and W. P. Hess, “Ultrafast imaging of surface plasmons propagating on a gold surface”, *Nano Letters*, vol. 15, no. 5, pp. 3472–3478, Apr. 2015. Available: https://doi.org/10.1021/acs.nanolett.5b00803.

[236] T. Wang, J. Guo, J. Shao, D. Wang, A. Chen, and M. Jin, “Ultrafast thermionic emission from metal irradiated using a femtosecond laser and an electric field in combination”, *Physics of Plasmas*, vol. 22, no. 3, p. 033 106, Mar. 2015. Available: https://doi.org/10.1063/1.4914164.

[237] B Barwick, C Corder, J Strohaber, N Chandler-Smith, C Uiterwaal, and H Batelaan, “Laser-induced ultrafast electron emission from a field emission tip”, *New Journal of Physics*, vol. 9, no. 5, pp. 142–142, May 2007. Available: https://doi.org/10.1088/1367-2630/9/5/142.

[238] *Tungsten: Properties, Chemistry, Technology of the Element, Alloys, and Chemical Compounds*. 1998.

[239] C. D. Valentin, F. Wang, and G. Pacchioni, “Tungsten oxide in catalysis and photocatalysis: Hints from DFT”, *Topics in Catalysis*, vol. 56, no. 15-17, pp. 1404–1419, Aug. 2013. Available: https://doi.org/10.1007/s11244-013-0147-6.

[240] P. P. González-Borrero *et al.*, “Optical band-gap determination of nanostructured WO3 film”, *Applied Physics Letters*, vol. 96, no. 6, p. 061 909, Feb. 2010. Available: https://doi.org/10.1063/1.3313945.

[241] M. Levinshtein, S. Rumyantsev, and M. Shur, *Properties of Advanced Semiconductor Materials: GaN, AIN, InN, BN, SiC, SiGe* (A Wiley-Interscience publication). Wiley, 2001. Available: https://books.google.ca/books?id=u26CpULkD_wC.

[242] R. M. Feenstra and J. A. Stroscio, “Tunneling spectroscopy of the gaas(110) surface”, *Journal of Vacuum Science & Technology B*, vol. 5, no. 4, 923–929, Jul. 1987. Available: http://dx.doi.org/10.1116/1.583691.

[243] J. Houard, A. Vella, F. Vurpillot, and B. Deconihout, “Conditions to cancel the laser polarization dependence of a subwavelength tip”, *Applied Physics Letters*, vol. 94, no. 12, p. 121 905, Mar. 2009. Available: https://doi.org/10.1063/1.3095829.

[244] E. S. Robins, M. J. G. Lee, and P. Langlois, “Effect of optical diffraction on laser heating of a field emitter”, *Canadian Journal of Physics*, vol. 64, no. 1, pp. 111–117, Jan. 1986. Available: https://doi.org/10.1139/p86-016.

[245] P. V. Chandrasekar, H. Lim, H. Jung, C. gyoun Kim, and D. Kim, “Structural and field emission properties of GaN–SWCNT nanocomposites”, *Journal of The Electrochemical Society*, vol. 157, no. 12, J415, 2010. Available: https://doi.org/10.1149/1.3497352.

[246] N. Xie *et al.*, “Tip expansion in a laser assisted scanning tunneling microscope”, *Applied Physics Letters*, vol. 101, no. 21, p. 213 104, Nov. 2012. Available: https://doi.org/10.1063/1.4767877.

[247] X. Wang, S. Nie, J. Li, R. Clinite, J. E. Clark, and J. Cao, "Temperature dependence of electron-phonon thermalization and its correlation to ultrafast magnetism", *Physical Review B*, vol. 81, no. 22, Jun. 2010. Available: https://doi.org/10.1103/physrevb.81.220301.

[248] S. Adachi, *The Handbook on Optical Constants of Metals*. WORLD SCIENTIFIC, May 2012. Available: https://doi.org/10.1142/8479.

[249] S. Adachi, *Optical Constants of Crystalline and Amorphous Semiconductors*. Springer US, 1999. Available: https://doi.org/10.1007/978-1-4615-5247-5.

[250] T. Soma, J. Satoh, and H. Matsuo, "Thermal expansion coefficient of GaAs and InP", *Solid State Communications*, vol. 42, no. 12, pp. 889–892, Jun. 1982. Available: https://doi.org/10.1016/0038-1098(82)90233-2.

[251] R. O. Carlson, G. A. Slack, and S. J. Silverman, "Thermal conductivity of GaAs and GaAs1-xPx laser semiconductors", *Journal of Applied Physics*, vol. 36, no. 2, pp. 505–507, Feb. 1965. Available: https://doi.org/10.1063/1.1714018.

[252] C. Roder, S. Einfeldt, S. Figge, and D. Hommel, "Temperature dependence of the thermal expansion of GaN", *Physical Review B*, vol. 72, no. 8, Aug. 2005. Available: https://doi.org/10.1103/physrevb.72.085218.

[253] E. Sichel and J. Pankove, "Thermal conductivity of GaN, 25–360 k", *Journal of Physics and Chemistry of Solids*, vol. 38, no. 3, p. 330, Jan. 1977. Available: https://doi.org/10.1016/0022-3697(77)90112-3.

[254] G. Nunes and D. Williams, "Thermal contraction of ultrahigh vacuum materials for scanning probe microscopy from 300 to 4 k", *Journal of Vacuum Science & Technology B*, vol. 13, no. 3, 1063–1065, May 1995. Available: http://dx.doi.org/10.1116/1.587905.

Appendix A: SEMITIP Matlab code

A.1 SEMITIP.m

```
function varargout = SEMITIP(varargin)
% SEMITIP MATLAB code for SEMITIP.fig
%      SEMITIP, by itself, creates a new SEMITIP or raises the existing
%      singleton*.
%
%      H = SEMITIP returns the handle to a new SEMITIP or the handle to
%      the existing singleton*.
%
%      SEMITIP('CALLBACK',hObject,eventData,handles,...) calls the local
%      function named CALLBACK in SEMITIP.M with the given input arguments.
%
%      SEMITIP('Property','Value',...) creates a new SEMITIP or raises the
%      existing singleton*.  Starting from the left, property value pairs are
%      applied to the GUI before SEMITIP_OpeningFcn gets called.  An
%      unrecognized property name or invalid value makes property application
%      stop.  All inputs are passed to SEMITIP_OpeningFcn via varargin.
%
%      *See GUI Options on GUIDE's Tools menu.  Choose "GUI allows only one
%      instance to run (singleton)".
%
% See also: GUIDE, GUIDATA, GUIHANDLES

% Edit the above text to modify the response to help SEMITIP

% Last Modified by GUIDE v2.5 04-Jan-2022 15:16:08

% Begin initialization code - DO NOT EDIT
gui_Singleton = 1;
gui_State = struct('gui_Name',       mfilename, ...
    'gui_Singleton',  gui_Singleton, ...
    'gui_OpeningFcn', @SEMITIP_OpeningFcn, ...
    'gui_OutputFcn',  @SEMITIP_OutputFcn, ...
    'gui_LayoutFcn',  [] , ...
    'gui_Callback',   []);
if nargin && ischar(varargin{1})
    gui_State.gui_Callback = str2func(varargin{1});
end

if nargout
    [varargout{1:nargout}] = gui_mainfcn(gui_State, varargin{:});
else
    gui_mainfcn(gui_State, varargin{:});
end
% End initialization code - DO NOT EDIT


% --- Executes just before SEMITIP is made visible.
function SEMITIP_OpeningFcn(hObject, eventdata, handles, varargin)
% This function has no output args, see OutputFcn.
% hObject    handle to figure
% eventdata  reserved - to be defined in a future version of MATLAB
% handles    structure with handles and user data (see GUIDATA)
% varargin   command line arguments to SEMITIP (see VARARGIN)

% Choose default command line output for SEMITIP
handles.output = hObject;

%set(handles.figure1, 'units', 'normalized', 'position', [0.05 0.15 0.9 0.8])

%handles.uictrl_info=uicontrol(...
%           'style','edit',...
%           'max',2,... % <- the trick...
%           'horizontalalignment','left',...
%           'FontUnits','normalized',...
```

```
%            'Units','normalized',...
%            'string',{'foo1','foo2'});
%handles.uictrl_info=uicontrol('position
    ',[0.4356796116504854,0.019548872180451128,0.549757281553398,0.9037593984962407]);

custom_folder='./Custom_Inputs';
str=Load_Filenames(custom_folder);
set(handles.custom_inputs,'string',['- Load custom inputs -' str])
handles.is_cycle=0;

guidata(hObject, handles);

if(get(handles.custom_inputs,'value')>1)
    custom_inputs_Callback(hObject, eventdata, handles)
else
    fname=load_inputs_from_files(handles);
    M=textread(fname,'%s','delimiter','\n');
    set(handles.uictrl_info,'string',M)
end
% UIWAIT makes SEMITIP wait for user response (see UIRESUME)
% uiwait(handles.figure1);


% --- Outputs from this function are returned to the command line.
function varargout = SEMITIP_OutputFcn(hObject, eventdata, handles)
% Get default command line output from handles structure
varargout{1} = handles.output;
%-----------------------------------------------------------------------
function semitip_version_CreateFcn(hObject, eventdata, handles)
if ispc && isequal(get(hObject,'BackgroundColor'), get(0,'defaultUicontrolBackgroundColor'))
    set(hObject,'BackgroundColor','white');
end
function custom_inputs_CreateFcn(hObject, eventdata, handles)
if ispc && isequal(get(hObject,'BackgroundColor'), get(0,'defaultUicontrolBackgroundColor'))
    set(hObject,'BackgroundColor','white');
end
function in_min_cycle_CreateFcn(hObject, eventdata, handles)
if ispc && isequal(get(hObject,'BackgroundColor'), get(0,'defaultUicontrolBackgroundColor'))
    set(hObject,'BackgroundColor','white');
end
function in_step_cycle_CreateFcn(hObject, eventdata, handles)
if ispc && isequal(get(hObject,'BackgroundColor'), get(0,'defaultUicontrolBackgroundColor'))
    set(hObject,'BackgroundColor','white');
end
function in_sec_per_frame_CreateFcn(hObject, eventdata, handles)
if ispc && isequal(get(hObject,'BackgroundColor'), get(0,'defaultUicontrolBackgroundColor'))
    set(hObject,'BackgroundColor','white');
end
function in_max_cycle_CreateFcn(hObject, eventdata, handles)
if ispc && isequal(get(hObject,'BackgroundColor'), get(0,'defaultUicontrolBackgroundColor'))
    set(hObject,'BackgroundColor','white');
end
function in_xlim_CreateFcn(hObject, eventdata, handles)
if ispc && isequal(get(hObject,'BackgroundColor'), get(0,'defaultUicontrolBackgroundColor'))
    set(hObject,'BackgroundColor','white');
end
function in_ylim_CreateFcn(hObject, eventdata, handles)
if ispc && isequal(get(hObject,'BackgroundColor'), get(0,'defaultUicontrolBackgroundColor'))
    set(hObject,'BackgroundColor','white');
end
function in_thz_points_CreateFcn(hObject, eventdata, handles)
if ispc && isequal(get(hObject,'BackgroundColor'), get(0,'defaultUicontrolBackgroundColor'))
    set(hObject,'BackgroundColor','white');
end
function in_vmax_CreateFcn(hObject, eventdata, handles)
if ispc && isequal(get(hObject,'BackgroundColor'), get(0,'defaultUicontrolBackgroundColor'))
    set(hObject,'BackgroundColor','white');
end
function uictrl_info_CreateFcn(hObject, eventdata, handles)
if ispc && isequal(get(hObject,'BackgroundColor'), get(0,'defaultUicontrolBackgroundColor'))
    set(hObject,'BackgroundColor','white');
end
function list_variable_param_CreateFcn(hObject, eventdata, handles)
if ispc && isequal(get(hObject,'BackgroundColor'), get(0,'defaultUicontrolBackgroundColor'))
    set(hObject,'BackgroundColor','white');
end
function uictrl_info_Callback(hObject, eventdata, handles)
function in_vmax_Callback(hObject, eventdata, handles)
function in_thz_points_Callback(hObject, eventdata, handles)
function in_min_cycle_Callback(hObject, eventdata, handles)
function in_step_cycle_Callback(hObject, eventdata, handles)
function in_sec_per_frame_Callback(hObject, eventdata, handles)
function in_max_cycle_Callback(hObject, eventdata, handles)
function in_xlim_Callback(hObject, eventdata, handles)
function in_ylim_Callback(hObject, eventdata, handles)
function is_raw_potential_Callback(hObject, eventdata, handles)
function is_band_diagram_Callback(hObject, eventdata, handles)
    set(handles.is_raw_potential,'enable','off')
function is_surface_pot_z_Callback(hObject, eventdata, handles)
    set(handles.is_raw_potential,'enable','on')
function is_surface_pot_r_Callback(hObject, eventdata, handles)
    set(handles.is_raw_potential,'enable','on')
```

```
function is_surface_pot_3d_Callback(hObject, eventdata, handles)
    set(handles.is_raw_potential,'enable','off')
function is_contours_Callback(hObject, eventdata, handles)
    set(handles.is_raw_potential,'enable','off')
function is_charge_den_r_Callback(hObject, eventdata, handles)
    set(handles.is_raw_potential,'enable','off')
function is_current_density_Callback(hObject, eventdata, handles)
    set(handles.is_raw_potential,'enable','off')


%-------------------  MAIN FUNCTION TO RUN SEMITIP  ----------------------
function btn_single_run_Callback(hObject, eventdata, handles)
figs = get(0,'children');
figs(figs == gcf) = []; % delete your current figure from the list
%close(figs)
exe_version=get_exe_version(get(handles.semitip_version,'value'));
vfolder=get_version_folder(handles);


delete([vfolder '/fort.*'])
delete([vfolder '/img*'])

fileID = fopen([vfolder '/fort.9'],'w');
inputs_info=get(handles.uictrl_info,'string');

% biasvpointspos=find(not(cellfun('isempty', strfind(inputs_info, 'voltage points'))));
% variable_txt=inputs_info{biasvpointspos};
% a=(strfind(variable_txt, ' '));
% if(isempty(a)); a=length(variable_txt)+1; end
% biasvpointstext=variable_txt(a(1):end);
% inputs_info{biasvpointspos}=['1' biasvpointstext];
% set(handles.uictrl_info,'string',inputs_info);

for row = 1:length(inputs_info)
    fprintf(fileID,'%s\n',inputs_info{row});
end
fclose(fileID);
pause(0.5)
flag = 1;
if(ismac)
    exe_path=[vfolder '/' exe_version '.exe'];
    system(['open ' exe_path]);
    if(handles.is_cycle) add_to_info(handles,['Running']);
    else set(handles.version_info,'string',{'Running'});
    end

    while (flag)
        pause(1) % check every _ seconds
        [q,w] = system(['tail -n ',num2str(1),' ',vfolder, '/fort.16']);
        if(strfind(w,'PRESS THE ENTER KEY TO EXIT'));  flag=0; end
        info=get(handles.version_info,'string'); info{end}=[info{end} '.'];
        set(handles.version_info,'string',info);
    end
    %system([exe_path])
    %waitfor(msgbox('semitip_v5.exe executed succesfully'))
elseif (ispc)
    if(vfolder=='./v5')
        set(handles.version_info,'string',{'v5 currently not supported in Windows'});
        return
    else
        exe_path=[vfolder '/UoA-' exe_version '.exe'];
        vfolder = [pwd strrep(vfolder(2:end) , '/' , '\' )];
        exe_path = [pwd strrep( exe_path(2:end-3) , '/' , '\' ) 'exe'];
        %robot = java.awt.Robot;
        %      flag=system(exe_path)
        winopen(exe_path)

        if(handles.is_cycle) add_to_info(handles,['Running']);
        else set(handles.version_info,'string',{'Running'});
        end

        while (flag)
            %robot.keyPress (java.awt.event.KeyEvent.VK_ENTER); %// press "enter" key
            %robot.keyRelease (java.awt.event.KeyEvent.VK_ENTER); %// release "enter" key
            pause(1) % check every _ seconds
            [q,w] = system(['powershell Get-Content ' pwd '\v6\fort.16 -tail 1']);
            if(strfind(w,'PRESS THE ENTER KEY TO EXIT'));  flag=0; end
            info=get(handles.version_info,'string'); info{end}=[info{end} '.'];
            set(handles.version_info,'string',info);
            %disp('.')
        end
        %disp('Done')
        %waitfor(msgbox('semitip_v5.exe executed succesfully'))
    end
else
    waitfor(msgbox('exe file could not be executed'));
    flag=0;
    return
end

%exe_path(3:end)
```

```matlab
info=get(handles.version_info,'string'); info{end}=[info{end} ' Done'];
set(handles.version_info,'string',info);

pause(0.2)
%------------------------------------------------------------------------
%------------------------  PLOTS ROUTINES  ------------------------------
%------------------------------------------------------------------------
function btn_single_plot_Callback(hObject, eventdata, handles)
btn_plots=get(get(handles.btn_group_plots,'SelectedObject'),'Tag');

switch btn_plots
    case 'is_band_diagram'
        btn_band_diagram_plot(handles);
    case 'is_contours'
        btn_contours_plot(handles);
    case 'is_surface_pot_z'
        if isfile('potential_at_surface_values.txt');     delete('potential_at_surface_values.txt'); end
        if isfile('potential_decay_tau.txt');     delete('potential_decay_tau.txt'); end
        btn_surface_pot_z_plot(handles);
    case 'is_surface_pot_r'
        if isfile('radial_potential_at_surface_FWHM.txt');     delete('radial_potential_at_surface_FWHM.txt'); end
        btn_surface_pot_r_plot(handles);
    case 'is_surface_pot_3d'
        handles=btn_surface_pot_3d_plot(handles);
    case 'is_charge_den_z'
        plot_charge_densities_z(handles);
    case 'is_charge_den_r'
        plot_charge_densities_r(handles);
    case 'is_current_density'
        if isfile('current_density_data.txt');     delete('current_density_data.txt'); end
        btn_current_density_plot(handles);
end
%------------------------------------------------------------------------
function handles=btn_band_diagram_plot(handles)
vfolder=get_version_folder(handles);
if ~(exist([vfolder, '/fort.11'], 'file'));
    set(handles.version_info,'string' ,{'Files not found for bands diagram.'});  return;
end
Plot11=load([vfolder '/fort.11']);

[pos tipheight thetext]=get_current_value_of('tipHeight',handles);
[pos biasV thetext]=get_current_value_of('biasV',handles);
[pos bandgap thetext]=get_current_value_of('bandgap',handles);
[pos NeutralityLevel thetext]=get_current_value_of('neutrality1',handles);
[pos workF thetext]=get_current_value_of('workF',handles);
[pos temperature thetext]=get_current_value_of('temperature',handles);
[pos tipradius thetext]=get_current_value_of('tipRadius',handles);

outputs_info=textread([vfolder '/fort.16'],'%s','delimiter','\n');
Ef_txt=outputs_info{find(not(cellfun('isempty', strfind(outputs_info, 'FERMI-LEVEL'))))};
Ef=str2num(Ef_txt(strfind(Ef_txt,'=')+1:end));
DeplWidth_txt=outputs_info{find(not(cellfun('isempty', strfind(outputs_info, 'DEPLETION WIDTH '))))};
DeplWidth=strtrim(DeplWidth_txt(strfind(DeplWidth_txt,'=')+1:end));
xlim=str2num(get(handles.in_xlim,'string'));
ylim=str2num(get(handles.in_ylim,'string'));
if(handles.is_cycle)
    if(handles.xaxlim_max < xlim); handles.xaxlim_max=xlim; end
    if(handles.xaxlim_min > -xlim); handles.xaxlim_min=-xlim; end
    if(handles.yaxlim_max < ylim); handles.yaxlim_max=ylim; end
    if(handles.yaxlim_min > -ylim); handles.yaxlim_min=-ylim; end
    xlim=[handles.xaxlim_min handles.xaxlim_max];
    ylim=[handles.yaxlim_min handles.yaxlim_max];
end
energy_band_diagram(Plot11,bandgap,tipheight,Ef,NeutralityLevel,workF,biasV,xlim,ylim);

dopantconc='';
[pos acceptorconc thetext]=get_current_value_of('acceptorconc',handles);
[pos donorconc thetext]=get_current_value_of('donorconc',handles);
if(acceptorconc==0 && donorconc~=0)
    dopantconc=['Donors concentration: ' sprintf('%0.5g',donorconc) ' cm^{-3}'];
elseif (donorconc==0 && acceptorconc~=0)
    dopantconc=['Acceptors concentration: ' sprintf('%0.5g',acceptorconc) ' cm^{-3}'];
elseif(donorconc~=0 && acceptorconc~=0)
    dopantconc=['Acceptors conc.: ' sprintf('%0.5g',acceptorconc) ' cm^{-3}' ', Donors conc.: ' sprintf('%0.5g',donorconc) ' cm^{-3}'];
end
dossconc='';
[pos doss1 thetext]=get_current_value_of('doss1',handles);
[pos doss2 thetext]=get_current_value_of('doss2',handles);
if(doss2==0 && doss1~=0)
    dossconc=['SS: ' sprintf('%0.5g', doss1) ' cm^{-2} eV^{-1}'];
elseif (doss1==0 && doss2~=0)
    dossconc=['SS: ' sprintf('%0.5g',doss2) ' cm^{-2} eV^{-1}'];
elseif(doss1~=0 && doss2~=0)
    dossconc=['1st SS: ' sprintf('%0.5g',doss1) ' cm^{-2} eV^{-1}' ', 2nd SS: ' sprintf('%0.5g',doss2) ' cm^{-2} eV^{-1}'];
else
    %dossconc=['Surface states in bandgap: ' num2str(doss1) ' cm^{-2} eV^{-1}'];
end
```

```
textarray={['Bandgap: ' num2str(bandgap) ' eV']};
%if(~strcmp(NeutralityLevel,'')) textarray{end+1}=['Charge neutrality level: ' num2str(
     NeutralityLevel) ' eV']; end
%if(~strcmp(DeplWidth,'')) textarray{end+1}=['Depletion width: ' DeplWidth ' nm']; end
if(~strcmp(dopantconc,'')) textarray{end+1}=dopantconc; end
%if(~strcmp(dossconc,'')) textarray{end+1}=dossconc; end
if(dossconc~="")
    textarray{end+1}=dossconc;
end
textarray{end+1}=['Temperature: ' num2str(temperature) ' K'];
textarray{end+1}=['TipRadius: ' num2str(tipradius) ' nm'];
text(-abs(xlim(1))*0.95,abs(ylim(1)),textarray,'VerticalAlignment', 'top')
gauss_dist(0,abs(xlim(1))/10,handles);

if(handles.is_cycle)
    axiss=axis;
    if(handles.xaxlim_max < axiss(2)); handles.xaxlim_max=axiss(2); end
    if(handles.xaxlim_min > axiss(1)); handles.xaxlim_min=axiss(1); end
    if(handles.yaxlim_max < axiss(4)); handles.yaxlim_max=axiss(4); end
    if(handles.yaxlim_min > axiss(3)); handles.yaxlim_min=axiss(3); end
end
%-----------------------------------------------------------------------
function btn_contours_plot(handles)
vfolder=get_version_folder(handles);
files=dir([vfolder '/fort.2*']);
if(isempty(files)); set(handles.version_info,'string' ,{'Files not found for potential contours.'
     }); return; end
figure('Name','SinglePlot')
[pos tipheight thetext]=get_current_value_of('tipHeight',handles);
[pos tipradius thetext]=get_current_value_of('tipRadius',handles);
[pos biasV thetext]=get_current_value_of('biasV',handles);
[pos tipshank thetext]=get_current_value_of('tipShank',handles);
miny=0;
outputs_info=textread([vfolder '/fort.16'],'%s','delimiter','\n');
cont_spac_txt=outputs_info{find(not(cellfun('isempty', strfind(outputs_info, 'CONTOUR SPACING'))))
     };
contour_spacing=str2num(cont_spac_txt(strfind(cont_spac_txt,'=')+1:end));
cont_spac_minmax_txt=outputs_info{find(not(cellfun('isempty', strfind(outputs_info, 'POTENTIAL
     VALUES'))))};
contour_spacing_minmax=(cont_spac_minmax_txt(strfind(cont_spac_minmax_txt,'=')+1:end));
contour_spacing_minmax=split(contour_spacing_minmax," ");
contour_spacing_minmax=contour_spacing_minmax(~cellfun('isempty',contour_spacing_minmax));
minPotential=str2num(contour_spacing_minmax{1});
maxPotential=str2num(contour_spacing_minmax{2});
disp(['biasV: ' num2str(biasV) ' V, min: ' num2str(minPotential) ', max: ' num2str(maxPotential)
     ])
C = {'k','r','m','b','c','g','y',[.5 .6 .7],[.8 .2 .6],[.3 .2 .6]};
xlim=str2num(get(handles.in_xlim,'string'));
ylim=str2num(get(handles.in_ylim,'string'));
%if(biasV<0); C=[C{1} flip(C(2:length(files)))]; end
contourCount=length(files);
fid = fopen([vfolder '/' files(2).name]);
firstContourMin=textscan(fid,' %s %s  ', 1);
fclose(fid);
fid = fopen([vfolder '/' files(contourCount).name]);
lastContourMin=textscan(fid,' %s %s  ', 1);
fclose(fid);
fieldPenetration=9E9;
voltageAtSurface=0;
voltageAtSurfaceMin=9E9;

Plot22=load([vfolder '/' files(1).name]);
Plot221= [-flipud(Plot22(:,1)); Plot22(:,1)];
Plot222= -[flipud(Plot22(:,2)); Plot22(:,2)];
legendInfo{1} = ['Tip'];
plot(Plot221,Plot222,'color',C{1},'LineWidth',1.2)
hold on
if(min(Plot222)<miny); miny=min(Plot222);  end

for i=2:contourCount
    if (minPotential+maxPotential>0)
        customIndex=contourCount-i+2;
    else
        customIndex=i;
    end
    Plot22=load([vfolder '/' files(customIndex).name]);
    Plot221= [-flipud(Plot22(:,1)); Plot22(:,1)];
    Plot222= -[flipud(Plot22(:,2)); Plot22(:,2)];
    if(min(Plot222)<fieldPenetration); fieldPenetration=min(Plot222); end
    if(abs(Plot222(1))<voltageAtSurfaceMin); voltageAtSurfaceMin=abs(Plot222(1)); voltageAtSurface
        =biasV; end

        plot(Plot221,Plot222,'color',C{contourCount-i+2})
    if (minPotential+maxPotential>0)
        legendInfo{i} = [num2str(minPotential+(i-1)*contour_spacing,3) ' V'];
    else
        legendInfo{i} = [num2str(maxPotential-(i-1)*contour_spacing,3) ' V'];
    end
    hold on
    if(min(Plot222)<miny); miny=min(Plot222);  end
end
```

```matlab
if (minPotential+maxPotential>0)
    legendInfo{contourCount+1} = [num2str(maxPotential,3) ' V (Sample)'];
else
    legendInfo{contourCount+1} = [num2str(minPotential,3) ' V (Sample)'];
end
%disp([num2str(biasV) ',' num2str(fieldPenetration)]) % Displays (biasV, fieldPenetration)
%disp(['Voltage at surface: ' num2str(voltageAtSurface)]) % Displays (biasV, fieldPenetration)
axiss=axis;
axis([-xlim xlim -ylim ylim]);
plot([axiss(1) axiss(2)],[0 0],'k','LineWidth',1.2)
legend(legendInfo,'location', 'southwest','AutoUpdate','off');
plot([axiss(1) axiss(2)],[tipheight tipheight],'--k')
title(['Equipotential contours ( TipHeight=' num2str(tipheight) ' nm, BiasV:' num2str(biasV) ' V )'])
xlabel('radial distance [nm]','fontsize',12);
ylabel(' z-distance [nm]','fontsize',12);
text(0,-ylim+ylim*0.1,['SAMPLE'],'fontsize',14,'horizontalAlignment', 'center')
text(0,ylim-ylim*0.1,['TIP'],'fontsize',14,'horizontalAlignment', 'center')
text(xlim*0.9,-ylim*0.9,{['Tip radius: ' num2str(tipradius) ' nm']; ['Tip shank: ' num2str(tipshank)]},'VerticalAlignment', 'bottom','horizontalAlignment', 'right')
%----------------------------------------------------------------------
function handles=btn_surface_pot_z_plot(handles)
vfolder=get_version_folder(handles);
files=dir([vfolder '/fort.11']);
if(isempty(files)); set(handles.version_info,'string' ,{'File not found for surface potentials.'}); return; end
xlim=min(str2num(get(handles.in_xlim,'string')));
figure('Name','SinglePlot')
Plot11=load([vfolder '/' files(1).name]);
Plot111= Plot11(:,1);
if(~get(handles.is_raw_potential, 'Value'))
    Plot112= -(Plot11(:,2)-Plot11(1,2));
    raw_text='';
else
    Plot112= Plot11(:,2);
    raw_text=', Raw';
end
%Plot123= Plot12(:,3);

plot(Plot111,Plot112,'LineWidth',1.5,'DisplayName','SEMITIP simulation'); hold on;
%set(c,'fontsize',12);
[pos tipheight thetext]=get_current_value_of('tipheight',handles);
[pos biasv thetext]=get_current_value_of('biasv',handles);
[pos tipradius thetext]=get_current_value_of('tipRadius',handles);

axis([-tipheight*2 xlim min(Plot112) max(Plot112)]);
axiss=axis;

[M,I] = min(abs(Plot111));
surface_potential=Plot112(I);
text(xlim,surface_potential,[num2str(surface_potential) ' eV'],'HorizontalAlignment', 'right', 'VerticalAlignment', 'top')
dlmwrite('potential_at_surface_values.txt',surface_potential,'-append','newline','pc')

plot([-tipheight -tipheight],[-15 15], 'Color', [150 150 150]/255,'LineWidth',0.5)
plot([0 0],[-15 15], 'Color', [150 150 150]/255,'LineWidth',0.5)
plot([axiss(1) axiss(2)],[surface_potential surface_potential],'--', 'Color', [150 150 150]/255,'LineWidth',0.5)


    text(-tipheight*1.5,(axiss(3)+axiss(4))*0.5,['Tip'],'rotation', 90, 'Color', [150 150 150]/255);
    text(-tipheight*0.5,(axiss(3)+axiss(4))*0.5,'Vacuum','rotation', 90, 'Color', [150 150 150]/255);
    text(+tipheight*0.5,(axiss(3)+axiss(4))*0.5,'Sample','rotation', 90, 'Color', [150 150 150]/255);


%Plot semitip 1D estimated depletion width
outputs_info=textread([vfolder '/fort.16'],'%s','delimiter','\n');
DeplWidth_txt=outputs_info{find(not(cellfun('isempty', strfind(outputs_info, 'DEPLETION WIDTH '))))};
DeplWidth=str2num(strtrim(DeplWidth_txt(strfind(DeplWidth_txt,'=')+1:end)));
plot([DeplWidth DeplWidth],[-15 15],'--', 'Color', [240 240 240]/255,'LineWidth',0.5)
text(DeplWidth,axiss(3),['Dep. width:' ' ' num2str(DeplWidth) ],'rotation', 90, 'Color', [220 220 220]/255,'HorizontalAlignment', 'left', 'VerticalAlignment', 'top');


% procedure to find the time constant of the exponential decay
Plot111=Plot11(Plot11(:,1)>=0,1); % Z distance  (Only values higher than 0, inside the sample)
Plot112=Plot11(Plot11(:,1)>=0,2); % Valence Band
f = fit(Plot111,Plot112,'exp1');
%plot(Plot111,Plot112)
if(~get(handles.is_raw_potential, 'Value'))
    plot(Plot111,-(f(Plot111)-Plot11(1,2)),'--')
else
    plot(Plot111,f(Plot111),'--')
end
tau=-1/f.b;
plot([tau tau],[-15 15],'--', 'Color', [240 240 240]/255,'LineWidth',0.5)
text(tau,axiss(3),['(1/e)' ' ' num2str(tau) ],'rotation', 90, 'Color', [220 220 220]/255,'HorizontalAlignment', 'left', 'VerticalAlignment', 'top');
```

```
dlmwrite('potential_decay_tau.txt',tau,'-append','newline','pc')


xlabel('Distance in z [nm]','fontsize',12);
ylabel('Potential energy [eV]','fontsize',12);
title(['Surface Potential along z ( TipHeight=' num2str(tipheight) ' nm, BiasV:' num2str(biasv) '
     V' raw_text  ', TipRadius:' num2str(tipradius) ' nm' ' )'])

if(handles.is_cycle)
    axiss=axis;
    if(handles.xaxlim_max < axiss(2)); handles.xaxlim_max=axiss(2); end
    if(handles.xaxlim_min > axiss(1)); handles.xaxlim_min=axiss(1); end
    if(handles.yaxlim_max < axiss(4)); handles.yaxlim_max=axiss(4); end
    if(handles.yaxlim_min > axiss(3)); handles.yaxlim_min=axiss(3); end
else
end
%-------------------------------------------------------------------------
function handles=btn_surface_pot_r_plot(handles)
vfolder=get_version_folder(handles);


files=dir([vfolder '/fort.12']);
if(isempty(files)); set(handles.version_info,'string' ,{'File not found for surface potentials.'})
     ; return; end
xlim=min(str2num(get(handles.in_xlim,'string')));
figure('Name','SinglePlot')
Plot12=load([vfolder '/' files(1).name]);
Plot121= Plot12(:,1);
Plot122= Plot12(:,2);
%Plot123= Plot12(:,3);
[pos tipheight thetext]=get_current_value_of('tipheight',handles);
[pos biasv thetext]=get_current_value_of('biasv',handles);
[pos tipradius thetext]=get_current_value_of('tipRadius',handles);

fitfun = fittype( @(a,c,x) a*exp(-(x/c).^2) );
[fitted_curve,gof] = fit(Plot121,Plot122,fitfun,'StartPoint',[1 1]);
%fitted_curve = fit(Plot121,Plot122,'gauss1')
plot(Plot121,fitted_curve(Plot121),'--');
FWHM = 2*sqrt(log(2)) * fitted_curve.c;
FWHM = 2*sqrt(2*log(2)) * (fitted_curve.c/sqrt(2));

%Up to here, we used the raw data from semitip. Now the potentials need to
%be shifted to make the potential at the tip ground (0 V)
if(~get(handles.is_raw_potential, 'Value'))
    files=dir([vfolder '/fort.11']);
    if(isempty(files)); set(handles.version_info,'string' ,{'File fort.11 not found for surface
         potentials.'}); return; end
    Plot11=load([vfolder '/' files(1).name]);
    tip_potential=Plot11(1,2);
    Plot122=tip_potential-Plot122;
    fitY=tip_potential-fitted_curve(Plot121);
    raw_text='';
else
    fitY=fitted_curve(Plot121);
    raw_text=', Raw';
end

plot(Plot121,Plot122,'LineWidth',1.5); hold on;
legendInfo{1} = 'SEMITIP Simulation';
axis([0 xlim min(Plot122) max(Plot122)]);
axiss=axis;

plot(Plot121,fitY,'--');
legendInfo{2} = ['Gauss fit: ' num2str(fitted_curve.a) '*exp(-(x/' num2str(fitted_curve.c) ')^2)'
     ];
xlabel('Radial distance [nm]','fontsize',12);
ylabel('Potential energy [eV]','fontsize',12);
title(['Radial surface potential ( TipHeight=' num2str(tipheight) ' nm, BiasV:' num2str(biasv) ' V
     ' raw_text  ', TipRadius:' num2str(tipradius) ' nm' ' )'])

if(Plot122(1)>Plot122(end))
    legend(legendInfo,'location', 'northeast','AutoUpdate','off');
    text(0,Plot122(1),[' ' num2str(Plot122(1)) ' eV'],'HorizontalAlignment', 'left', '
         VerticalAlignment', 'top')
    text(xlim,Plot122(end),[' ' num2str(Plot122(end)) ' eV '],'HorizontalAlignment', 'right', '
         VerticalAlignment', 'bottom')
else
    legend(legendInfo,'location', 'southeast','AutoUpdate','off');

    text(0,Plot122(1),[' ' num2str(Plot122(1)) ' eV'],'HorizontalAlignment', 'left', '
         VerticalAlignment', 'bottom')
    text(xlim,Plot122(end),[' ' num2str(Plot122(end)) ' eV '],'HorizontalAlignment', 'right', '
         VerticalAlignment', 'top')
end
text(FWHM/2,axiss(3),[' ' num2str(FWHM/2) ' nm'],'rotation', 90, 'Color', [150 150 150]/255,'
     HorizontalAlignment', 'left', 'VerticalAlignment', 'top');
%plot([axiss(1) axiss(2)],[fitted_curve.a/2 fitted_curve.a/2],'--', 'Color', [150 150 150]/255,'
     LineWidth',0.5)
plot([FWHM/2 FWHM/2],[-15 15],'--', 'Color', [150 150 150]/255,'LineWidth',0.5)
%text(FWHM/2,axiss(3),[' FWHM/2: ' num2str(FWHM/2) ],'rotation', 90, 'Color', [220 220 220]/255,'
     HorizontalAlignment', 'left', 'VerticalAlignment', 'top');
dlmwrite('radial_potential_at_surface_FWHM.txt',FWHM,'-append','newline','pc')
```

```matlab
if(handles.is_cycle)
    axiss=axis;
    if(handles.xaxlim_max < axiss(2)); handles.xaxlim_max=axiss(2); end
    if(handles.xaxlim_min > axiss(1)); handles.xaxlim_min=axiss(1); end
    if(handles.yaxlim_max < axiss(4)); handles.yaxlim_max=axiss(4); end
    if(handles.yaxlim_min > axiss(3)); handles.yaxlim_min=axiss(3); end
else
end
%------------------------------------------------------------------------
function handles=btn_surface_pot_3d_plot(handles)
vfolder=get_version_folder(handles);
files=dir([vfolder '/fort.12']);
if(isempty(files)); set(handles.version_info,'string' ,{'File not found for surface potentials.'}); return; end
xlim=min([str2num(get(handles.in_xlim,'string')) str2num(get(handles.in_ylim,'string'))]);
figure('Name','SinglePlot')
Plot12=load([vfolder '/' files(1).name]);
Plot121= Plot12(:,1);
Plot122= Plot12(:,2);
%Plot123= Plot12(:,3);
r = 0:0.1:pi;
z = sin(r);
%theta2=0:0.01:2*pi;
theta = linspace(0,2*pi,length(Plot121));
xx = bsxfun(@times,Plot121,cos(theta));
yy = bsxfun(@times,Plot121,sin(theta));
zz = repmat(Plot122,1,length(theta));
surf(xx,yy,zz, 'EdgeColor', 'k','LineStyle',':','FaceLighting','flat') %
c=colorbar('location','eastoutside');
c.Label.String = 'Electrostatic potential energy [eV]';
%set(c,'fontsize',12);
xlabel('radial distance [nm]','fontsize',12);
ylabel('radial distance [nm]','fontsize',12);
[pos tipheight thetext]=get_current_value_of('tipheight',handles);
[pos biasv thetext]=get_current_value_of('biasv',handles);
title(['3D Surface Potential ( TipHeight=' num2str(tipheight) ' nm, BiasV:' num2str(biasv) ' V )'])
axiss=axis;

[idx idx] = min(abs(Plot121-xlim));
zaxlim_min=min(Plot122(1:idx));
zaxlim_max=max(Plot122(1:idx));

if(~handles.is_cycle); axis([-xlim xlim -xlim xlim zaxlim_min zaxlim_max]); end
%view(2)
if(handles.is_cycle)
    if(handles.zaxlim_max < zaxlim_max); handles.zaxlim_max=zaxlim_max; end
    if(handles.zaxlim_min > zaxlim_min); handles.zaxlim_min=zaxlim_min; end
end
%------------------------------------------------------------------------
function handles=plot_charge_densities_z(handles)
% provides the charge densities on the central axis (column 2) as a function of z-distance along the central axis (column 1). Also, columns 3 and 4 provide the contributions to the charge densities of extended states and localized states, respectively.
vfolder=get_version_folder(handles);
files=dir([vfolder '/fort.17']);
if(isempty(files)); set(handles.version_info,'string' ,{'File not found for charge densities plot.'}); return; end
xlim=str2num(get(handles.in_xlim,'string'));
figure('Name','SinglePlot')
Plot14=load([vfolder '/' files(1).name]);
Plot141= Plot14(:,1); % z-distance
Plot142= (Plot14(:,2)); % Charge densities
%Plot143= (Plot14(:,3)); % contributions to the charge densities of extended states and localized states, respectively
[a b]=find(Plot141(2:end)<Plot141(1:end-1));
if(length(Plot141)/2 == a)
    plot(-Plot141(1:a),Plot142(1:a),'-',-Plot141(a+1:end),Plot142(a+1:end),'-')
    hold on
    %plot(-Plot141(1:a),Plot143(1:a),'-',-Plot141(a+1:end),Plot143(a+1:end),'-')
    %legend('Charge density on the central axis', 'Charge density on the central axis','Contributions of extended states and localized states','Contributions of extended states and localized states','location', 'northwest')
    text(0,Plot142(1),sprintf('%0.3g',Plot142(1)),'horizontalAlignment', 'right', 'VerticalAlignment', 'top')
    %text(0,Plot142(a+1),sprintf('%0.3g',Plot142(a+1)),'horizontalAlignment', 'right')
    %text(0,Plot143(1),sprintf('%0.3g',Plot143(1)),'horizontalAlignment', 'left')
    %text(0,Plot143(a+1),sprintf('%0.3g',Plot143(a+1)),'horizontalAlignment', 'left')
else
    plot(-Plot141,Plot142,'^-')
    hold on
    %plot(-Plot141,Plot143,'*--')
    legend('Charge density on the central axis','Contributions of extended states and localized states','location', 'northwest')
    text(0,Plot142(1),sprintf('%0.3g',Plot142(1)),'horizontalAlignment', 'right', 'VerticalAlignment', 'top')
    %text(0,Plot143(1),sprintf('%0.3g',Plot143(1)),'horizontalAlignment', 'left')
end
% A=[Plot141(1:a) Plot142(1:a) Plot142(a+1:end) Plot143(1:a) Plot143(a+1:end)];
% A(:,6)=A(:,2)+A(:,3);
```

```
% A(:,7)=A(:,4)+A(:,5);
[idx idx] = min(abs(Plot141-xlim));

%plot(-Plot141,Plot142,'^-')
 %   hold on
xlabel('z-distance [nm]','fontsize',12);
ylabel('Charge densities []','fontsize',12);
[pos tipheight thetext]=get_current_value_of('tipheight',handles);
[pos biasv thetext]=get_current_value_of('biasv',handles);
[pos tipradius thetext]=get_current_value_of('tipradius',handles);
th=title({['Charge densities on the central axis(z)' ],[ ' (TipHeight=' num2str(tipheight) ' nm, BiasV:' num2str(biasv) ' V'  ', TipRadius:' num2str(tipradius) ' nm' ' )']});
%axis([-xlim 0 Plot142(idx) max([Plot142; Plot143])]);

%titlePos = get( th , 'position');
%titlePos(1) = -17;
%set( th , 'position' , titlePos);


yaxlim_min=min([Plot142(1:idx); Plot142(1:idx) ]);
yaxlim_max=max([Plot142(1:idx); Plot142(1:idx) ]);
if(yaxlim_min==yaxlim_max); yaxlim_min=-1; yaxlim_max=1; end
if(~handles.is_cycle); axis([-xlim 0 yaxlim_min yaxlim_max]); end
if(handles.is_cycle)
    if(handles.xaxlim_max < 0); handles.xaxlim_max=0; end
    if(handles.xaxlim_min > -xlim); handles.xaxlim_min=-xlim; end
    if(handles.yaxlim_max < yaxlim_max); handles.yaxlim_max=yaxlim_max; end
    if(handles.yaxlim_min > yaxlim_min); handles.yaxlim_min=yaxlim_min; end
    %if(handles.zaxlim_max < max(max(zz))); handles.zaxlim_max=max(max(zz)); end
    %if(handles.zaxlim_min > min(min(zz))); handles.zaxlim_min=min(min(zz)); end
end
%-------------------------------------------------------------------------
function handles=plot_charge_densities_r(handles)
%provides the surface charge densities (column 2) as a function of radial distance away from the central axis (column 1). Also, columns 3 and 4 provide the contributions to the charge densities of extended states and localized states, respectively.
vfolder=get_version_folder(handles);
files=dir([vfolder '/fort.18']);
if(isempty(files)); set(handles.version_info,'string' ,{'File not found for IV curves.'}); return; end
xlim=abs([str2num(get(handles.in_xlim,'string'))]);

Plot18=load([vfolder '/' files(1).name]);
Plot181= (Plot18(:,1)); % Radial distance
Plot182= (Plot18(:,2)); % Charge density
%if(min(Plot182)~=max(Plot182))
figure('Name','SinglePlot')
[a b]=find(Plot181(2:end)<Plot181(1:end-1));

%Plot182 = sign(Plot182).*log10(abs(Plot182));
if(length(Plot181)/2 == a)
    FirstPlotX=Plot181(1:a);
    FirstPlotY=Plot182(1:a);
    SecondPlotX=Plot181(a+1:end);
    SecondPlotY=Plot182(a+1:end);

    plot(-FirstPlotX,FirstPlotY,'-',-SecondPlotX,SecondPlotY,'-')
    %legend('1st Surface charge density','2nd Surface charge density','location', 'northwest')
    text(0,FirstPlotY(1),sprintf('%0.3g',FirstPlotY(1)),'horizontalAlignment', 'right', 'VerticalAlignment', 'top')
    %text(0,SecondPlotY(1),sprintf('%0.3g',SecondPlotY(1)),'horizontalAlignment', 'right', 'VerticalAlignment', 'top')
else
    plot(Plot181,Plot182,'^-')
    legend('1st Surface charge density','location', 'northwest')
    text(0,Plot182(1),sprintf('%0.3g',Plot182(1)),'horizontalAlignment', 'right', 'VerticalAlignment', 'top')
end
[pos tipheight thetext]=get_current_value_of('tipheight',handles);
[pos biasv thetext]=get_current_value_of('biasv',handles);
[pos tipradius thetext]=get_current_value_of('tipradius',handles);
%title(['Surface charge densities ( TipHeight=' num2str(tipheight) ' nm, BiasV:' num2str(biasv) ' V )'])
th=title({['Surface charge densities (r)' ],[ ' (TipHeight=' num2str(tipheight) ' nm, BiasV:' num2str(biasv) ' V'  ', TipRadius:' num2str(tipradius) ' nm' ' )']});
[idx idx] = min(abs(FirstPlotX-xlim));
[idx2 idx2] = min(abs(SecondPlotX-xlim));
yaxlim_min=min([FirstPlotY(1:idx); SecondPlotY(1:idx2) ]);
yaxlim_max=max(Plot182);
if(yaxlim_min==yaxlim_max); yaxlim_min=-1; yaxlim_max=1; end
if(~handles.is_cycle); axis([-xlim 0 yaxlim_min yaxlim_max]); end
xlabel('Radial distance [nm]','fontsize',12);
ylabel('Surface charge densities [cm^{-3}]','fontsize',12);
%yl = get(gca,'ytick');
%set(gca,'yticklabel',sign(yl).*10.^abs(yl))
%symlog(gca,'y')
%--------------------------
inset=0;
if(inset)
    apos=get(gca,'Position');
    axes('Position',[apos(1)+apos(3)/20 apos(2)+apos(4)/20 apos(3)/2 apos(4)/2]);
    box on
```

```
    plot(-FirstPlotX,FirstPlotY,'-',-SecondPlotX,SecondPlotY,'-')
    set(gca, 'YAxisLocation', 'right', 'XAxisLocation', 'top')
    if(~handles.is_cycle); axis([-xlim 0 yaxlim_min yaxlim_max]); end

    disp('Hello');
end

if(0)
    figure
    theta = linspace(0,2*pi,length(SecondPlotX));
    xx = bsxfun(@times,SecondPlotX,cos(theta));
    yy = bsxfun(@times,SecondPlotX,sin(theta));
    zz = repmat(SecondPlotY,1,length(theta));
    %surf(xx,yy,zz, 'EdgeColor', 'k','LineStyle',':','FaceLighting','flat')
    %set(gca, 'XScale', 'linear', 'YScale', 'linear', 'ZScale', 'log')
    contourf(xx,yy,zz,length(SecondPlotX)/2)
    axiss=axis;
    if(~handles.is_cycle); axis([-xlim xlim -xlim xlim]); end
    [idx idx] = min(abs(SecondPlotX-xlim));
    c=colorbar('location','eastoutside');
    c.Label.String = 'Surface charge densities [cm^{-3}]';
    %caxis([SecondPlotY(idx),max(SecondPlotY)])
    %set(c,'fontsize',12);
    xlabel('radial distance [nm]','fontsize',12);
    ylabel('radial distance [nm]','fontsize',12);
    [pos tipheight thetext]=get_current_value_of('tipheight',handles);
    [pos biasv thetext]=get_current_value_of('biasv',handles);
    title(['Surface charge densities [cm^{-3}] ( TipHeight=' num2str(tipheight) ' nm, BiasV:' num2str(biasv) ' V )'])
    %view(2)
end

if(handles.is_cycle)
    if(handles.xaxlim_max < 0); handles.xaxlim_max=0; end
    if(handles.xaxlim_min > -xlim); handles.xaxlim_min=-xlim; end
    if(handles.yaxlim_max < yaxlim_max); handles.yaxlim_max=yaxlim_max; end
    if(handles.yaxlim_min > yaxlim_min); handles.yaxlim_min=yaxlim_min; end
    %if(handles.zaxlim_max < max(max(zz))); handles.zaxlim_max=max(max(zz)); end
    %if(handles.zaxlim_min > min(min(zz))); handles.zaxlim_min=min(min(zz)); end
end
%------------------------------------------------------------------------
function handles=btn_current_density_plot(handles)
vfolder=get_version_folder(handles);
files=dir([vfolder '/fort.14']);
if(isempty(files)); set(handles.version_info,'string' ,{'File not found for surface potentials.'}); return; end

if(~handles.is_cycle)
    [pos tipheight thetext]=get_current_value_of('tipheight',handles);
    figure('Name','SinglePlot');
    Plot14=load([vfolder '/' files(1).name]);
    Plot141= Plot14(:,1);
    Plot142= Plot14(:,2);

    plot(Plot141,Plot142,'*'); hold on;
    axis([min(Plot141) max(Plot141) min(Plot142) max(Plot142)]);
    axiss=axis;

    xlabel('Bias Voltage [V]','fontsize',12);
    ylabel('Current density [A/nm^2]','fontsize',12);
    title(['Current density ( TipHeight=' num2str(tipheight) ' nm )'])
end

st2 = fileread([vfolder '/' files(1).name]);
[fid,msg] = fopen('current_density_data.txt','at');
%assert(fid>=3,msg)
fprintf(fid,'%s',st2);
fclose(fid);

%------------------------------------------------------------------------
function plot_charge_densities_z_Callback(hObject, eventdata, handles)
plot_charge_densities_z(handles)
%------------------------------------------------------------------------
function plot_charge_densities_r_Callback(hObject, eventdata, handles)
plot_charge_densities_r(handles)
%------------------------------------------------------------------------
function plot_conductance_vs_v_Callback(hObject, eventdata, handles)
% provides the conductance dI/dV (A/(V nm^2)) (column 2) as a function of sample voltage (V) (column 1). Also, columns 3 and 4 provide the contributions to the conductance of extended states and localized states, respectively. Separate contributions from the valence band and conduction band go in to FORT.93 and FORT.94, respectively.
vfolder=get_version_folder(handles);
files=dir([vfolder '/fort.15']);
if(isempty(files)); set(handles.version_info,'string' ,{'File not found for conductance vs V plot.'}); return; end
xlim=min([str2num(get(handles.in_xlim,'string')) str2num(get(handles.in_ylim,'string'))]);
figure('Name','SinglePlot')
Plot14=load([vfolder '/' files(1).name]);
Plot141= Plot14(:,1); % Voltage
Plot142= Plot14(:,2); % Current
Plot143= Plot14(:,3); % contributions to the current of extended states
Plot144= Plot14(:,4); % contributions to the current of  localized states
```

```
plot(Plot141,Plot142,'o')
hold on
plot(Plot141,Plot143,'+',Plot141,Plot144,'x')
xlabel('Voltage [V]','fontsize',12);
ylabel('Conductance dI/dV [A/(V nm^2)]','fontsize',12);
[pos tipheight thetext]=get_current_value_of('tipheight',handles);
[pos biasv thetext]=get_current_value_of('biasv',handles);
title(['Conductance dI/dV as a function of sample voltage ( TipHeight=' num2str(tipheight) ' nm'])
legend('Current', 'Extended states current contribution','Localized states current contribution','
    location', 'southeast')
% if(min(Plot142)~=max(Plot142))
%     axis([min(Plot141) max(Plot141) min(Plot142) max(Plot142)]);
% else
%     xlim([min(Plot141) max(Plot141)]);
% end
%-------------------------------------------------------------------------
%------------------------  RUN CYCLES  ------------------------------------
%-------------------------------------------------------------------------
function btn_run_cycle(variable,eventdata, handles)
handles.is_cycle=1; %guidata(hObject, handles);
in_min=str2num(get(handles.in_min_cycle,'string'));
in_max=str2num(get(handles.in_max_cycle,'string'));
in_step=str2num(get(handles.in_step_cycle,'string'));
if(in_max<in_min); in_step=-abs(in_step); else in_step=abs(in_step); end
%array=linspace(in_min,in_max,abs((in_max-in_min)/in_step)+1);
array=[in_min:in_step:in_max];
if(strcmp(variable,'Acceptors') || strcmp(variable,'Donors') || strcmp(variable,'DOSS1'))
    array=logspace(in_min,in_max,((in_max-in_min)+1));
end
inputs_info=get(handles.uictrl_info,'string');
[variablepos value thetext]=get_current_value_of(variable,handles);
[biasvpointspos value biasvpointstext]=get_current_value_of('biasvpoints',handles);
inputs_info{biasvpointspos}=['1' biasvpointstext];

set(handles.version_info,'string',{''});
vfolder=get_version_folder(handles);
delete(['./Last_run/*'])
count=1;
for ivariable = array
    if(length(get(handles.version_info,'string'))>12); set(handles.version_info,'string',{''});
        end
    add_to_info(handles,[variable ': ', num2str(ivariable)]);
    inputs_info{variablepos}=[num2str(ivariable) thetext];
    set(handles.uictrl_info,'string',inputs_info);
    btn_single_run_Callback(handles.btn_single_run, eventdata, handles)
    fortFiles = dir([ vfolder '/fort.' '*']);
    for i=1:length(fortFiles)
        copyfile([vfolder '/' fortFiles(i).name], ['./Last_run/frame' num2str(count) '_' fortFiles
            (i).name], 'f')
    end
    count=count+1;
end
set(handles.version_info,'string',{'Cycles finished'});
handles.is_cycle=0;
%-------------------------------------------------------------------------
function btn_thz_pulse_Callback(hObject, eventdata, handles)
handles.xaxlim_max=0; handles.xaxlim_min=inf;
handles.yaxlim_max=0; handles.yaxlim_min=inf;
moviename=['Movie_THzPulse_Band_diagram'];
handles.is_cycle=1; %guidata(hObject, handles);
writerObj = VideoWriter([moviename '.mp4'],'MPEG-4');
in_sec_per_frame=str2num(get(handles.in_sec_per_frame,'string'));
writerObj.FrameRate = in_sec_per_frame; % How many frames per second.

[biaspos value thetext]=get_current_value_of('biasv',handles);
inputs_info=get(handles.uictrl_info,'string');
set(handles.version_info,'string',{''});

tlim=1.2;
V0=str2num(get(handles.in_vmax,'string')); %V
THzPoints=str2num(get(handles.in_thz_points,'string'));
if(THzPoints<5)
    THzWaveform=load('THzWaveform001.txt');
    t=THzWaveform(:,1)'; % -min(THzWaveform(:,1))
    VTHz=-THzWaveform(:,2)';
    VTHz=(VTHz/max(abs(VTHz)))*V0; % <-- To Normalize
    writerObj.FrameRate = 16;
else
    t=linspace(-tlim-0.2,tlim,THzPoints);
    VTHz=(1.278*V0)*exp(-3.25.*t.^2).*sin(1.6*pi()*t);
end
open(writerObj);
count=0;
for biasV = VTHz
    count=count+1;
    if(length(get(handles.version_info,'string'))>12); set(handles.version_info,'string',{''});
        end
    add_to_info(handles,['BiasV: ', num2str(biasV)]);
    inputs_info{biaspos}=[num2str(biasV) thetext];
    set(handles.uictrl_info,'string',inputs_info);
    btn_single_run_Callback(handles.btn_single_run, eventdata, handles)
        btn_band_diagram_plot(handles);
```

```
        f2=plot_to_subplots(t,VTHz,count,gcf);
        writeVideo(writerObj, getframe(f2));
    close(f2)

end

if(get(handles.is_surface_pot_3d,'value'))
    for i=1:1:count
        f1=openfig(['fig_' num2str(i) '.fig']);
        caxis([handles.zaxlim_min handles.zaxlim_max]);
        f2=plot_to_subplots(t,VTHz,i,f1);
        writeVideo(writerObj, getframe(f2));
        close(f2)
    end
    delete(['fig*.fig'])
end
close(writerObj);
set(handles.version_info,'string',{'Cycles finished'});
handles.is_cycle=0;
%---------------------------------------------------------------------------
%----------------------   MOVIE CREATION   ---------------------------------
%---------------------------------------------------------------------------
function btn_create_movie_Callback(hObject, eventdata, handles)
set(handles.version_info,'string' ,{'In progress...'});
handles.is_cycle=1; %guidata(hObject, handles);
numframes=dir(['./Last_run/frame*fort.9']);
if(length(numframes)==0); set(handles.version_info,'string' ,{'Files from last run not found.'});
     return; end
vfolder=get_version_folder(handles);
handles.zaxlim_max=0; handles.zaxlim_min=inf;
handles.xaxlim_max=0; handles.xaxlim_min=inf;
handles.yaxlim_max=0; handles.yaxlim_min=inf;
moviename=['Movie'];
writerObj = VideoWriter([moviename '.mp4'],'MPEG-4');
in_sec_per_frame=str2num(get(handles.in_sec_per_frame,'string'));
writerObj.FrameRate = in_sec_per_frame; % How many frames per second.
open(writerObj);
btn_plots=get(get(handles.btn_group_plots,'SelectedObject'),'Tag');
if (isfile('potential_at_surface_values.txt') && strcmp(btn_plots,'is_surface_pot_z'));     delete
     ('potential_at_surface_values.txt'); end
if (isfile('potential_decay_tau.txt') && strcmp(btn_plots,'is_surface_pot_z'));     delete('
     potential_decay_tau.txt'); end
if (isfile('current_density_data.txt') && strcmp(btn_plots,'is_current_density'));     delete('
     current_density_data.txt'); end
if (isfile('radial_potential_at_surface_FWHM.txt') && strcmp(btn_plots,'is_surface_pot_r'));
     delete('radial_potential_at_surface_FWHM.txt'); end
for i=1:length(numframes)
    fortFiles = dir([ './Last_run/frame' num2str(i) '*']);
    for j=1:length(fortFiles)
        a=(strfind(fortFiles(j).name, '_')+1);
        copyfile(['./Last_run/' fortFiles(j).name], [vfolder '/' fortFiles(j).name(a:end)], 'f')
    end
    switch btn_plots
        case 'is_band_diagram'
            moviename='band_diagram';
            handles=btn_band_diagram_plot(handles);
            %sp = findobj( 'Type', 'Figure', 'Name', 'SinglePlot' );
            %writeVideo(writerObj, getframe(sp));
            %savefig(sp,['./Last_run/' moviename '_fig_' num2str(i)],'compact');
            sp = findobj( 'Type', 'Figure', 'Name', 'SinglePlot' );
            close(sp)
        case 'is_contours'
            files=dir([vfolder '/fort.2*']);
            if(isempty(files)); set(handles.version_info,'string' ,{'Files not found for potential
                 contours.'}); return; end
            moviename='equipot_contours';
            btn_contours_plot(handles)
            sp = findobj( 'Type', 'Figure', 'Name', 'SinglePlot' );
            %savefig(sp,['./Last_run/' moviename '_fig_' num2str(i)],'compact');
            writeVideo(writerObj, getframe(sp));
            close(sp)
        case 'is_surface_pot_z'
            moviename='surface_pot_z';
            handles=btn_surface_pot_z_plot(handles);
            sp = findobj( 'Type', 'Figure', 'Name', 'SinglePlot' );
            savefig(sp,['./Last_run/' moviename '_fig_' num2str(i)],'compact');
            close(sp)
        case 'is_surface_pot_r'
            moviename='surface_pot_r';
            handles=btn_surface_pot_r_plot(handles);
            sp = findobj( 'Type', 'Figure', 'Name', 'SinglePlot' );
            savefig(sp,['./Last_run/' moviename '_fig_' num2str(i)],'compact');
            close(sp)
        case 'is_surface_pot_3d'
            moviename='surface_pot_3d';
            handles=btn_surface_pot_3d_plot(handles);
            sp = findobj( 'Type', 'Figure', 'Name', 'SinglePlot' );
            savefig(sp,['./Last_run/' moviename '_fig_' num2str(i)],'compact');
            close(sp)
        case 'is_charge_den_z'
            moviename='charge_density_z';
            handles=plot_charge_densities_z(handles);
```

```
            sp = findobj( 'Type', 'Figure', 'Name', 'SinglePlot' );
            savefig(sp,['./Last_run/' moviename '_fig_' num2str(i)],'compact');
            close(sp)
        case 'is_charge_den_r'
            moviename='charge_density_r';
            handles=plot_charge_densities_r(handles);
            sp = findobj( 'Type', 'Figure', 'Name', 'SinglePlot' );
            savefig(sp,['./Last_run/' moviename '_fig_' num2str(i)],'compact');
            close(sp)
        case 'is_current_density'
            moviename='current_density';
            btn_current_density_plot(handles);
    end

end

if(strcmp(moviename,'band_diagram'))
    for i=1:length(numframes)
        fortFiles = dir([ './Last_run/frame' num2str(i) '*']);
        for j=1:length(fortFiles)
            a=(strfind(fortFiles(j).name, '_')+1);
            copyfile(['./Last_run/' fortFiles(j).name], [vfolder '/' fortFiles(j).name(a:end)], 'f')
        end
        handles=btn_band_diagram_plot(handles);
        sp = findobj( 'Type', 'Figure', 'Name', 'SinglePlot' );
        savefig(sp,['./Last_run/' moviename '_fig_' num2str(i)],'compact');
        close(sp)
    end
end
FigFiles = dir(['./Last_run/' moviename '_fig_' '*']);
if(~strcmp(moviename,'equipot_contours')&&~strcmp(moviename,'current_density'))
    for i=1:1:length(FigFiles)
        pause(0.005)
        openfig(['./Last_run/' moviename '_fig_' num2str(i) '.fig']);
        switch btn_plots
            case 'is_band_diagram'
                %disp('Nothing')
                %close(sp)
                %handles=btn_band_diagram_plot(handles);
                %axis([handles.xaxlim_min handles.xaxlim_max handles.yaxlim_min handles.yaxlim_max]);
            case 'is_contours'
                %disp('Nothing')
            case 'is_surface_pot_z'
                axis([handles.xaxlim_min handles.xaxlim_max handles.yaxlim_min handles.yaxlim_max]);
            case 'is_surface_pot_r'
                axis([handles.xaxlim_min handles.xaxlim_max handles.yaxlim_min handles.yaxlim_max]);
            case 'is_surface_pot_3d'
                xlim=min([str2num(get(handles.in_xlim,'string')) str2num(get(handles.in_ylim,'string'))]);
                axis([-xlim xlim -xlim xlim]);
                caxis([handles.zaxlim_min handles.zaxlim_max]);
            case 'is_charge_den_z'
                axis([handles.xaxlim_min handles.xaxlim_max handles.yaxlim_min handles.yaxlim_max]);
            case 'is_charge_den_r'
                axis([handles.xaxlim_min handles.xaxlim_max handles.yaxlim_min handles.yaxlim_max]);
        end
        pause(0.1)
        sp = findobj( 'Type', 'Figure', 'Name', 'SinglePlot' );
        writeVideo(writerObj, getframe(sp));
        close(sp)
    end
end
if(strcmp(moviename,'current_density'))
    vfolder=get_version_folder(handles);
    [pos tipheight thetext]=get_current_value_of('tipheight',handles);
    if(isempty('current_density_data.txt')); set(handles.version_info,'string' ,{'File current_density_data.txt not found for current density.'}); return; end
    figure('Name','SinglePlot');
    Plot14=load('current_density_data.txt');
    Plot141= Plot14(:,1);
    Plot142= Plot14(:,2);

    plot(Plot141,Plot142); hold on;
    axis([min(Plot141) max(Plot141) min(Plot142) max(Plot142)]);

    xlabel('Bias Voltage [V]','fontsize',12);
    ylabel('Current density [A/nm^2]','fontsize',12);
    title(['Current density ( TipHeight=' num2str(tipheight) ' nm )'])
    sp = findobj( 'Type', 'Figure', 'Name', 'SinglePlot' );
    savefig(sp,['./' moviename ],'compact');
    saveas(sp,['./' moviename '.png'])
    for i=1:1:10
        writeVideo(writerObj, getframe(sp));
    end
    close(sp)
end
```

```
%count=41; handles.xaxlim_min=-60; handles.xaxlim_max=0; handles.yaxlim_min=-1.01e15; handles.yaxlim_max=6.96e19;
close(writerObj);
copyfile(['Movie.mp4'], [moviename '.mp4'], 'f')
delete(['Movie.mp4'])
handles.is_cycle=0;
set(handles.version_info,'string' ,{'Movie created.'});
%-------------------------------------------------------------------------
%--------------------------  SUBROUTINES  --------------------------------
%-------------------------------------------------------------------------
function semitip_version_Callback(hObject, eventdata, handles)
fname=load_inputs_from_files(handles);
M=textread(fname,'%s','delimiter','\n');
set(handles.uictrl_info,'string',M)
set(handles.custom_inputs,'value',1)
set(handles.btn_save,'enable','off')
%-------------------------------------------------------------------------
function fname=load_inputs_from_files(handles)
switch get(handles.semitip_version,'value')
    case 1
        goldenfname='./v5/fort_backup.9';
        set(handles.version_info,'string','This program computes the electrostatic potential and resulting tunnel current produced by a metallic probe tip near a semiconductor.')
    case 2
        goldenfname='./v6/fort_Uni1.9';
        set(handles.version_info,'string','Potential computations for a uniform semiconductor, in a planar geometry (1D potential).')
    case 3
        goldenfname='./v6/fort_UniInt1.9';
        set(handles.version_info,'string','Potential computations for a uniform semiconductor, along with computations of tunnel current using numerical integration of Schrodingers equation, in a planar geometry (the potential is 1D, in the z direction, but the current is computed with full inclusion of quantum states traveling in the x and y directions as well).')
    case 4
        goldenfname='./v6/fort_UniIntSC1.9';
        set(handles.version_info,'string','Potential computations for a uniform semiconductor, along with computations of tunnel current using numerical integration of Schrodingers equation, in a planar geometry. The potential is computed self-consistently, using the quantum states from the solution to Schrodingers equation, so that e.g. inversion or accumulation layer states are computed exactly.')
    case 5
        goldenfname='./v6/fort_Uni2.9';
        set(handles.version_info,'string','Potential computations for a uniform semiconductor, with a hyperbolic shaped probe tip, in a 3D geometry with azimuthal symmetry.')
    case 6
        goldenfname='./v6/fort_UniInt2.9';
        set(handles.version_info,'string','Potential computations for a uniform semiconductor, along with computations of tunnel current using numerical integration of Schrodingers equation along the central axis, in a 3D geometry with azimuthal symmetry.')
    case 7
        goldenfname='./v6/fort_UniIntSC2.9';
        set(handles.version_info,'string','Potential computations for a uniform semiconductor, along with computations of tunnel current using numerical integration of Schrodingers equation along the central axis. The potential is computed self-consistently, using the quantum states from the solution to Schrodingers equation that are computed at a series of different radial distances from the central axis.')
    case 8
        goldenfname='./v6/fort_Uni3.9';
        set(handles.version_info,'string','Potential computations for a uniform semiconductor, in a fully 3D geometry.')
    case 9
        goldenfname='./v6/fort_UniInt3.9';
        set(handles.version_info,'string','Potential computations for a uniform semiconductor, along with computations of tunnel current using numerical integration of Schrodingers equation along the central axis, in a fully 3D geometry.')
    case 10
        goldenfname='./v6/fort_UniPlane3.9';
        set(handles.version_info,'string','Potential computations for a uniform semiconductor, in a fully 3D geometry. The tunnel current is computed using a plane wave expansion method. The plane wave method necessarily includes only a relatively small spatial region centered about the point on the semiconductor surface opposite the apex of the probe tip, but the results nevertheless provide a good approximation in many cases. A localized potential such as occurs e.g. for a quantum dot can be included in the computation of the tunnel current.')
    otherwise
end
vfolder=get_version_folder(handles);
fname=[vfolder '/fort.9'];
if exist(fname, 'file');
    delete(fname);
end
copyfile(goldenfname, fname)
%-------------------------------------------------------------------------
function btn_save_Callback(hObject, eventdata, handles)
if(get(handles.custom_inputs,'value')==1); return; end
custom_folder='./Custom_Inputs';
custom_name=get(handles.custom_inputs,'string');
%a=(strfind(custom_name{get(handles.custom_inputs,'value')}, '_')+1)
%custom_name=[custom_folder '/' custom_name(a(2):end-2)]
custom_name=[custom_folder '/' custom_name{get(handles.custom_inputs,'value')}];
```

```
fileID = fopen(custom_name,'w');
inputs_info=get(handles.uictrl_info,'string');
for row = 1:length(inputs_info)
    fprintf(fileID,'%s\n',inputs_info{row});
end
fclose(fileID);
%-------------------------------------------------------------------------
function vfolder=get_version_folder(handles)
switch get(handles.semitip_version,'value')
    case 1
        vfolder='./v5';
    case {2,3,4,5,6,7,8,9,10}
        vfolder='./v6';
    otherwise
end
%-------------------------------------------------------------------------
function exe_version=get_exe_version(value)
switch value
    case 1
        exe_version='semitip_v5';
    case 2
        exe_version='Uni1';
    case 3
        exe_version='UniInt1';
    case 4
        exe_version='UniIntSC1';
    case 5
        exe_version='Uni2';
    case 6
        exe_version='UniInt2';
    case 7
        exe_version='UniIntSC2';
    case 8
        exe_version='Uni3';
    case 9
        exe_version='UniInt3';
    case 10
        exe_version='UniPlane3';
    otherwise
end
%-------------------------------------------------------------------------
function close_figures(hObject, eventdata, handles)
figs = get(0,'children');
figs(figs == gcf) = []; % delete your current figure from the list
close(figs)
%-------------------------------------------------------------------------
function ListOfFileNames=Load_Filenames(custom_folder)
% ================================================================
% --- Load up the listbox with image files in folder
ListOfFileNames = {};
if (nargin==0); custom_folder = './STM_Images'; end
if exist(custom_folder,'dir') == false
    msgboxw(['Folder ' custom_folder ' does not exist.']);
    return;
end
% If it gets to here, the folder is good.
ImageFiles = dir([custom_folder '/*.*']);
for Index = 1:length(ImageFiles)
    baseFileName = ImageFiles(Index).name;
    [folder, name, extension] = fileparts(baseFileName);
    extension = upper(extension);
    switch lower(extension)
        case {'.9'}
            % Allow only PNG, TIF, JPG, or BMP images
            ListOfFileNames = [ListOfFileNames baseFileName];
        otherwise
    end
end
return
%-------------------------------------------------------------------------
function custom_inputs_Callback(hObject, eventdata, handles)
if(get(handles.custom_inputs,'value')==1);
    set(handles.btn_save,'enable','off'); return;
else   set(handles.btn_save,'enable','on');
end
custominputname=get(handles.custom_inputs,'string');
goldenfname=custominputname{get(handles.custom_inputs,'value')};
a=(strfind(goldenfname, '_')+1); b=(strfind(goldenfname(a(1):end), '_')-1);
switch goldenfname(a(1):b(1)+a(1)-1)
    case 'semitip-v5'
        value=1;
    case 'Uni1'
        value=2;
    case 'UniInt1'
        value=3;
    case 'UniIntSC1'
        value=4;
    case 'Uni2'
        value=5;
    case 'UniInt2'
        value=6;
    case 'UniIntSC2'
```

```
        value=7;
    case 'Uni3'
        value=8;
    case 'UniInt3'
        value=9;
    case 'UniPlane3'
        value=10;
    otherwise
end

set(handles.semitip_version,'value',value)
goldenfname=['./Custom_Inputs/' goldenfname];
vfolder=get_version_folder(handles);

fname=[vfolder '/fort.9'];
if exist(fname, 'file');
    delete(fname);
end
copyfile(goldenfname, fname)
M=textread(fname,'%s','delimiter','\n');
set(handles.uictrl_info,'string',M)
%-------------------------------------------------------------------------
function btn_save_as_Callback(hObject, eventdata, handles)
custom_folder='./Custom_Inputs';
cd(custom_folder);
[FileName,PathName] = uiputfile;
[folder, name, extension] = fileparts(FileName);
exe_version=get_exe_version(get(handles.semitip_version,'value'));
vfolder = regexprep(get_version_folder(handles),'[./]','');
name=[vfolder '_' exe_version '_' name '.9'];

fileID = fopen([PathName name],'w');
inputs_info=get(handles.uictrl_info,'string');
for row = 1:length(inputs_info)
    fprintf(fileID,'%s\n',inputs_info{row});
end
fclose(fileID);
cd ..
str=Load_Filenames(custom_folder);
set(handles.custom_inputs,'string',['- Load custom inputs -' str])
%-------------------------------------------------------------------------
function h = circle(x,y,r)
d = r*2; px = x-r; py = y-r;
h = rectangle('Position',[px py d d],'Curvature',[1,1],'LineStyle', '--','EdgeColor','y');
daspect([1,1,1])
%-------------------------------------------------------------------------
function add_to_info(handles,str)
info=get(handles.version_info,'string');
info{end+1} = str;
set(handles.version_info,'string',info);
%-------------------------------------------------------------------------
function [pos value thetext] =get_current_value_of(str,handles)
vfolder = regexprep(get_version_folder(handles),'[./]','');
%outputs_info=textread([vfolder '/fort.16'],'%s','delimiter','\n');
inputs_info=textread([vfolder '/fort.9'],'%s','delimiter','\n');
exe_version=get_exe_version(get(handles.semitip_version,'value'));
name=[vfolder '_' exe_version];
variable_txt='';
switch name
    case 'v5_semitip_v5'   %%  <--- NEED TO SET VALUES FOR V5 VERSION
        tipshank=2;
        tipheight=3;
        tipradius=4;
        protrusionradius=5;
        workF=6;
        donorconc=7;
        acceptorconc=8;
        bandgap=9;
        modulationv=19;
        doss1=23;
        neutralitylvl1=24;
        fwhm1=25;
        centroidgauss1=26;
        doss2=27;
        neutralitylvl2=28;
        fwhm2=29;
        centroidgauss2=30;
        eAffinity=31;
        Ef=32;
        outputparam=50;
        biasvpoints=51;
        biasv=52;
    case {'v6_Uni1','v6_UniInt1','v6_UniIntSC1'}
        tipheight=2;
        workF=3;
        donorconc=4;
        acceptorconc=5;
        bandgap=6;
        doss1=18;
        neutralitylvl1=19;
        fwhm1=20;
        centroidgauss1=21;
```

```
        doss2=22;
        neutralitylvl2=23;
        fwhm2=24;
        centroidgauss2=25;
        outputparam=34;
        biasvpoints=35;
        biasv=36;
    case {'v6_Uni1'}
        contourspacing=38;
        eAffinity=39;
        Ef=40;
    case {'v6_UniInt1','v6_UniIntSC1'}
        eAffinity=37;
        Ef=38;
        semicdepth=42;
        modulationv=43;
    case {'v6_Uni2','v6_UniInt2','v6_UniIntSC2'}
        tipshank=2;
        tipheight=3;
        tipradius=4;
        protrusionradius=5;
        workF=6;
        donorconc=7;
        acceptorconc=8;
        bandgap=9;
        doss1=21;
        neutralitylvl1=22;
        fwhm1=23;
        centroidgauss1=24;
        doss2=25;
        neutralitylvl2=26;
        fwhm2=27;
        centroidgauss2=28;
        outputparam=38;
        biasvpoints=39;
        biasv=40;
        contourspacing=42;
    case {'v6_UniInt2','v6_UniIntSC2'}
        eAffinity=43;
        Ef=44;
        semicdepth=48;
        modulationv=49;
    case {'v6_Uni3','v6_UniInt3','v6_UniPlane3'}
        tipshank=2;
        tipheight=3;
        tipradius=4;
        protrusionradius=5;
        workF=6;
        donorconc=7;
        acceptorconc=8;
        bandgap=9;
        doss1=21;
        neutralitylvl1=22;
        fwhm1=23;
        centroidgauss1=24;
        doss2=25;
        neutralitylvl2=26;
        fwhm2=27;
        centroidgauss2=28;
        outputparam=40;
        biasvpoints=41;
        biasv=42;
        contourspacing=44;
    case {'v6_UniInt3','v6_UniPlane3'}
        eAffinity=46;
        Ef=47;
        modulationv=52;
    otherwise
        disp('Inputs positions not found')
end
switch lower(str)
    case {'tipheight','tip_height'}
        pos=find(not(cellfun('isempty', strfind(inputs_info, 'tip-sample separation'))));
    case {'tip_shank','tipshank'}
        pos=find(not(cellfun('isempty', strfind(inputs_info, 'shank slope'))));
    case {'tip_radius','tipradius'}
        pos=find(not(cellfun('isempty', strfind(inputs_info, 'tip radius'))));
    case {'workf','work_f','workfunction'}
        pos=find(not(cellfun('isempty', strfind(inputs_info, 'contact potential'))));
    case {'bandgap', 'band_gap'}
        pos=find(not(cellfun('isempty', strfind(inputs_info, 'band gap'))));
    case {'outputparam', 'output_parameter'}
        pos=find(not(cellfun('isempty', strfind(inputs_info, 'output parameter'))));
    case {'bias_v','biasv'}
        %          a=(strfind(inputs_info{biasv}, ' '));
        %          if(isempty(a)); a=length(inputs_info{biasv})+1; end
        %          value=str2num(inputs_info{biasv}(1:a(1)-1));
        %variable_txt=inputs_info{biasv};
        pos=biasv;
    case {'bias_v_points','biasvpoints'}
        pos=find(not(cellfun('isempty', strfind(inputs_info, 'voltage points'))));
    case {'contourspacing', 'contour_spacing'}
```

```
        pos=find(not(cellfun('isempty', strfind(inputs_info, 'spacing of potential contours'))));
    case {'eaffinity','e_affinity'}
        pos=find(not(cellfun('isempty', strfind(inputs_info, 'electron affinity'))));
    case {'fermienergy','ef','fermi_energy'}
        pos=find(not(cellfun('isempty', strfind(inputs_info, 'Fermi energy of tip'))));
    case {'temperature'}
        pos=find(not(cellfun('isempty', strfind(inputs_info, 'temperature (K)'))));
    case {'doss1','dos'}
        pos=doss1;
    case {'neutrality','neutrality1','neutralitylvl','neutralitylvl1'}
        pos=neutralitylvl1;
    case {'fwhm1','fwhm'}
        pos=fwhm1;
    case {'centroidgauss1','centroidgauss'}
        pos=centroidgauss1;
    case {'doss2'}
        pos=doss2;
    case {'neutrality2','neutralitylvl2'}
        pos=neutralitylvl2;
    case {'fwhm2'}
        pos=fwhm2;
    case {'centroidgauss2'}
        pos=centroidgauss2;
    case {'donors','donorconc','donor_concentration'}
        pos=donorconc;
    case {'acceptors','acceptorconc','acceptor_concentration'}
        pos=acceptorconc;
end
variable_txt=inputs_info{pos};
a=(strfind(variable_txt, ' '));
if(isempty(a)); a=length(variable_txt)+1; end
value=str2num(variable_txt(1:a(1)-1));
thetext=variable_txt(a(1):end);
%-----------------------------------------------------------------------
function btn_database_Callback(hObject, eventdata, handles)
web('https://1drv.ms/x/s!AkYi44QZrVK2pUyEWfchhl5LS4ym','-browser');
%-----------------------------------------------------------------------
function btn_extended_info_Callback(hObject, eventdata, handles)
web('http://www.andrew.cmu.edu/user/feenstra/semitip_v6/TechManual.html#Input','-browser');
%-----------------------------------------------------------------------
function gauss_dist(xmin,xmax,handles)

[pos doss1 thetext]=get_current_value_of('doss1',handles);
[pos neutralitylvl1 thetext]=get_current_value_of('neutralitylvl1',handles);
[pos fwhm1 thetext]=get_current_value_of('fwhm1',handles);
[pos centroidgauss1 thetext]=get_current_value_of('centroidgauss1',handles);
sigma1=fwhm1/(2*sqrt(2*log(2)));
if(doss1>0 && fwhm1 ~= 0)
    y =linspace(centroidgauss1-2*fwhm1,centroidgauss1+2*fwhm1,100);
    norm =normpdf2(y,centroidgauss1,sigma1);
    norm=norm/(max(norm))*(xmax-xmin)+xmin;
    plot(norm,y,'g')
    hold on
    plot([xmin xmax], [neutralitylvl1 neutralitylvl1], '--m')
    text(xmax,neutralitylvl1,'E_N','color','m')
    text(xmax,centroidgauss1,'SS','color','g','horizontalAlignment', 'right')
    %plot([centroidgauss1 centroidgauss1], [0 max(norm)], '--k')
    %     plot([-3 5], [max(norm)/2 max(norm)/2], '--k')
elseif(doss1>0 && fwhm1==0)
    [pos Eg thetext]=get_current_value_of('bandgap',handles);
    plot([xmax xmax],[0 Eg],'g')  %Vertical straight line
    hold on
    plot([0 xmax],[Eg Eg],'g')%Horizontal straight line
    plot([0 xmax],[0 0],'g')%Horizontal straight line
    plot([xmin xmax], [neutralitylvl1 neutralitylvl1], '--m')
    text(xmax,neutralitylvl1,' E_N','color','m')
    text(xmax,Eg,'SS','color','g','horizontalAlignment', 'right')
    %plot([centroidgauss1 centroidgauss1], [0 max(x)], '--k')
end
[pos doss2 thetext]=get_current_value_of('doss2',handles);
[pos neutralitylvl2 thetext]=get_current_value_of('neutralitylvl2',handles);
[pos fwhm2 thetext]=get_current_value_of('fwhm2',handles);
[pos centroidgauss2 thetext]=get_current_value_of('centroidgauss2',handles);
sigma2=fwhm2/(2*sqrt(2*log(2)));
if(doss2*fwhm2>0)
    y =linspace(centroidgauss2-2*fwhm2,centroidgauss2+2*fwhm2,100);
    norm =normpdf2(y,centroidgauss2,sigma2);
    norm=norm/(max(norm))*(xmax-xmin)+xmin;
    plot(norm,y,'y')
    hold on
    %plot([xmin xmax], [neutralitylvl2 neutralitylvl2], '--y')
    %text(xmax,neutralitylvl2,'E_N','color','y')
end
%-----------------------------------------------------------------------
function y = normpdf2(x, mu, sigma)
f = @(u,o,x) 1/sqrt(2*pi*o^2) * exp(-(x-u).^2 / (2*o^2));
y = feval(f, mu, sigma, x);
%-----------------------------------------------------------------------
function f2=plot_to_subplots(t,VTHz,i,f1)
f1=gcf;
ax1=gca;
aux=get(ax1,'children');
```

```
xlab=get(get(ax1,'xlabel'),'string');
ylab=get(get(ax1,'ylabel'),'string');
tit=get(get(ax1,'title'),'string');
axlim=get(ax1,'xlim');
aylim=get(ax1,'ylim');
screensize=get(0,'Screensize'); screensize=screensize*0.8;
f2=figure('Position', screensize);
s1 = subplot(1,2,1);
plot(t,VTHz,'c')
hold on
mark=plot(t(i),VTHz(i),'bo');
title(['Theoretical THz pulse ( E-Field=' num2str(VTHz(i))  ' V )'])
xlabel('time [ps]')
ylabel('E-Field [V]')
s2 = subplot(1,2,2);
for j=1:size(aux)
    fig2 = aux(j);
    copyobj(fig2,s2);
    hold on
end
xlabel(xlab);ylabel(ylab);title(tit); xlim(axlim); ylim(aylim);
close(f1)
%-----------------------------------------------------------------------
function btn_ivcurve_Callback(hObject, eventdata, handles)
exe_version=get_exe_version(get(handles.semitip_version,'value'));
if(isempty(strfind(exe_version,'Int'))); set(handles.version_info,'string' ,{[exe_version ' version does not support IV curves.']}); return; end
in_min=str2num(get(handles.in_min_cycle,'string'));
in_max=str2num(get(handles.in_max_cycle,'string'));
in_step=str2num(get(handles.in_step_cycle,'string'));
array=linspace(in_min,in_max,abs((in_max-in_min)/in_step)+1);
biasVarray = sprintf('%0.5g,' , array);
biasVarray = biasVarray(1:end-1); % strip final comma
[biaspos value biastext]=get_current_value_of('biasV',handles);
[biaspointpos value biaspointstext]=get_current_value_of('biasVpoints',handles);
[pos value outputtext]=get_current_value_of('outputparam',handles);
inputs_info=get(handles.uictrl_info,'string');
inputs_info{biaspointpos}=[num2str(length(array)) biaspointstext];
inputs_info{biaspos}=[biasVarray biastext];
inputs_info{biaspointpos-1}=[num2str(3) outputtext];
set(handles.uictrl_info,'string',inputs_info);
set(handles.version_info,'string',{''});

btn_single_run_Callback(handles.btn_single_run, eventdata, handles)
set(handles.version_info,'string',{'IV curve finished'});

vfolder=get_version_folder(handles);
files=dir([vfolder '/fort.14']);

if(isempty(files)); set(handles.version_info,'string' ,{'File not found for IV curves.'}); return; end
xlim=min([str2num(get(handles.in_xlim,'string')) str2num(get(handles.in_ylim,'string'))]);
figure
Plot14=load([vfolder '/' files(1).name]);
Plot141= Plot14(:,1); % Voltage
Plot142= Plot14(:,2); % Current
Plot143= Plot14(:,3); % contributions to the current of extended states
Plot144= Plot14(:,4); % contributions to the current of  localized states

plot(Plot141,Plot142)
hold on
plot(Plot141,Plot143,Plot141,Plot144)
xlabel('Voltage [V]','fontsize',12);
ylabel('Current [A/nm^2]','fontsize',12);
[pos tipheight thetext]=get_current_value_of('tipheight',handles);
[pos biasv thetext]=get_current_value_of('biasv',handles);
title(['Current as a function of sample voltage ( TipHeight=' num2str(tipheight) ' nm)'])
legend('Current', 'Extended states current contribution','Localized states current contribution','location', 'southeast')
if(~handles.is_cycle && min(Plot142)~=max(Plot142)); axis([min(Plot141) max(Plot141) min(Plot142) max(Plot142)]); end
%plot_conductance_vs_v(handles);
%plot_charge_densities_z(handles);
%plot_charge_densities_r(handles);
%-----------------------------------------------------------------------
function btn_multiple_run_Callback(hObject, eventdata, handles)
variable_param=get(handles.list_variable_param,'string');
variable_param=variable_param{get(handles.list_variable_param,'value')};
switch variable_param
    case {'Tip Height','Acceptors concentration','Donors concentration','Tip Radius','Shank slope','Temperature'}
        if((str2num(get(handles.in_min_cycle,'string'))<0) || (str2num(get(handles.in_max_cycle,'string'))<0))
            set(handles.version_info,'string','Range cannot be less than 0'); return;
        end
end
switch variable_param
    case 'IV curve'
        btn_ivcurve_Callback(hObject, eventdata, handles)
    case 'Bias Voltage'
        %btn_bias_cycle_Callback(hObject, eventdata, handles)
        btn_run_cycle('BiasV',eventdata, handles)
```

```
    case 'Tip Height'
        btn_run_cycle('TipHeight',eventdata, handles)
    case 'Acceptors concentration'
        btn_run_cycle('Acceptors',eventdata, handles)
    case 'Donors concentration'
        btn_run_cycle('Donors',eventdata, handles)
    case 'Tip Radius'
        btn_run_cycle('TipRadius',eventdata, handles)
    case 'Shank slope'
        btn_run_cycle('TipShank',eventdata, handles)
    case 'Temperature'
        btn_run_cycle('Temperature',eventdata, handles)
    case '1st Density Surface States'
        btn_run_cycle('DOSS1',eventdata, handles)
    case 'THz Pulse Sim'
        btn_thz_pulse_Callback(hObject, eventdata, handles);
end
%---------------------------------------------------------------------
function list_variable_param_Callback(hObject, eventdata, handles)
variable_param=get(handles.list_variable_param,'string');
variable_param=variable_param{get(handles.list_variable_param,'value')};
switch variable_param
    case 'THz Pulse Sim'
        set(handles.in_thz_points,'visible','on')
        set(handles.text12,'visible','on')
        set(handles.in_vmax,'visible','on')
        set(handles.text13,'visible','on')
    otherwise
        set(handles.in_thz_points,'visible','off')
        set(handles.text12,'visible','off')
        set(handles.in_vmax,'visible','off')
        set(handles.text13,'visible','off')
end
%---------------------------------------------------------------------
```

A.2 energy_band_diagram.m

```
function energy_band_diagram(Plot11,bandgap,tipheight,Ef,NeutralityLevel,workF,biasV,
    xlim,ylim)
if (nargin==0)
    vfolder ='./v6/Example2';
    Plot11=load([vfolder '/fort.11']);
    bandgap=1.42;
    tipheight=12;
    NeutralityLevel=bandgap*0.5;
    workF=0.23;
    biasV=1.5;
    disp('Using input values from example')
end
multi=length(xlim);
if(length(biasV)>1); biasV=biasV(end); end
if(length(xlim)==1); xlim=[-xlim xlim]; end
if(length(ylim)==1); ylim=[-ylim ylim]; end
thickLinesWidth=1.8;

TipF=Ef+biasV;

Plot111=-Plot11(Plot11(:,1)>=0,1); % Z distance  (Only values higher than 0, inside
    the sample)
Plot112=Plot11(Plot11(:,1)>=0,2); % Valence Band
%Plot113=Plot11(Plot11(:,1)>=0,3); % Conductive Band
Plot113=Plot112+bandgap;
figure('Name','SinglePlot')
plot(Plot111,Plot112,'b','LineWidth',thickLinesWidth)
hold on;
plot(Plot111,Plot113,'r','LineWidth',thickLinesWidth)

if (nargin<8);
    xlim=max(abs(Plot111(Plot112>max(Plot112)*0.2)));
    ylim=(max(Plot112)+bandgap)*1.2;
    ymin=min([Plot112 ; TipF*1.3 ; -max(Plot112); -0.3/1.2])*1.2;
    xlimr=tipheight+xlim/tipheight;
    xlimr=tipheight+abs(xlim(1))/4+tipheight/4;
```

```
    axis([-xlim xlimr ymin ylim]);
else
    disp('--------');
    xlim(2);
    max([xlim(2)/5+tipheight/4]);
    xlimr=tipheight+max([abs(xlim(1))/5+tipheight/4]);
    if(multi<=1)
        xlim(2)=xlimr;
    else
        %xlimr=tipheight+xlim(2)/tipheight
        if(xlimr > xlim(2)); xlim(2)=xlimr; end
    end
    %%Custom limits:
    %xlim(2)=xlimr;
    %ylim(1)=-0.2;
    %%%%%%%%
    axis([xlim(1) xlim(2) ylim(1) ylim(2)])
end
[idx idx] = min(abs(abs(Plot111)-abs(xlim(1))));
%fill(Plot111,Plot112,'b')
plot([0 0], [ylim(1) ylim(2)], '--k')
plot([tipheight tipheight], [ylim(1) ylim(2)], '--k')
plot([xlim(1) xlim(2)], [Ef Ef],'--c','LineWidth',1.2)
%plot([-xlim 0], [NeutralityLevel NeutralityLevel],'--y')
plot([tipheight xlim(2)], [TipF TipF], 'k','LineWidth',thickLinesWidth)
title(['Energy Band Diagram (BiasV:' num2str(biasV) ' V )'])
xlabel('z distance [nm]')
ylabel('Potential [eV]')
yshift=ylim(2)*0.07;
%text(-xlim*0.95,ylim-yshift,{['Bandgap: ' num2str(bandgap) ' eV']; ['Charge
    neutrality level: ' num2str(NeutralityLevel) ' eV']},'VerticalAlignment', 'top')
     %; ['Neutrality level: ' num2str(NeutralityLevel)] ; ['Fermi Energy: ' num2str(
    Ef) ' eV']
%text(-xlim/2,NeutralityLevel-yshift,'Neutrality level','color','y')
%text(-xlim,Ef,[' E_f ' ])
text(xlim(2),Ef-0.6,['E_f= '  num2str(Ef,'%4.3f') ' '],'Color','c','
    horizontalAlignment', 'right')
text(xlim(1),Plot112(idx)-yshift,' E_v','Color','b')
text(xlim(1),Plot112(idx)+yshift+bandgap,' E_c','Color','r')
text(xlim(1)/2,ylim(1)*0.9,{['(' num2str(biasV) ' V)'];['SEMICONDUCTOR']},'
    horizontalAlignment', 'center','verticalAlignment', 'bottom')
vactxt=text(tipheight/2,ylim(1)*0.9,'VACUUM','rotation', 90);
text((xlim(2)-tipheight)/2+tipheight,ylim(1)*0.9,{['(0 V)'];['TIP']},'
    horizontalAlignment', 'center','verticalAlignment', 'bottom')
text(tipheight,ylim(1)+yshift,[' ' num2str(tipheight) ' nm']) % Tip Height Value
%text(0,max(abs(Plot113))+yshift,num2str(max(abs(Plot113))),'horizontalAlignment', '
    right')  % Max value in Valence Band
%text(0,max(abs(Plot112))+yshift,num2str(max(abs(Plot112))),'horizontalAlignment', '
    right')  % Max value in Conduct Band
text(0,Plot112(1)+yshift,num2str(Plot112(1)),'Color','b','horizontalAlignment', '
    right')  % Max value in Valence Band
text(0,Plot113(1)+yshift,num2str(Plot113(1)),'Color','r','horizontalAlignment', '
    right')  % Max value in Conduct Band
%text((xlim-tipheight)/2+tipheight,TipF+yshift,['Bias= 0 V']) % Bias Voltage value
%text((-xlim)/2,TipF+yshift,['Bias=' num2str(biasV) ' V']) % Bias Voltage value
text(tipheight,TipF+yshift,[num2str(TipF,'%4.3f')]) % Tip Fermi line
```